

UNIVERSITY OF STRATHCLYDE
DEPARTMENT OF PHYSICS

EMP mitigation and novel detection strategies for laser-plasma experiments



by

Eglė Žemaitytė

in partial fulfilment of the requirements for the degree of Doctor of Philosophy in
Physics

2020

Copyright Declaration

This thesis is the result of the author's original research. It has been composed by the author and has not been previously submitted for examination which has led to the award of a degree.

The copyright of the thesis belongs to the author under the terms of the United Kingdom Copyright Act as qualified by University of Strathclyde Regulation 3.50. Due acknowledgement must always be made of the use of any material contained in, or derived from, this thesis.

Signed: 

Date: 11/11/2020

Abstract

Laser driven particle and radiation sources have the potential to become an alternative to conventional accelerators for a number of applications. Many laser-driven sources have been demonstrated, including x-rays, protons, electrons and positrons. The laser driven production of exotic particles such as muons has been theorised. Proposed applications for some of these novel particle and photon sources include a compact source of ions for cancer treatment, electrons for radar imaging, x-rays for probing high density objects, and muons to be deployed for the imaging of large dense structures including nuclear reactor cores and inspect large containers for forbidden fissile elements, to name a few. Ideally, to achieve these applications, laser-driven sources must be developed to have high conversion efficiency, high resolution and controlled directionality.

Electromagnetic pulse (EMP) emission is prevalent in high power laser-plasma interactions and primarily arises due to the return current induced by the ejection of hot electrons from the target. It is important to study these emissions at high power laser facilities as it has been shown to interfere with experimental diagnostics. Many facilities currently under development will be able to produce higher intensity laser pulses at a high repetition rate and therefore EMP may become significantly disruptive to experiments. Due to this, EMP has recently attracted considerable interest and therefore the first two experimental chapters of this thesis focus on EMP energy correlations with proton and electron measurements, and EMP control and mitigation.

The first investigation reports on experimental studies into the EMP scaling with sheath accelerated protons in laser-solid interactions in the intensity region of $< 10^{19}$ W/cm². The results demonstrate that EMP increases with the maximum proton en-

ergy, supported by additional escaping electron data. Producing higher energy protons may become a concern for more powerful high repetition rate systems and will require implementation of EMP mitigation techniques. This is studied in the second experimental chapter in a laser-solid interaction with an intensity of 10^{21} W/cm². It was demonstrated that the generated EMP can be successfully reduced by introducing longer target mounting stalks, and by the use of insulating materials. The EMP production also displayed a considerable increase with target substrate size.

For high repetition rates of the order of >10 Hz, there will be a need for improved diagnostics which can operate at such repetition rates, and are also resistant to EMP. The final study presents the development of an optical based technique coupled to a fast and sensitive photon detector, able to operate at high repetition rates and is largely unaffected by EMP. It can be used to detect any relativistic charged particles, and can measure relative beam charge providing an on-shot electron beam diagnostic in electron acceleration experiments.

Acknowledgements

The completion of this thesis would not have been possible without the support of a number of people. Firstly, I would like to thank my three supervisors; David, Paul and Ross. David, thank you for the opportunities you have provided me throughout my time at the CLF, and thank you for your enthusiastic and pragmatic support. I am thankful for being given the chance to participate in interesting experiments. Paul, you have contributed inspiration and structure to my academic thought processes and scientific writing. Ross, thank you for your continuous support and guidance. Your support over the last few months has been instrumental in helping me finalise this thesis. I am grateful to everyone at Strathclyde for insightful discussions.

Thanks to all of the collaborators who I have had the pleasure of working with. Thanks to the staff at the CLF, the experiments would not have run as smoothly as they did without your dedication and expertise.

I would like to thank Dean, you have taught me a lot. Chris, I am grateful for your help in getting the data for my thesis. Graeme, the office was not the same without you. Robbie, many thanks for checking my thesis and providing encouragement.

I would like to thank my friends, especially Hannah for supporting me and driving me on through this PhD. Ieva, no matter how far apart we are, you are always there for me. Alana, you have been a supportive friend.

I would like to give thanks to my A-level physics teacher Mr. Denchfield for his enthusiasm and encouragement.

Finally, I would like to thank my family. Thanks to my mum for the unconditional support, and my grandparents for the inspiration to pursue science. Will, thank you

for your support and humour to keep me going. Also – my dog Dylan, who is always there for me after a long day of work.

Role of the Author

Throughout this PhD study, the author gained experience in the design and implementation of experimental campaigns, and acquired skills in diagnostics and measurement of laser-plasma interactions. The author's work involved use of the Gemini and Vulcan lasers at the Central Laser Facility. The author also undertook work at the ISIS muon facility. The majority of the data presented in this thesis was analysed by the author. The measurements were taken over several experimental campaigns. The author took part in most of the experiments. The author had a contributing role in planning and executing experiments, in particular chapter 6.

Chapter 4 The author operated the Thomson parabola ion spectrometer, and analysed the measurements using a Matlab based Thomson parabola analysis software developed by Satyabrata Kar. EMP measurements were made by P. Bradford and analysed by the author. Supplementary electron measurements were made using a Cherenkov fibre array diagnostic designed and operated by H. Liu, and an electron spectrometer which was operated by Y. Zhang. The respective analyses were performed by H. Liu and Y. Zhang. The Target Area Operator (TAO) for the experiment was G. G. Scott.

Chapter 5 The EMP diagnostics were operated by D. C. Carroll, R. J. Clarke and P. Smith. The author completed the analysis of the EMP measurements, however did not actively participate in the experiment.

Chapter 6 Measurements reported on in this chapter were taken in two separate experiments. The author lead the experiment and made optical measurements in the Isis muon facility, with major assistance from A. Hillier, D. Rusby and D. Neely. The diagnostic used was designed by the author, and the mechanical design drawings were delivered by S. Hook. The analysis was undertaken by the author. D. Rusby provided assistance in Monte Carlo modelling and analysis. Additionally, optical measurements were made in an experiment using the Gemini laser. Major support and discussions were provided by C. Armstrong (TAO), D. Neely and A. Horne. Experimental data analysis was carried out by the author.

Publications

1. **Laser produced electromagnetic pulses: generation, detection and mitigation**

F. Consoli, V. T. Tikhonchuk, M. Bardon, P. Bradford, D. C. Carroll, J. Cikhardt, M. Cipriani, R. J. Clarke, T. E. Cowan, C. N. Danson, R. De Angelis, M. De Marco, J. Dubois, B. Etchessahar, A. Laso Garcia, D. I. Hillier, A. Honsa, W. Jiang, V. Kmetik, J. Krása, Y. Li, F. Lubrano, P. McKenna, J. Metzkes-Ng, A. Poyé, I. Prencipe, P. Rączka, R. A. Smith, R. Vrana, N. C. Woolsey, **E. Zemaityte**, Y. Zhang, Z. Zhang, B. Zielbauer, and D. Neely, *High Power Laser Science and Engineering*, **8**, (2020).

2. **Towards terawatt-scale spectrally-tunable terahertz pulses via relativistic laser-foil interactions**

Guo. Liao, H. Liu, G. G. Scott, Y. Zhang, B. Zhu, Z. Zhang, Y. Li, C. Armstrong, **E. Zemaityte**, P. Bradford, D. R. Rusby, D. Neely, P. G. Huggard, P. McKenna, C. M. Brenner, N. C. Woolsey, W. Wang, Z. Sheng, and J. Zhang, *Physical Review X*, **10** 031062, (2020).

3. **Bremsstrahlung emission profile from intense laser-solid interactions as a function of laser focal spot size**

C. D. Armstrong, C. M. Brenner, **E. Zemaityte**, G. G. Scott, D. R. Rusby, G. Liao, H. Liu, Y. Li, Z. Zhang, B. Zhu, P. Bradford, N. C. Woolsey, P. Oliveira, C. Spindloe, W. Wang, P. McKenna, and D. Neely, *Plasma Physics and Controlled Fusion*, **61** 034001, (2019).

4. **Multimillijoule coherent terahertz bursts from picosecond laser-irradiated metal foils**

G. Liao, Y. Li, H. Liu, G. G. Scott, D. Neely, Y. Zhang, B. Zhu, Z. Zhang, C. Armstrong, **E. Zemaityte**, P. Bradford, P. G. Huggard, D. R. Rusby, P. McKenna, C. M. Brenner, N. C. Woolsey, W. Wang, Z. Sheng, and J. Zhang, *Plasma Physics and Controlled Fusion*, **116**, (2019).

5. **EMP control and characterization on high-power laser systems**

P. Bradford, N. C. Woolsey, G. G. Scott, G. Liao, H. Liu, Y. Zhang, B. Zhu, C. Armstrong, S. Astbury, C. Brenner, P. Brummitt, F. Consoli, I. East, R. Gray, D. Haddock, P. Huggard, P. J. R. Jones, E. Montgomery, I. Musgrave, P. Oliveira, D. R. Rusby, C. Spindloe, B. Summers, **E. Zemaityte**, Z. Zhang, Y. Li, P. McKenna, and D. Neely, *High Power Laser Science and Engineering*, **6**, (2018).

6. **Cherenkov radiation-based optical fibre diagnostics of fast electrons generated in intense laser-plasma interactions**

H. Liu, G.Q. Liao, Y.-H. Zhang, B.-J. Zhu, Z. Zhang, Y.-T. Li, G. G. Scott, D. R. Rusby, C. Armstrong, **E. Zemaityte**, D. C. Carroll, S. Astbury, P. Bradford, N. C. Woolsey, P. McKenna, and D. Neely, *Review of Scientific Instruments*, **89**, (2018).

7. **Dual ion species plasma expansion from isotopically layered cryogenic targets**

G. G. Scott, D. C. Carroll, Astbury, R. J. Clarke, C. Hernandez-Gomez, M. King, A. Alejo, I. Y. Arteaga, R. J. Dance, A. Higginson, S. Hook, G. Liao, H. Liu, S. R. Mirfayzi, D. R. Rusby, M. P. Selwood, C. Spindloe, M. K. Tolley, F. Wagner, **E. Zemaityte**, M. Borghesi, S. Kar, Y. Li, M. Roth, P. McKenna, and D. Neely, *Physical Review Letters*, **120**, (2018).

Contents

Abstract	i
Acknowledgements	iii
Role of the Author	v
Publications	vii
List of figures	xiv
List of tables	xxvi
1 Introduction	1
1.1 Motivation	3
1.2 Thesis outline	4
2 Underpinning laser-plasma interaction physics	6
2.1 Ionisation	6
2.1.1 Multiphoton Ionisation	7
2.1.2 Barrier suppression ionisation	8
2.2 Single electron motion in an electromagnetic wave	9
2.2.1 Infinite plane waves	9
2.2.2 Single electron in an inhomogeneous field	10
2.3 Plasma	11
2.3.1 Plasma expansion	12

2.3.2	Electromagnetic wave propagation in a plasma	13
2.4	Absorption mechanisms in overdense plasmas	16
2.4.1	Collisional absorption	16
2.4.2	Collisionless absorption	17
2.5	Hot electron production and transport	19
2.6	Proton acceleration	23
2.6.1	Target Normal Sheath Acceleration	23
2.7	EMP generation mechanisms	25
3	Methodology	33
3.1	High power laser technology	33
3.1.1	Chirped Pulse Amplification	33
3.1.2	Amplified spontaneous emission	34
3.1.3	Optical Parametric Chirped Pulse Amplification	35
3.2	Experimental facilities	36
3.2.1	The Vulcan laser	37
3.2.2	Astra-Gemini	39
3.3	Diagnostics	40
3.3.1	Magnetic electron spectrometer	40
3.3.2	Cherenkov optical fibre	42
3.3.3	Thomson parabola spectrometer	44
3.3.4	EMP probes	45
3.4	Particle and radiation detectors	46
3.4.1	Image plate	47
3.4.2	Microchannel plates	48
3.4.3	Scintillators	50
3.4.4	Digital cameras	52
3.5	Simulations	54
3.5.1	Monte-Carlo simulations	55
3.5.2	Particle-in-cell simulations	56

3.6	Summary	58
4	Scaling of EMP and proton acceleration in the TNSA regime of laser-solid interactions	60
4.1	Introduction	60
4.2	Experimental method	62
4.3	Experimental results	64
4.3.1	Protons in energy and defocus scan	65
4.3.2	Escaping electrons in energy and defocus scans	67
4.3.3	Maximum proton energy and hot electron temperature in energy and defocus scans	71
4.3.4	EMP measurements	72
4.4	Discussion	74
4.4.1	EMP correlations with protons and electrons in energy and defocus scan	74
4.4.2	EMP and proton relationship – model	77
4.5	Conclusions	80
5	EMP mitigation in laser-solid interactions by modifying the target and mounting system	83
5.1	Introduction	83
5.2	Experimental method	84
5.3	Experimental results	85
5.3.1	Target mounting system variations	86
5.3.2	Target diameter scan	89
5.3.3	Stalk length scan	93
5.4	Conclusions	95
6	Particle detection via Cherenkov radiation	98
6.1	Introduction	98
6.2	Particles and applications	99

6.3	Why muons?	100
6.4	Laser-driven muon production	103
6.5	GEANT4 simulations	106
6.6	A Cherenkov radiation based muon detector	111
6.6.1	Cherenkov threshold energy	112
6.6.2	Cherenkov emission angle	113
6.6.3	Cherenkov light yield	114
6.6.4	Total internal reflection of Cherenkov radiation in a medium	115
6.7	Muon Cherenkov detector design	116
6.7.1	Secondary particle discrimination	117
6.7.2	Investigation of materials and their properties and optimisation	119
6.7.3	Maximising escaping muon Cherenkov photons	122
6.7.4	Muon Cherenkov light collection and detection	125
6.7.5	Muon energy loss in fused silica	126
6.7.6	Angular dispersion correction	128
6.7.7	Final optimised detector design	129
6.8	Muon Cherenkov detector testing in ISIS facility	130
6.8.1	Experiment description	130
6.8.2	Results	132
6.9	Summary of the muon Cherenkov detector	135
6.10	Electron Cherenkov radiation generation and measurement in Gemini laser facility	137
6.10.1	Experimental method	137
6.10.2	Experimental results	139
6.11	Conclusions	151
7	Summary and conclusions	154
7.1	Scaling of EMP and proton acceleration in laser-solid interactions	154
7.2	Study of EMP Mitigation in Laser-Solid Interaction	156
7.3	Particle detection via Cherenkov radiation	157

List of Figures

2.1	Hot electron temperature as a function of laser intensity using the Beg, Wilks and Haines scalings.	22
2.2	A typical spectrum of laser accelerated protons obtained on Vulcan Target Area West as well as detection threshold of the diagnostic resulting from noise level of the detector. Laser energy on target was 60 J, pulse duration was ≈ 2 ps. The maximum energy of the protons in this shot is approximately 16 MeV. The threshold energy of the detected protons is 1 MeV indicated in pink.	23
2.3	A basic schematic of TNSA. A laser pulse is incident onto the front surface of the target and generates intense electron current J_F or fast electrons which propagate through the target and produce a sheath field at the rear surface. This induces a space charge effect which accelerates the ions.	24
2.4	Initially discussed by Poye <i>et al.</i> and Dubois <i>et al.</i> [1, 2], laser-driven ejection of hot electrons create a charge imbalance between the target and the ground making it positively charged. Return current is drawn and the system acts as an antenna which results in EMP emission.	27
2.5	Time-frequency history diagram of an EMP signal from a single laser shot. Chamber resonant modes cause the low frequency signal, while the high frequency component is target and stalk related.	32
3.1	A layout of the Vulcan laser (https://www.clf.stfc.ac.uk/). Target areas West and Petawatt are highlighted in blue and red respectively.	37

3.2	Basic schematic of a magnetic spectrometer. Relevant parts and quantities are indicated.	40
3.3	a) A photograph of a looped fibre array, placed behind the interaction, able to capture a large solid angle. b) A schematic of the geometrical structure of a curved loop.	42
3.4	Basic schematic of a Thomson Parabola Spectrometer. Laser is incident from the right on a target. The sheath field set up by hot electrons results in acceleration of an ion beam in the forward direction. A pencil beam of ions is selected by a pinhole and travel through regions of parallel magnetic and electric fields applied transversely to the beam, before reaching the detector plane – in this case image plate.	44
3.5	A microchannel plate consists of many channels. The converted electrons strike the channel walls and are multiplied through secondary emission. Each channel has a potential which accelerates the electrons along. The electron signal is collected at the output anode at the end of the channel.	50
3.6	a) Energy band structures of an inorganic pure and activated crystals. b) Energy levels of molecules in an organic scintillator.	51
3.7	iXon EMCCD average noise counts per pixel when no signal is present as a function of exposure time for different detector array temperatures. The cooling of the array significantly reduces the noise counts.	55
3.8	Standard algorithm for PIC simulation codes.	58
4.1	a) A laser pulse irradiates a solid target and causes some of the electrons to escape, positively charging the target. b) The escaped electrons set up a sheath field which accelerates the protons in the TNSA regime. c) EMP is emitted due to a return current drawn to neutralise the positive target charge. Typical EMP signals in the Vulcan facility are several hundreds of ns in duration.	61

4.2	a) Schematic of experimental layout in TAW. The Thomson parabola spectrometer was positioned 1.2 m away at target normal angle subtending a solid angle of 26.2 nsr. The electron spectrometer was placed on the laser axis while the Cherenkov fibre was wrapped around the rear of the target covering 55°. D-dot East is indicated by a black dashed box as its data was used primarily. Two B-dot probes were located on the east and west sides of the chamber. b) An enlarged view.	63
4.3	Proton measurements for laser energy scan. a) The measured number of protons and b) the maximum proton energy as a function of laser energy on target. c) Mora maximum proton energy is plotted as a function of measured maximum proton energy. Black squares represent data using nominal 2 ps pulse duration determined from average pulse duration during a period of the campaign, and red implements 0.7 ps pulse duration which provides the best fit. Red squares in d) show E_{pmax} calculated using the Mora model, where experimental parameters and experimental T_e were employed. The trend is very similar to the experimentally measured, however the model appears to overestimate the maximum proton energy.	66
4.4	N_p and E_{pmax} plotted as a function of defocus (a) and b)). The data is scattered and show less clear trends compared to the energy scan results, nevertheless there is a general increase with intensity as shown in c) and d).	68
4.5	Electron spectrometer measurements made during the energy scan. Temperature and the detected number of electrons are plotted as function of laser energy in a) and b). The graph in c) has both number and temperature plotted as a function of intensity. Additionally, Wilks, Beg and Haines models are shown. The data appears to fall somewhere between the Wilks and Beg/Haines model.	69

4.6	Escaping electron data in the defocus scan. In this scan, the electron Cherenkov fibre was utilised for detection of the number of electrons. The temperature follows a Gaussian like shape scaling, but the relationship is less clear for the number of electrons. Beg, Wilks and Hained models for hot electron temperature are added in c). Detected temperature is much higher than those predicted by the models. Self focussing of the laser beam may be the cause.	70
4.7	Maximum proton energy obtained during the energy scan on the left and defocus scan on the right panel. These are supported by previous experiments and theory. The scatter in the energy scan data may be due to low statistics, resulting in a less clear relationship.	71
4.8	EMP measurement results. Laser intensity was varied in two ways: 1) by changing the laser energy on target and 2) by changing the laser spot focus position. a) Graph shows a linear relationship between EMP energy and laser energy for all three EMP probes. b) EMP in defocus scan is plotted. c) and d) display EMP energy plotted against laser intensity as a function of energy and defocus respectively. The EMP energy with respect to both, laser energy and defocus results, have been recently published in Bradford <i>et al.</i> [3].	72
4.9	Electron correlations. EMP is plotted as a function of both temperature and number of escaping electrons. Generally more EMP was measured for higher electron numbers and temperatures in both energy (a) and c)) and defocus scans (b) and d)).	74
4.10	Correlations between the EMP energy and the maximum energy and number of protons are shown in the plots in both energy and defocus scans. Lower EMP is detected where the proton energies numbers are lower and vice versa. There are some outliers in the defocus scan results due to possible laser self focussing.	76

4.11	Energy scan. a) Experimental data as well as Mora model proton maximum energy calculated using experimental parameters. The Wilks and Beg models incorporate experimental parameters to calculate T_e which is then input into the Mora model. Wilks likely overestimates electron temperature, overestimating maximum proton energy as well. The data agrees with Beg scaling well. b) EMP experimental data is shown in grey and the normalised model values are plotted in red against intensity. c) Shows that the EMP and maximum proton energy are correlated through laser intensity. The EMP energy is proportional to the square of the maximum proton energy, and if multiplied by a conversion factor of ≈ 2 , would give an even better match to experiment. This conversion factor between measured and modelled values could be due to the detector response function, however that was not available at the time.	78
4.12	Defocus scan. a) Experimental data as well as Mora model proton maximum energy calculated using experimental parameters. The Wilks and Beg models incorporate experimental parameters to calculate T_e which is then input into the Mora model. E_{pmax} is greater than expected for such intensities and data lies well above the model scalings. b) EMP experimental data is shown in grey and the normalised model valued are plotted in red as a function of intensity. c) EMP and maximum proton energy correlation through intensity.	79
5.1	A schematic of the experimental setup used to carry out EMP measurements. The EMP B-dot and D-dot probes were placed inside the vacuum chamber, 173 cm away from the laser-plasma interaction.	85
5.2	Photographs of the metal and plastic wheels of 68 mm in diameter and stalks marked in green ($L=25$ mm above wheel edge, $A=7$ mm ²) used in the experiment. The geometry of target stalks used are shown. Metal and plastic cylindrical stalks and a plastic spiral stalk were employed.	87

5.3	EMP energy divided by the laser energy E_{laser} is plotted for a) 100 μm thick Ta targets and b) 10 μm thick Ta targets. Low frequencies are the chamber modes and high frequencies are stalk and target contributions. The error bars were deduced based on several shots with similar conditions.	88
5.4	Normalised EMP energy measured by the D-dot and B-dot per joule of laser energy as a function of target diameter. The targets were 100 μm thick Ta foils of varying transverse sizes. Targets were mounted on 25 mm long 3 mm wide plastic stalks slotted into a plastic target wheel 68 mm in diameter. Black solid lines denote the ChoCoLaT2 simulation predictions (received during personal communications with A. Poyé). a) The experimental data from D-dot probe exhibits a square root like growth with the target size (dashed line). EMP energy continues to increase for targets larger than 10 mm, contrary to the Poyé model (solid line). b) The B-dot data scales very closely with the ChoCoLaT2 simulation predictions, where saturation is reached at 10 mm target size.	90
5.5	EMP energy as a function of plastic stalk length for 100 μm thick Ta targets in a metal target wheel a) Total EMP per joule of E_{Laser} is lowered by the introduction of longer target stalks due to increased distance for return current. Chamber mode frequencies (low) remain approximately constant but target and stalk contribution (high) is reduced by a significant amount with increased stalk length for both b) B-dot and c) D-dot probes.	94
5.6	EMP energy (both low and high frequencies) as a function of plastic stalk length for 100 μm thick Ta targets in a metal target wheel a) Total EMP per joule of E_{Laser} is lowered by the introduction of longer target stalks due to increased distance for return current. Chamber mode frequencies (low) remain approximately constant but the target and stalk contributions (high) are reduced by a significant amount with increased stalk length for both b) B-dot and c) D-dot probes. The dashed lilac dashed curve indicates proportionality to $1/l_s$.	96

6.1	A chart showing the main muon applications. Low energy muon applications ($\approx 3\text{--}33$ MeV at ISIS) range from chemical studies to magnetic probing to investigate superconductivity. Highly energetic cosmic ray muons have applications in imaging of large dense objects, monitoring of nuclear reactor and nuclear waste and homeland security.	101
6.2	Energy deposited in copper by positive muons (solid) (calculated using Groom <i>et al.</i>), and electrons (dashed) using ESTAR NIST database. . .	102
6.3	Muon production processes. a) Cosmic ray decay into muons. b) Spallation reactions. c) Laser wakefield electron induced muons: bremsstrahlung gamma or direct electron interaction (Adapted from reference [4]). . . .	103
6.4	Cross section for muon production in a gold target from electrons (dashed) and gammas as a function of incident energy. Adapted from [4].	104
6.5	Differential cross sections of muon pair production as a function of polar angle θ_q in eA process on the left graph and in γA process on the right, adapted from Titov [4].	106
6.6	Basic schematic of GEANT4 simulation set up used to model the directionality and flux of the muon beam. The simulations were carried out using 10^5 incident 1) electrons and 2) x-rays of single energy and were repeated for different incident electron beam energies and several converter target thickness. The converter target was situated 1 m from the particle source. The muons were detected by a large $1\text{ m}\times 1\text{ m}$ detector positioned 1 m behind the converter target.	106
6.7	a) Muon energy spectrum for 2 cm thick lead converter target for several electron energies ranging 1-10 GeV and b) energy spectrum for constant energy of 2 GeV and different target thicknesses.	107
6.8	Number of muons as a) a function of incident particle energy and b) converter target thickness. Simulations performed using GEANT4 with 10^5 incident particles. The cross section of the muon production was raised by $\times 10000$ to increase the probability of the reactions occurring.	109

6.9	Simulations carried out using GEANT4. The directionality of the muon beam for different electron beam energies.	110
6.10	Illustration of Cherenkov radiation emission in a dielectric medium – blue arrows. Particles with velocity less than c_{medium} radiate dipoles but there is no constructive interference of the wavefronts therefore no Cherenkov emission. Particles whose velocity is greater than c_{medium} radiate dipoles that overlap and constructively interfere emitting light at small angle $\theta_{Cherenkov}$. When the velocity is much greater than c_{medium} , $\theta_{Cherenkov}$ is large.	111
6.11	Cherenkov radiation is emitted in a cone. It makes a half-angle θ_1 with the charged particle, and refracts at θ_2 forming a ring on a detector screen.	113
6.12	a) Energy relationship of co-propagating muons and electrons; 100 MeV muons follow the same path as 180 MeV electrons. b) Deflection of muons and electrons as a function of particle energy for a 1 Tesla 10 cm long magnet.	118
6.13	The difference in time-of-flight between muons and electrons for a 1 metre path. This time difference could be advantageous for time-gating. A 28 MeV muon and an 80 MeV electron deflection is 20° , a 1 m path time of flight difference is 2.2 ns.	118
6.14	Summary of threshold energies for muon Cherenkov emission (Energy min) and the co-propagating electron energies, as well as muon energies (Energy max) whose photons escape in a flat geometry, for several materials.	119
6.15	The refractive index of various materials dependence on the wavelength of light (obtained from a refractive index database: https://refractiveindex.info). It is highest at short wavelength.	120

6.16 Muon Cherenkov light yield dN/dx for BGO, sapphire, plastic and fused silica for wavelengths 350-500 nm. The coloured horizontal lines indicate the critical angle for total internal reflection, and the shaded areas represent the muon energy region in which the generated Cherenkov photons escape in a flat geometry.	121
6.17 Tilt plots. For higher refractive index materials, tilting could be used to maximise escaping light (a)). To further maximise escaping photons, use symmetrical-cone design as shown in b).	122
6.18 For higher refractive index materials, tilting could be used to maximise escaping light (a)). To further maximise escaping photons, use symmetrical-cone design as shown in b).	123
6.19 Cherenkov emission angle (left) in flat geometry and light yield dN/dx (right) due to electrons (e) and muons (μ) in fused silica for wavelengths 350-500 nm. Blue line marks the critical angle at which total internal reflection will occur, and the pink line shows the maximum Cherenkov emission angle. Grey area is the region of interest (20-120 MeV). Total internal reflection occurs at angle $\approx 43^\circ$ equivalent to 0.87 MeV electrons and 175 MeV muons.	124
6.20 Graph showing muon energy after 1 cm travel through fused silica in blue and the difference in exit angle due to energy loss in red vs. initial muon energy.	127
6.21 Plot showing the dependence of the Cherenkov light exit angle upon the wavelength of light. The dispersion is greater for shorter wavelengths. The region of interest is 380-700 nm. 380 nm is the lower wavelength cut-off for transmission in PMMA (prism), and beyond 700 nm Cherenkov emission is minimal.	128

6.22	A schematic of the detector. It includes the 1 cm thick and 5 cm wide fused silica window as Cherenkov radiator, a 77° circular prism for correcting chromatic dispersion and an f/0.6 90° off-axis aluminium coated parabolic mirror for focusing the light onto the Andor iXon EMCCD camera chip. Note that the prism has a 5 cm wide hole (filled with black nylon) in the middle to prevent more radiation being created inside it. The blue dashed lines represent Cherenkov radiation due to co-propagating electrons, which is emitted such that it misses the mirror.	130
6.23	Drawing of the detector set-up. A fused silica cylinder at the front entrance for Cherenkov radiation, the prism for angular dispersion correction, the parabola for focussing and camera for light recording. The system is enclosed in a light tight black metal box.	131
6.24	Data images obtained on the iXon EMCCD detector for different muon energies ranging from 3.4 MeV to 33 MeV. Data was taken with the muon flux reduced by 50% and with the muon beam off for reference. Horizontal lineouts of the beam profiles are plotted.	132
6.25	SRIM simulations of 3.4 MeV, 15.9 MeV, 23.9 MeV and 33 MeV muons in 8 mm sapphire.	133
6.26	Top view diagram of the experimental layout. The four cameras used are Andor Neo, and were located at angles and distances shown next to them, measured from the beam axis (0°), and the reference point is the start of the fused silica cylinder (marked with green circle). A fibre optic with a collimating lens was also used coupled to an Andor Shamrock imaging spectrometer, to measure the spectrum of the light unsuccessfully.	137
6.27	Electron range in SiO ₂ as a function of incident electron energy. Range calculated from ESTAR NIST database.	140

6.28	A montage of each camera images on shot. The images show data for the four viewing angles for 4 different shots where the laser energy was varied. The electron beam is incident from the left. Indicated in white are the observed distances of the cylinder from each viewing angle. The height, h remains constant.	141
6.29	Dashed box indicates the sampled area which was used for the analysis. Background integrated counts were subtracted from the integrated counts of the sampled area.	142
6.30	a) The integrated counts grow with increasing laser energy for all viewing angles with most pronounced signal measured by the camera situated at the smallest viewing angle, and lower signals for less narrow angles. b) Relationship between the forward beam integrated density and the viewing angle. The integrated counts are averaged over multiple shots with similar laser energies.	143
6.31	Doped (black) and undoped (red) scintillator peak signals plotted against integrated counts on Neo cameras (shown on the left). There is a linear like correlation between the two. Peak scintillator signals as a function of laser energy. Both undoped and doped scintillator peak signals grow with energy, analogous to the integrated counts on the Andor Neo detectors in figure 6.30.	144
6.32	a) Vertical dashed line marks where the lineout was taken. The internal angles were measured from approximately the middle of the block (ie. 10 cm). b) Normalised counts as a function of internal angle are shown for different laser energies (viewed from 10°). No change in width is observed.	145
6.33	a) The angular profile of the forward beam as viewed from viewing angles of 10° , 25° and 40° . The beam is centrally peaked for all viewing angles. b) The smoothed data is presented on the same plot for comparison of brightness. The highest brightness was recorded on the 10° viewing angle camera. c) The smoothed data is normalised to 1 and peaks centered. .	147

6.34 a) The concept of Ring Imaging Cherenkov Detector. Using this set up where the detector plane is some distance away from the Cherenkov radiator, a ring image with highest intensity at the edges is obtained. b) In the case of this experiment where the detector plane is the scatter screen, which is part of the cherenkov radiator, the ring (or diameter of the cone) is not able to spread, and thus the profile of this beam would not necessarily be a doughnut-like shape. Depending on the geometry and the size of the radiator many variants are possible. The radiator used in this experiment has a complicated shape which makes predicting the beam profile and confirming the mechanism/ source of the light extremely complicated. 148

List of Tables

5.1	A list of stalk and wheel combinations used, and the system's estimated combined electrical resistance ($R_{\Omega} = \rho L/A$).	87
-----	---	----

Chapter 1

Introduction

The intrinsic properties of a laser make it an ideal driver for high energy density physics investigations as the light is monochromatic, highly directional, and can be focused to a tight spot to achieve high energy densities. As a result, conditions which otherwise cannot be easily created on the earth, other than by nuclear explosions, can be created using high power laser systems, enabling experimental investigation into a range of phenomena including nuclear fusion.

The first optical laser was first demonstrated in 1960 by Maiman [5], and almost immediately the laser light was considered for laboratory produced plasma [6, 7]. Accelerated ions were measured from interactions at low intensities of approximately 10^{10} W/cm² and long pulse lengths of tens of nanoseconds in the mid 1960s [8, 9]. Compact laser-driven electron acceleration was first proposed by Tajima and Dawson in 1979 [10], and finally became a reality when the laser intensities reached 10^{15} W/cm² enabling it to be explored experimentally. Until the mid-1980s the rate of increase in laser intensity was slow. This was due to the limits on amplification dictated by the damage thresholds of the materials in the laser chain. In 1987, the chirped pulse amplification (CPA) technique was developed for lasers by Strickland and Mourou [11] which was a major breakthrough enabling substantial increases in the peak laser intensity. CPA involves the stretching (chirping) of an ultra-short pulse temporally and spectrally, so that the peak intensity passing through the amplification chain is reduced. This way the issue of breaching the damage threshold of the optical components is avoided, and

therefore it is possible to amplify the laser pulse, and recompress the pulse back to short pulse durations, to attain higher intensities, which can now reach 10^{22} W/cm². The introduction of CPA in lasers enabled new regimes of laser-plasma interactions. Since then, laser-driven particle acceleration has undergone continual development and has become key to many areas of laser-plasma physics. See [12–14] for detailed reviews.

Intensities of the order of 10^{18} W/cm² for laser light of wavelength around 1 μm enable electrons to be accelerated to velocities close to the speed of light. In an interaction where a foil is irradiated by a laser, relativistic electrons are ejected from the target, setting up TV/m electric fields on the surface, and in turn accelerating the ions to tens of MeV energies in a short distance of several microns. This is advantageous over conventional accelerators, where such acceleration would require metres to achieve. In addition to the compactness of a laser-plasma accelerator, the ion beams produced have desirable properties, such as high laminarity, small source size and can be readily focused, which are imperative for many applications. The laser intensities predicted at new laser facilities such as Extreme Light Infrastructure (ELI) and EPAC will be even higher [15], and together with high repetition rates, will make it possible to achieve even higher proton energies, which may open up applications such as in hadron cancer therapy.

The laser accelerated electrons that escape the target and drive the ion acceleration are also responsible for the generation of pulses of electromagnetic radiation (EMP). As the electrons escape the target, a positive charge is built up, consequently a return current is drawn through the target mounting system and EMP is emitted [1, 16, 17]. Improved high energy and intensity lasers [15] will be able to produce even greater numbers of energetic electrons, which will increase the EMP production [3, 18]. It is important to address this issue, because electric and electronic equipment, often used for diagnostics in experiments, is susceptible to EMP damage and interference, which can jeopardise the experimental results. In addition, high laser repetition rates will cause continual EMP generation, which can have a detrimental impact on active diagnostics and measurements. Therefore, in order to create higher flux more energetic secondary particle sources, we have to study the EMP mechanisms and explore ways

to control and mitigate it.

1.1 Motivation

The generation of novel, compact particle sources with desirable properties for applications is currently a topic of substantial interest in laser-plasma research. High energy x-rays, protons, electrons and neutrons can be produced by laser-driven acceleration. It has been theorised that using high energy wakefield electron beams can be used to drive muon acceleration in a high atomic number converter target [4, 19]. The elusive muons are currently only produced in spallation sources, like the ISIS at the Rutherford Appleton Laboratory [20], and at high current particle colliders like the Large Hadron Collider at CERN [21]. With rapid developments, laser-driven sources may become even smaller, mobile and deployable. Muons generated in laser-plasma interactions require innovative, specialised diagnostics, which is addressed in this thesis.

High energy particle and radiation source generation research requires more powerful and higher repetition rate laser systems to conduct experiments. In particular for industry applications in imaging, short pulse intense lasers capable of very high repetition rates are necessary. The low repetition rate of lasers is a considerable disadvantage when comparing to conventional accelerators. With the increase in laser intensity as well as the repetition rate, electromagnetic pulse generation can become crippling for essential active diagnostics such as cameras, and other electronic equipment like computers or oscilloscopes. EMP has been shown to scale with laser energy and intensity [1, 3, 22], and can cause destruction of electronic equipment and interfere with experimental measurements. Therefore while pursuing the development of innovative secondary or tertiary particle sources, it is important to solve the EMP issue along the way. This is one of the main road blocks in very high intensity and repetition rate facilities where it can be difficult to get accurate experimental measurements without electronic equipment being destroyed, or having to be restarted due to EMP irradiation. Mitigation of EMP has been reported in a recent experimental campaign by the use of insulating target stalks of various shapes [3] as well as by the use of a ‘bird-house’

idea which surrounds the target stopping the hot electrons from escaping [23].

It is important to note that while the EMP can be effectively mitigated by shielding, or for example by employing the techniques reported on in this thesis, it cannot be eradicated completely. For this reason, it is imperative that new diagnostic techniques unsusceptible to EMP are explored. Typical beam charge (or current) monitors used in conventional particle accelerators (essentially EMP-free environments) are prone to EMP, therefore are not reliable in laser-plasma experiments.

1.2 Thesis outline

The thesis starts with an overview of the underpinning physics relevant to short pulse, intense laser interactions with plasma, which is presented in chapter 2. The chapter reviews the interaction of lasers and electrons and introduces the physics of laser absorption and hot electron production which are important for this work. This is followed by chapter 3, where high power laser technology, laser facilities and the detector technology and diagnostic techniques used for the work in this thesis are described.

Chapter 4 reports on experimental studies investigating the scaling of proton acceleration and EMP energy generated in picosecond pulse laser-solid interactions. EMP mitigation effects by variation of target mounting materials and geometry are examined experimentally and supported by theory models in chapter 4. Chapter 6 reports on an investigation into the feasibility of using Cherenkov radiation as an EMP-resistant means to detect charged particles in laser-plasma experiments. In addition to laser-accelerated electrons, we extend this study to include the potential to measure laser-driven muon production. Laser-driven muon generation and their benefits are discussed, and a detailed detector design for muons based on Cherenkov light is presented. The second part discusses results from an experimental campaign using the Astra-Gemini laser, aimed at detection of high energy electrons via measuring the induced light emission.

Chapter 7 encompasses an overview of the main conclusions of the results that can be drawn from the studies reported in chapters 4-6, and discusses future work

possibilities for building on the work presented.

Chapter 2

Underpinning laser-plasma interaction physics

Laser-solid interactions involve a number of processes which cross many areas of physics, such as electromagnetism, plasma, nuclear and quantum. This chapter provides an overview of underpinning laser-plasma physics, examining the ionisation of atoms, plasma parameters and expansion, and the generation of high energy electron populations in a laser-plasma interaction. These hot electrons are responsible for driving the proton acceleration and EMP production, which is one of the topics investigated in this thesis.

2.1 Ionisation

In order for electrons to be accelerated, they have to be liberated from their atom. Ionisation of an atom due to a laser pulse can be considered by examining the simple case of a hydrogen atom and the Bohr model. The Bohr radius, a_B , is:

$$a_B = \frac{4\pi\epsilon_0\hbar^2}{m_e e^2} = 5.3 \times 10^{-11} \text{ m} \quad (2.1)$$

where the reduced Planck's constant $\hbar = h/2\pi$, ϵ_0 is the permittivity of free space, and m_e and e are the electron mass and charge respectively. The electron is bound to the

nucleus by the electrostatic force (known as the atomic unit of electric field), E_{atom}

$$E_{atom} = \frac{e}{4\pi\epsilon_0 a_B^2} = 5.15 \times 10^9 \text{ V/m} \quad (2.2)$$

The electric field required for a laser pulse to ionise the atom in this model is given in Equation 2.2. This leads to a definition of the atomic unit of intensity, which is the laser intensity, I_{atomic} , at which the field of the laser equals the binding field experienced by the electron:

$$I_{atomic} = \frac{\epsilon_0 c E_{atom}^2}{2} = 3.51 \times 10^{16} \text{ W/cm}^2 \quad (2.3)$$

This first order estimate sets a basic limit for the laser intensity to ionise a hydrogen atom. Even though this value is rather high, ionisation is also observed at lower intensities, owing to the processes outlined in the following section. Nevertheless, the larger part of laser driven ion acceleration experiments are performed utilising intensities exceeding I_{atomic} to guarantee ionisation of the target.

2.1.1 Multiphoton Ionisation

As stated ionisation can take place at intensities below I_{atomic} . An electron can be liberated from the atom by the absorption of a high energy photon with energy, $\hbar\omega$, if the photon's energy is greater than the threshold for ionisation, E_{ion} , as in the photoelectric effect. In the case that the photon energy is below the threshold, the electron does not gain enough energy to escape, and instead photons are re-emitted. The electron has a relaxation time between receiving the incident photon's energy and re-emission. If during that time another photon is absorbed, this electron can then gain additional energy. An electron can escape, if the energy absorbed from multiple photons surpasses E_{ion} , and is known as multiphoton ionisation [24]. Laser intensities above 10^{10} W/cm^2 are adequate for this process to be observed [25]. Above-threshold ionisation [25, 26], where an electron absorbs more photons than needed to escape the atom, has also been reported. It will have some energy which is multiple of the total energy of the absorbed photons with the ionisation potential subtracted. This

mechanism enables the intensity threshold to be lower than for the ionisation case when considering the Bohr radius and the hydrogen atom. The final kinetic energy of the electron, E_f , can therefore be written as:

$$E_f = (n + s)\hbar\omega - E_{ion} \quad (2.4)$$

where n is the number of required photons, s is the number of excess laser photons that may be absorbed, ω is the angular frequency and E_{ion} is the ionisation threshold energy.

2.1.2 Barrier suppression ionisation

When laser intensities begin to approach the atomic intensity, the laser electric field is strong enough to significantly distort the binding field felt by the electron. The presence of strong laser pulse fields causes the potential well trapping the electron to be altered, and this in turn enables the electron to quantum mechanically tunnel through the potential barrier with some probability. This process is known as tunnelling ionisation. If the laser field is sufficiently high, the barrier can be entirely suppressed, enabling the electron to escape, in a process known as barrier suppression ionisation. The Keldysh parameter [27] describes the amount by which the barrier suppression or multiphoton/above-threshold ionisation dominates the ionisation processes, by considering whether the laser's electric field is considerably distorting the Coulomb potential experienced by an electron:

$$\gamma_K = \omega_L \sqrt{\frac{2E_{ion}}{I_L}} \quad (2.5)$$

where ω_L is the laser's angular frequency and I_L is the laser intensity. If $\gamma_K > 1$, then multiphoton ionisation is predominant, and for $\gamma_K < 1$, the ionisation is dominated by tunnelling/barrier suppression. A plasma can be formed if a significantly large portion of atoms is ionised.

2.2 Single electron motion in an electromagnetic wave

2.2.1 Infinite plane waves

Considering the motion of a single electron is useful in order to describe the electron behaviour in intense laser fields. The motion of a single electron of charge, e , and velocity, v , in the electric field, E , and magnetic field, B , of the laser can be described using the Lorentz force equation

$$\mathbf{F} = \frac{d\mathbf{p}}{dt} = e(\mathbf{E} + \mathbf{v} \times \mathbf{B}) \quad (2.6)$$

where $\mathbf{p} = \gamma m_e \mathbf{v}$ is the relativistic electron momentum. The magnitude of the magnetic field is a factor of c smaller than the electric field in the classical case, and therefore the $\mathbf{v} \times \mathbf{B}$ term can be neglected. The quiver velocity, v_q , of the electron oscillating in an electric field of an amplitude E_0 can be obtained:

$$\begin{aligned} \frac{\partial v}{\partial t} &= \frac{e\mathbf{E}}{m}, \\ \mathbf{E} &= E_0 \cos \omega_L t \end{aligned} \quad (2.7)$$

$$v_q = \frac{e}{m_e \omega_L} E_0 \sin \omega_L t = a_0 c \sin \omega_L t \quad (2.8)$$

a_0 being the normalised vector potential – the ratio of the classical and relativistic momenta. A intensity threshold exists past which the electron velocity reaches the relativistic regime oscillating in the field; these interactions are typically defined as having $a_0 > 1$. Substituting the expression for the quiver velocity into the Poynting vector leads to an expression in more useful units, defining the relativistic regime to hold for laser irradiances above $1.37 \times 10^{18} \text{Wcm}^{-2} \mu\text{m}^2$ for a $1 \mu\text{m}$ wavelength laser:

$$a_0 \equiv \frac{eE_0}{m_e \omega_L c} \cong 0.85 \sqrt{\frac{I_L \lambda^2}{1.37 \times 10^{18} \text{Wcm}^{-2} \mu \text{m}^2}} \quad (2.9)$$

At a point where the quiver velocities in the laser field are relativistic, i.e. $a_0 > 1$, the magnetic field can no longer be ignored. The $\mathbf{v} \times \mathbf{B}$ in Equation 2.6 dictates that the electrons experience a force in the direction of the laser propagation. The electrons

are accelerated to the drift velocity, v_{drift} , which can be computed by substituting the quiver velocity, v_q in Equation 2.8, into the Lorentz equation 2.6.

$$v_{drift} = \frac{e^2}{4m_e^2\omega_L^2 c} E_0^2 \cos(2\omega_L t) = \frac{a_0^2}{4} c \cos(2\omega_L t) \quad (2.10)$$

By this simple analysis it can be demonstrated that the laser field which enables relativistic electron velocities, gives rise to a force accelerating electrons to the characteristic drift velocity. The velocity peaks at twice the laser frequency and is always in the laser direction, as the cross product of the velocity and the magnetic field is always in the same direction.

2.2.2 Single electron in an inhomogeneous field

So far, the assumption of an infinite plane wave was a simplification of the interaction between the laser and an electron, however in practice the laser has a finite temporal and spatial intensity profile.

An electron oscillating in a region of high intensity will be pushed to a region of lower intensity during one half cycle of the laser. During the second half cycle, the restoring force experienced by the electron at the region of lower intensity is reduced. Over time this results in a net drift of the electron from high to low intensity regions of the pulse. During this process, the electron will gain net momentum, away from high intensity regions, meaning there is a net force in the direction away from high intensity. This is referred to as the ponderomotive force, \mathbf{F}_{pond} , which can be shown to be the negative gradient of the ponderomotive potential and is given by Gibbon as the following [28]:

$$\mathbf{F}_{pond} = -\nabla\Phi_{pond} = -\frac{e^2}{4m_e\omega_L^2} \nabla\mathbf{E}^2 \quad (2.11)$$

The ponderomotive force becomes that in Equation 2.12 under relativistic treatment with $\gamma = \sqrt{1 + a_0^2/2}$. The kinetic energy transferred from the laser to the electrons from the ponderomotive force in a linearly polarised laser cycle can be shown to be as in Equation 2.13.

$$\mathbf{F}_{pond} = -m_e c^2 \nabla \gamma \quad (2.12)$$

$$U_p = m_e c^2 (\gamma - 1) = m_e c^2 \left(\sqrt{1 + \frac{a_0^2}{2}} - 1 \right) \quad (2.13)$$

This kinetic energy can be thought of as being the effective temperature of the electron accelerated through this process [29]. While this section covered an example of absorption for a single electron, absorption processes of laser energy to plasma electrons in different intensity regimes will be discussed in section 2.4.

2.3 Plasma

The ionisation can be brought about by a sufficiently intense laser pulse, and occurs as a result of several mechanisms. This leads to a transformation of a material from solid state to a plasma. A plasma is formally described as ‘a quasineutral gas of charged particles which exhibits collective behaviour’ [30] and consists of positive ions and free electrons whose proportions are more or less lead to no overall charge. Plasma differs from the other states (solids, liquids and gases) of matter in that one charged particle influences many other particles nearby simultaneously via the generation of electromagnetic forces – which is described as having collective behaviour. The Debye length, λ_D , is the characteristic scale length over which the electric potential of a charge falls off by a factor of $1/e$ due to the screening from nearby charges. This potential is expressed in Equation 2.14. The Debye length is used to depict the distance beyond which the electric field of an ion is shielded such that it has a negligible effect on the other surrounding plasma.

$$\phi(x) = \phi_0 \exp\left(-\frac{x}{\lambda_D}\right) \quad (2.14)$$

with Debye length, λ_D ,

$$\lambda_D = \sqrt{\frac{\epsilon_0 k_B T_e}{n_e e^2}} \quad (2.15)$$

where $k_B T_e$ is the electron distribution temperature and n_e is the electron number density. The expression shows that the Debye shielding length dictates the exponential attenuation of the potential due to a charge in the plasma. This is in contrast with the inverse square decay of the Coulomb field in free space. A plasma can be described using the plasma parameter, Λ :

$$\Lambda = 4\pi n_e \lambda_D^3 = 1.7 \times T_e^{3/2} n_e^{-1/2} \quad (2.16)$$

The plasma parameter governs the number of electrons within the Debye sphere – a sphere whose radius is equal to the Debye length. When Λ is greater than 1, the plasma condition is satisfied and the plasma is said to be ideal. The plasma is said to have collective behaviour when collective electrostatic collisions are dominant in comparison with the single particle collisions.

We can consider the potential and kinetic energies of the plasma to determine whether a plasma is weakly or strongly coupled. The potential energy, PE , is a consequence of the electrostatic interactions while the kinetic energy, KE , is the plasma temperature or the average energy. The potential to kinetic energy ratio is given below:

$$\frac{PE}{KE} \approx \frac{e^2 n_e^{1/3}}{T_e} \quad (2.17)$$

A plasma which has a low electron number density and/or a high temperature is said to be weakly coupled, while high electron density and low temperature are characteristics of a strongly coupled plasma.

2.3.1 Plasma expansion

The heating and consequent pressure gradient generated by the laser-plasma interaction results in the expansion of the plasma into the vacuum away from the target with a constant temperature. The density gradient falls off exponentially:

$$n_e(x) = n_0 e^{-x/L} \quad (2.18)$$

where $n_0=10^{21} \text{ cm}^{-3}$ is the initial solid number density, x is the distance from the target front surface and L is the plasma scale length. The plasma scale length represents the distance over which the electron density reduces by $1/e \sim 0.37n_0$.

$$L \approx c_0 \tau_L \tag{2.19}$$

where τ_L is laser pulse duration or expansion time and c_0 is the ion sound speed:

$$c_s = \sqrt{\frac{k_B (ZT_e + T_i)}{m_i}} \tag{2.20}$$

Plasmas are described as having 'short' or 'long' scale lengths. Those are commonly compared to the wavelength of the laser, λ_L . When $L \leq \lambda_L$, plasma is defined as 'short' scale, and when $L \gg \lambda_L$ it is said to be 'long'. It is an important parameter as it can indicate as to how the laser energy is absorbed by the plasma electrons (Section 2.4). The interaction of the electromagnetic wave and plasma is covered in the next section.

2.3.2 Electromagnetic wave propagation in a plasma

Maxwell's equations can be used to derive the nature of an electromagnetic wave propagating in plasma from first principles. Plasma consists of freely moving charged particles – the electron and the ions, which are acted upon by strong fields. Due to the ions having a much greater mass than the electrons, their motion is considered negligible in comparison to the electrons, and thus they can be considered as a quasistationary background. The electrons on the other hand are more mobile under the effect of external forces induced by a short laser pulse. The laser field can thus be considered to displace the electrons from the ions, which in turn set up a large electrostatic restoring force as a result of charge separation:

$$\mathbf{F}_e = m_e \frac{d^2 \mathbf{r}}{dt^2} = -e \mathbf{E} \tag{2.21}$$

The oscillating electrons have a non-zero current density, $\mathbf{j} = en_e d\mathbf{r}/dt$, in the Ampere-Maxwell law, unlike the vacuum case, which means that there is an additional term to

be added to the vacuum wave equation:

$$\nabla^2 \mathbf{E} = \frac{1}{c^2} \frac{\partial \mathbf{E}}{\partial t^2} + \mu_0 \frac{\partial \mathbf{j}}{\partial t} \quad (2.22)$$

where μ_0 is the permeability of free space. Fields will influence the electrons as the electromagnetic wave travels through the plasma, which will consequently modify the dispersion relation. It can be shown that the dispersion relation for an electromagnetic wave propagating in plasma is the following:

$$\begin{aligned} \omega_L^2 - \frac{n_e e^2}{\epsilon_0 m_e} &= k^2 c^2 \\ \omega_L^2 - \omega_p^2 &= k^2 c^2 \end{aligned} \quad (2.23)$$

This is very similar to that of the vacuum relation, apart from the inclusion of the plasma frequency term, ω_p , which is defined as the natural frequency that the plasma oscillates at, and is given by:

$$\omega_p = \sqrt{\frac{n_e e^2}{\gamma \epsilon_0 m_e}} \quad (2.24)$$

where $\gamma = 1/\sqrt{1 - (v^2/c^2)}$ is the Lorentz factor and represents the relativistic electron mass correction, where v is the particle's velocity. From this it can be seen that the plasma frequency parameter varies only with the electron number density and the Lorentz factor. At a point where plasma frequency equals the laser frequency, the laser pulse cannot propagate any further and is thus reflected. This point is known as the critical density. Critical density, n_c , can be obtained by rearranging Equation 2.24 and letting ω_p be equal to ω_L , making the wavevector k zero:

$$n_c = \frac{\epsilon_0 \gamma m_e \omega_L^2}{e^2} \quad (2.25)$$

Plasma electron densities below n_c are considered to be underdense, while densities above this value are overdense. The Lorentz factor in the above equation is relevant if the electron oscillating in the intense laser field are moving relativistically. In the relativistic case, the Lorentz factor effectively increases the electron mass, which reduces

the plasma frequency, effectively decreasing the critical density. This effect enables the laser to propagate further into the target and is known as relativistically induced transparency.

The laser can penetrate slightly past the critical surface even in the case that the target is relativistically overdense. This is because an evanescent wave can be shown to exist, which decays exponentially as it penetrates the critical surface. The characteristic penetration depth that the laser can reach is described by the skin depth, δ . This is when the electric field reduces by a factor of e after the critical surface.

$$E(z) = e^{ikz} = e^{-|k|x} = e^{-x/\delta} \quad (2.26)$$

$$\delta = |k|^{-1} = \frac{c}{(\omega_p^2 - \omega_L^2)^{1/2}}$$

The intensity of the laser can increase during the propagation through an underdense plasma due to non-linear effects, such as relativistic focusing. Relativistic self-focusing arises due to the non-uniform refractive index of the plasma, η , which is dependent on the laser and plasma frequencies and therefore the electron density. It can be shown to be approximately the following:

$$\eta = \sqrt{1 - \left(\frac{\omega_p}{\omega_L}\right)^2} = \sqrt{1 - \left(\frac{n_e}{n_c}\right)^2} \quad (2.27)$$

The intensity of a focused gaussian beam is highest in the centre, and the plasma index of refraction is lower at the centre than the wings. The Lorentz factor will have the highest impact in the centre of the beam. This refractive index profile will focus the laser beam by acting as a positive lens, thereby increasing its intensity.

Another effect which can cause self-focusing of the laser beam is known as the ponderomotive expulsion, in which the electrons are pushed out of the regions of high intensity. The critical power threshold, P_c for this type of self-focusing to take place was developed numerically as well as experimentally [31],

$$P_c \cong 17.5 \left(\frac{\omega_L}{\omega_p}\right)^2 \text{ GW} \quad (2.28)$$

The refractive index difference across the beam profile is a result of the beam intensity.

A phase difference over the beam profile is created, resulting from the fact that the on-axis part of the beam travels more slowly than the edge. This phase difference of the centre and outer regions determine the focusing angle. The focusing is determined by the intensity and the beam profile, and thus there is a dependency on the power. A depleted electron density in the central region of the beam, caused by ponderomotive expulsion, contributes to the induced relativistic electron density profile from the laser profile, and can lead to an enhanced self-focusing compared with the laser profile alone.

2.4 Absorption mechanisms in overdense plasmas

Energy transfer from the laser to plasma electrons is a result of many different absorption mechanisms. We can identify the conditions under which each mechanism is dominant by considering parameters including laser intensity, polarisation, contrast and plasma density scale length.

2.4.1 Collisional absorption

Collisional absorption is often referred to as inverse bremsstrahlung. It is the mechanism by which particles in the plasma gain energy from the laser in the presence of colliding ions. It occurs when plasma electrons oscillate in a relatively weak laser field with intensity $I_L < 10^{15}$ W/cm².

Electrons oscillate at the quiver velocity under the influence of the laser field. The electron motion is damped during these oscillations due to collisions with the background ions that are present in the plasma. This results in the scattering of the quivering electrons, and energy is transferred from the electrons to the ions in the plasma. This process dominates in conditions of low temperature, long scale length collisional plasmas, in regions of underdense plasma up to the critical surface. This process happens on average at the electron-ion collision frequency:

$$\nu_{ei}(n_c) \propto \frac{n_c Z^*}{T_e^{3/2}} \quad (2.29)$$

where Z^* denotes the effective charge of the ionised atom (i.e. the number of electrons

per ion). The fraction of laser energy absorbed [29] by the plasma over a scale length L in inverse bremsstrahlung is given as:

$$f_{abs} = 1 - \exp\left(\frac{32}{15} \frac{\nu_{ei}(n_c)}{c} L\right) \quad (2.30)$$

It is apparent that the collision frequency will decrease as the electron temperature increases (Equation 2.29). This is a result of high energy electrons having a smaller cross section, which effectively reduces the collision frequency. Therefore the efficacy of this mechanism will reduce for higher intensity beams [32,33], and collisionless processes become the dominant absorption mechanism.

2.4.2 Collisionless absorption

There are a number of ways through which collisionless absorption of laser energy into electrons can be attained. Davies summarises the common mechanisms they possess [34], that result from driving electron oscillations across a density gradient. A p-polarised laser is assumed in further discussion.

Resonance absorption

The presence of a nonuniform plasma formation prior to the arrival of the main pulse caused by the amplified spontaneous emission (section 3.1.2), known as preplasma, may considerably affect the laser propagation. Consider a p-polarised laser beam incident on to a solid target at an oblique angle θ_i with some nonuniform plasma density. The laser traverses an increasing electron density, described as $\nabla n_e = \nabla(n_e, 0, 0)$, as it propagates into the plasma with a wave vector $k = ((\omega_L/c)\sin\theta_i, k_y, 0)$. Then the dispersion relation in Equation 2.23 becomes

$$\omega_L^2(1 - \sin^2\theta_i) = \omega_p^2 + c^2 k_y^2 \quad (2.31)$$

The wave-vector, k_y , changes in the density gradient, and when $k_y=0$, the beam is reflected at $n_e = n_c \cos^2\theta_i$ which takes place before the critical density. The electric field can tunnel to the critical density in the case of a p-polarised laser beam, and

resonantly excite a plasma wave. This resonance occurs at the critical density where the frequencies of the laser and the plasma match. The electric field is attenuated exponentially past the critical density, thus yielding a weak restoring field. This leads to the plasma wave breaking, which enables the electrons to gain energy as they are accelerated into the target.

The Denisov function [35], ζ , is used to describe the angle of incidence relationship and is given as:

$$\zeta = (kL)^{1/3} \sin\theta_i \quad (2.32)$$

It is related to the fraction of energy absorbed, f_{abs} , by this mechanism as:

$$f_{abs} \propto \zeta \exp\left(-\frac{2}{3}\zeta^3\right) \quad (2.33)$$

The angle of incidence, θ_i , and the scale length, L , will influence the absorption. This is because a scale length, $L > \lambda_L$, must exist for resonance absorption mechanism to happen. The angle determines how close the laser reaches the critical density. Resonance absorption is dominant at laser intensities of 10^{12-17} W/cm² (for a 1 μ m laser). There is good agreement with this model and experimental data up to 10^{17} W/cm². Above these intensities resonance absorption still occurs, but is no longer a dominant effect, as relativistic effects become more important.

Vacuum (Brunel) heating

For cases where the scale length of the preplasma is shorter than the amplitude of the electron oscillation, Vacuum (Brunel) heating occurs, which was proposed by Brunel [36] and observed in PIC codes by Gibbon and Bell [37]. Electrons can be pulled by the electric field of a p-polarised laser beam into the vacuum on one half cycle of the laser period, and on the second half accelerated back into the target. In this scheme, when the laser electric field interacts with a steep density gradient of overdense plasma, the electrons do not encounter an equal restoring force as they cross the critical surface, yielding a net acceleration of the electron.

Relativistic $\mathbf{j} \times \mathbf{B}$ heating

It was shown in an earlier section 2.2.1, that electrons acquire relativistic quiver velocities above an irradiance of $10^{18} \text{ Wcm}^{-2}\mu\text{m}^2$. This results in a non negligible magnetic field contribution to the Lorentz force, which causes the electrons to move in the direction of the laser at a drift velocity, v_{drift} . The electrons gain net energy from the laser as they move past the critical density whilst moving at v_{drift} . The electric field of the laser also acts upon the electrons via the Ponderomotive force (section 2.2.2). These effects are reported by Kruer and Estabrook [38] who determine the total force to be:

$$\mathbf{F} = -\frac{m}{4}\nabla v_q^2(1 - \cos 2\omega_L t) \quad (2.34)$$

The net force is due to the electrons being pushed via the ponderomotive force as well as accelerated at twice the laser frequency by the fast $\mathbf{v} \times \mathbf{B}$ component, with a period twice that of the laser and in the laser direction. This does not depend on the direction of oscillation relative to a plasma density gradient, unlike the previously discussed absorption mechanisms. Therefore, the electrons can be accelerated across the density gradient by either s or p-polarised laser pulses. The difference between $\mathbf{v} \times \mathbf{B}$ and resonance and vacuum heating is that in $\mathbf{v} \times \mathbf{B}$ the electrons are not accelerated normal to the critical density but rather along the laser axis. Resonance and vacuum heating are only a result of the laser electric field, while $\mathbf{v} \times \mathbf{B}$ arises from the magnetic component. This mechanism is optimised at high electron densities, and thus is most effective for oblique laser incidences.

2.5 Hot electron production and transport

The previous sections explored how the laser energy is transferred to the electrons via several mechanisms. Electron transport physics in solid targets is fundamental in transmitting energy from the laser to the ions which are accelerated from the rear surface of the target [39]. The electrons are injected into the target, once they cross the critical surface and are no longer within reach of the laser field. The currents of the injected electron populations can reach mega amperes. A 350 fs laser pulse accelerated

electron beam, possessing 2.8×10^{12} electrons with a total kinetic energy of 0.29 J, has a current of 1.3 mega-amperes [40]. This high current exceeds the Alfvén limit, \mathbf{j}_A , [41,42], which predicts the maximum current that can propagate without the enormous self-generated magnetic field being induced. These magnetic fields will start to break down the electron beam and by reversing their flow against the direction of beam propagation, effectively prevent the hot electrons from propagating. The maximum current that can propagate, without inducing self-generated magnetic fields that reverse the flow of electrons, is given by the Alfvén limit, I_A :

$$I_A \cong \frac{m_e c^2 \beta \gamma}{e} = 1.7 \times 10^4 \beta \gamma \quad (2.35)$$

where $\beta = v_e/c$ with v_e the electron velocity and $\gamma = 1/\sqrt{1-\beta^2}$. The Alfvén limit for interactions in the work of this thesis is of the order of several tens of kA and is typically exceeded by the electron beam current that is accelerated into the target. This means that there must be additional effects taking place, which ensure that the net current does not breach the Alfvén limit, and enable the fast electrons to propagate into the target. A return current is drawn from the background plasma that balances the forward propagating electron beam. This current acts locally and is drawn in the opposite direction to the main electron current. It can be described by the current balance relation [43] in terms of the hot electron current density, \mathbf{j}_{hot} , and the cold return current, \mathbf{j}_r :

$$\mathbf{j}_{hot} + \mathbf{j}_r \approx 0 \quad (2.36)$$

The return current comprises a greater number of electrons which are also cooler than the hot electron current.

The laser energy is coupled to a population of hot electrons as a result of the absorption mechanisms discussed in an earlier section. This population of electrons is now travelling through the target and exhibits a Maxwellian-like spectrum. This was shown for resonance absorption by Bezzerides *et al.* [44]. A Maxwellian energy distribution as a function of the hot electron energy, E_{hot} , with a single temperature,

T_{hot} , is described as the following:

$$f(E_{hot}) = N_{hot} \sqrt{\frac{4E_{hot}}{\pi(k_B T_{hot})^3}} \exp\left(-\frac{E_{hot}}{k_B T_{hot}}\right) \quad (2.37)$$

where E_{hot} and T_{hot} are the energy and the temperature of the hot electrons, respectively, and N_{hot} is the total number of hot electrons.

The energy distribution expression suggests that the parameters that can be used to describe the hot electron population are the hot electron temperature and the total number of hot electrons. These are important and play a significant role in proton acceleration, which is described in the next section, and govern the properties of the ion beam accelerated from the rear of the target.

The number of accelerated electrons, N_{hot} is dictated by the electron temperature and the fraction of the absorbed laser energy. The absorption can reach up to 80% for some ideal laser conditions, however more typically the value is between 20-40% [34, 45–47]. Davies gives a fit to the data as [34]:

$$f_{abs} = \left(\frac{I \lambda^2}{4.3 \times 10^{21} \text{ W cm}^{-2} \mu\text{m}^2} \right)^{0.2661} \quad (2.38)$$

The hot electron temperature is dependent upon the incident laser intensity as well the wavelength. This is commonly represented using the electron temperature scaling laws which are outlined below.

There are a number of scaling laws that determine the hot electron temperature, T_{hot} . The model introduced by Beg *et al.* [48], was derived using the high energy photons emitted from a plastic target, where the intensities measured $\approx 2\text{-}8 \times 10^{18}$ W/cm². Assuming that the the electrons producing the photons in the target have a Maxwellian distribution, the temperature of hot electrons was shown to scale as:

$$T_{hot[Beg]} [keV] = 215 (I_{18} \lambda_{\mu}^2)^{1/3} \quad (2.39)$$

where I_{18} is the laser intensity in the units of 10^{18} W/cm² and λ_{μ} is the laser wavelength measured in μm . The hot electron temperature is 215 keV for a laser intensity 10^{18}

W/cm^2 and wavelength $1 \mu\text{m}$ according to this model. A ponderomotive scaling law derived by Wilks *et al.* [49] uses the ponderomotive potential and the hot electron temperature scales as

$$T_{hot[Wilks]} [keV] = 511 \left[\sqrt{1 + \left(\frac{I\lambda_\mu^2}{1.37 \times 10^{18}} \right)} - 1 \right] \quad (2.40)$$

An analytically developed scaling by Haines *et al.* [50] is given by

$$T_{hot[Haines]} [keV] = 511 \left[1 + \sqrt{2} \left(\sqrt{\frac{I\lambda_\mu^2}{1.37 \times 10^{18}}} \right) \right]^{1/2} - 1 \quad (2.41)$$

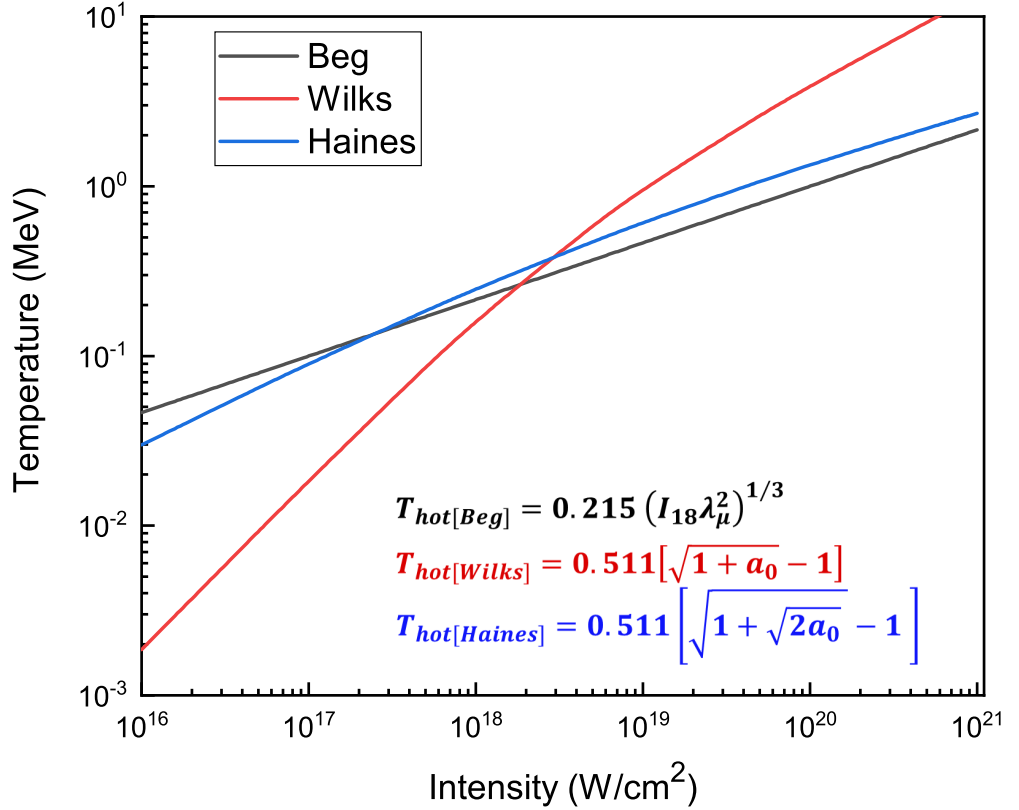


Figure 2.1: Hot electron temperature as a function of laser intensity using the Beg, Wilks and Haines scalings.

$\sqrt{I\lambda_\mu^2/1.37 \times 10^{18}}$ is the normalised vector potential, a_0 . T_{hot} can also be calculated using the scaling relation obtained by Lefebvre *et al.* [51]. An increase in either the hot electron temperature, the number of hot electrons or acceleration time will lead to an increased maximum proton energy. A more detailed description of the equation can be found in reference [52].

2.6 Proton acceleration

2.6.1 Target Normal Sheath Acceleration

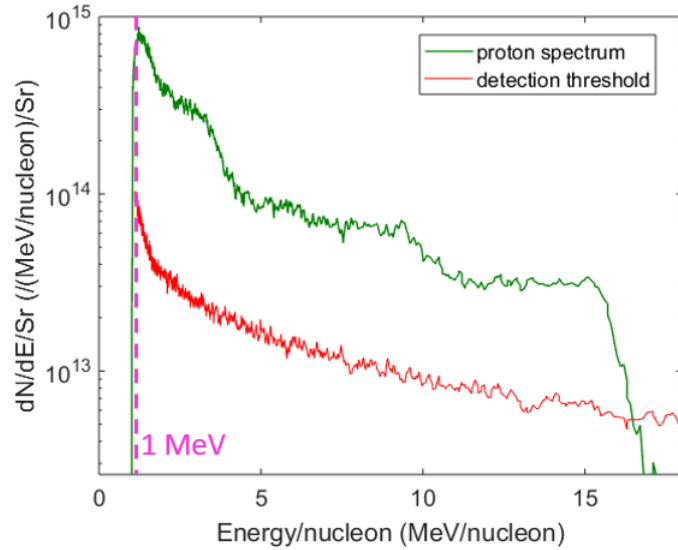


Figure 2.2: A typical spectrum of laser accelerated protons obtained on Vulcan Target Area West as well as detection threshold of the diagnostic resulting from noise level of the detector. Laser energy on target was 60 J, pulse duration was ≈ 2 ps. The maximum energy of the protons in this shot is approximately 16 MeV. The threshold energy of the detected protons is 1 MeV indicated in pink.

The sheath field which drives the acceleration of ions is also believed to be correlated to EMP emission. The primary mechanism of proton generation in thick foils is target normal sheath acceleration (TNSA) [53]. TNSA is based on the efficient generation of fast electrons in the relativistic regime ($a_0 > 1$ or $I_L I_L^2 > 10^{18} \text{ W } \mu\text{m}^2 \text{ cm}^{-2}$). These fast electrons are intense electrical currents of fast electrons, J_f , which propagate through the target and escape, charging the target and causing the formation of a rear surface

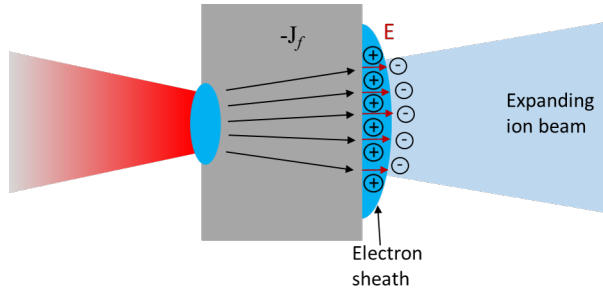


Figure 2.3: A basic schematic of TNSA. A laser pulse is incident onto the front surface of the target and generates intense electron current J_F or fast electrons which propagate through the target and produce a sheath field at the rear surface. This induces a space charge effect which accelerates the ions.

sheath field. Typical foil targets used in experiments have contaminant layers (nm) deposited on their surfaces, mainly formed by hydrocarbons and water vapour. The species with the largest charge-to-mass ratio, i.e. protons, will experience the highest acceleration. The induced charge separation electric field accelerates ions normal to the target rear. Protons are accelerated preferentially, from the contaminant layers containing hydrogen on the target rear surface, due to their high charge to mass ratio.

It has been shown that TNSA fields can be described by $\varepsilon_{acc} = T_{hot}/e\lambda_D$ [54], where ε_{acc} is the accelerating field, T_{hot} is the hot electron temperature (depends on the laser intensity between 10^{17} – 10^{20} W/cm²) between 10 keV and 10 MeV, and λ_D is the hot electron Debye length, which is typically of the order of a micron resulting in field strengths between 10^8 – 10^{11} V/cm. Maximum proton energy has been modelled in terms of the laser intensity and the properties of the sheath field, in works by Mora [55], Schreiber *et al.* [56], Wilks *et al.* [53] and more recent studies of Zani *et al.* [57], Robson *et al.* [58], Lefebvre *et al.* [51] and Coury *et al.* [59]. Maximum proton energy, E_{pmax} , can be derived as a function of the hot electron temperature T_{hot} , and Schreiber *et al.* derive E_{pmax} in terms of the power of the laser and the radius of the charge distribution at the target rear surface. Maximum proton energy derived from the Mora model based on a self-similar 1D expansion model:

$$E_{pmax} \sim 2T_{hot} \left[\ln \left(\tau_{eff} + \sqrt{1 + \tau_{eff}^2} \right) \right]^2 \quad (2.42)$$

where τ_{eff} is the normalised acceleration time and is given by

$$\tau_{eff} = \frac{\omega_{pi}\tau_{acc}}{\sqrt{2exp(1)}} \quad (2.43)$$

with plasma ion frequency

$$\omega_{pi} = \sqrt{\frac{n_{hot}Ze^2}{m_i\epsilon_0}} \quad (2.44)$$

and the acceleration time τ_{acc} which was fixed at $1.3 \times \tau_{laser}$. It was argued by Brenner *et al.* that τ_{acc} depends on the laser pulse duration, τ_{laser} , the expansion time, $\tau_{expansion}$, and the average time for electrons to escape the acceleration volume transversely. These can be written as:

$$\tau_{acc} \sim \sqrt{\tau_{laser}^2 + \tau_{expansion}^2 + \left(\frac{D_L}{2u_e}\right)^2} \quad (2.45)$$

where D_L and u_e are the the focal spot size and the average electron velocity, respectively.

The strength of the electrostatic sheath set up by the electrons at the target rear is given by in Equation 2.46.

$$E(z) = \frac{2k_B T_{hot}}{e} \frac{1}{z + \sqrt{2}\lambda_D} \quad (2.46)$$

2.7 EMP generation mechanisms

The hot electrons ejected from the target are believed to be the dominant driver of currents during and after the end of the laser pulse [60, 61]. The mechanisms of EMP generation could be related with the current associated with the fast electrons escaping from the target [62] or with a discharge current to a positively charged target, however they have so far not been investigated in detail. Additionally, the ejected electrons may induce secondary dipoles when striking metallic objects in the interaction and chamber walls [62, 63]. Previous experimental data indicate that the EMP signal strength depends on the target material and geometry as well as on the shape and locations of metallic elements of the target chamber and the laser pulse intensity and duration.

Researchers at Lawrence Livermore National Laboratory measured EMP as well as electrons which had escaped from the target in NIF and Titan. They used the energy and the spatial distribution of escaped electrons acquired from experimental measurements as input for the 3D electromagnetic code EMSolve, to model EMP generation when these electrons flow inside the chamber and hit the metal chamber walls. The simulation results are in agreement with experimental data, which confirmed that escaped electrons are the dominant source of EMP [61,64,65]. It was found in experiments that EMP in short-pulse laser interactions has higher intensity and wider bandwidth than that in long pulse laser plasma interactions [60,64]. Other studies demonstrated that EMP is associated with target size and material [66,67], the chamber geometry [68,69] and the laser parameters [61]. Research at the French Atomic Energy Commission established the target charging model describing the source of EMP as the neutralisation current flowing through the target stalk induced by escaped electrons [2]. Poye *et al.* described the physical processes that cause generation of EMP at high power laser facilities, and presented a simple model for estimating the intensity and the dominant frequencies of the EMP pulses [2]. A model for an accurate estimate of the charge accumulation on a metal target surface irradiated by an intense laser pulse of fs-ps duration, and laser intensity $2 \cdot 10^{18}$ W/cm², is proposed by Dubois *et al.* and confirmed by experiments [1]. Dubois research on return current induced EMP was advanced further by Raczka *et al.*. Their study found that EMP emission is stronger for thin targets than thick targets [70]. Studies by Cikhardt *et al.* measuring EMP and the neutralisation current using a sub-ns kJ-class laser facility, validated that the neutralisation current causes significant EMP emission [22,70].

The charge separation effect causes a strong electrostatic field to be established on the target surface, which restricts further emission of electrons. The majority of the electrons ejected from the target are decelerated and subsequently accelerated back towards the target due to the electrostatic field. The electrons that are energetic enough to overcome the potential barrier, escape the target and propagate in the vacuum chamber. The escaped electrons strike the metal walls of the chamber inducing a large transient current and strong EMP, and positively charge the target causing a return

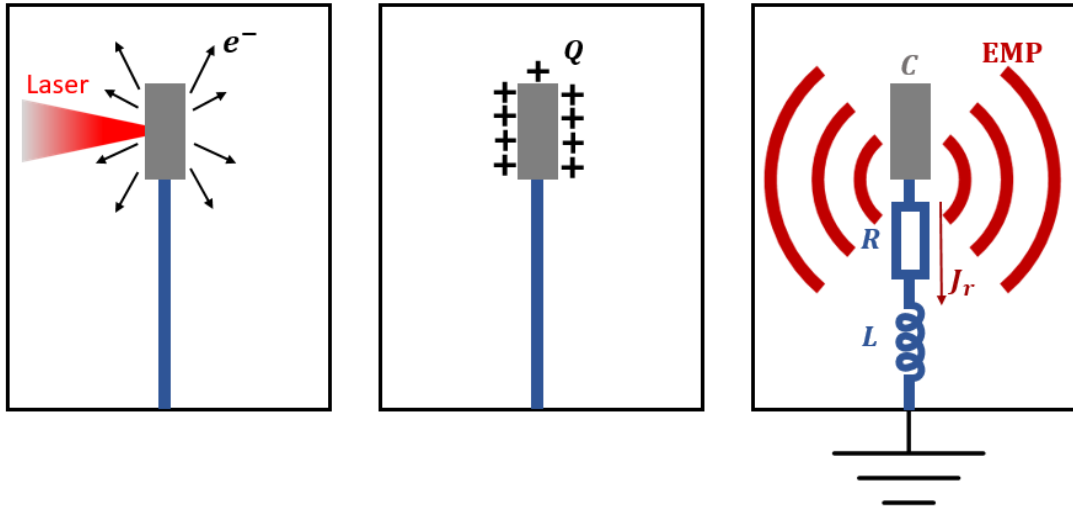


Figure 2.4: Initially discussed by Poye *et al.* and Dubois *et al.* [1,2], laser-driven ejection of hot electrons create a charge imbalance between the target and the ground making it positively charged. Return current is drawn and the system acts as an antenna which results in EMP emission.

current J_r to be drawn as shown in figure 2.4. Due to multiple possible EMP emission mechanisms several frequency components are observed as demonstrated in figure 2.5. The low frequencies (few hundreds of MHz) are believed to be resonant modes of the target chamber as observed by Mead *et al.* on the Vulcan laser [62]. They propose that EMP is instigated by the escaped electrons which strike the chamber walls inducing a cavity resonance. The high frequencies are thought to be a return current contribution from the target and stalk (above 1 GHz). A recently developed time-resolved electro-optic probe with high noise immunity, was used to characterise EMP [REF Robinson 2017 and Consoli 2016] [71, 72]. The EMP spectra diagnosed utilising this method on the Vulcan laser agreed with the investigations carried out by Mead *et al.* [62].

Polarisation of the target

As the electrons are accelerated by the alaser pulse, the potential of the electrostatic sheath increases (TV/m), and is strong enough to pull the forward propagating electrons back injecting them back into the target (refluxing/recirculation) [73]. Thus the total number of escaped electrons is defined by the dynamic competition between

the high energy of escaping electrons and the electric potential increase. This section describes the methods for charge evaluation for metal targets irradiated with laser intensities of the order of 10^{18-20} W/cm².

The target potential Φ_t is comparable to the laser accelerated hot electron temperature T_{hot}

$$\Phi_t \sim T_{hot}/e \quad (2.47)$$

where e is the elementary charge. T_{hot} can be assimilated with the ponderomotive energy of the electrons oscillating in the laser field [49]:

$$T_{hot} \simeq (\gamma_0 - 1)m_e c^2 \quad (2.48)$$

with the relativistic gamma factor for a linearly polarised laser pulse $\gamma_0 = \sqrt{1 + a_0^2/2}$ and for a circularly polarised laser pulse $\gamma_0 = \sqrt{1 + a_0^2}$ with a_0 quoted in equation 2.9.

In order to compute the accumulated charge it is necessary to know the capacitance of the target, C_t . The capacitance can be considered to be approximately equal to that of a conducting disc with a diameter d_t [74].

$$C_t \simeq 4\epsilon_0 d_t \quad (2.49)$$

since $C_t = Q_t/V$ and $V = Q/4\pi\epsilon_0 d_t$, where Q_t is the charge and V is the Coulomb potential. d_t could be considered to be the transverse size of a metal target or the size of the ionised region building up the charge in a dielectric target. The capacitance of a 5 mm target is of the order of 0.2 pF. The accumulated charge is dependent on the laser energy and focusing conditions [65, 75] and can be expressed as

$$Q_t \simeq C_t T_{hot}/e \quad (2.50)$$

As the hot electron temperature is determined by the laser intensity, the accumulated target charge is also limited by it. Q_t is also limited by the energy of the laser pulse, E_{laser} , as the greater the laser energy, the more energy is converted to hot electrons ($Q_t \simeq e\eta_{laser}E_{laser}$, where η_{laser} is the conversion efficiency from laser to hot

electrons). The accumulated target charge depends on the the laser pulse energy and intensity, and has values ranging from a few nC to a few tens of μC which is determined by the laser energy focusing conditions [65,75]. On experiments in petawatt class lasers where more energetic electrons are produced, the accumulated target charge can reach tens of μC . To study EMP, Dubois *et al.* demonstrated measurements of the charge accumulated on the target using laser energies of 0.01–0.1 J [1] confirming these charge values. An increase in the accumulated electric charge as a function of target lateral size was measured by Chen *et al.* [67].

It is imperative to know how fast the charge is accumulated and how long it is maintained on the target. The laser pulse duration and the hot electron cooling time are the two time parameters defining the charge accumulation. The electrons cool via collisions with atomic electrons within the target and due to bremsstrahlung. The cooling time of electrons is material dependent and is calculated in [17]. The cooling time of a 3 MeV electron, t_{cool} , is 5 ps in tantalum, 7 ps in copper and 24 ps in aluminium. Poye *et al.* demonstrated experimentally a weak dependence of electron ejection time on the laser pulse duration (sub ps pulses), however it is evidently strongly influenced by the laser energy as well as the target material. The discharge time is governed by the size of the target and the impedance of the target mounting system; stalk and wheel. Typically the stalks used are $l_s \approx 25$ mm in length and a few mm in diameter. The time taken for a signal to propagate across the target is $\Delta_t \simeq d_t/c$ and is approximately 15 ps for a 5 mm target. Thus for laser pulse durations of the order of a few ps and less, the processes of target charging and discharge are temporally distinct. In the case of long pulse durations, a target potential is established by the balance between the rate of electron ejection and the amplitude of the current through the stalk to the ground. The discharge time for a 25 mm stalk is then $l_s/c \approx 80$ ps and is the upper bound of the pulse duration subject to the generation of intense EMP signals. This also accounts for the EMP emission problems being of particular importance for short (ps and sub-ps) pulses, while it attracted much less interest in long pulse (ns) experiments.

Terahertz. Electromagnetic radiation emission produced during the electron ejection

tion – during and after the laser pulse on the characteristic time of electron cooling $t_{cool} \approx$ few ps, are of particular importance. The corresponding frequency domain is going down from 1 THz and such frequencies are the most damaging to electronics. The amplitudes of the EMP signals in this range are significantly high and risk jeopardising experiments. Two predominant sources of the emission of EMP have been identified as associated to the 1) ejected electrons and 2) the return current, J_r .

For ps and sub-ps laser pulses, the electron ejection time $t_{ej} \approx 1-3$ ps corresponds to a bunch size of $l_{ej} = ct_{ej} \approx 300-1000$ μm . This can be considered as a dipole formation with effective charge Q_t . The radiated power is proportional to the second derivative of the dipole moment as given by the Larmor formula [74]:

$$P_E = \frac{\mu_0}{6\pi c} |\ddot{D}|^2 \quad (2.51)$$

where $|\ddot{D}| = Q_t \ddot{l}_{ej}$ and μ_0 is the permeability of free space. During the first picosecond, the electron bunch parts from the target, the dipole moment, D , increases rapidly and non-linearly to $\approx Q_t l_{ej}$. After this the charge is constant and the dipole length increases almost linearly as it moves away. Therefore \ddot{D} is only significant during the electron ejection. Provided that D varies quadratically with time, the total energy radiated during the electron ejection is estimated as

$$E_{THz} \simeq \frac{Z_0}{6\pi t_{ej}} Q_t^2 \quad (2.52)$$

where $Z_0 = \sqrt{\mu_0/\epsilon_0} \approx 377$ Ω is the vacuum impedance. This relation indicates that the radiated energy is proportional to the square of the accumulated charge and inversely proportional to the electron ejection time. Electron ejection time is short for short laser pulses (few ps), thus this emission is of importance. Recent studies [76–80] have reported the detection of THz radiation in the plane perpendicular to the electron emission direction. Weak dependence on the target material, and scaling with laser energy and intensity have been observed.

Additional sources of EMP emission include the escaped electrons inducing secondary dipoles when impacting the vacuum chamber walls and metallic components

inside the chamber [62,63]. The hard x-rays emitted from the laser spot are also likely to produce secondary emissions. The laser pulse duration determines the frequency range; THz for sub-ps and GHz and MHz for ns pulses. The secondary emissions excite the resonant modes of the interaction chamber which last for up to a microsecond time scales [18]. The frequency domain of these is dictated by the size of the interaction chamber; for example a cavity $\lambda_{ch}/2=1-2$ m, $f = c/\lambda_{ch}=150-75$ MHz. Data provided in chapter 4 includes analysis of low and high frequency components, where a 500 MHz split was chosen to divide the two.

Gigahertz. Electromagnetic radiation emission in the range 100-300 GHz are generated over a time scale longer than 30-100 ps and are linked to the relaxation of the accumulated target charge during the laser pulse. We can consider an example of a metallic disc shaped target of a diameter, $d_t \sim 1$ cm, mounted on a stalk of length, $l_s \sim 5$ cm, and diameter, $d_s \sim 0.1$ cm, connected to a ground plate. We assume that the laser pulse duration in the sub-ps range, then a charge, Q_t , is established on the target before the formation of the discharge current. This discharge current propagates from the target through the stalk to the ground. The current duration is the time taken to propagate the charge across the target, $\Delta t_j \simeq d_t/c$, and has been measured experimentally [1, 81–83]. The current pulse with an intensity $J_t = Q_t/\Delta t$ travels down the stalk, reflects at the ground and returns to the target, thus oscillating along the stalk. The target mounting system and the ground are an example of a linear antenna. In this case the current pulse length is shorter than the antenna length. The characteristic emission wavelength is four times the stalk length, $\lambda_{EMP} = 4l_s$, [84], and the period of a full oscillation is $4l_s/c$. This corresponds to a principal frequency $\omega_s = \pi c/2l_s$, which is in the GHz range for $l_s=5$ cm. A time-frequency history plot of EMP for <2.5 GHz is shown in figure 2.5. The radiation field is created when the current pulse enters the stalk and inverts its motion, and consists of a sequence of pulses of duration equal to the current duration [84]. The emission spectrum consists of the main frequency and higher harmonics. The details of the current shape dictates the emission spectrum, however the number of harmonics can be estimated as a ratio of the main oscillation period to the current pulse duration, $N_h \sim 4l_s/d_t$.

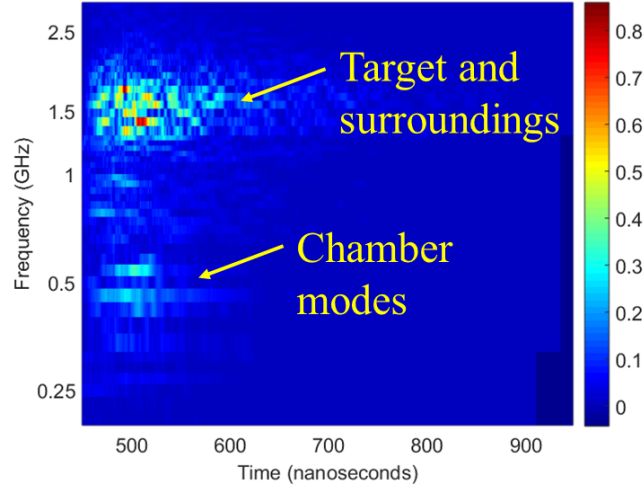


Figure 2.5: Time-frequency history diagram of an EMP signal from a single laser shot. Chamber resonant modes cause the low frequency signal, while the high frequency component is target and stalk related.

The EMP emission power at the main frequency of the target mounting structure can be estimated using the formula for a linear half-wavelength antenna [74]:

$$P_{EMP} = \frac{2.44}{8\pi} Z_0 |J_{\omega_s}|^2 \quad (2.53)$$

where $J_{\omega_s} \sim J_t/N_h = Q_t c/4l_s$ and is the Fourier component of the total current at the emission frequency. From this we can see that the emission power is proportional to the accumulated target charge, and inversely proportional to the stalk length. The total emitted EMP energy in the GHz domain is estimated as the sum of all harmonics and is given in equation 2.54 [18]:

$$E_{GHz} \simeq \frac{2.44c}{32\pi l_s} Z_0 Q_t^2 N_{hot} \simeq 0.1 \frac{c}{d_t} Z_0 Q_t^2 \quad (2.54)$$

Chapter 3

Methodology

This chapter describes the high power laser facilities and other key methodologies relevant for the work carried out in this thesis. Introduces the main diagnostic and detector technologies employed, and briefly describes the simulation methods relevant for the research topics relevant to this thesis. This discussion will aid in the understanding of the experimental measurements presented in the next chapters.

3.1 High power laser technology

3.1.1 Chirped Pulse Amplification

Chirped Pulse Amplification (CPA) is a technique used for amplifying short low energy laser pulses. It was introduced in 1985 by Strickland and Mourou [11]. Efficient amplification of a pulse requires that the fluence of the pulse prior to the amplifier is of the order of the saturation fluence, $\Gamma = \hbar\omega_L/\beta\sigma_{em}$, where \hbar is the reduced Planck's constant, ω_L the central frequency of the laser and σ_{em} is the emission cross section. The maximum energy than can be delivered by a laser system is limited by the damage threshold of its optical components. One of the main challenges in high peak intensity systems is preventing the amplified pulse from damaging optics and gain media in the laser chain. The main driver of the onset of damage is the non-linear refractive index, which can result in self-focusing of pulses which are initially much lower than the damage threshold to intensities above this. The CPA scheme provides a way to further

amplify the pulse while avoiding the onset of these nonlinear effects.

A short pulse from the oscillator (1 nJ energy and 120 fs duration) is temporally stretched by a factor of 10^3 – 10^5 . A device known as a stretcher usually consisting of a pair of gratings is used to introduce positive dispersion – shorter wavelengths take longer to pass through the setup compared to longer wavelengths. The pulse is stretched in time by this path difference. Once the power is reduced to below the damage threshold of the gain medium, it proceeds to the amplification stage. The stretched pulses are amplified in a chain of one or more amplifiers. The duration of the chirped pulses (100 ps) is many orders of magnitude longer than the original pulse, therefore they can be amplified to higher energies than in the absence of stretching, by a factor approximately equal to the stretch factor. The amplified chirped pulse is recompressed to a short pulse length (1 ps), by passing it through a compressor with negative dispersion applied to reverse the effect of the positive dispersion in the stretcher phase. Prior to the first demonstration of the CPA technique, peak laser intensities were of the order of 10^{16} W/cm²; CPA enabled systems to date to achieve intensities up to 10^{22} W/cm² (HERCULES laser system [85]).

3.1.2 Amplified spontaneous emission

Amplified spontaneous emission (ASE) is an undesirable lower intensity laser temporal pedestal caused by spontaneous emission in the gain medium, which is also amplified in the process together with the main pulse. The excited atoms in the amplifiers decay spontaneously to lower energy states, instead of being stimulated to decay by a coherent laser photon; this occurs on both sides of the main laser pulse due to the optical pumping of the gain medium on the ns time scale around the temporal arrival of pulse, however the pedestal before the main pulse is the main issue. The photons are emitted over 4π sr due to the random nature of this process. In the case that the spontaneous emission happens at angles such that the propagation of light can occur along the rest of the laser chain, this unwanted part will be amplified as well as the main laser pulse. The result is a pedestal on both sides of the main laser pulse. The fraction of the pedestal intensity to the peak intensity of the main pulse is known as

the temporal intensity contrast. It is often quoted as a ratio of the pedestal to peak intensity and given with respect to the time at which the ratio was measured. Modern laser systems exhibit contrast ratios ranging 10^{6-12} W/cm² [86,87]. In the case of the large scale, petawatt class systems relevant for this thesis, where peak laser intensities are of the order of 10^{19} W/cm², the ASE pedestal will be 10^{12} W/cm². This is intense enough to ionise the surface of solid targets and cause plasma expansion at the target front. This will change the physics of the laser-plasma interaction and give rise to a state favourable for instability growth . It is possible to gate out the majority of ASE employing a Pockels cell, used by many laser systems, where an applied voltage (electric field) to the electro-optic crystal produces linear changes in the birefringence of the crystal. Applying a constant voltage allows the Pockels cell to operate as a voltage-controlled wave-plate. However, due to the minimum gating time of ≈ 1 ns, some of the ASE still remains and is transmitted along the system to the target. Another technique is plasma mirrors, where the pedestal is transmitted through a high quality glass slab, the rising edge of the main pulse arrives at an intensity which is adequate to ionise its surface and form an overdense plasma, and the peak pulse is reflected from the plasma surface.

3.1.3 Optical Parametric Chirped Pulse Amplification

Optical parametric chirped pulse amplification (OPCPA) is similar to CPA in that it uses a stretcher for beam power reduction before the amplification stage prior to the final compression of the beam. In this scheme a signal pulse (the pulse from the oscillator) is passed through a nonlinear crystal in the presence of a high frequency and high energy pump pulse (higher than the main pulse). The pump and signal pulse interaction with the nonlinear crystal leads to a third frequency pulse, called the idler, to be generated. There is a net energy transfer from the pump to the signal and the idler pulses. OPCPA system requires fewer amplification stages, as the parametric gain within a single pass through a nonlinear crystal can be tens of decibels. This means these systems can be built with simpler compact setups without multipass geometries.

OPCPA has several advantages over the conventional chirped pulse amplification

based on laser gain media. Since parametric amplification is possible for very large bandwidth pulses, this reduces the effect of gain narrowing; the amplification of the central frequency of the dispersed pulse much more than the wings, and therefore this allows the for pulse to be more effectively compressed. For many laser materials typically a few nm of bandwidth can be amplified, whereas tens of nm can be amplified here. The minimum pulse duration achievable with a pair of gratings is inversely proportional to the spectral width of the laser, as stated by the time bandwidth product. Due to this large bandwidth, significant compression can be achieved, leading to short pulse lengths, in turn producing higher intensities. Thermal effects are also much weaker in the amplifier crystal than in a laser amplifier, due to the energy transfer between the pump and the signal being very efficient resulting in very little heating in the crystal. This means that the effect of thermal lensing is less of an issue. Thermal lensing is prevalent in amplifiers, where there is a refractive index profile across the crystal, which causes focusing and may cause damage. This and the high quantum efficiency results in very high energy and peak powers. As the thermal effects in the crystal are negligible, this allows the system to operate at a higher repetition rate (several to tens of Hz). The parametric gain takes place within the duration of the pump pulse, and so the contribution of ASE is reduced improving the contrast in high gain laser amplifiers. Thus very clean, high energy pulses with a very high intensity contrast are produced, which is critical for laser-solid interactions. After preamplification, the pulse is passed back to the stretched for spectral dispersion to a pulse length of 4.8 ns in the case of Vulcan Petawatt.

3.2 Experimental facilities

The facilities used for the work in the experimental chapters of this thesis are all located at the Rutherford Appleton Laboratory (RAL) in the UK, which is a host to world class research facilities including the Central Laser Facility (CLF) and the ISIS neutron and muon source. The experimental campaigns in chapters 4 and 5 took place at Vulcan's Target Area West and Target Area Petawatt, respectively. The work of the

final experimental chapter 6 consists of measurements from Astra-Gemini, as well as the ISIS neutron and muon source, where the high energy muon RIKEN beamline was employed. This section gives a brief overview of these laser and muon facilities.

3.2.1 The Vulcan laser

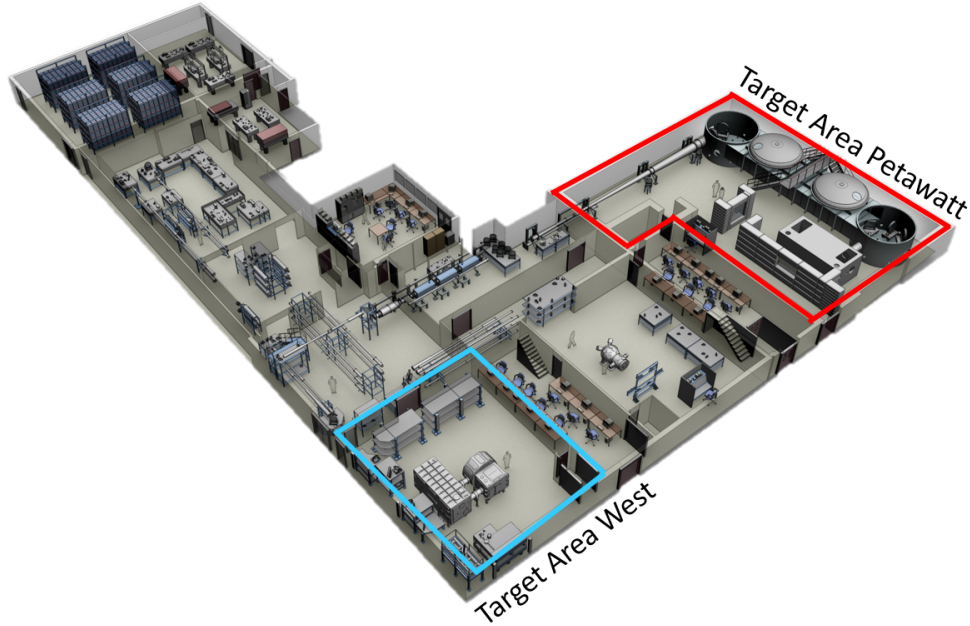


Figure 3.1: A layout of the Vulcan laser (<https://www.clf.stfc.ac.uk/>). Target areas West and Petawatt are highlighted in blue and red respectively.

Vulcan is a laser system based at the Central Laser Facility (CLF) [88], Rutherford Appleton Laboratory. It is one of the first lasers of the generation that are able to generate petawatt scale laser pulses. It is a Nd:glass laser that provides 8 beams, 6 of which are long pulses (\sim ns) and 2 which can be compressed to provide short pulses (\sim ps) to Target Area West (TAW). Target Area Petawatt (TAP) is configured to utilise two beamlines, the ultra-high intensity 1 PW beamline and a nanosecond duration pulse beam. The layout is shown in figure 3.1.

The main amplification stages use Nd:YAG – primarily a four-level laser gain medium, with central emission wavelength 1054 nm, and is pumped using flash lamps. The laser pulse starts in a mode locked oscillator feeding a stretcher with ultra-short 120

fs pulses. In Vulcan the oscillator is a Ti:sapphire laser medium pumped by a Nd:YAG laser, able to produce a large bandwidth pulse (222 nm (FWHM)), which enables for it to be compressed to very short pulse durations. The beam is then propagated into the stretcher where the pulse length is increased sufficiently in preparation for the main amplification stages. The pulse is passed to the preamplifier, where OPCPA is used to produce ≈ 10 mJ pulses. The laser beam is then pointed to the main amplification stages; here the energy of the beam is increased to 85 J in a 150 mm diameter beam. The beam diameter is gradually increased as it is amplified, to ensure the intensity is below the damage threshold of the gain medium. The pulse is directed to the final stage – amplifiers that raise the energy of the pulse to approximately 650 J. Both amplification stages use adaptive optics in order to maintain the quality of the wavefront and thus the final focal spot when the pulse is focusing in the chamber. In addition, the high frequency components are removed resulting in a smoother beam, by the use of pinholes 10-20 times the diffraction limit, known as spatial filters. Before the laser pulse can be focused, it is recompressed to a pulse duration of ≈ 0.5 -1 ps. The TAP Petawatt compressor uses two 940 nm diameter gratings to compress the pulse to < 1 ps. The compressor throughput after this yields approximately 450 J. Finally, the laser is focused to a focal spot of $\approx 5 \mu\text{m}$ (FWHM) by an f/3 off-axis parabola (OAP) resulting in peak intensities up to 10^{20} W/cm². The experiment reported in chapter 5 was conducted using the ultra-high intensity 1 ps TAP beamline.

Target Area West (TAW) is the second target area of the Vulcan laser [89]. It features 8 beamlines, two of which are high power beam lines, which deliver pulses of 1 ps (beam 7) and 10 ps (beam 8) after compression, and 6 long pulse (nanoseconds) beams, each delivering up to 200 J of energy on target. The 1 ps beamline (beam 7), which was used for an experiment in this thesis (chapter 4), utilises the CPA technique [11] and yields approximately 60 J of energy on target after compression. Beam 8 is able to deliver up to 300 J of energy in a 10 ns pulse also via the CPA technique. The TAW oscillator generates 1 nJ pulses with a duration of 120 fs from an 80 MHz laser cavity. Both of the laser pulses are typically focused onto target by an f/3 OAP. For the experiment presented in chapter 4, the 1 ps beam 7 was used in the f/3 configuration,

where the focal spot was $\approx 5\mu\text{m}$ (FWHM), resulting in peak intensities of the order of 10^{19} W/cm².

3.2.2 Astra-Gemini

The Astra-Gemini laser system located at the Rutherford Appleton Laboratory in the UK [90] is based on light amplification in Ti:sapphire, instead of Nd:glass as for the Vulcan laser. The advantage of Ti:sapphire is that it has a very large gain bandwidth. Consequently, a high number of frequencies can be amplified and compressed, yielding considerably shorter pulse durations of the order of a few tens of femtoseconds. The central wavelength of the light is 800 nm. Astra-Gemini comprises three amplification stages. The three early amplifier stages are the Astra laser, delivering ≈ 1 J of energy in 35-50 fs to the target area at a repetition rate of 1 Hz. The Gemini laser is essentially the fourth stage of amplification for the Astra laser pulse. At the final stage the laser pulse from Astra is split into two, where each beam line employs a Ti:sapphire crystal which is pumped using Nd:glass based laser that has been frequency doubled to green. These deliver ≈ 25 J of laser pulse energy to the final amplifiers, resulting in the final laser energy of ≈ 15 -20J. At the last amplification stage, the pump lasers have the capability to fire every 20 s, limiting the repetition rate of the Astra-Gemini system. Before the laser beam enters the target area, it is compressed to a pulse of < 50 fs. The same process is carried out for both of the two beams, which can be fired concurrently. Laser-solid and laser wakefield experiments are performed at Gemini. For the experiment in this thesis (chapter 6) the Gemini laser in the f/40 focusing configuration (spot size $\approx 30 \mu\text{m}$ (FWHM)) was used for laser wakefield acceleration. Even though the final energy delivered on target is much lower at this facility compared to Vulcan, the short pulse durations are still capable of producing intensities of 10^{19} W/cm² in the f/40 configuration.

3.3 Diagnostics

The key diagnostic techniques relevant to the work in this thesis are described in this section. These include energy resolving, electron and ion spectrometers, an electron diagnostic based on optical Cherenkov emission and conductive EMP probes, which were employed to obtain the experimental data presented in the subsequent chapters.

3.3.1 Magnetic electron spectrometer

A magnetic electron spectrometer is a widely used diagnostic technique. It is used in both laser-solid interactions to detect escaping electron spectra, and in wakefield acceleration experiments to characterise the electron beam charge and spectrum.

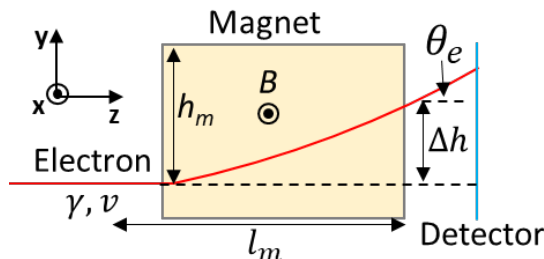


Figure 3.2: Basic schematic of a magnetic spectrometer. Relevant parts and quantities are indicated.

Figure 3.2 provides a schematic of a simple magnetic electron spectrometer. An electron propagates along the z -axis with a velocity, v , and a Lorentz factor (in relativistic cases), γ . It enters a magnet of a uniform magnetic field, B , length, l_m , and height, h_m . The electron then exits the magnet at an angle θ_e , and is incident onto a detector plane. The detector plane can be angled to provide a higher resolution. This is often done in wakefield acceleration experiments, where the electron beam energies reach several GeV. The spectrometer's ability to resolve the energies accurately is determined by the way the dispersion position depends on the electron energy. The position of an electron inside the magnet is governed by the Lorentz force:

$$\mathbf{F} = \frac{d\gamma m_e \mathbf{v}}{dt} = e \mathbf{v} \times \mathbf{B} \quad (3.1)$$

γ is constant as the magnetic field does no work on the electron. The Lorentz equation can be expanded into cartesian components as in equations 3.2-3.4

$$\frac{dv_x}{dt} = 0 \quad (3.2)$$

$$\frac{dv_y}{dt} = -\frac{Be}{\gamma m_e} v_z \quad (3.3)$$

$$\frac{dv_z}{dt} = -\frac{Be}{\gamma m_e} v_y \quad (3.4)$$

If an electron has a drift velocity along the field direction as it enters the magnetic field, this component will be unchanged by the field. The y and z components follow the simple harmonic motion, $\ddot{v} + \omega^2 v = 0$, for the cyclotron frequency, $\omega = Be/\gamma m_e$. We can show that the path of the electron in the y and z directions is a circle of a radius, $R = v/\omega$, by integrating for a second time. The electron exit angle, θ_e , and the change in height, h_m , are given in equations 3.5 and 3.6;

$$\sin\theta_e = \frac{l_m}{R} \quad (3.5)$$

$$\Delta h = R(1 - \cos\theta_e) \quad (3.6)$$

Laser-solid experiments utilise this technique to detect the electrons escaping from the rear of the target. The main detecting media are typically image plates or MCPs (discussed later in section 3.4.2), however the use of scintillators, such as LYSO ($\text{Lu}_{1.8}\text{Y}_{0.2}\text{SiO}_5:\text{Ce}$), are starting to be deployed. An electron spectrometer was used to measure the escaping electrons in the experiment reported in chapter 4. It was composed of a pair of magnets with a magnetic field strength of ≈ 0.1 T, and an image plate as a detector.

3.3.2 Cherenkov optical fibre

The Cherenkov radiation based fibre is an innovative diagnostic technique used to measure the number of hot electrons escaping the target in laser-plasma interactions. Cherenkov radiation is induced when a charged particle travels through a dielectric medium at a velocity greater than the local velocity of light, and has been exploited for decades in particle and high energy physics. In the Cherenkov fibre diagnostic, an electron traverses an optical fibre at a speed greater than the speed of light in that medium and has a characteristic half angle of emission for a given energy. The diameter of the fibre core dictates the path length of the electron inside the fibre and the fibre area which is exposed to the electron beam, both of which will increase the Cherenkov yield. Details of the mechanism for the generation of Cherenkov radiation are given in chapter 6 section 6.6. The Cherenkov fibre is a new recently published technique for laser-plasma experiments [91], nevertheless it is commonly used to measure radiation dose in electron beam therapy.

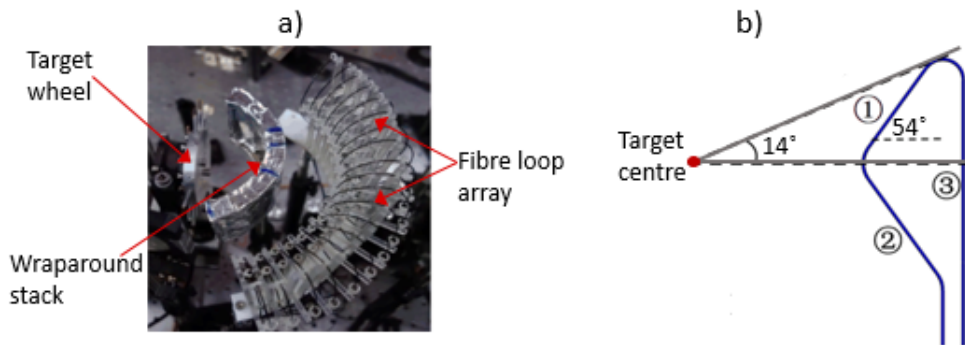


Figure 3.3: a) A photograph of a looped fibre array, placed behind the interaction, able to capture a large solid angle. b) A schematic of the geometrical structure of a curved loop.

A silica optical fibre described in this section was used to measure the flux of escaping electrons in Chapter 4, by measuring the light generated in the fibre using an MCP-PMT. The Cherenkov signal intensity inside the fibre depends linearly on the number of escaping electrons, which was determined by calibrations using a wraparound stack of image plates [92] placed between the target and the fibre array (figure 3.3 a)).

The angle between the propagation direction and the fibre axis must be smaller than the accepting angle, in order for the photons to be collected. Varying the incidence angle governs how many of the generated photons can be collected. It was reported by Liu *et al* [91] that to acquire strong, relativistic electron induced Cherenkov signal, a high hydroxyl (OH) concentration silica core (to increase transmission in the UV region where Cherenkov is mostly produced) and electron incidence angle of 45° is favoured. The diagnostic is a curved fibre array consisting of several curved loops of fibre wounded from a single long one. Each loop responds only to the electrons above a specific threshold energy, dictated by the angles of the fibre loops. The Cherenkov fibre is also capable of measuring escaping electron angular distributions. The fibre loops situated around the target, cover a horizontal angle of 85° with a 5° spacing between the adjacent loops. The geometrical structure of each loop is shown in figure 3.3 b), where segment 1) and 2) sample the escaping electron beam, and the incidence angle is typically between 40° – 54° . The angle of incidence onto segment 3) is too large for the generated photons to be collected, therefore it creates a time separation between the Cherenkov signals from two adjacent loops, enabling the output signals from the end of the fibre to be captured using a single MCP-PMT detector and subsequently recorded on an oscilloscope.

One of the prime advantages of this technique is that it provides immediate read-out, unlike image plate based diagnostics. This means that it is able to operate at high repetition rates without having to recycle image plates. This is especially important for the new facilities being commissioned, which are able to deliver repetition rates greater than 1 Hz. Due to the nature of Cherenkov radiation, whereby only charged particles induce photon emission, it also means that contributions to the background signal due to x-rays are strongly reduced. Additionally it is also immune to protons generated in the laser facilities relevant to this thesis; although charged, they are too massive to attain relativistic energies under the experimental conditions considered in this thesis, which are required for proton Cherenkov emission.

3.3.3 Thomson parabola spectrometer

The Thomson parabola spectrometer (TPS) (see figure 3.4 for a schematic) [93,94] is the most commonly deployed spectrometer for ions accelerated in laser-solid interactions and has the ability to energy resolve the ion spectra and separate the ion species by charge-to-mass ratio.

A basic design involves a small pinhole (tens to hundreds of μm in diameter), selecting a pencil beam of ions, which is situated at the entrance of the TPS. The role of the pinhole is to select a small solid angle of the ion beam. This limits the angular acceptance into the TPS and thus improves the energy resolution. It also limits the flux onto the detector medium, which would otherwise saturate the signal. The ions then travel through regions of parallel magnetic and electric fields applied transversely to the beam, before reaching the detector (IP) plane. The magnetic field is typically provided by a pair of high field strength permanent NdFeB magnets of field strength 0.1-1 T (0.6 T is used in the setup described in this thesis), and the electric field is generated using a pair of copper plates attached to a high voltage power supply with typical voltages of 5 kV and above. The electric field induced by such a voltage, for a plate separation of 2 mm, reaches 2.5×10^6 V/m.

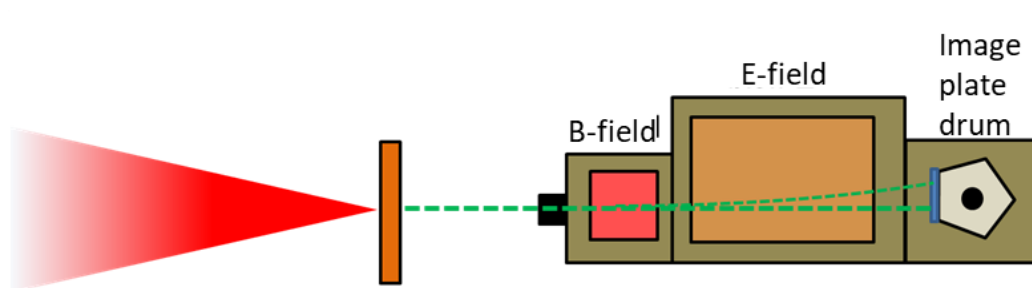


Figure 3.4: Basic schematic of a Thomson Parabola Spectrometer. Laser is incident from the right on a target. The sheath field set up by hot electrons results in acceleration of an ion beam in the forward direction. A pencil beam of ions is selected by a pinhole and travel through regions of parallel magnetic and electric fields applied transversely to the beam, before reaching the detector plane – in this case image plate.

The ion species are deflected according to their charge-to-mass ratio and energy in the magnetic field and all positive ion species experience a deflection in the same direction in a magnetic field. The second deflection by the electric field cause the

deflection in the direction of the electric field, orthogonal to the magnetic field. The resulting dispersion can be calculated using the Lorentz force equation, $\mathbf{F} = q(\mathbf{E} + \mathbf{v} \times \mathbf{B})$. The displacements from each plate, d_B and d_E , induced by the magnetic, B_0 , and electric, E_0 , fields can be expressed as:

$$d_{By} = \frac{q}{m} B_0 \frac{L_B^2}{v_z} \left(\frac{1}{2} L_B + d_B \right) \quad (3.7)$$

$$d_{Ex} = \frac{q}{m} E_0 \frac{L_E^2}{v_z^2} \left(\frac{1}{2} L_E + d_E \right) \quad (3.8)$$

where v_z is the velocity component of the ion as it traverses the fields, L_B and L_E are the lengths of the magnetic and electric fields, respectively, along the direction of ion propagation, and d_B and d_E are the distances between the end of the magnetic and electric fields and the detector plane, respectively. Therefore the position of the ions on the y-axis of the detector medium is dependent upon the particle velocity (or energy) determined by the magnetic field, while the position of the ions on the x-axis is determined by the electric field governed by the charge (q) to mass (m) ratio and the ion velocity. The ion species separated according to their charge-to-mass ratio and energy will result in parabolic paths (hence the name Thomson Parabola) at the detector plane, where the ion energy is proportional to its deflection in the magnetic field, which is due to slower ions spending longer in each field.

3.3.4 EMP probes

There are multiple diagnostics and techniques that can be employed for electromagnetic pulse (EMP) detection. Many work on the following principle: a conductor placed in the presence of an electromagnetic field (i.e. induced by EMP) becomes a source of current, and exhibits features related to the applied electromagnetic field. This current can be transferred to a transmission line, where the associated electromagnetic wave travels with low attenuation to a detection device. The resulting wave form is recorded and stored on an oscilloscope, and can be related to the electromagnetic field, which can ultimately tell us about the spectral intensity characteristics of the EMP. The

early examples of EMP measuring devices are simple dipolar antennas and resonating loops [95,96]. B-dot and D-dot probes that measure the rate of change of magnetic and electric fields, respectively, are often used. There are also probes for detection of neutralisation current, also known as return current, which is defined as the current flowing between the target and the ground through the target mounting system. In the work of this thesis, Prodyn B-dot and D-dot sensors were used. The output of which is a voltage as a function of time, to which a fast Fourier transform can be applied to obtain the frequency spectrum.

The D-Dot sensors measure the time derivative of electric displacement from near DC to >50 GHz (3 dB point) [97] with an output voltage given by the following relations:

$$V_0 = R \cdot A_{eq} \cdot \frac{dD}{dt} \text{ or } V_0 = R \cdot A_{eq} \cdot \frac{dq_s}{dt} \quad (3.9)$$

where V_0 is the sensor output (volts), R is the sensor characteristic load impedance (50 ohms), $A_{eq}=1.54 \times 10^{-5} \text{ m}^2$ is the sensor equivalent area quoted by the manufacturer, D is the magnitude of the electric displacement vector ($D = \epsilon_0 E$ in Coulomb/m²) and q_s is the surface current density (Coulomb/m²) [97]. The B-Dot sensors measure the time derivative of the magnetic field with a frequency response of ≈ 8.5 GHz, governed by the equation:

$$V_0 = A_{eq} \cdot \frac{dB}{dt} \quad (3.10)$$

where B is the magnetic flux density vector measured in T, and $A_{eq}=9 \times 10^{-6} \text{ m}^2$ is the sensor equivalent area given by the manufacturer [98]. The response of the FD-5 D-dot probes (the type employed in the measurements presented in this thesis) to different frequencies was experimentally tested by Raczka *et al* [99]. More details on EMP diagnostics can be found in reference [18].

3.4 Particle and radiation detectors

A variety of detectors can be employed within the diagnostics described in the previous section, based on what information needs to be extracted. The detectors used for

measurements presented in this thesis include image plates, MCP-PMTs, scintillators, and digital photon detectors, which are commonly utilised in laser-plasma experiments. A description of each is provided below.

3.4.1 Image plate

The detection media often used in Thomson parabola spectrometers are the following: image plate (IP), California-Resin 39 (CR-39) or a microchannel plate (MCP). IPs were used in the experiment reported in this thesis, and is described in this section. However, advances in laser technology, in particular improving repetition rates, are forcing the exploration of additional active detector media, less susceptible to EMP, such as scintillators described in section 3.4.3.

Since the advent of Fujifilm image plates (IPs), they have become a common detector in charged particle (electrons, protons, ions) and x-ray diagnosis in various disciplines of experimental science, such as medicine, biology, materials research. The benefits of these detectors include large active area, high resolution (typically $25\ \mu\text{m}$) and dynamic range ($>10^5$) while also being reusable and unaffected by electromagnetic pulses present during experiments at high power laser facilities. There are several types of commercially available IPs, based on the same mechanisms, but possessing modifications to optimise them for a particular use. BAS-SR and BAS-MS have a protective mylar layer on the sensitive layer to provide water resistance, with small differences to improve either the resolution or the sensitivity, respectively. Fujifilm BAS-TR were used in the work presented in this thesis, as they have a thinner sensitive layer and no protective mylar layer, making it more sensitive to low energy particles.

IPs operate via a process known as photostimulated luminescence (PSL) – the release of stored energy within a phosphor by stimulation with visible light to produce a luminescent signal. IP comprises an active layer (typically of $100\ \mu\text{m}$ thickness) of barium fluorahalide phosphor crystals doped with europium (Eu) atoms ($\text{BaF}(\text{Br},\text{I}):\text{Eu}^{2+}$). When the active layer is exposed to an incoming X-ray photon or a high energy particle, electron-hole pairs are created (electrons are liberated from the Eu^{2+} ions) and trapped in metastable lattice defects (so-called F-centres or colour centres). These

electrons remain in a metastable state until they decay to the ground state either via spontaneous emission or via stimulated emission by using a secondary illumination. The decay can be induced due to spontaneous recombination of electron-hole pairs leading to a gradual fade. The IP is processed by using an optical scanner, where it is exposed to secondary illumination – a red laser (e.g. He-Ne with 680 nm wavelength). This causes the electrons to recombine with the Eu^{3+} ions followed by a decay to a lower energy level and release of blue light (390 nm); this is known as PSL. The intensity of the emitted light is proportional to the incident radiation. An IP scanner can extract the position and brightness of this emission, which provides spatial and intensity information about the particle beam incident on the IP. The blue light released in the stimulated emission is detected by a photomultiplier tube (PMT) inside an IP scanner and the signal is amplified and converted to a digital image by an analogue to digital converted (ADC). The same pieces of IP films can be used again after all the metastable electrons are depopulated, which is simply exposing the IPs to a white light source also known as ‘wiping’; this is a major benefit. IPs are often used in Thomson parabola spectrometers [93, 94], magnetic electron spectrometers [100, 101] and x-ray spectrometers [102–104]. However, IPs represent a major barrier in the repetition rate of laser-plasma experiments given the time needed to scan and record data.

3.4.2 Microchannel plates

Microchannel plates (MCPs), are used for the detection of a number of particles including electrons, ions and neutrons and radiation. They work by a similar principle to a standard photomultiplier tube (PMT), by the multiplication of electrons via secondary emission. In the case of detecting electrons, ions or neutrons, a scintillating material layer is placed at the entrance to the MCP, where the photons are produced. A photon incident onto the photocathode liberates an electron by photoelectric effect, which is multiplied at the next stage by secondary emission, and then multiplied again at the next in a dynode structure and eventually is pulled to the anode under the applied electric field. Light is converted to electrical signal, which can then be measured using an oscilloscope. The dynode structure present in a PMT is replaced by an MCP. An

MCP is a thin plate of approximately 2 mm thickness and is typically made of a highly resistive material such as glass, with an array of 10-100 μm diameter holes, which act as a continuous dynode structure. The channels are spaced apart by approximately 15 μm and are parallel to each other, and often at a small angle to the surface. A strong electric field is applied across the MCP, and so each individual microchannel becomes a continuous dynode electron multiplier. As a particle or a photon enters one of the microchannels, it is certain to be incident onto the channel wall, due to them being at an angle to the plate. Consequently, a cascade of electrons is started which propagates through the length of the channel, amplifying the signal at each impact by several orders of magnitude. In the case where an MCP-PMT set up is used, the electrons leave the channels on the opposite end of the plate and are collected by the anode, at which point the signal has been amplified many times. Often two or three MCPs are assembled one after another inside a photodetector to achieve higher amplification. The separate channels add an advantage in that it can provide extra spatial resolution. Therefore MCPs can also be used as image intensifier, where a phosphor screen is used instead of the anode. The secondary emission electrons that exit the microchannels maintain the positions of the photoelectrons on its input and strike a phosphor screen which releases a photon for every electron.

MCPs are ideal for high speed single photon counting applications, as they offer low dark count rates and high dynamic range. They have high gain of 10^6 and high collection efficiency of $\approx 60\%$. They additionally have the capability to be gated with current models able to achieve temporal resolution on the order of 1/6 ns. This is particularly useful in laser-plasma experiments, where a high background of secondary particles is often present; undesired signal can be gated out. MCP-PMTs are often used coupled to a scintillator, which is briefly described in the next section 3.4.3. As the scintillator is transparent the MCP-PMT can image the back of it. A set up like this was used for background x-ray detection in for the results presented in chapter 6.

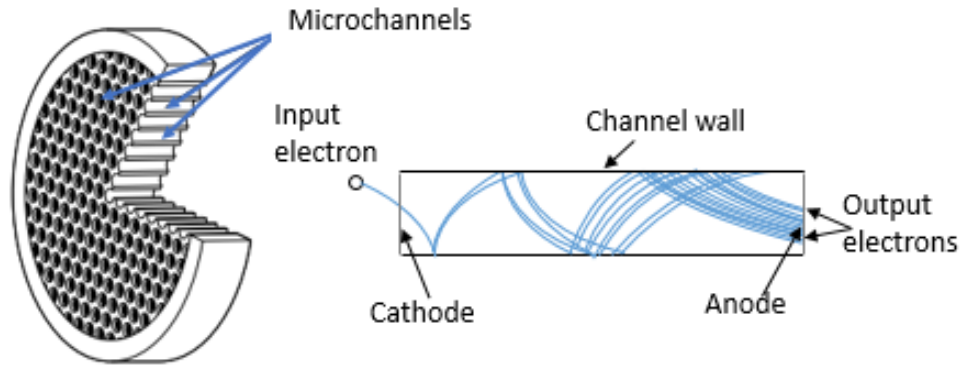


Figure 3.5: A microchannel plate consists of many channels. The converted electrons strike the channel walls and are multiplied through secondary emission. Each channel has a potential which accelerates the electrons along. The electron signal is collected at the output anode at the end of the channel.

3.4.3 Scintillators

A scintillator is a material which absorbs the energy of an incoming particle or radiation and re-emits the absorbed energy in the form of light emission. There are two main types of scintillators, organic and inorganic, which differ chemically as well as in the process by which they release photons. Scintillation (also referred to as luminescence) in inorganic scintillators is primarily a crystal property. Inorganic scintillators, such as bismuth germanate (BGO), are crystalline compounds, where the luminescence originates from emission centres in the compounds themselves or generated by activating agents. These types of scintillators are typically insulators or semiconductors possessing a band gap, E_g (few eV), between the conduction and the valence bands. If ionising radiation of sufficient energy strikes, the electrons can gain enough energy and be promoted from the valence to the conduction band, leaving behind positive holes in the valence band. Those electrons can also go on to create secondary electrons via Coulomb scattering. The electron-hole recombination results in scintillation photon emission. The activators (or impurities) that may be added to the compound, create sites in the lattice where the energy band gap is modified, where the electrons can de-excite before falling back to the valence band. If a high energy particle is incident

onto the scintillator, many secondary electrons are created, and those act in the same way as in the case of x-rays. In organic compounds scintillation is a molecular phenomenon. The luminescence in these compounds is associated with electron transitions between the different energy levels of a single molecule. The electron decays from its excited state before transitioning to the ground state. In the case of organic scintillators, the energy from a particle is absorbed, exciting the electron into a number of excited states. The decay can be via a singlet state (referred to as luminescence) or a triplet state which has longer time scales (referred to as phosphorescence). The singlet (S) levels are subdivided into a series of finer levels which correspond to the vibrational states of the molecule. Inorganic crystals such as BGO have slow decay times (μs) and have high scintillation yield, while the organic ones such as the BC422 are much faster (10 ns), but suffer from a lesser scintillation yield. Short decay time is important as it reduces the dead time – the minimum time interval that two successive counts must be separated by to be recorded as two distinct events, and can accommodate high repetition rate events.

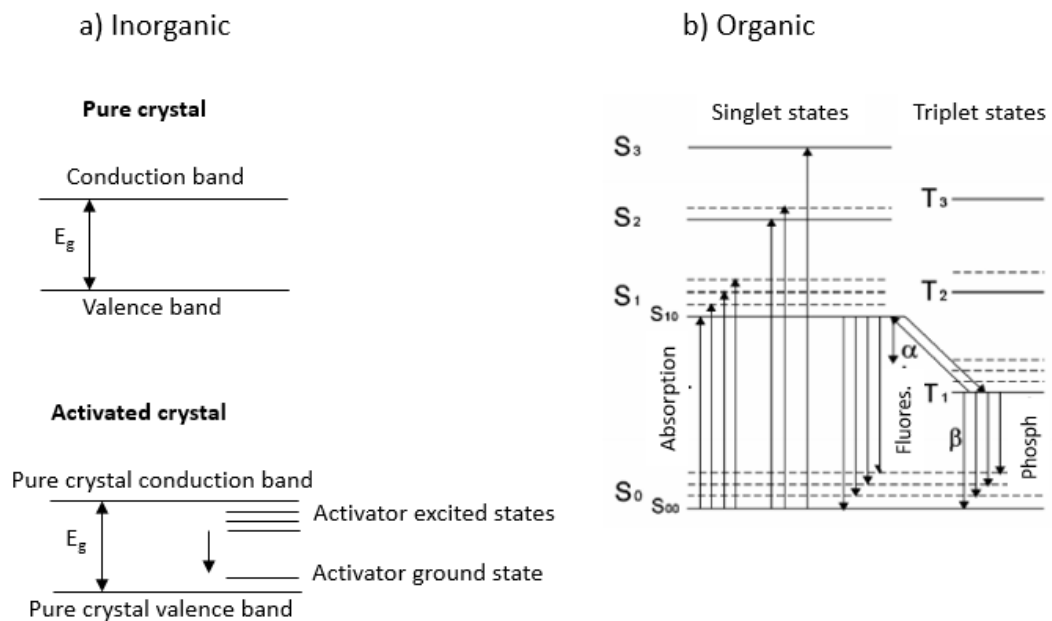


Figure 3.6: a) Energy band structures of an inorganic pure and activated crystals. b) Energy levels of molecules in an organic scintillator.

The type of scintillator most relevant for this thesis is an organic BC422 (or EJ-232 equivalent from a different supplier) – a plastic scintillator designed for fast timing applications. It was coupled to an MCP-PMT for x-ray detection in the experiment described in chapter 6. Energy from a particle is absorbed, exciting the electron into an excited state when the electron drops back to its ground state, the energy is emitted as a photon – a process of fluorescence. The average distance travelled by a moving photon between successive collisions is known as the optical mean free path, and for these scintillators is approximately 10 cm due to the small emission wavelength, therefore for best light collection and optimised timing these should be smaller than 10 cm to minimise photon scattering effects and preserve the spatial resolution. Thin layers should be used for the best possible resolution, where a considerable amount of light is emitted. Where the incident radiation/particles are scarce, it may be beneficial to increase the thickness in order to maximise the energy deposition. The deposited energy by the particle is proportional to the scintillation light; it is usually measured in photons per MeV. BC422Q (EJ-232Q) is a quenched variant intended specifically for ultra-fast counting applications. The doping material introduced in this scintillator is benzophenone whose effect is shortening the timing properties for achievement of very high counting rates or improved coincidence timing. The quenching reduces the scintillation efficiency (light output) while the emission spectrum is unaffected.

Scintillators are used for the detection of various particles, such as photons [105], protons [106], electrons and muons, in high power laser, and high current conventional particle accelerators. They are often coupled to a camera such as a CCD, EMCCD or a CMOS (discussed in section 3.4.4), or alternatively to MCP and PMTs. Scintillators are commonly employed in x-ray spectrometers [105], and are also becoming popular in electron spectrometers.

3.4.4 Digital cameras

CCDs were invented in 1969 at Bell Labs by Willard Boyle and George Smith as an image sensor and could also be used as a method of semiconductor memory. CCD digital cameras are made of semiconductor materials, typically silicon. Like all digital cameras

they work by converting the incident photons into electrons through the photoelectric effect. The charge moves across the surface of a semiconductor and serially passes pixel information to its output channel. The charge generated by each pixel is proportional to the amount of light absorbed by the pixel. In applications where there are ultra low light conditions, the read noise floor can become the dominant detection limit. This compromises the overall signal to noise ratio and therefore the ability to resolve the features. This inability to maintain low noise at faster readout speeds limits the overall flexibility of a CCD camera.

CMOS sensors are based on metal-oxide-semiconductor (MOS) technology with sensors based on MOS field-effect-transistor (MOSFET) amplifiers. Just like CCDs they work by capturing light and converting it to electrical signal which can be readout. They were first conceived in the late 1960s, and became commercialised in the 1990s as the microfabrication technology advanced. CMOS cameras were launched as an alternative to CCDs. CMOS can be implemented with fewer components, have a lower power consumption and are cheaper than CCDs. They provide a faster readout than CCDs which is advantageous in fast timing applications. The faster readout is a result of each pixel having a photodiode and a CMOS transistor switch, which enables the pixel signals to be amplified individually, which means that pixel signals can be accessed directly and at much faster speed than CCD sensors. Another big advantage that the individual amplifiers provide is the reduction of noise which occurs during the reading of electrical signals. Current CMOS technology is very advanced and science grade CMOS cameras have high sensitivity and high dynamic range, and are perfectly adequate for many applications in laser-plasma experiments.

In the early 2000s the Electron Multiplying CCD (EMCCD) technology was launched by several companies including Texas Instruments, Teledyne (previously known as e2v) and Andor. The EMCCD is a modified CCD, in which the signal is amplified by the on-chip amplification mechanism called Impact Ionisation, which multiplies the photoelectrons generated in the silicon. The employment of this technology enables for the signal generated from a single photon to be amplified above the read noise floor at MHz readout speeds. This makes EMCCDs capable of single photon sensitivity at fast

frame rates (e.g. 34 fps with a 512 x 512 array for an Andor EMCCD).

Photon detecting cameras are common in many diagnostics used in laser-plasma experiments, from reflectivity monitors to electron spectrometers. Continual development of photon detector technologies, such as improved sensitivity and reduced noise, enables more accurate measurements to be taken. Both CMOS and EMCCD cameras were utilised in the work of this thesis. An EMCCD was employed in the muon Cherenkov detector reported in chapter 6, due to its ability to multiply very low intensity signals. The high dynamic range of a CMOS camera was exploited to record optical light emissions in glass in chapter 6. It is important for the camera to possess a high dynamic range, which is typically described as the difference between the most and least bright detectable features of the environment that is being imaged. This is important in laser-plasma experiments as there are often bright secondary particle emissions or undesired leaks in the system, which may potentially saturate the camera and prevent from seeing the weaker signals. Many modern digital cameras such as CCDs, EMCCDS and CMOS, involve the cooling of the photosensitive array, which reduces the thermal and electronic noise (see figure 3.7), potentially allowing for single photon counting applications, or very dim signal measurements.

3.5 Simulations

Numerical simulation codes are a powerful and useful tool in the study of laser-plasma interactions. They can be used as a predictive tool for experiments, and to help interpret the results and the underlying physics. Additionally, often a limited number of diagnostics can be deployed to characterise the interaction, and therefore modelling can be used to probe parameters that cannot be directly measured. Analytical modelling can be useful to gain insight into some of the problems, however this can become very complex as the number of parameters to consider can often be large. Therefore a deeper understanding can be gained by using numerical models which include a much larger number of physical parameters and effects, which are outlined in this section.

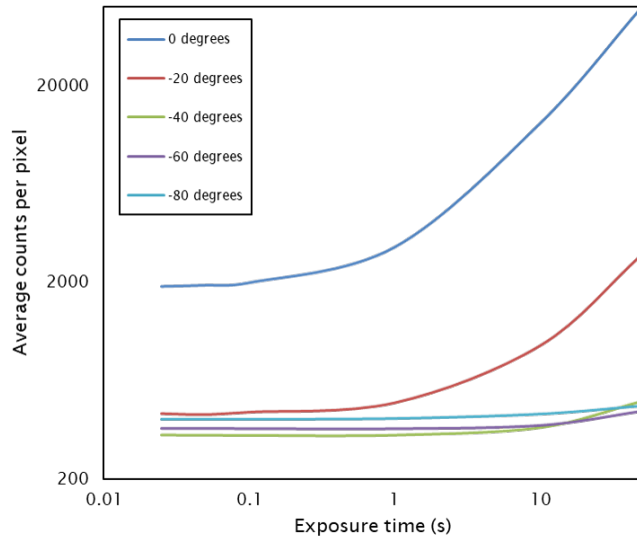


Figure 3.7: iXon EMCCD average noise counts per pixel when no signal is present as a function of exposure time for different detector array temperatures. The cooling of the array significantly reduces the noise counts.

3.5.1 Monte-Carlo simulations

The Monte Carlo methods are computational algorithms relying on random sampling to generate numerical results and are used to model the probability of different outcomes of a process. It is based on the concept of solving deterministic problems using randomness. The algorithm is repeated until the average statistical behaviour of the system can be approximated.

GEANT4, an example of a Monte Carlo based code, was used in this thesis to simulate muon production in a solid converter target irradiated by a high energy electron (and x-ray) beam. It was used to determine the number of muons as well as the beam position properties, and aid experimental and diagnostic design. GEANT4 (GEometry ANd Tracking) is a highly flexible and functional toolkit, based on the Monte Carlo method, for the simulation of the passage of particles through matter based on Monte Carlo simulation method, using different physics models and geometry and tracking methods [107]. It was developed as an object-oriented simulation programme by CERN and other collaborators. Its main applications are in high energy physics, accelerator and nuclear physics, but is also common in medical as well as laser-plasma

physics. The GEANT4 platform was released in 1998 and has been well maintained by the Geant4 international collaboration. Geant4 has a high coverage of the physics from a combination of theory driven cross section tables as well as empirical formulae which can be combined into one particular process. GEANT4 is capable of simulating a number of different interactions – from hadronic and electromagnetic [108–110] to neutron transport [107]. It comes with a complete set of electromagnetic models which can operate at different energy regions. The user is able to select the physics processes and models to be taken into account in the simulations.

At the start of a typical simulation, a particle is created with some particular given energy, location and direction and is allowed to propagate into the geometry. Those particles are each assigned a random number differentiating them from other initial particles. In this way the particles' unique interactions via various physical processes (particle decay, photoelectric effect, Compton and Rayleigh scattering, muon pair production, ionisation, bremsstrahlung to name a few) can be determined. The interactions will depend upon the transport data of a particular material that the particle is traversing, which are obtained from theoretical and experimental models. The initial particle may create second and tertiary particles and/or radiation during its journey, and those are also simulated. When the total kinetic energy of the systems equals zero, then a new particle is established with another random number and the process repeats.

It is a convenient time saving toolkit, as the researchers can spend less time on the low level details and start on the more significant elements of the simulation. Nevertheless there are some limitations, including its failure to take into account the inter particle interactions. As a result it is more useful for studying environments such as interaction for particles with bulk materials, where collective effects can be neglected.

3.5.2 Particle-in-cell simulations

Particle-in-cell (PIC) codes are used for modelling the plasma dynamics using the kinetic approach. In an ideal case such a description of the plasma begins with solving the Fokker-Planck equation that describes the particle velocity distribution function

for each species:

$$\frac{\partial f_{VFP}}{\partial t} + \mathbf{v} \frac{\partial f_{VFP}}{\partial x} + q(\mathbf{E} + \mathbf{v} \times \mathbf{B}) \frac{\partial f_{VFP}}{\partial \mathbf{p}} = C(f) \quad (3.11)$$

where $f_{VFP}(r, p, t)$ is the distribution function and $C(f)$ is the collision term. Typically a laser plasma is assumed to be collisionless as the ionisation rate is fixed, resulting in the Vlasov equation. The distribution function is six-dimensional (three spatial and three momentum), thus it is very difficult to solve. It also requires a lot of computational memory, as the computational requirements increase with the number of particles to the power of six. Instead of the the distribution function being made up of real particle numbers, in PIC codes this is solved by treating a number of real particles as weighted macroparticle which approximates the distribution of the real particles. Those macroparticles have the same charge-to-mass ratio as the represented particles. The macroparticles are mapped onto a grid, which allows calculation of their position, current and density. In a PIC code the fields propagate relative to the grid and macroparticles are free to move between the grids. When the current and density are determined for a given grid position, the resulting magnetic and electric fields can be computed by solving the Maxwell's equations, and subsequently the motion due to Lorentz force can be determined. This gives a new value to the current and the density, and brings us to the beginning of the loop. This algorithm is iterated for the duration of the simulation and follows four principle steps, shown in figure 3.8

There are a number of potential issues associated with PIC codes. Numerical instabilities can occur if the conditions of spatio-thermal requirements to resolve the highest frequency, i.e. the plasma frequency in laser-solid interactions, and the length scales of the order of the Debye length, are not met. Non-linear self-heating of the system will occur if the Debye length is not well resolved, until the condition is met, leading to non-physical behaviour. Additional effects include phenomena such as ionisation and collisions, which are typically left out of the algorithm, and can result in non-physical behaviours, for example unrealistic growth of magnetic field since dissipation of the field due to collisions is not included. As with most simulation codes, PIC codes do

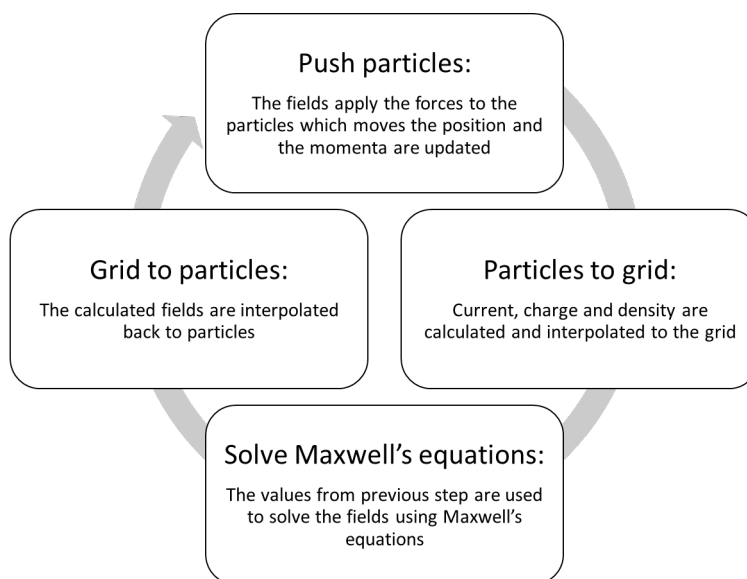


Figure 3.8: Standard algorithm for PIC simulation codes.

not simulate all physics which is occurring in the system, but is still relevant and representative of the physics being simulated. One of the most commonly use codes used for laser-plasma interaction research is EPOCH, a fully relativistic 3D PIC code [111]. Results from PIC simulations were used to motivate and support some of the experiments reported in this thesis, although PIC simulations are not directly used in this work.

3.6 Summary

In summary, performing experiments to investigate laser-plasma interactions requires knowledge and use of several areas of physics, a combination of key laser technologies and the implementation of numerous detectors and diagnostic techniques as well as analytical and numerical modelling. Laser technology is continually improving to provide short, intense laser pulses at high repetition rate, which are well diagnosed. These areas require considerable effort in coordinating and planning prior to the beginning of the experiment. Multiple diagnostic techniques are implemented on experiments in order to develop an understanding of the key processes occurring during the complex laser-plasma interactions. Additionally, numerical and analytical modelling are often

involved, to help attain a comprehensive understanding.

Chapter 4

Scaling of EMP and proton acceleration in the TNSA regime of laser-solid interactions

4.1 Introduction

High power laser-solid interactions generate hot electrons, which subsequently drive ion acceleration, and produce x-ray and terahertz emission. Amongst these phenomena, is the EMP (electromagnetic pulse) intense broadband electromagnetic pulses ranging across a wide frequency range from radio [112] to optical and x-ray [113]. EMP produced in the interaction of a petawatt class short laser pulse and a solid density material is in the gigahertz to terahertz domain, exceeding 1 MV/m [65, 114], which may interfere with or even damage electronic equipment used to diagnose the interaction. For many years, shielding was used to reduce the impact of EMP on the electronic equipment, with moderate success. The advancements of high power laser technology [15, 114] have led to renewed interest in understanding the characteristics and mechanisms of EMP emission for more effective shielding and techniques to reduce EMP production in laser-plasma interactions. It is widely accepted that the EMP generation arises due to the ejection of hot electrons from a solid target when a laser pulse of high power

interacts with a solid target [61, 64, 65]. The act of the electrons escaping the target creates a charge imbalance in the target leaving it positively charged, which causes a neutralisation current to be drawn through the stalk. This now behaves like an antenna where the discharge current oscillates along the stalk and target [16], as illustrated in the schematic in figure 4.1. The electromagnetic environment created in the target chamber of a high power laser facility can also contain secondary sources of EMP caused by electron currents created when emitted x-rays irradiate metal surfaces or cables. While EMP is often an undesirable effect in high power laser-plasma interactions, there are a number of multidisciplinary applications, including biological studies of microwave interactions with cells [115], space communications [116], medical engineering [117] and EMP radiation hardening of materials [118], to name a few examples.

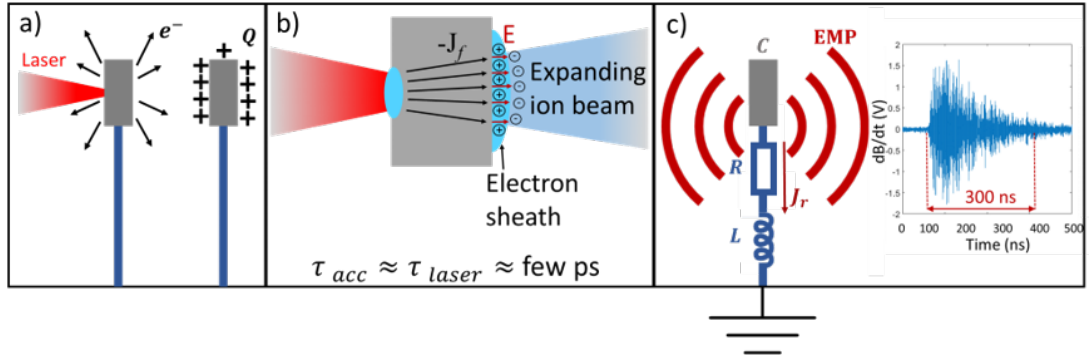


Figure 4.1: a) A laser pulse irradiates a solid target and causes some of the electrons to escape, positively charging the target. b) The escaped electrons set up a sheath field which accelerates the protons in the TNSA regime. c) EMP is emitted due to a return current drawn to neutralise the positive target charge. Typical EMP signals in the Vulcan facility are several hundreds of ns in duration.

It is believed that there are multiple mechanisms that contribute to the generation of EMP in laser facilities. However, the interplay between different mechanisms has so far remained uncertain. The excitation of resonant modes of the target chamber (EM waves bouncing off the chamber walls) are thought to enhance the low frequency signal (few hundreds of MHz for the interaction chambers in this study) [62, 63], while high frequency components of the generated EMP can arise due to x-ray irradiation of cables and metal chamber components. The main high frequency signal is believed to result from the previously mentioned charging of the target [1, 2, 16].

Due to the new developments of high power laser technology and laser powers exceeding 1 PW [15,119], EMP is becoming an increasing issue disrupting experiments. In order to understand the sources of EMP and be able to mitigate it in high power laser plasma interactions, a study was carried out to investigate the correlation between the sheath field that drives the protons, and the emission of EMP. This is a first study of its kind, opening up a new understanding to EMP and ways of characterising it, in this relatively simple manner.

4.2 Experimental method

The experiment was conducted in the Target Area West of the VULCAN laser system. A short pulse of ≈ 2 ps duration was used, with energies on target ranging from 1 to 70 J. This pulse was p-polarised and of wavelength 1054 nm was focused by an f/3 parabola onto a target at 30° to the target normal. Intensity was varied in two different ways: 1) by changing the laser energy and 2) changing the focal spot size and will be referred to as energy and defocus scans, respectively. The focal spot size was kept constant at $3.5 \mu\text{m}$ (FWHM) for the energy scan. The intensity was varied in the range of 10^{17} W/cm^2 to 10^{20} W/cm^2 . Three probes were used to measure the EMP during the experiment – two B-dot probes and a D-dot probe, as discussed in section 3.3.4, that measure the rate of change of magnetic field and the rate of change of electric field, respectively. These were positioned behind a glass port on the east side of the chamber, 0° vertically from the target chamber centre (TCC). Another B-dot probe was located on the opposite west side of the chamber, behind a glass port 35° vertically from TCC. The three probes were all outside of the vacuum chamber in air, as seen in figure 4.2. Both B and D-dot probes were manufactured by Prodyn Technologies. B-dot probes were B-24 detectors connected to a BIB-100G matching box, and the D-dot was a FD-5C model. The measurements were passed through 35 m double shielded BNC cables to an oscilloscope located outside of the target area. A Tektronix model DPO 71254C oscilloscope with 12.5 GHz analog bandwidth was used. However, the cable parameters effectively limited measurements to frequencies below 3 GHz.

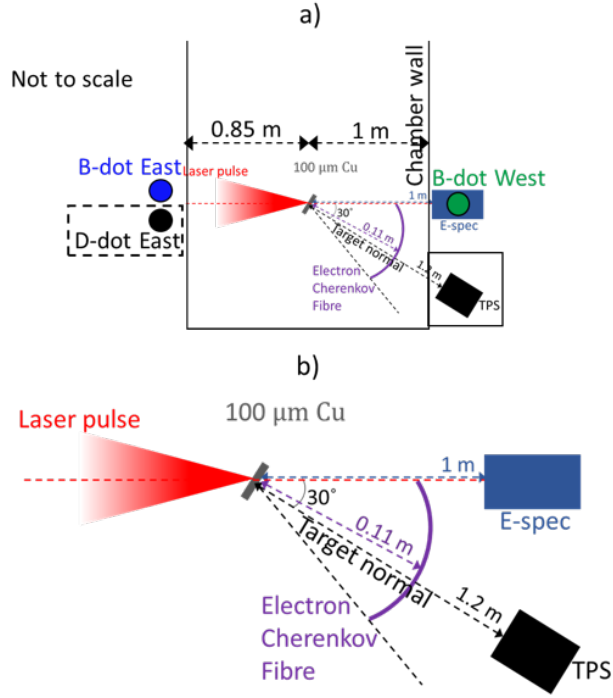


Figure 4.2: a) Schematic of experimental layout in TAW. The Thomson parabola spectrometer was positioned 1.2 m away at target normal angle subtending a solid angle of 26.2 nsr. The electron spectrometer was placed on the laser axis while the Cherenkov fibre was wrapped around the rear of the target covering 55°. D-dot East is indicated by a black dashed box as its data was used primarily. Two B-dot probes were located on the east and west sides of the chamber. b) An enlarged view.

TNSA and EMP are both related to the sheath field introduced by the ejection of hot electrons from the target [53, 60, 61], therefore along with EMP measurements we also made proton measurements in order to relate EMP to proton acceleration due to the electron sheath. Additionally, electron data from an electron spectrometer (E-Spec) (section 3.3.1) and the electron Cherenkov fibre (section 3.3.2) is also presented to aid in understanding the escaping hot electron flux scaling. To measure the proton spectra, we used a Thomson parabola ion spectrometer (TPS), which has the ability to energy resolve the ion spectra by charge-to-mass ratio, though the study here focuses on the laser-driven protons only. The detector was placed in a separate vacuum chamber 1.2 m away from TCC. A 200 μm diameter pinhole positioned at the entrance of the TPS selected a pencil beam of ions (26.2 nsr), which then travelled through

regions of parallel magnetic and electric fields applied transversely to the beam, before reaching the detector plane. The detector used in this campaign was Fujifilm BAS-TR image plates, which are digitised using an image plate scanner utilising photostimulated luminescence.

4.3 Experimental results

In this section, measurements from laser energy and defocus scans are presented and correlations between the EMP emission and the maximum proton energy and number are provided. In addition, electron data and correlations are also presented. The error bars for proton and electron data are calculated similarly to EMP, where shots with similar conditions are compared, and the standard deviation determined. The laser intensity was changed in two ways: 1) by changing the laser energy and 2) by changing the focal spot size (defocusing). In the energy scan the laser pulse duration and spot size were maintained constant. The laser pulse duration and energy were near constant in the defocus scan. For intensity calculations, laser energy and pulse duration were obtained from the Central Laser Facility database eCat. Individual energy scan pulse durations were not available on the system, therefore an average from multiple shots was computed and used for intensity calculation. The focal spot size and quality were taken into account when calculating the intensity.

An energy scan was performed to confirm the previously measured and published data for protons and electrons [51, 57, 120, 121]. This was then used to investigate the relationship between EMP and proton generation. In the experiment, ≈ 2 ps laser pulses irradiated 100 μm thick copper foil targets mounted on plastic cylindrical stalks. The laser energy on target was varied between 1 and 70 J, corresponding to intensities of 7.2×10^{18} and 3.5×10^{19} W/cm^2 , respectively.

We also studied the effect of laser defocus (i.e. focal spot size) on EMP energy and the relationship between the EMP and the maximum proton energy. For this scan, the laser energy on target was in the range of 54-64 J and the pulse duration 2 ± 0.6 ps. The distance from nominal laser focus was varied between -300 and $+350$ μm , corresponding

to 100 and 110 μm diameters. The intensity ranged from 9.1×10^{16} – 8.2×10^{19} W/cm^2 . As for the energy scan, the laser was incident on 100 μm thick copper foils on plastic cylindrical stalks.

EMP output data from the oscilloscope was processed in the following way: A Fast Fourier Transform was applied to the output voltage from the oscilloscope to produce a frequency spectrum (voltage vs frequency). The voltage amplitudes were squared and integrated over the range of frequencies. The result is proportional to EMP energy and has units V^2/s or $\text{V}^2 \cdot \text{Hz}$. It is known that the square of voltage is proportional to energy (joules), $E = V^2 t / R_\Omega$, where R_Ω is the electric resistance in ohms and t represents time (pulse duration). The error bars for the EMP data are calculated as percentage standard deviation based on several shots with similar laser conditions.

Proton data was analysed using Thomson Parabola software written by Satyabrata Kar.

4.3.1 Protons in energy and defocus scan

The scans were carried out in order to compare with previous work and confirm that the data is as expected. Laser energy and defocus effects on the number of detected protons, N_p , and the maximum proton energy, E_{pmax} , are shown in figure 4.3 a) and b). Maximum proton energy calculated using the nominal 2 ps laser pulse (averaged over 14 shots during the campaign) as well as 0.7 ps are plotted in c). 0.7 ps laser pulse duration with acceleration scaling of 1.3 provided the best fit between model and experiment. Due to the unavailability of pulse durations during this scan, it cannot be said definitively what the durations were, therefore it is possible that they were shorter than 2 ps. In further analyses and discussions the nominal duration of 2 ps is used. It is clear that both N_p and E_{pmax} increase with increasing laser energy and intensity, as previously found in references [58, 59, 122]. The red squares in figure 4.3 d) show E_{pmax} calculated from the Mora model (section 2.6.1), where experimental laser and target parameters as well as experimentally measured hot electron temperature, T_e , are used. The resulting trend agrees well with the measured E_{pmax} , however the Mora model appears to overestimate the proton energies, likely due its simple 1D nature and

isothermal electron population and arbitrary acceleration time cut-off. The acceleration scaling of 1.3 ($\tau_{acc} = 1.3 \times \tau_{laser}$) from Fuchs empirical data [122] was used in the Mora model.

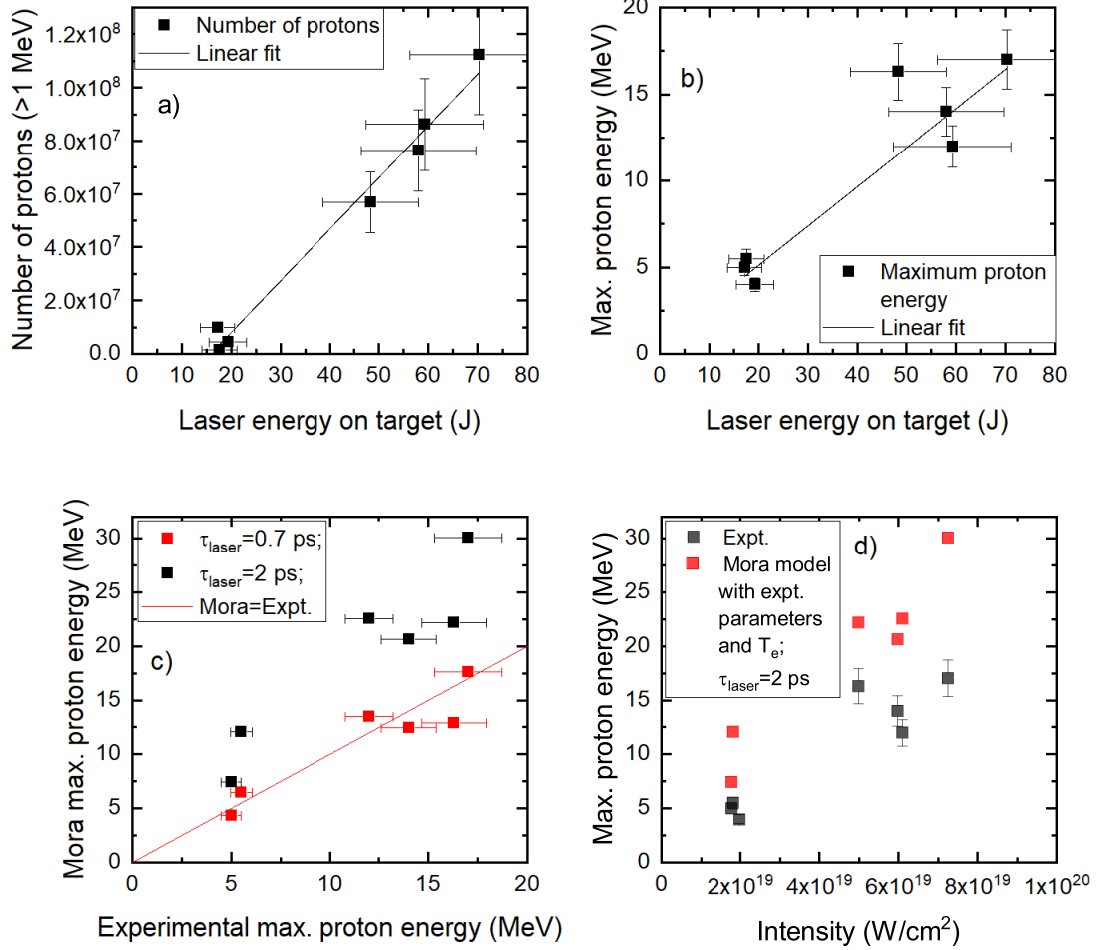


Figure 4.3: Proton measurements for laser energy scan. a) The measured number of protons and b) the maximum proton energy as a function of laser energy on target. c) Mora maximum proton energy is plotted as a function of measured maximum proton energy. Black squares represent data using nominal 2 ps pulse duration determined from average pulse duration during a period of the campaign, and red implements 0.7 ps pulse duration which provides the best fit. Red squares in d) show E_{pmax} calculated using the Mora model, where experimental parameters and experimental T_e were employed. The trend is very similar to the experimentally measured, however the model appears to overestimate the maximum proton energy.

N_p and E_{pmax} in the intensity scan as a function of laser spot size show less clear trends, as displayed in figure 4.4 a)–d). There is a general increase with intensity. The

quality of the spot before focus is far better than after it goes through focus due to Gouy phase shifts. If the laser is self focused as a result of preplasma, then the actual intensity is higher, and subsequently the hot electrons are more energetic causing greater E_{pmax} too. Benefits of employing larger focal spot sizes have been highlighted in previous work [59,123]. Dover *et al.* report that a tighter laser focus does not significantly boost the hot electron temperature or the maximum proton energy, and confirm that the Mora model underestimates the maximum proton energy for larger focal spots considerably [124]. The model assumes that electrons contribute to the sheath only once, however electron recirculation can also increase the accelerating potential [125,126]. The sheath is larger for larger spot sizes and electrons can contribute to the sheath, while for small sheath size recirculating electrons are unlikely to reappear within the same area [124]. Furthermore, a study reported in Gray *et al.* [127] using similar laser conditions as the work in this chapter, found a much higher laser absorption for large focal spots compared to tight focus at equivalent intensity. PIC simulation results [127] revealed that this enhanced absorption observed in the case of relatively large focal spots is a result of additional heating of the relativistic electrons which recirculate within the target between the sheath fields formed on the surfaces [128].

4.3.2 Escaping electrons in energy and defocus scans

Supporting electron measurements were also made. The results in the energy and defocus scan are displayed in figures 4.5 and 4.6. As in the proton plots in the previous section, T_e and N_e are shown as a function of energy as well as intensity(E) (figure 4.5), and as a function of defocus and intensity(Z) (figure 4.6).

The hot electron temperature (for electrons above 1 MeV energy) was determined from the E-spec data, for both intensity as a function of energy and intensity as a function of defocus scans. The number of escaping electrons was measured from the E-spec for the energy scan, as the Cherenkov fibre was not operational at that time. In the defocus scan the electrons detected by the Cherenkov fibre are used. The fibre is able to capture a greater solid angle, therefore the number of electrons is more representative of the total number of escaping electrons.

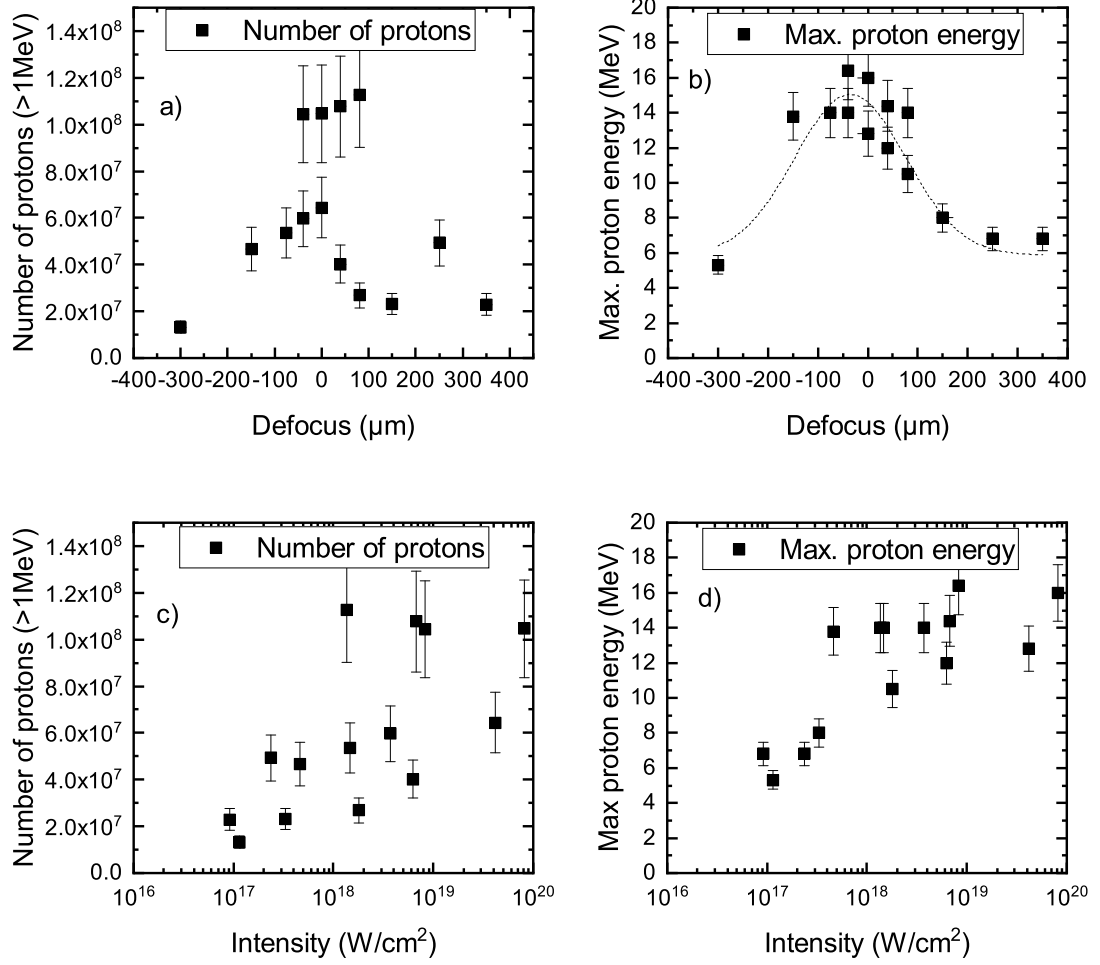


Figure 4.4: N_p and E_{pmax} plotted as a function of defocus (a) and b)). The data is scattered and show less clear trends compared to the energy scan results, nevertheless there is a general increase with intensity as shown in c) and d).

A general increase in T_e and N_e as a function of laser energy on target is evident. Low statistics prevents from drawing detailed conclusions. Nevertheless, from the plot in figure 4.5 c), we can see that low laser intensities produce less electrons with lower temperatures, while higher intensities generate a greater number of escaping energetic electrons. Wilks [53], Beg [48] and Haines [50] scalings are plotted to show model predictions using the experimental parameters. Due to pulse durations not being available, those were taken as 2 ps averaged over a number of shots during the campaign. Beg scaling slightly underestimates the electron temperatures, however the trend fits

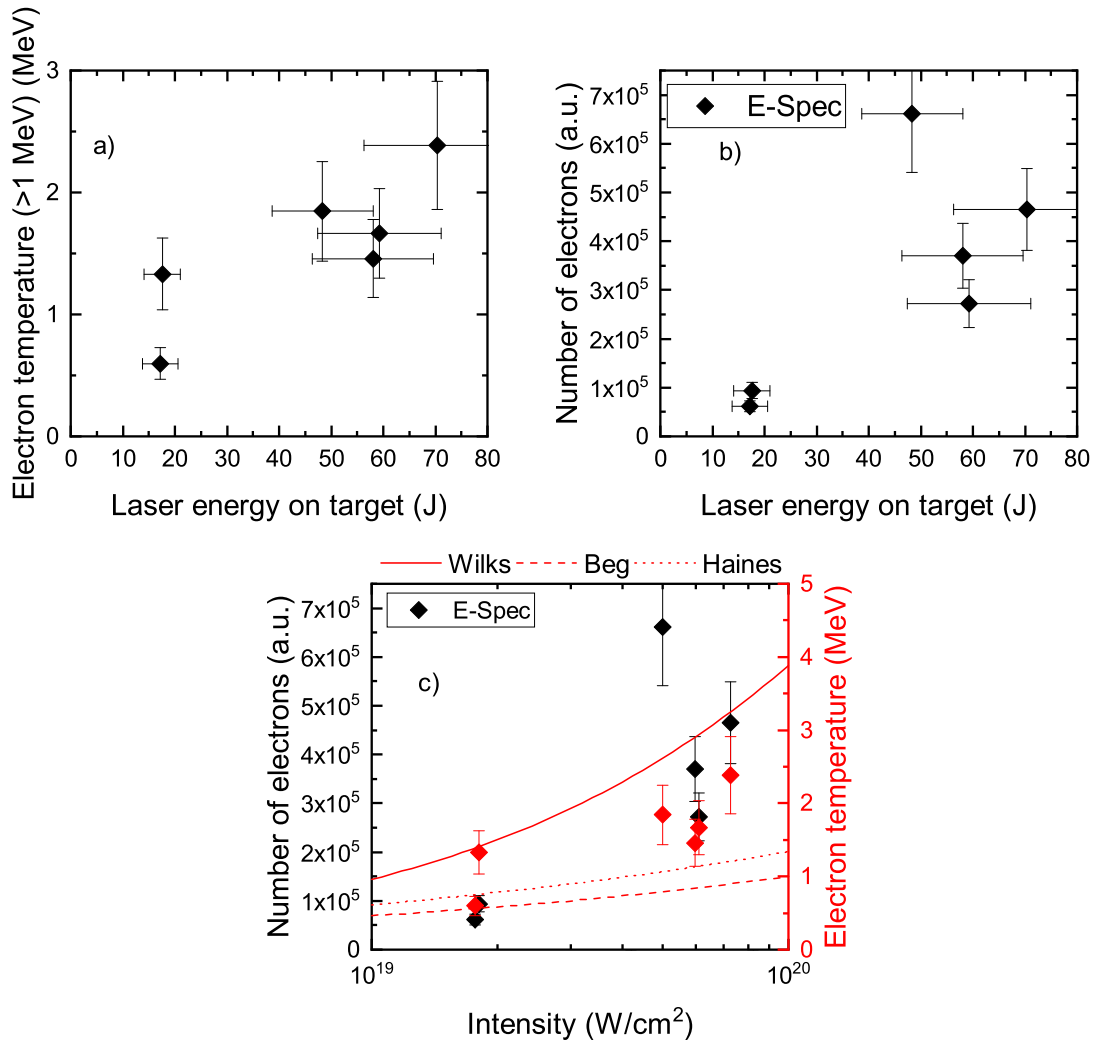


Figure 4.5: Electron spectrometer measurements made during the energy scan. Temperature and the detected number of electrons are plotted as function of laser energy in a) and b). The graph in c) has both number and temperature plotted as a function of intensity. Additionally, Wilks, Beg and Haines models are shown. The data appears to fall somewhere between the Wilks and Beg/Haines model.

reasonably well to the data. The Wilks scaling appears to slightly overestimate the hot electron temperature. The data lies between the two scalings.

Defocus scan data follows a Gaussian-like shape scaling for electron temperature, but the relationship is less clear for the number of escaping electrons as shown in figure 4.6 a) and b). Wilks, Beg and Haines T_e scalings are added to the experimental data plot. It can be seen that the measured T_e tends to be much higher than ones predicted

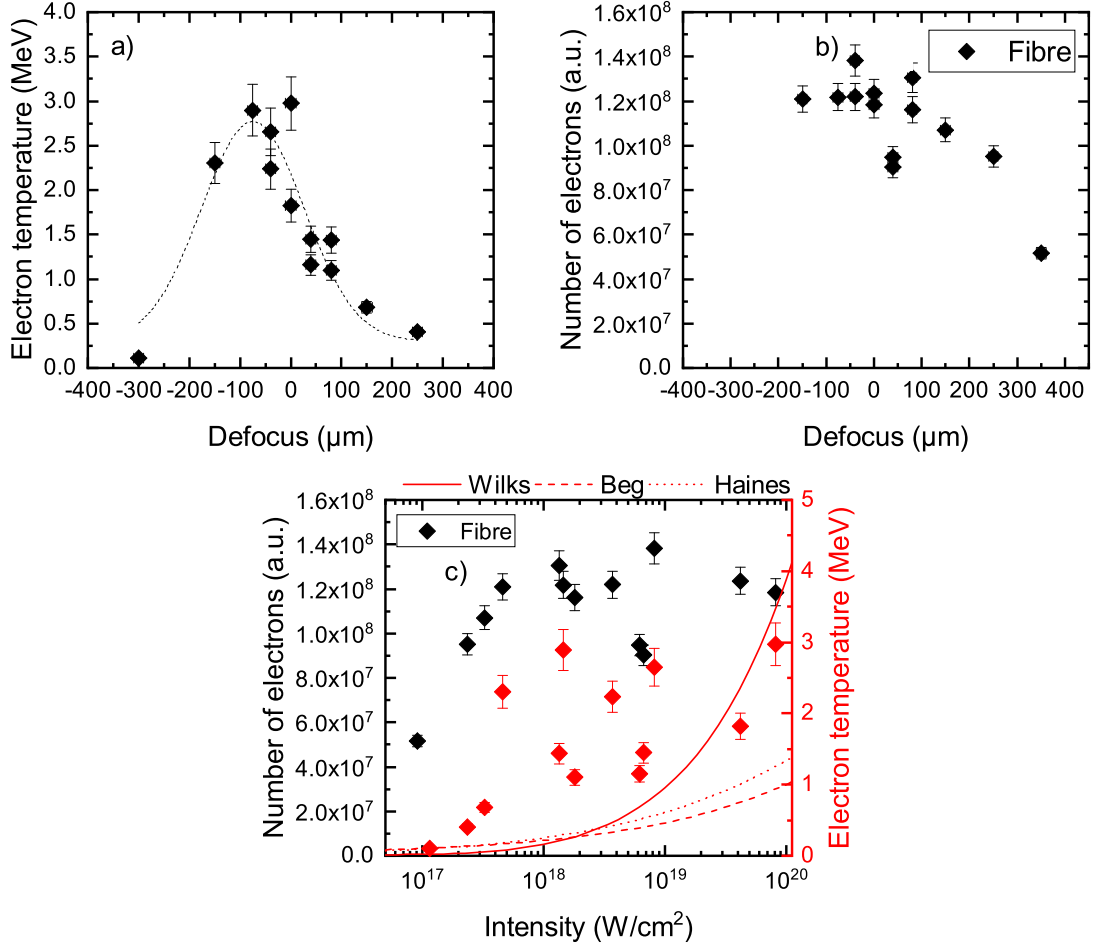


Figure 4.6: Escaping electron data in the defocus scan. In this scan, the electron Cherenkov fibre was utilised for detection of the number of electrons. The temperature follows a Gaussian like shape scaling, but the relationship is less clear for the number of electrons. Beg, Wilks and Hained models for hot electron temperature are added in c). Detected temperature is much higher that those predicted by the models. Self focussing of the laser beam may be the cause.

from all of these models. Even at very low intensities the electron temperature is unintuitively high. The aforementioned self focusing of the laser beam and electron refluxing [129] are likely reasons for the increased T_e . Essentially no difference was observed in the electron spectra for a small and a large focal spot measured from the PIC simulations, as reported in Gray *et al.* [127]. This would also explain the higher then expected proton energies. It was shown via PIC simulations in MacKinnon *et*

al. [125] that the recirculation of relativistic electrons between the sheath fields [128] built up on target surfaces increase the overall electron density and temperature at the target rear, and subsequently enhances the energy of the TNSA protons. It has also been shown that moderate defocusing of the laser does not cause reduction in the hot electron temperature [130]. A greater number and temperature of electrons escaping the target, drives a stronger sheath at the rear of the foil target, and hence more protons are accelerated to higher energies.

4.3.3 Maximum proton energy and hot electron temperature in energy and defocus scans

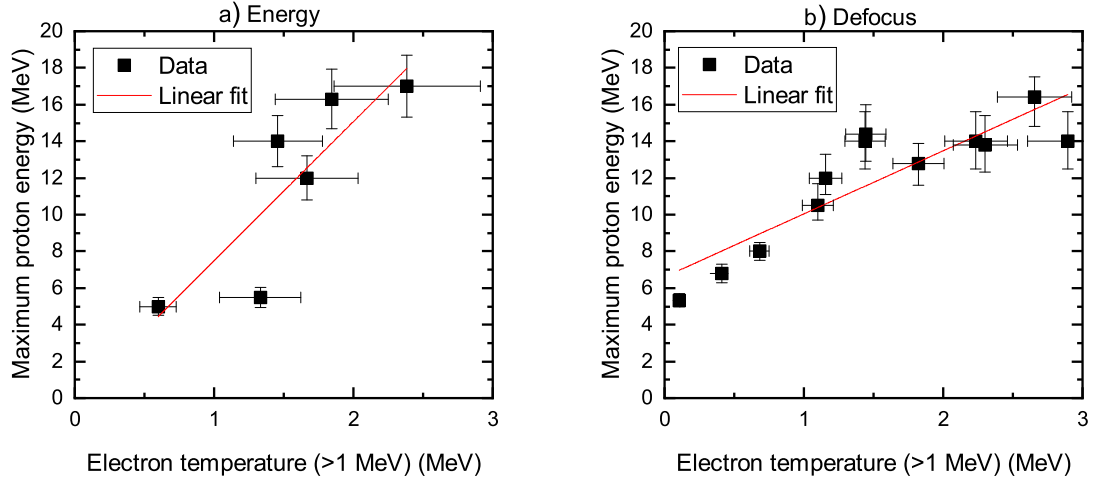


Figure 4.7: Maximum proton energy obtained during the energy scan on the left and defocus scan on the right panel. These are supported by previous experiments and theory. The scatter in the energy scan data may be due to low statistics, resulting in a less clear relationship.

Additional evidence is provided in figure 4.7, where in both, energy (a)) and defocus (b)) scans E_{pmax} is positively correlated to T_e . This is similar to previous studies and theoretical predictions [55]. The defocus scan data in figure 4.7 b) is proportional, but implies that $E_{pmax} = T_e \times constant$. The measurements confirm the predictions, and thus we know the data is sensible and the further measurements and correlations performed are reasonable. The proton maximum energy and hot electron temperature

relationship is clearer in the defocus scan. Due to limited number of shots in the experiment the energy scan lacks statistics for a clearer trend, nevertheless it can be seen that lower hot electron temperatures cause lower energy protons. A straight line fit is expected as predicted by the Mora model [55], and empirical relationships from Fuchs *et al.* [122].

4.3.4 EMP measurements

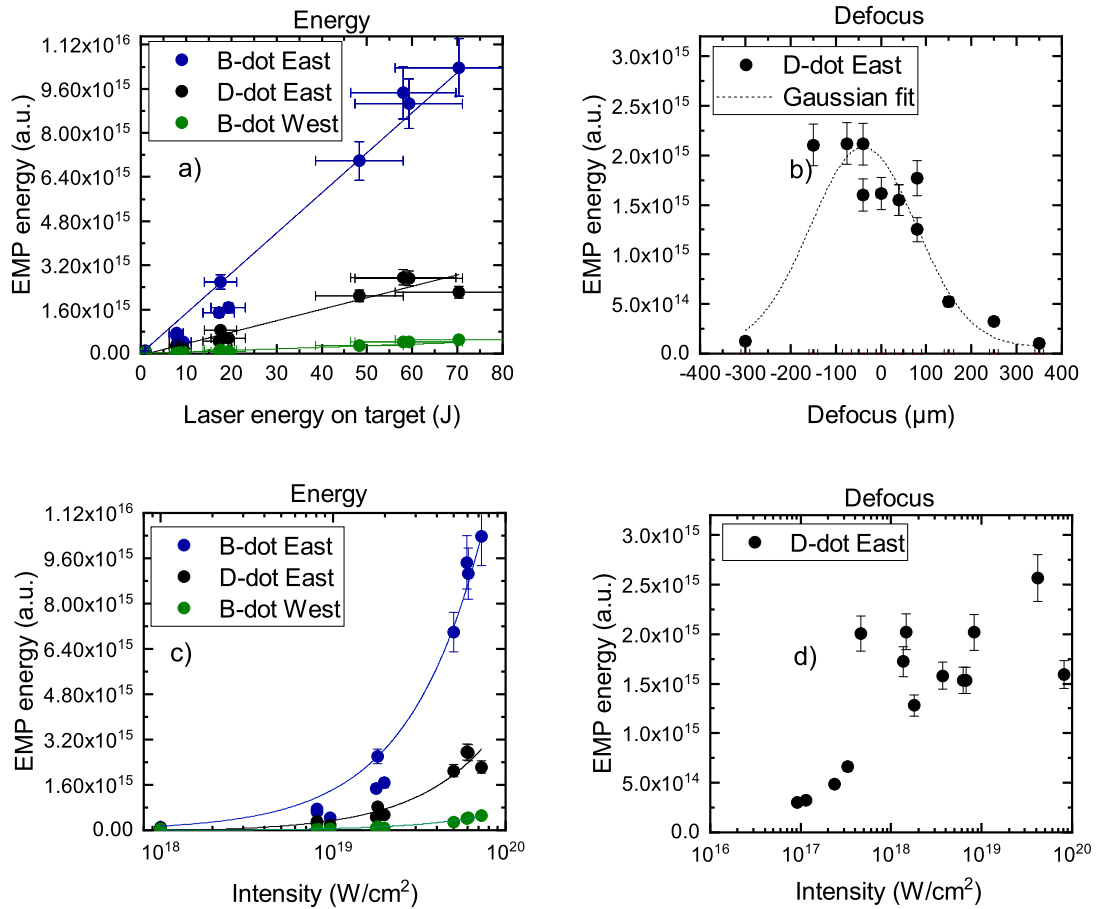


Figure 4.8: EMP measurement results. Laser intensity was varied in two ways: 1) by changing the laser energy on target and 2) by changing the laser spot focus position. a) Graph shows a linear relationship between EMP energy and laser energy for all three EMP probes. b) EMP in defocus scan is plotted. c) and d) display EMP energy plotted against laser intensity as a function energy and defocus respectively. The EMP energy with respect to both, laser energy and defocus results, have been recently published in Bradford *et al.* [3].

A linear relationship between the EMP and laser energy was observed for all three probes as shown in figure 4.8 a). The model presented in a review paper by Consoli *et al.* agrees with this experimental data [18]. This observation suggests that EMP may be a simple and effective measure of laser-target coupling. The data agrees with experiments performed by Cikhardt *et al.*, who investigated the current flowing through the target irradiated by a 510 J laser pulse of 400 ps, and showed that for various target materials the maximum target current increased with increasing laser energy [22]. Their obtained values for charge accumulation on the target, due to deficit of electrons in the laser spot, correlate with ones determined theoretically by Dubois *et al.* for ps lasers delivering hundreds of joules of energy on target [1].

The highest EMP emission was detected for shots using best laser focus (0 μm defocus) and a drop-off is seen for increased distance from focus as illustrated in figure 4.8 b). The EMP energy is also plotted as a function of intensity where there it is clear that EMP energy is greater for higher laser intensities. The laser intensity on target is maximum for best focus, for which the produced electrons are more energetic and numerous, setting up a higher return current in the target stalk, and also introducing a stronger sheath field for proton acceleration. We observed very similar trends between the maximum proton energy and laser defocus; highest energies were achieved for best laser focus as illustrated in figure 4.4 a).

EMP measurements were made in parallel to the previously discussed measurements of electrons and protons. As outlined in Consoli *et al.*, and shown in several experiments (see references and data therein), this data also confirms that the generated EMP energy is proportional to laser energy as well as intensity. In addition it was observed and is shown in figure 4.8 how EMP changes when intensity is changed by changing the focal spot size. The correlation for this scan is similar to the laser energy scan, however with some outliers. It is important to recall from previous figures of electron data that significant scatter was present. The defocus scan has a less obvious trend and could be affected by a higher T_e at larger defocus than expected, thus increasing the EMP, as some EMP values are relatively high for low intensities.

4.4 Discussion

4.4.1 EMP correlations with protons and electrons in energy and defocus scan

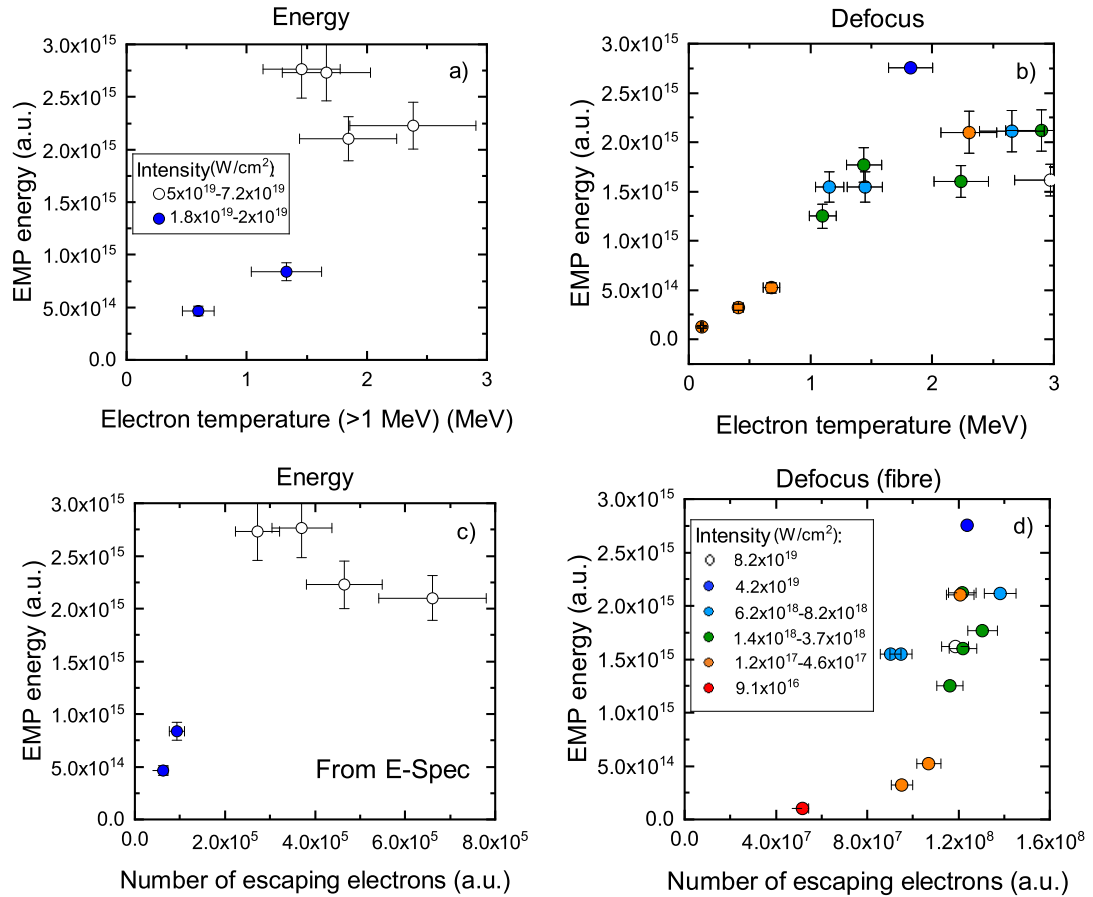


Figure 4.9: Electron correlations. EMP is plotted as a function of both temperature and number of escaping electrons. Generally more EMP was measured for higher electron numbers and temperatures in both energy (a) and c)) and defocus scans (b) and d)).

The relationship between the EMP and the number of electrons was studied. Studies have reported that the EMP is caused predominantly by the escape of electrons from the foil in a laser-target interaction. The results from this experimental campaign are plotted in figure 4.9. The measured EMP energy observed during the laser energy scan is small for low hot electron temperatures, and greater for higher electron temperatures as displayed in figure 4.9 a). A similar relationship is observed for the number of electrons

(b)). The blue and white circles indicate different intensity ranges. It is difficult to draw a definitive trend due to the small number of experimental shots. It should be noted that in the energy scan data, the number of electrons is deduced from the electron spectrometer data which only captures the electrons on the laser axis, and is a very small sample of the escaping electron fraction, and thus could be susceptible to spatial flux variations throughout the electron beam.

More measurements were taken during the defocus scan. The trend is much clearer here (figure 4.9 b) and d)). There is a clear correlation between the EMP energy and escaping hot electron temperature (figure 4.9 b)) and number (figure 4.9 d)). The electron number here is from the Cherenkov fibre, which captures a greater solid angle [91], and is therefore more reliable than the electron spectrometer which subtends a much smaller solid angle.

We also investigated the relationship between the EMP and the number of protons sampled by a Thomson parabola spectrometer which is plotted in figures 4.10 c) and d)). The relationship between the EMP and the number of protons is also linear indicating a clear relationship between the EMP generation and the sheath field responsible the acceleration of protons. The behaviour is very similar as reported in the previous figure 4.9 for electrons. The maximum proton energy as well as number are higher where the EMP is greater. There is a positive correlation between the proton maximum energy and EMP in the defocus scan. The number of protons as a function of EMP energy in the defocus scan indicates a general increasing trend, however the data is more scattered with several outliers. This could be a result of the sample size of the Thomson parabola spectrometer, as it only samples a small solid angle, and beam non-uniformities can mean that there is significant scatter shot-to-shot.

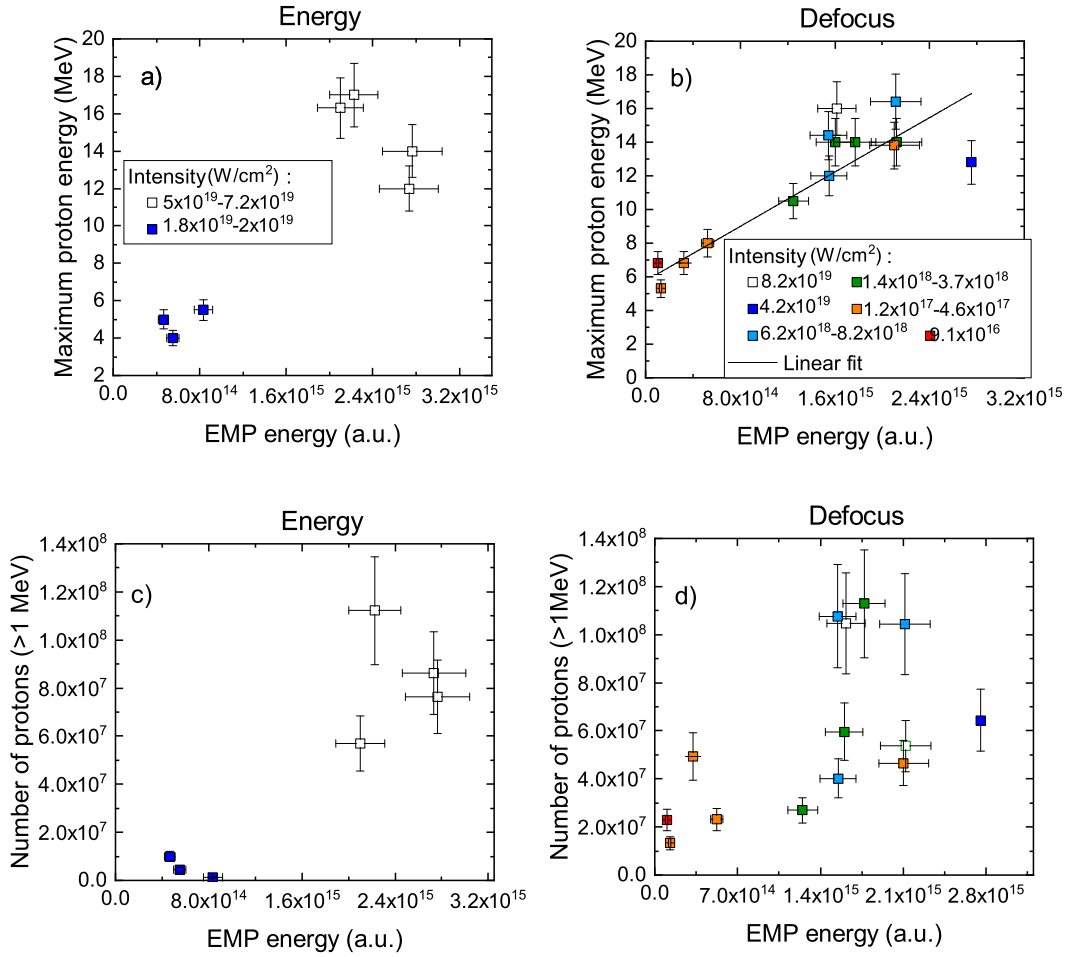


Figure 4.10: Correlations between the EMP energy and the maximum energy and number of protons are shown in the plots in both energy and defocus scans. Lower EMP is detected where the proton energies numbers are lower and vice versa. There are some outliers in the defocus scan results due to possible laser self focussing.

4.4.2 EMP and proton relationship – model

The main aim of this work was to investigate the relationship between the sheath field driving the proton acceleration and EMP energy in picosecond laser-solid interactions, by measuring the EMP energy and the maximum proton energy in the laser energy (figure 4.11) and defocus scans (figure 4.12), and through theoretical EMP energy predictions.

Experimental maximum proton energy as a function of laser intensity measured during the energy scan is plotted, as well as Mora model predictions. Experimental parameters and experimentally measured hot electron temperatures were used in the Mora equation for the maximum proton energy, with an acceleration time of $1.3 \times \tau_{laser}$, as obtained by Fuchs *et al.* [122]. The red solid and dashed red curves show the energies predicted by the Mora model, where the hot electron temperature is calculated using Wilks and Beg scalings respectively. Wilks model overestimates the hot electron temperature, in turn overestimating the proton energy. The experimental data and the Mora model with experimental hot electron temperature agree much better with the Beg fit, which demonstrates that the data is consistent. EMP energy is also plotted as a function of laser intensity (black circles). In addition, normalised EMP energy using the model from Consoli *et al.* is shown in red circles. The theoretical model predicts that the EMP energy is proportional to laser intensity if the target size and other parameters are kept constant. Hence, it is also proportional to the square of hot electron temperature. This means that the EMP energy is also proportional to the square of maximum proton energy. This empirical relationship is shown in figure 4.11 c) indicated by a solid black line. The data has some outliers but generally appears to follow the trend. From the Mora model $E_{pmax} \sim T_e$ [55], from Consoli *et al.* $EMP \sim I_{laser} \sim T_e^2$ [18] and therefore it can be deduced that EMP energy scales as the square of the maximum proton energy multiplied by a constant.

$$EMP \sim aE_{pmax}^2 \tag{4.1}$$

A similar analysis procedure was performed for the data of the defocus scan shown in

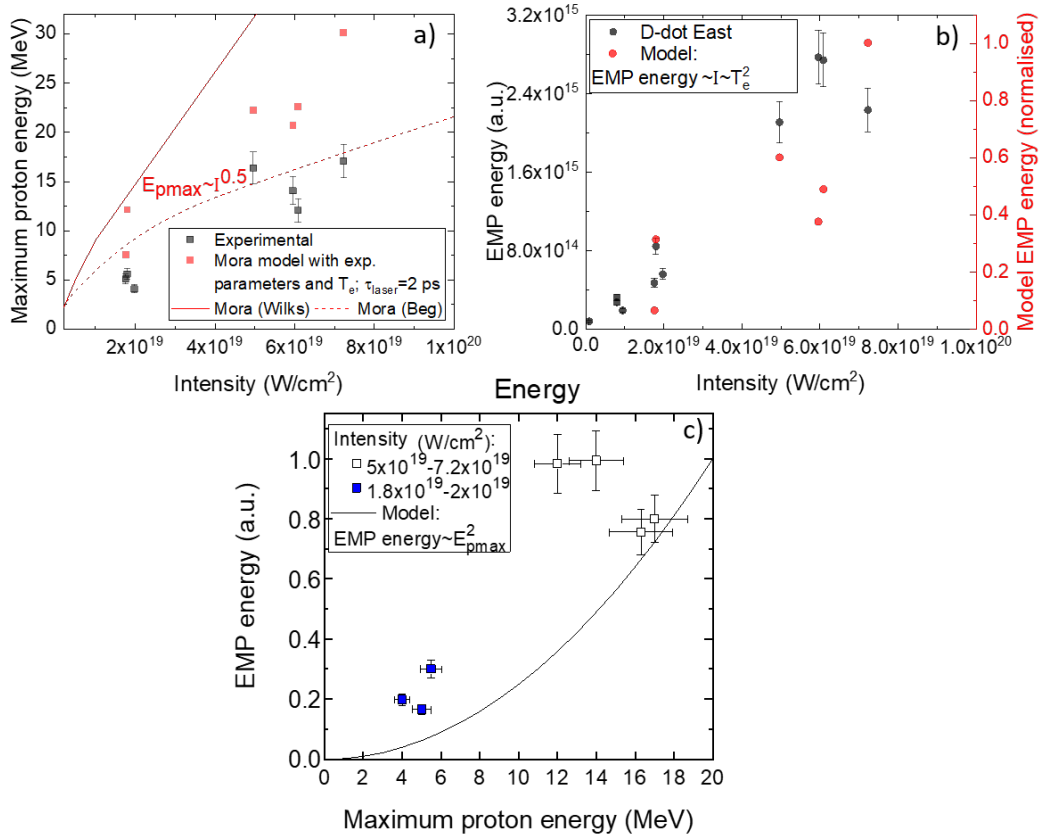


Figure 4.11: Energy scan. a) Experimental data as well as Mora model proton maximum energy calculated using experimental parameters. The Wilks and Beg models incorporate experimental parameters to calculate T_e which is then input into the Mora model. Wilks likely overestimates electron temperature, overestimating maximum proton energy as well. The data agrees with Beg scaling well. b) EMP experimental data is shown in grey and the normalised model values are plotted in red against intensity. c) Shows that the EMP and maximum proton energy are correlated through laser intensity. The EMP energy is proportional to the square of the maximum proton energy, and if multiplied by a conversion factor of ≈ 2 , would give an even better match to experiment. This conversion factor between measured and modelled values could be due to the detector response function, however that was not available at the time.

figure 4.12. In a) it is clear that that the experimental T_e is much greater than expected by Beg and Wilks models. This is especially prominent for low laser intensities. The previously mentioned study in Gray et al. showing a high laser absorption for large focal spots due to electron recirculation is also a likely contribution to the enhanced electron

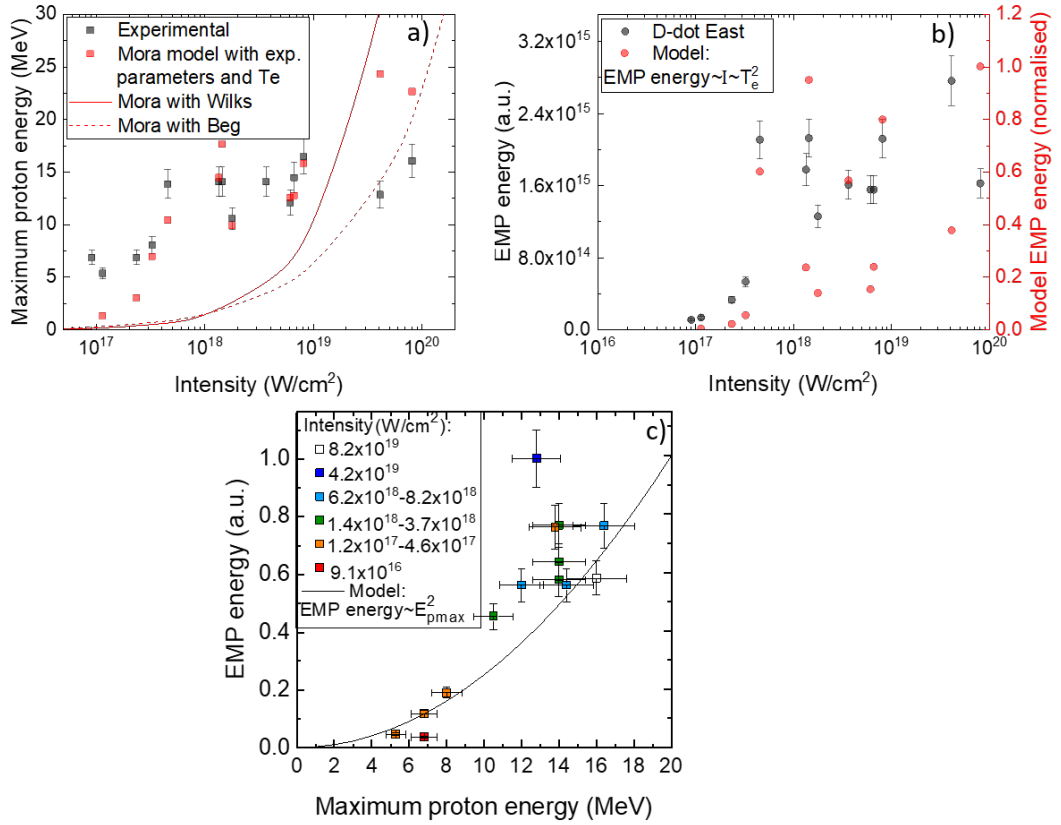


Figure 4.12: Defocus scan. a) Experimental data as well as Mora model proton maximum energy calculated using experimental parameters. The Wilks and Beg models incorporate experimental parameters to calculate T_e which is then input into the Mora model. E_{pmax} is greater than expected for such intensities and data lies well above the model scalings. b) EMP experimental data is shown in grey and the normalised model values are plotted in red as a function of intensity. c) EMP and maximum proton energy correlation through intensity.

temperature. Similarly in b) EMP vs intensity, the data is very scattered, and so are the model values, as these utilise the experimentally measured values. Nevertheless, in c) it can be confirmed through the EMP theoretical model that there is a clear correlation between the EMP and the maximum proton energy where EMP scales as E_{pmax}^2 . Here, the relationship is much clearer as there are more data points which gives greater confidence. There is a strong correlation between E_{pmax} and EMP energy through laser intensity.

4.5 Conclusions

A systematic approach was taken to investigate the relationship between EMP energy generation and proton acceleration in picosecond laser-solid interactions. In this study the laser intensity was varied in two ways: changing the focal spot size (or defocus) and changing the laser energy, while maintaining the remaining laser and target parameters constant. Escaping electrons from the target cause a charge imbalance, and hence a current is drawn through the stalk, which generates EMP emission. Escaping electrons also set up a sheath field at the rear of the target which accelerates protons. EMP has gained interest in the recent years due to high power laser technology improvements. An experimental campaign carried using the the Vulcan laser provided valuable insights into the effects of laser parameters on EMP production and the correlation between the EMP and escaping electrons and protons.

We confirmed that the electron and proton data in both energy and defocus scans were in line with expectations from earlier experimental studies. The relationships between maximum proton energy and laser intensity as well as the number of protons are of linear scaling in energy scan as expected. Defocus scan data is less clear and more scatter is present. There is a general increase in maximum proton energy with intensity, however it is possible that the self focusing of the laser causes the intensity to be greater than we expect. This may be the cause of higher than expected proton energies at low intensities (real intensity could be higher). A lot of scatter is apparent in the electron defocus scan data. It was confirmed that in both energy and defocus scans the maximum proton energy and hot electron temperature have a linear relationship, which agrees with the Mora model.

EMP measurements reveal that EMP strength is linearly dependent on laser energy (and/or intensity) for three probes in the energy scan. There is also general EMP growth with laser intensity in the defocus scan with a few outliers hence the relationship is less clear in this data set. It was observed that EMP energy correlates with hot escaping electron temperature and number. Furthermore, proton data was also consistent with the electron results.

Theoretical EMP model trends were compared with experiment. There is a clear relationship between the EMP and laser intensity where intensity was set by changing the laser energy. Examining the EMP and maximum proton energy relationship with intensity, it was confirmed that EMP and maximum proton energy are correlated through the hot escaping electrons, whose temperature can be indirectly measured by measuring the EMP. It can be predicted how much EMP will be produced for a given maximum proton energy using the scaling in equation 4.1 confirmed in this work. The defocus scan data show less clear correlations when EMP and proton energy are plotted as a function of intensity. This may be due to increase in actual intensity due to self focusing of the laser and refluxing electrons. Nevertheless, the EMP and the maximum proton energy in this data set agree very well, with few outliers. There is clear evidence that the escaping hot electron temperature and the maximum proton energy are changing in this scan, however any randomness disappears when plotting them as a function of EMP, providing indirect measurements of both the hot electron temperature and the maximum proton energy.

This work clearly demonstrates that we need more and hotter electrons to generate greater numbers and higher energy protons in the TNSA regime. We also found that the EMP increases with more escaping electrons and hence protons. Therefore to achieve even higher energy protons means that the EMP will also increase. This can become especially problematic in future high repetition rate and high power laser facilities, where many diagnostics will be online and therefore highly prone to damage and disruption due to EMP waves. This will mean that additional shielding and other measures will be required in the future. It will be discussed in the next chapter EMP emission for different target and stalk geometries showed that EMP can be effectively decreased by increasing stalk length, reducing the target size and using insulating materials. These could be implemented in future systems, to reduce EMP due to photoionisation, charge implantation and electrical breakdown without influencing the ion acceleration. It will be important to make such changes to the target mounting and chamber systems such that it does not affect the proton emission from the target. Ongoing studies will be needed to test the online diagnostics for EMP damage or

interference when those improved laser facilities become fully operational.

Chapter 5

EMP mitigation in laser-solid interactions by modifying the target and mounting system

5.1 Introduction

Significant EMP emissions have been observed at high power laser facilities, where the primary driving mechanism is due to hot electrons escaping a solid target that is irradiated by an intense laser pulse. Ion acceleration also occurs as a result of a sheath field generated by the same hot electrons. This thesis chapter reports on an investigation of EMP generation and control. Previous studies by Bradford *et al* have revealed a linear scaling between the EMP and the driving laser energy [3], which is indicative of the potential to use EMP measurements as a novel diagnostic of laser energy coupling to the hot electrons.

As next generation laser facilities, such as ELI (Extreme Light Infrastructure) [131–133], come online, many of them plan to operate at higher repetition rates ($> \text{Hz}$) and some of them are looking at shooting metallic tape or target arrays [15]. Such facilities will produce high EMP signals, which may interfere with diagnostics and experimental measurements. Reduction of these emissions is imperative for ensuring

that electronic equipment and data acquisition are not disrupted. To investigate how the EMP scaling with target diameter develops for large (2-20 mm) substrate sizes, an EMP study was carried out at the Target Area Petawatt (TAP) of the Vulcan laser at the STFC's Rutherford Appleton Laboratory (RAL). The effect of conductivity of the target mounting on the emitted EMP using two types of target wheels namely a proprietary VeroBlackPlus (RGD875) [134] plastic and aluminium, and different types of targets and stalks is investigated.

5.2 Experimental method

Vulcan laser Target Area Petawatt is capable of delivering ≈ 400 J of energy on target in a 0.5 ps pulse reaching intensities of up to 10^{21} W/cm². The laser beam was focused by an f/3 off-axis parabola onto tantalum targets at an angle of incidence of $\approx 15^\circ$. The focus of this research was to investigate the effects of target mounting materials and examine ways to reduce the EMP induced primarily by the return current generation, and the likelihood of using it as a future diagnostic tool. Until recently, the materials routinely used in the mounting systems were metals, which were all well earthed. Targets were mounted onto 3 mm diameter aluminium stalks which are placed in a rotating aluminium/plastic target wheel which enables experimenters to select the target for the next shot and take multiple shots without the need for vacuum cycling of the interaction chamber.

Employing insulating materials enables experimenters to maintain the ability to conduct experiments in a similar way to present. Multiple targets can be mounted on the target wheel, and the stability of the mounting system is preserved. The metal stalks and target wheel were substituted by plastic ones. Target stalk and mounting parameters were varied, namely material, length and diameter, and the material of the target wheel, changed between conductor (aluminium) and insulator (VeroBlackPlus plastic). Several target parameter scans were also measured, such as substrate material, thickness and surface area to explore capacitance effects.

A schematic of the experimental set up is shown in figure 5.1. The EMP diagnostics

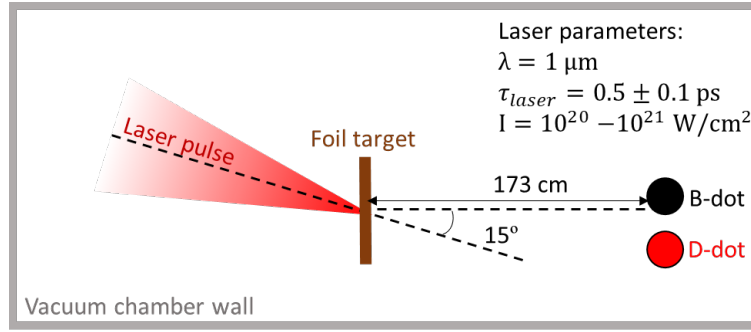


Figure 5.1: A schematic of the experimental setup used to carry out EMP measurements. The EMP B-dot and D-dot probes were placed inside the vacuum chamber, 173 cm away from the laser-plasma interaction.

used were a set of Prodyn Technologies B-24 full loop B-dot sensors and FD-5 D-dot sensors. The B and D-dot probes measure the rate of change of magnetic and electric fields respectively. The two detectors were placed inside the vacuum chamber $173 \text{ cm} \pm 0.5 \text{ cm}$ from the rear of the target at an angle close to the target normal. The probes were connected to a 12.5 GHz Tektronix DPO71254C digital phosphor oscilloscope via SMA cables (type Rg402). The oscilloscope was located outside of the experimental area to minimise direct noise pickup, thus the SMA cables were passed through BNC feedthroughs, and cables of $\approx 20 \text{ m}$ in length, effectively limiting the reliable frequency measurement to approximately 3 GHz. Each of the probes used two times -3 dB 18 GHz attenuators and a 20 dB attenuator for oscilloscope protection.

5.3 Experimental results

Output data from the oscilloscope was processed in the following order: A fast Fourier transform was applied to the output voltage from the oscilloscope to produce a frequency spectrum (voltage vs frequency). In order to calculate EMP energy, the voltages were squared and integrated over the range of accessible frequencies, as this results in a value proportional to the EMP energy and has units of $\text{volts}^2/\text{second}$ or $\text{volts}^2 \times \text{hertz}$. It is known that the square of voltage is proportional to energy ($E = V^2 t / R_\Omega$, where R_Ω is the electric resistance). As stated in chapter 2, previous studies have demonstrated that the low frequency portion of the spectrum (few hundreds of MHz) can

occur as a result of reflections and resonant modes of the vacuum chamber [62]. It is believed that the oscillations due to the target and stalk contribute to much higher frequencies (>1 GHz) as the resonant frequencies are much higher due to their small dimensions. For the TAP chamber of size $2\text{ m} \times 2.2\text{ m} \times 4.8\text{ m}$, the resonant modes are expected to be of the order of 75 MHz, 68 MHz and 31 MHz ($\nu=c/2s$). In addition, any metal components within the chamber would have resonance modes up to a GHz and may contribute to the total signal. To interrogate in more detail the behaviour trends of the two emission sources, a split was placed at 0.5 GHz, and the low and high frequency components were analysed separately.

5.3.1 Target mounting system variations

Metals are good conductors of electricity while insulating materials such as plastics are good insulators and resist current flow. Metal and plastic cylindrical stalks as well as a plastic spiral stalk on metal and plastic target wheels were used in order to investigate the effects of varying the materials of the target mounting system components. The spiral plastic stalk was used as a previous study had shown it to be effective in reducing the detected EMP [3]. The combinations are summarised in Table 5.1. The table also contains the combined electrical resistance of the stalk-wheel mounting system, calculated treating the stalk ($L=25\text{ mm}$) and wheel as wires. In order to calculate the resistance, the wheel was approximated to a cuboid with $L=22\text{ mm}$ and width of 10 mm and cross sectional area $A=22 \times 10\text{ mm}^2$. The wheel length approximation is due to the fact that the distance between the wheel connection to the stage and the edge of the wheel is 22 mm . For the two data sets presented in this section Ta targets employed were $5\text{ mm} \times 5\text{ mm}$, where the target thickness was a) $100\text{ }\mu\text{m}$ and b) $10\text{ }\mu\text{m}$, the laser energy on target, laser pulse duration and the intensity were: a) $E_{laser}=363 \pm 38\text{ J}$, $\tau_{laser}=527 \pm 220\text{ fs}$ and $I=8.3 \times 10^{20} - 2.3 \times 10^{21}\text{ W/cm}^2$, and b) $E_{laser}=395 \pm 40\text{ J}$, $\tau_{laser}=421 \pm 47\text{ fs}$ and $I=1.8 \times 10^{21} - 2.5 \times 10^{21}\text{ W/cm}^2$. Each data set consists of four shots.

Materials such as plastics, with high resistivity of $\approx 10^{14}\text{ }\Omega\text{m}$ at room temperature, resist the current flow due the lack of free electrons. This means the return current through the target stalk is decreased lowering the EMP emissions. Aluminium has

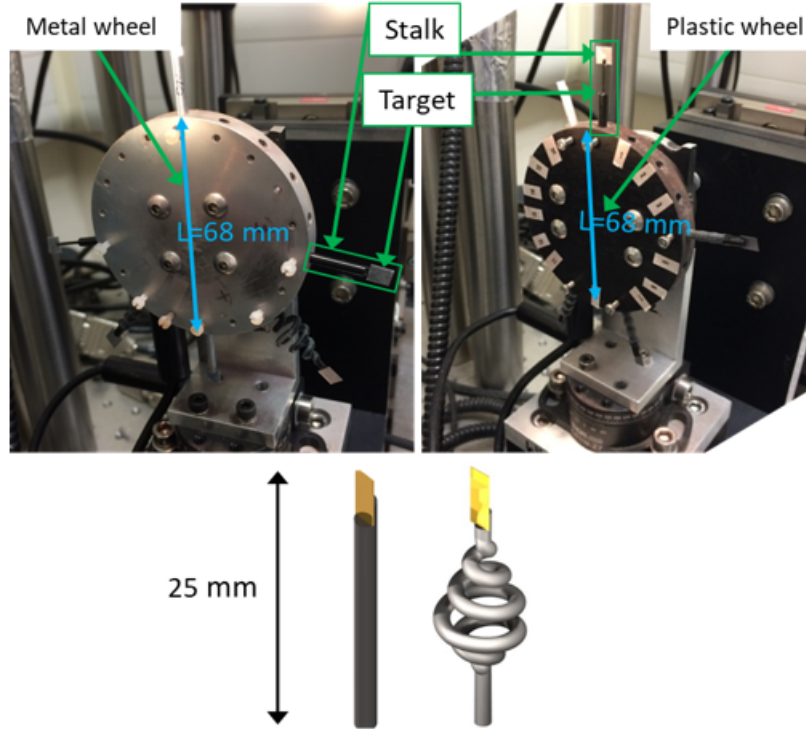


Figure 5.2: Photographs of the metal and plastic wheels of 68 mm in diameter and stalks marked in green ($L=25$ mm above wheel edge, $A=7$ mm²) used in the experiment. The geometry of target stalks used are shown. Metal and plastic cylindrical stalks and a plastic spiral stalk were employed.

Abbreviation	Stalk	Wheel	R_{Ω} of mounting system(Ω)
MM	Metal	Metal	1×10^{-4}
PM	Plastic	Metal	3.5×10^{17}
MP	Metal	Plastic	1×10^{16}
PP	Plastic	Plastic	3.6×10^{17}
SP	Spiral	Plastic	1.5×10^{19}

Table 5.1: A list of stalk and wheel combinations used, and the system's estimated combined electrical resistance ($R_{\Omega} = \rho L/A$).

a much lower resistivity ($\approx 2.8 \times 10^{-8}$ Ω m), resulting from increased electron mobility. The combinations including an insulating component show an overall decrease in EMP as shown by the plots in figure 5.3. The reduction is caused by the increased resistivity in the mounting components. Furthermore, a spiral stalk on a plastic wheel was tested which is expected to enhance the mitigation effect by introducing a longer geodesic

insulating path.

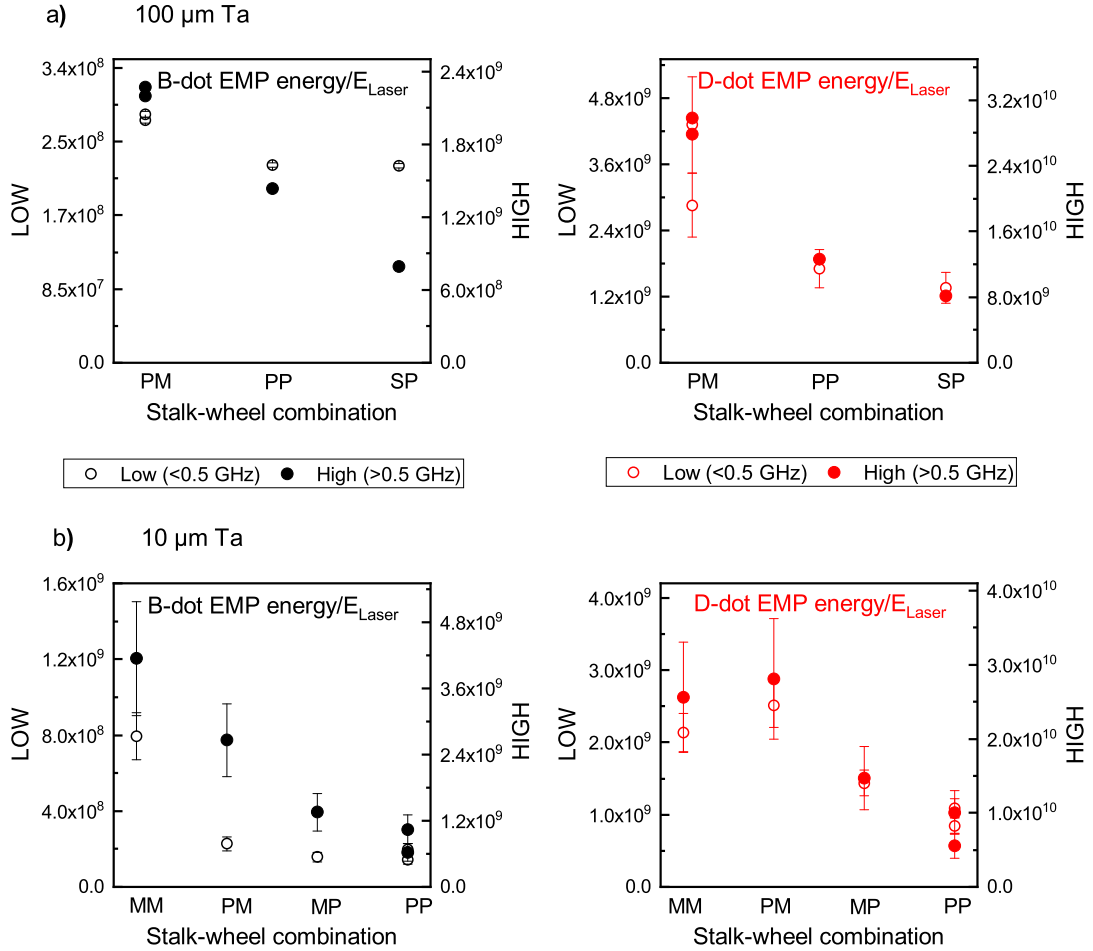


Figure 5.3: EMP energy divided by the laser energy E_{laser} is plotted for a) 100 μm thick Ta targets and b) 10 μm thick Ta targets. Low frequencies are the chamber modes and high frequencies are stalk and target contributions. The error bars were deduced based on several shots with similar conditions.

The high fields associated with the target charging may be capable of ionising the stalk near to the target. It could be that a large portion of the stalk is ionised by the radiation thus reducing the actual length of insulator material between target and wheel, which is why the change to plastic target wheel continues to contribute to the reduction in EMP. A high enough potential difference (due to target charging) may cause electrical breakdown of a material, which is otherwise an insulator.

It is important to note that, while generally the data indicate that conductive

components have an enhancing effect on the emitted EMP, the measured values do not correspond to the estimated resistance of the target mounting system/circuit as displayed in figure 5.3 b). The stalk-wheel combination plastic-metal (PM) has a greater resistance ($3.5 \times 10^{17} \Omega$) than that of MP ($1 \times 10^{16} \Omega$). However the measured EMP is greater for the PM case. Given the lack of repeat shots, the higher EMP for the PM case could be due to shot to shot variation and ionisation or breakdown effects. To draw more detailed conclusions, additional measurements would ideally be made.

The calculated combined resistances of the mounting systems (i.e. MM, PM, MP, PP) are estimates and have not been experimentally measured. The system of stalk and wheel were approximated to wires of different diameters and added in series. The most impactful resistance effect will be due to the stalk as it has a much smaller wire cross sectional area making its resistance term dominate. This is why the calculated resistances are similar. Other factors could have played a role on the greater EMP emission by higher resistance system, such as the effective target capacitance being modified due to ionisation or shot-to-shot variation. A more thorough study with higher statistics could be carried out in future investigations to interrogate this.

Most plastics have a dielectric strength of 100-300 kV/cm [135]. If the applied electric field (or potential difference) is high enough, it can cause electrical breakdown of a material which is otherwise an insulator. Although the calculated electric fields due to the escaped electrons is less than the typical breakdown voltages for plastics, the increase in the surface temperature of the stalk due to radiation from the plasma would change its electric properties. A portion of an insulating component may become electrically conductive.

5.3.2 Target diameter scan

The effect of target diameter, d_t , on the EMP emission was investigated. The targets used were 100 μm thick tantalum targets of varying transverse sizes: 2 mm, 5 mm, 10 mm and 20 mm. The targets were mounted on 25 mm long plastic stalks which were attached to a 68 mm diameter plastic wheel. In this data set the laser energy and pulse duration were 340 ± 60 J and 540 ± 210 fs respectively. An increase was observed

in EMP signal with increasing target size. Normalised EMP energy for B-dot and D-dot probes is shown in figure 5.4. In addition to the capacitance effects, the electron sheath and the target are also acting like capacitor plates, inducing charge imbalance and increasing the inflow of cold electrons.

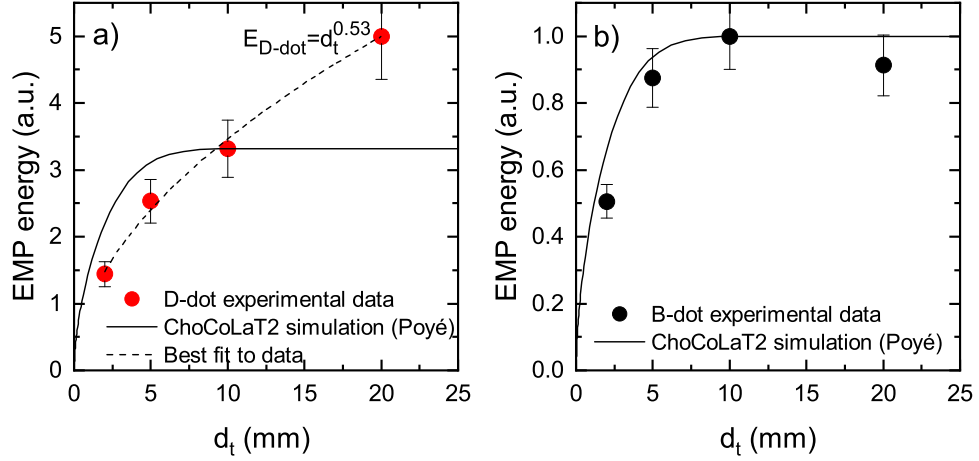


Figure 5.4: Normalised EMP energy measured by the D-dot and B-dot per joule of laser energy as a function of target diameter. The targets were $100 \mu\text{m}$ thick Ta foils of varying transverse sizes. Targets were mounted on 25 mm long 3 mm wide plastic stalks slotted into a plastic target wheel 68 mm in diameter. Black solid lines denote the ChoCoLaT2 simulation predictions (received during personal communications with A. Poyé). a) The experimental data from D-dot probe exhibits a square root like growth with the target size (dashed line). EMP energy continues to increase for targets larger than 10 mm, contrary to the Poyé model (solid line). b) The B-dot data scales very closely with the ChoCoLaT2 simulation predictions, where saturation is reached at 10 mm target size.

This increase in EMP with target surface area can be explained by treating the target as a capacitor (see section 2.7). According to the theory, the larger the transverse size of the target, d_t , the greater the target capacitance C_t which is proportional to the accumulated target charge, Q_t . The result is a greater return current I_r drawn through the stalk and hence stronger EMP. The laser intensity for the four data points in figure 5.4 was $8.3 \times 10^{20} - 2.1 \times 10^{21} \text{ W/cm}^2$ due to shot to shot variations in laser energy and pulse duration. The hot electron temperature of 2.5 MeV was extracted

from the Equation (2.39) of the empirical Beg scaling [48]. The relationship between the target diameter and target charge was found using the following relation obtained from reference [136]:

$$Q_t \simeq 4\epsilon_0 d_t \frac{T_{hot}}{e} \quad (5.1)$$

which simply equates to the charge being equal to the product of the capacitance and the electric potential. The target charge increases linearly with increasing hot electron temperature according to this simple model. The recorded experimental data from D-dot (figure 5.4 a) follow a similar trend as the model predicts. For large targets (>2 mm in this data set), a square root like trend gives a much better fit to the data. This could be due to the fact that the simple model does not account for electron cooling. Electrons cool as a result of collisions and target heating. For the case of large targets, as electrons will lose energy and effectively cool traversing the target, the emission zone expansion is predicted to slow down ($<c$), causing linearity to break down. This effect is evident in the experimental data and the simulations presented in figure 5.4 a) and b). In small targets, the sheath field at the rear of the target is modified by the hot electrons, which spread laterally along the target surface, as described numerically by Psikal *et al* [137]. Those electrons then reflect at the edges and propagate back into the central region enhancing the sheath field strength which acts to contain the electrons in the target [138]. Furthermore, for smaller targets, electrons travel less distance interacting within the target. As a result, they experience fewer collisions, and consequently lose less energy; the emission zone expands at $\approx c$. The model does not account for this decrease in emission zone expansion velocity which means that it applies only up to a certain target size. For the duration of the laser pulse the electrons are connected intrinsically, however at times greater than the laser pulse duration, energy is no longer being added into the driving electromagnetic wave, resulting in imminent saturation. Consequently, electrons are not able to overcome the potential barrier of the target to escape.

The saturation is demonstrated in the simulations carried out using the fortran

ChoCoLaT2 [2, 17] simulation code (Simulation results credit: Alexandre Poyé – personal communications) for modelling escaping electronic charge, with similar laser parameters. ChoCoLaT2 program calculates the time evolution of the ejected electron cloud parameters, as well as the evolution of the ejected current distribution, the evolution of the potential barrier, and the hot electron cloud cooling by current ejection. 100 μm Ta foils were irradiated by a 0.5 ps laser pulse with 350 J of energy in a 3.5 μm (FWHM) laser focal spot. Normalised accumulated charge ($Q_t \propto \text{EMP energy}$) appears to grow faster for small targets (<1 mm), slows down as the target size is increased further, and begins to saturate for targets of several mm. It is predicted by simulations that the saturation of charge and the emitted energy prevails at target sizes of 10 mm for typical Vulcan laser parameters ([18]– Section II C.). The model is in agreement with the experimental results for the B-dot probe (figure 5.4 b)), indicating that the emitted energy begins to saturate when the targets become larger than 10 mm. This result is important for future high repetition rate facilities which are planning on firing many shots into large sheets of conductive target material as it highlights how the EMP scaling is expected to increase even for substrates of 20 mm or larger dimension.

Experiments conducted at the Orion laser facility, AWE, show that the EMP energy per joule of laser energy scales linearly with target size, supporting the simple model for small targets. The experiment used gold 125 μm foils of 0.2-3 mm size mounted on glass stalks [18]. It was also shown in the Vulcan TAW campaign that the EMP energy (and also target charge) increased with increasing escaped electron number and temperature (see chapter 4 figure 4.9 and reference [3]).

Interestingly, the data collected using the B-dot probe closely follows the simulation prediction. The EMP energy exhibits a sharp increase up to ≈ 5 mm target diameter. Up to this point the expansion of the potential Φ_E is dependent on the target diameter. After this point, the growth rate slows down, reaching saturation at 10 mm target diameter. The threshold value is controlled by the electron cooling time t_{cool} which is subject to the laser intensity, and potentially absorption changes due to preplasma which could be capable of generating a hotter electron distribution than expected [139]. The greater the laser intensity, the longer the electron cooling time and the larger the

potential spread (if not limited by target size). In cases where the potential spread is limited by the target size, it means that the charge is more concentrated and the potential is stronger, and the final escaping charge is therefore less.

5.3.3 Stalk length scan

The EMP from plastic stalks of several lengths (12 mm, 25 mm, 35 mm) which modified the path for the return current was examined. Lengthening the stalk decreases the intensity and the measured frequency of the EMP emission. The stalks were 3 mm in diameter made of plastic and mounted on a metal target wheel. The targets used were 5 mm×5 mm 100 μm thick tantalum foils. The laser energy on target and pulse duration were 363 ± 39 J and 420 ± 45 fs respectively, equivalent to peak intensities from 1.6 to 2.3×10^{21} W/cm². As expected, the experimental results revealed an overall decrease in EMP with increasing stalk length for both B and D-dot probes as shown in figure 5.5 a).

This was further analysed by splitting the EMP into low and high frequency components as displayed in 5.5 b). The low frequencies component which is believed to arise due to the chamber resonant modes remains largely constant—no decreasing trend is observed for the two probes (figure 5.6 b) and c)), whereas the high frequency contribution evidently exhibits a marked decline for longer stalks. This result corroborates that introduction of longer return current paths has a significant effect on EMP reduction. According to Equation 2.54, the EMP energy $\propto 1/l_s$. This model is represented by the lilac dashed curve in figure 5.6 a). Figure 5.6 displays normalised data from figure 5.5. The data follows a decreasing trend and closely scales as the model. Nevertheless, the EMP energy does not appear to drop off as fast as predicted by the model. This could be due to a number of reasons. Firstly, while the length of the stalk is the only variable, shot-to-shot noise variations may occur. Secondly, the model takes into account only the return current effects, and not the chamber resonance modes. Contribution of the chamber modes is a likely explanation to why the reduction is not as pronounced as the model. Though not measured in this data set, it is known that greater number of escaped electrons caused higher EMP emission, as those escaped electrons induce

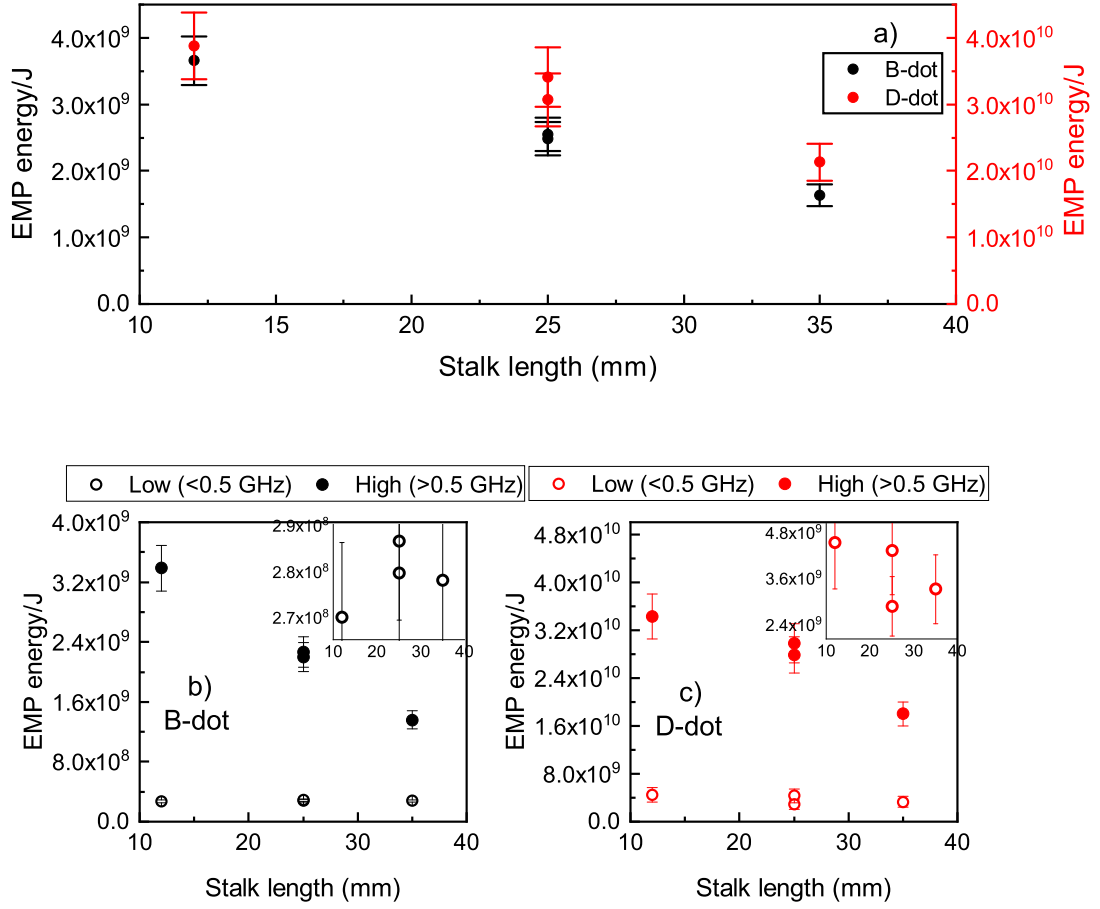


Figure 5.5: EMP energy as a function of plastic stalk length for 100 μm thick Ta targets in a metal target wheel a) Total EMP per joule of E_{Laser} is lowered by the introduction of longer target stalks due to increased distance for return current. Chamber mode frequencies (low) remain approximately constant but target and stalk contribution (high) is reduced by a significant amount with increased stalk length for both b) B-dot and c) D-dot probes.

dipoles in other metal components inside the vacuum chamber. In addition, plastics are not conductors and may behave in ways that are not yet fully understood in this scenario.

The target and stalk attached to the ground can be thought of as a linear dipole antenna. For a current pulse length shorter than the antenna length, the characteristic wavelength (or frequency) of emission is 4 times the stalk length, $\lambda_{EMP} = 4l_s$ ($\nu = c/4l_s$). This concept can be understood by considering the ground plane to be a plane of symmetry, the stalk on the ground is equivalent electrically to a straight wire of a

length $2l_s$ with positive ($+Q$) and negative ($-Q$) charge terminals attached to its ends at the initial time. This can be considered as a dipole of a length $2l_s$. Beginning from initial time $t = 0$ the charges propagate along the wire, meet in the middle at time $t = l_s/c$ and invert the polarity at $t = 2l_s/c$. The period of a full oscillation is then $t = 4l_s/c$ and corresponds to the wavelength $4l_s$ and frequency $\nu = c/4l_s$. For the stalk length $l_s=30$ mm, the period of oscillation is ≈ 0.5 ns with corresponding frequency range in the GHz domain. Therefore the frequency of emission can be reduced simply by increasing the stalk length. The data in figures 5.5 and 5.6 clearly shows a reduction with increased stalk length, although further investigation would be required to explore in more detail how the frequencies of the emitted pulse are affected.

The total energy emitted is also influenced by the stalk length. Quoting equation 2.54 in chapter 2 it can be seen that the EMP energy is proportional to $1/l_s$. Both the emission power and frequency are reduced by increasing the stalk length and discharge time.

In reality, the stalk emission is broad band rather than monochromatic. This is because the emission time is just a few periods, and the current is quickly dissipated due to resistive losses. Previously shown expressions for emitted energy in the GHz and THz domain reveal that more energy is emitted in the latter, however the interest in GHz domain is much more relevant due to its disruptive effects on electronic apparatus.

5.4 Conclusions

A study was carried out to investigate what factors affect EMP levels, how they can be controlled and used. These emissions in laser-solid interactions can be controlled by varying the materials of the target mounting system, target size and the length of the stalk, without appearing to have a significant effect on the $>MeV$ escaping electron or ion populations. EMP reduction was achieved by exchanging metallic mounting components to insulating materials. This was done to compare the effects of conducting and insulating materials with low and high resistivity, respectively. No obvious dependence on the target thickness was found at the Orion laser (AWE) for 10-125 μm gold

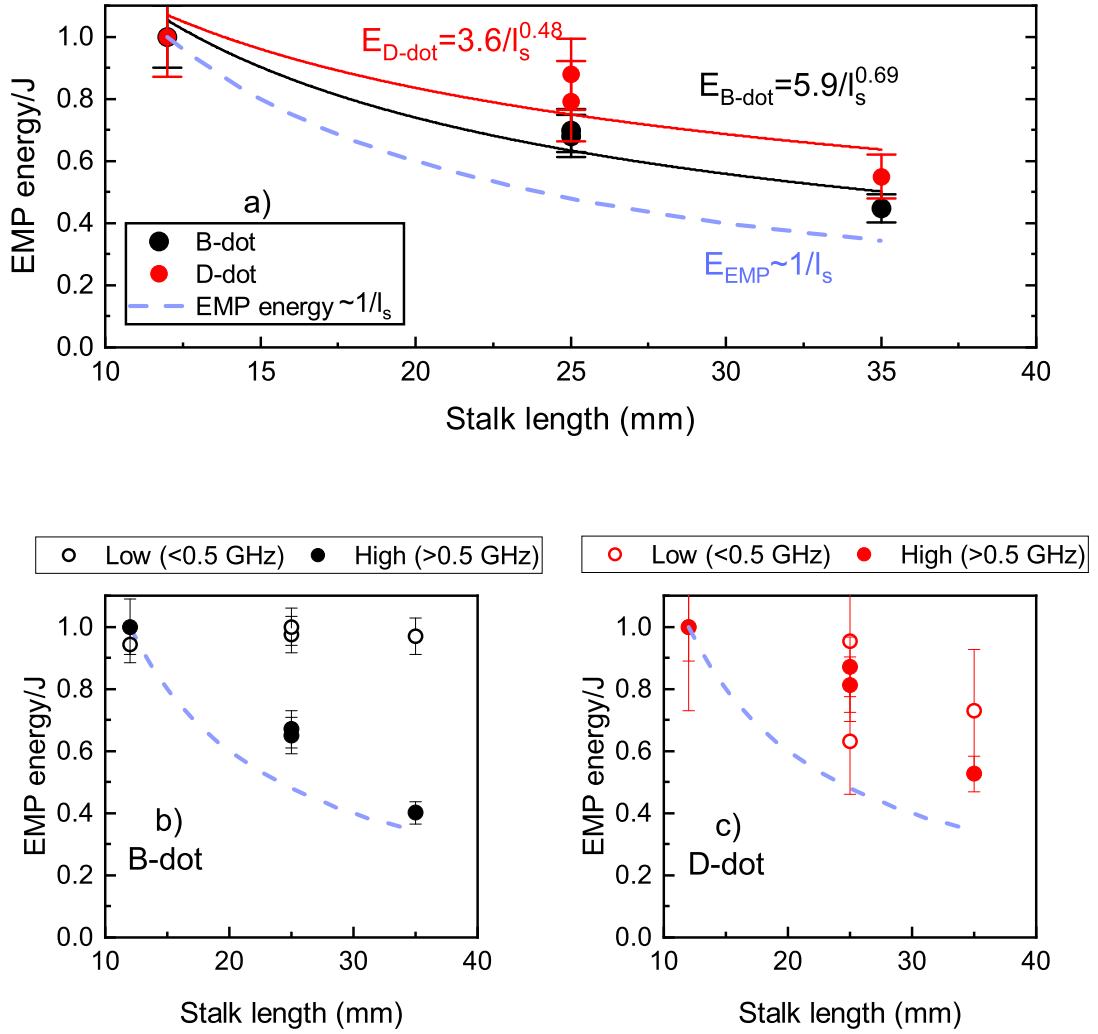


Figure 5.6: EMP energy (both low and high frequencies) as a function of plastic stalk length for 100 μm thick Ta targets in a metal target wheel a) Total EMP per joule of E_{Laser} is lowered by the introduction of longer target stalks due to increased distance for return current. Chamber mode frequencies (low) remain approximately constant but the target and stalk contributions (high) are reduced by a significant amount with increased stalk length for both b) B-dot and c) D-dot probes. The dashed lilac dashed curve indicates proportionality to $1/l_s$.

targets [18]. Similar observations were made in TAP for 10-100 μm thick tantalum and aluminium foils. This is as predicted; electrons penetrate fully through the target, without substantial energy loss at these laser intensities. The electron beam divergence is the same for thin and thick targets leading to larger escape area at the rear of the

thick target than the thin target. This means that the sheath strength is weaker due to the larger escape area, enabling more electrons to escape the target. Nevertheless, thin targets experience a greater effect of electron refluxing, which acts to enhance the escape area, thus weakening the sheath field strength [140] and enabling more electrons to exit the target. Further detailed studies may help to understand the effects of the interplay of the electron transport in thick and thin targets on the EMP generation.

Moreover, decreasing the diameter of the target produced less EMP due to larger targets being able to attain greater capacitance and escaping charge, thus causing greater return current. B-dot data is in agreement with simulation, indicating that the EMP energy reaches saturation limit and no longer increases for targets greater than 10 mm. EMP energy measured using the D-dot probe appears to continue to grow past the saturation limit of the model. Increasing the stalk length and consequently lengthening the path of return current, also reduced the EMP as expected. To lower the EMP by a factor of 2, the recommended stalk length should be >35 mm for plastic stalks. Larger upper stalk lengths, causing the surface current density to decrease resulting in lower EMP signal, also proved to be effective. Sinusoidally modulated stalks (with varying wavelengths) of the same bulk length as standard were also used with the aim of increasing the geodesic path length, as this technique proved to be effective in a previous study performed using the 100 TW arm (TAW) of the Vulcan laser. However, it proved to be ineffective using the PW beam in TAP. Although the use of spiral stalks demonstrated a significant reduction in EMP in a previous experimental campaign in TAW reported by Bradford *et al* [3], the decrease was not as pronounced in TAP (figure 5.3 (a)).

The requirements for improved high power and high repetition rate laser facilities to mitigate EMP effects without disrupting the desired experimental measurements include an optimised target mounting system design as well as shielding equipment for improved diagnostic operation.

Chapter 6

Particle detection via Cherenkov radiation

6.1 Introduction

In the recent decades, and particularly since the demonstration of monoenergetic electron beam production in 2004 [141], laser driven electron beams have been exploited for the creation of secondary radiation sources [142–146]. The generation of muons becomes viable when the electron beam energy is above 0.7 GeV. Given that laser-driven high energy electron beam generation exceeding this energy has already been demonstrated (the current record energy of 4.2 GeV was achieved by Leemans et al. in 2014 [147]), it should in principle be possible to produce laser-driven muons. A muon is a second generation lepton, a particle very similar to an electron, with the same charge but 207 times heavier. The interactions of negative muons are very similar to those of an electron, and a positive muon can be thought of as acting like a light proton. The main advantage of these elusive particles is their low stopping power at high energies, making them highly penetrating and suitable for imaging applications of large and dense high atomic number (Z) objects [148–153]. Current muon sources are high current particle accelerators such as the Large Hadron Collider (LHC) at CERN, Switzerland [21], and the ISIS neutron and muon source at the Rutherford Appleton

Laboratory, UK [20]. The large size and immobility of the particle accelerators make them impractical for industrial applications where portability of the device is required. An alternative to using large particle accelerators is to use naturally occurring cosmic ray sources, however low flux causes long image acquisition times. Laser driven radiation sources are potentially much more compact and could potentially become portable industrial devices.

The structure of this chapter is as follows. Firstly muons are introduced, and their advantages for applications are described. Laser wakefield driven muon processes are presented and the muon flux and directionality are examined by employing GEANT4 simulations. A novel muon Cherenkov detector design development for measuring muons in the presence of the high background environment typical of a laser-plasma interaction is presented. As a result of difficulties in detecting muons using current laser and electron beam parameters, the detector was tested using a muon source at the ISIS facility. Finally, work was carried out to examine the Cherenkov mechanism by using an electron beam to induce electron Cherenkov radiation.

6.2 Particles and applications

Diagnostic imaging techniques in medicine, industry and security utilise many different types of particles such as protons, neutrons, electrons, positrons, x-rays and muons. The work in this thesis chapter focuses on particle generation, and detection via optical means – Cherenkov radiation. This technique can be used to detect relativistic charged particles. This chapter specifically focuses on the generation of muons and electrons. Various detectors for muons are used in nuclear and particle physics research, such as drift tubes, cathode strip chambers and resistive plate chambers at the Compact Muon Solenoid (CMS) experiment, [154] scintillators coupled with silicon photomultipliers, [155] gas electron multiplier (GEM) detectors [156] and others. Many of these techniques are unsuitable to use in the presence of high background and low signal to noise ratio present during laser plasma interactions. Techniques used in nuclear physics for neutron and proton detection, such as the CR-39 and bubble detectors, are promis-

ing potential candidates for muon detection in a laser plasma environment in future high flux muon sources.

On the other hand, the detection of laser-driven electrons is relatively straightforward. Relativistic electrons are typically diagnosed using scintillating screens, such as lanex, coupled to a high dynamic range (EM)CCD or CMOS cameras. Sub 100 MeV electrons are measured using image plates, or scintillators coupled to a camera.

Many of these techniques, either for the detection of electrons or muons, are highly susceptible to the EMP pulses generated during laser-plasma interactions. As discussed in previous chapters, modern computers and electronic devices have become less shielded and it is the smaller scale electronics that make them more susceptible to EMP. Oscilloscopes which contain computers are often used and are typically inside target areas during the laser shots, making them vulnerable to EMP damage and potential distortion of the data measurements. In order to realise a laser-driven muon source and to improve the detection of laser-driven electrons we must develop a technique which is less sensitive to EMP.

6.3 Why muons?

Muons penetrating through material suffer relatively little scattering and thus have very straight paths. This means they are well suited for tracking and provide reliable angular information. For electrons to penetrate deep into a material they need to be relativistic, but due to low mass, their velocity changes cannot be measured due to lack of fast detectors. Therefore, muons being 207 times heavier than electrons can offer an advantage when measuring time of flight.

Applications of muons depend on their energy. Low energy muons produced in spallation sources are utilised in chemical physics, superconductivity and charge transport studies and others [157, 158]. Naturally occurring high energy muons are employed in imaging of geological structures, inspection of large containers for fissile elements, interrogating damage to nuclear reactor cores etc. Some applications are summarised in figure 6.1. A downside of cosmic muons is their low flux – 1 muon/cm²/min, resulting

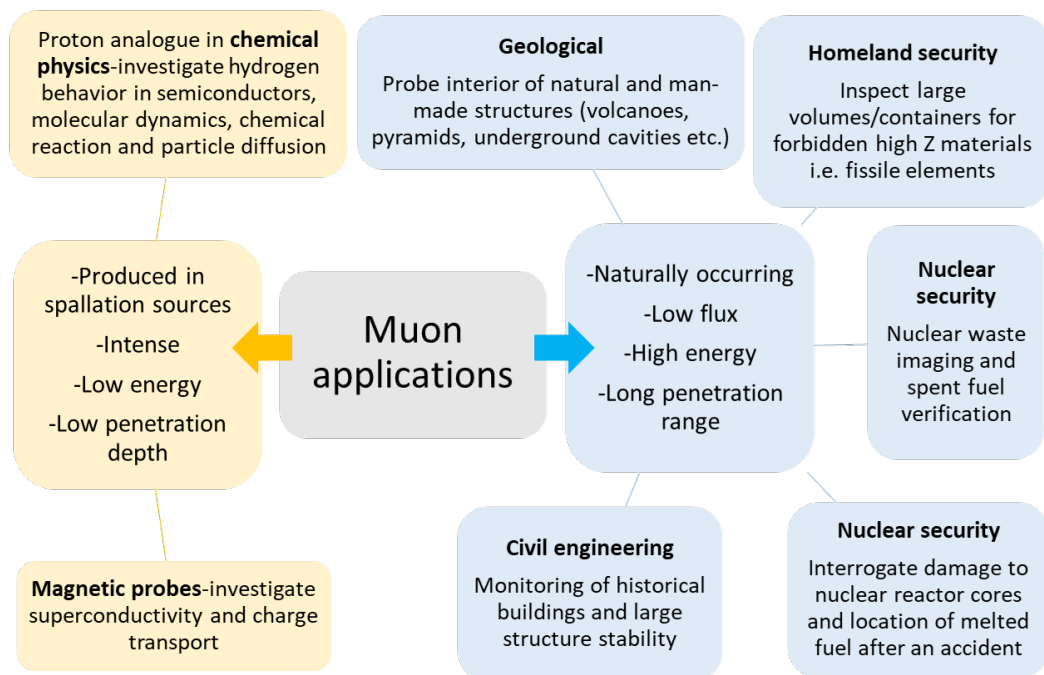


Figure 6.1: A chart showing the main muon applications. Low energy muon applications ($\approx 3\text{--}33$ MeV at ISIS) range from chemical studies to magnetic probing to investigate superconductivity. Highly energetic cosmic ray muons have applications in imaging of large dense objects, monitoring of nuclear reactor and nuclear waste and homeland security.

in very long acquisition times.

Muons are a good candidate for imaging applications in the security sector. Generation of these sources are becoming a realistic possibility with improving laser systems [15]. High energy beams combined with high repetition rate lasers are required in order to pave the way for applications of laser-plasma accelerators. High power laser-gas and laser-solid interactions induce many interactions within the target, which results in a high number of secondary particles. Some can be useful and utilised for a specific purpose, others, for example EMP emission, are a source of unwanted noise and disruption. Specialised detector development for muon detection in laser-plasma ex-

periments is required. This is due to the aforementioned high background environment. With current laser parameters, the muon flux compared to the rest of the secondary particles is very low. This means that detectors are likely to be flooded by unwanted particles, making muon detection very difficult. Detectors immune to other particles and radiation are necessary for laser based experiments where high background noise is present.

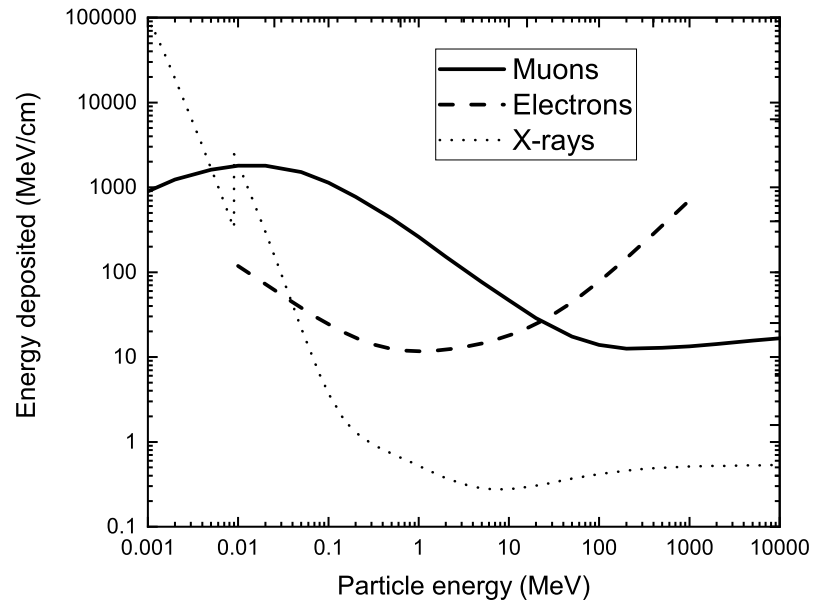


Figure 6.2: Energy deposited in copper by positive muons (solid) (calculated using Groom *et al.*), and electrons (dashed) using ESTAR NIST database.

Above 30 MeV energy, the stopping power of electrons is much higher than the stopping power of muons. This indicates that the electrons are stopped more easily in the target whereas muons are more likely to escape. It is evident from the graph in figure 6.2 [159] that above an energy of around 10 MeV the muon stopping power curve falls to a broad minimum. This is a useful property as it increases the probability of detecting muons by reducing the number of escaping electrons.

6.4 Laser-driven muon production

There are three main ways that muons are produced. High energy cosmic ray particles (such as protons) originate from the sun, outside the solar system, and from distant galaxies. Upon impact with the atmosphere molecules, these can produce cascades of lighter particles, for example pions, which decay to muons and neutrinos as illustrated in figure 6.3 a). Muons can also be made in spallation reactions. High energy proton beams are fired at a graphite target to produce pions, which then decay into muons (figure 6.3 b)). An example of such a facility is the ISIS Neutron and Muon Source. High power lasers can also be used to create muon sources. A high repetition short pulse laser fired at a gas cell/jet/capillary induces wakefield electron acceleration. The electrons go on to collide into a secondary converter target, and produce muons. Here we focus mainly on wakefield electron induced muons (figure 6.3 c)).

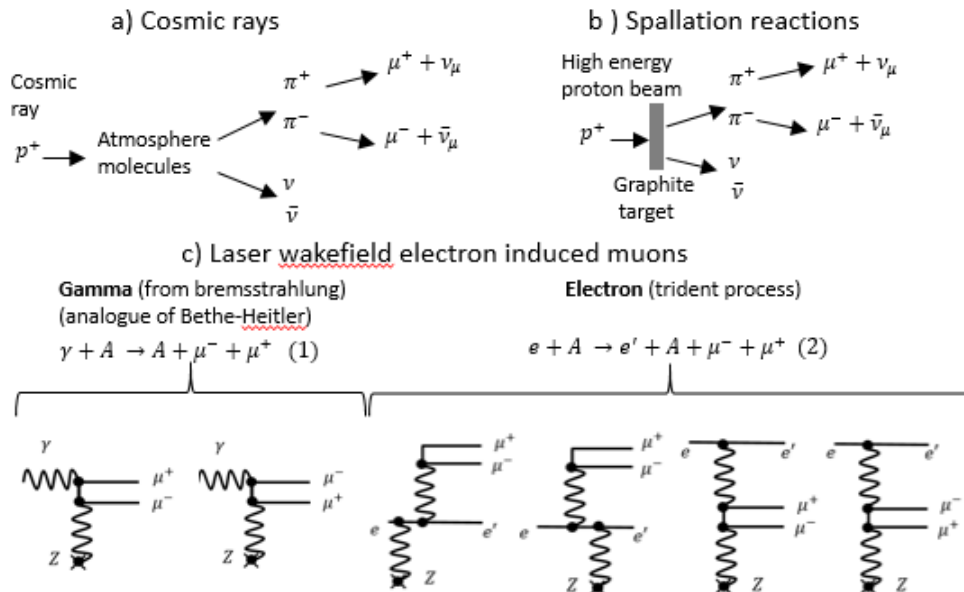


Figure 6.3: Muon production processes. a) Cosmic ray decay into muons. b) Spallation reactions. c) Laser wakefield electron induced muons: bremsstrahlung gamma or direct electron interaction (Adapted from reference [4]).

There are two elementary processes that describe muon-antimuon ($\mu^- \mu^+$) pair production in high atomic number (high Z) targets (A denotes high Z atomic nu-

cleus). These processes are illustrated by Feynman diagrams in figure 6.3. Process (1) represents the production of muons in the interaction of real gamma photons (from bremsstrahlung) within the electric field of the high Z target nuclei. This case is an analog of the process for electron-positron (e^-e^+) creation, known as Bethe-Heitler process. Process (2) denotes the production of $\mu^-\mu^+$ in the interaction of high energy electrons with high Z target nuclei, known as the trident process, which produces $\pi^-\pi^+$ pair directly without an intermediate real photon.

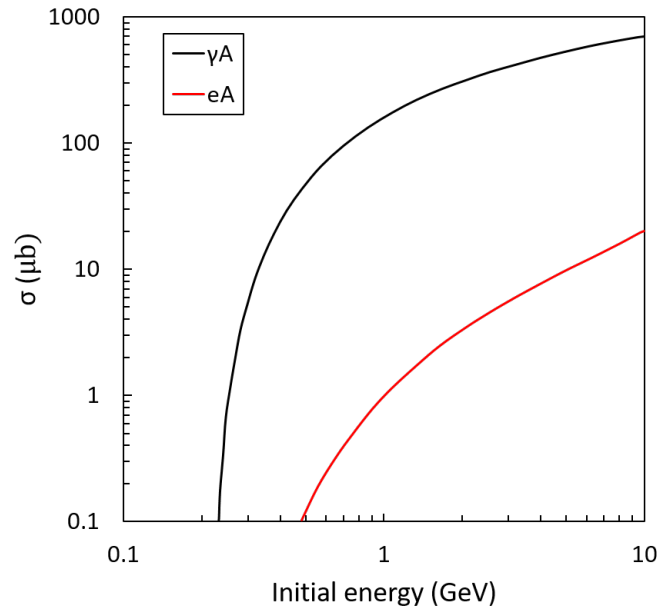


Figure 6.4: Cross section for muon production in a gold target from electrons (dashed) and gammas as a function of incident energy. Adapted from [4].

Titov *et al.* investigated muon pair production using laser-wakefield acceleration of electrons [4]. The total cross sections of the production of $\mu^-\mu^+$ as a function of initial energy in the two processes described above, are shown in figure 6.4 adapted from Titov *et al.*. The black line represents process (1) and the red curve represents process (2). This graph shows the cross section of muon production in gold targets. Gold has a very high atomic number therefore is considered to be one of the best candidates for this purpose. It can be seen from the graph that the generation of muons from gamma photon interactions with the target nuclei has a cross section ≈ 200 times greater than

that from high energy electron at the energy of 1 GeV. In high power laser acceleration with presently available lasers, we expect a combination of the above processes. The incoming electron beams will generate high energy bremsstrahlung as they propagate through the high Z convertor material for a γA induced process, and also electrons with energy greater than 1 GeV for eA induced process.

The effects of the energy of the electron beam were also examined. Their results highlight the significance of an increase in the electron beam energy. For a gold target of 1 cm thickness, a 20 pC (equivalent to $\approx 10^8$ electrons) electron beam at an energy of 700 MeV, yields approximately 50 $\mu^- \mu^+$ pairs and approximately 100 $\mu^- \mu^+$ pairs at 1 GeV electron energy. The muon yield increases considerably as a function of increasing electron energy. An energy increase from 1 GeV to 3 GeV boosts the number of $\mu^- \mu^+$ pairs produced by an order of magnitude. The thickness of the target needs to be considered as it affects the escaping particles and radiation. In order to decrease the number of escaping electrons, a thicker target can be used. In addition, increasing the target thickness leads to higher muon production. On the other hand, the lower energy muons may not be energetic enough to leave target. Titov *et al.* model does not take into account muon stopping within the target which may have a significant effect on lower energy muons.

The cross sections as a function of emission angle of muons for the two main processes of $\mu^- \mu^+$ pair production are depicted in figure 6.5. The γA process on the right hand side of the figure has a much higher cross section than eA . It can be seen that for both reactions lower energy (1 GeV) gamma photons or electrons give a broad angular emission peaking at angle greater than 3° . Higher energy (10 GeV) results in a smaller angular distribution narrower beam in a more forward direction. For the initial energy of 10 GeV the angular emission of muons is narrower and peaks below 1° . It is also evident from the cross sections that higher initial energy results in higher differential cross sections of $\mu^- \mu^+$ pairs.

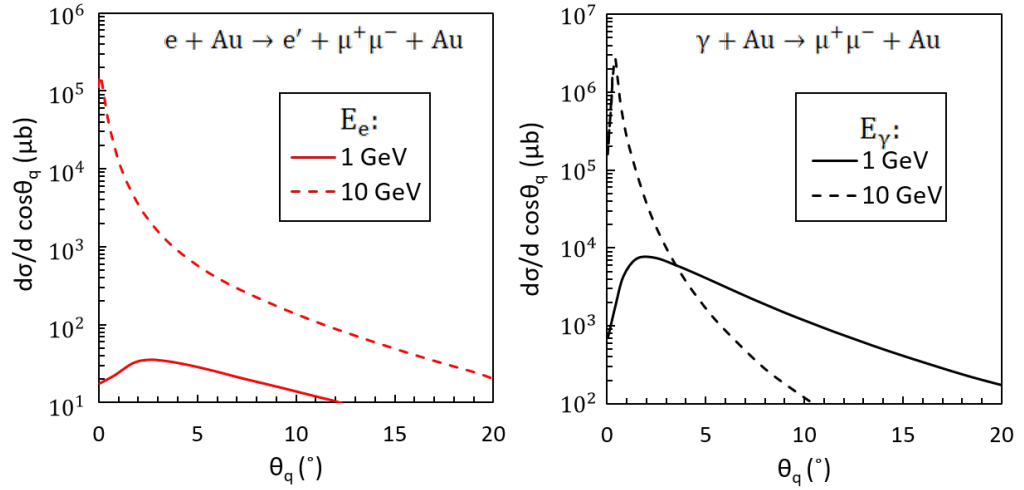


Figure 6.5: Differential cross sections of muon pair production as a function of polar angle θ_q in eA process on the left graph and in γA process on the right, adapted from Titov [4].

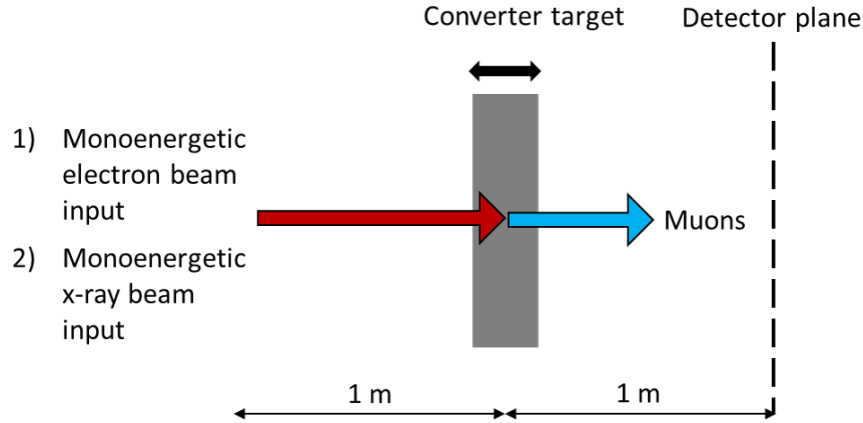


Figure 6.6: Basic schematic of GEANT4 simulation set up used to model the directionality and flux of the muon beam. The simulations were carried out using 10^5 incident 1) electrons and 2) x-rays of single energy and were repeated for different incident electron beam energies and several converter target thickness. The converter target was situated 1 m from the particle source. The muons were detected by a large $1\text{ m} \times 1\text{ m}$ detector positioned 1 m behind the converter target.

6.5 GEANT4 simulations

Numerical simulations of the muon generation were conducted using the GEANT4 code. Two scenarios were simulated, including the effects of electron beam energy and the converter target thickness on the generated muon flux, energy spectrum and

the directionality of the muon beam. The simulation set-up is displayed in figure 6.6. These two simulation scenarios were based on firing a mono-energetic electron beam and mono-energetic x-ray beam at a lead converter target. Lead was chosen due to its high atomic number Z , and being widely commercially available. The simulations were repeated for discrete energies ranging 1-10 GeV and for lead converter thicknesses 2-20 cm. The converter target was placed 1 m behind the particle source, and the detector plane was 1 m behind the converter. In each simulation 10^5 incident particles equivalent to a charge of 0.016 pC were used to reduce computation time, but with cross section of the muon production raised by $\times 10000$ to increase the probability of reactions occurring; typically the electron bunch charge above 1 GeV is several pC on the Gemini laser. They were fired at the converter where the muons were produced, which were then detected by the detector. The detector was $1\text{ m} \times 1\text{ m}$ in size allowing for a solid angle of approximately 0.8 sr. The FTFP_BERT physics list which contains all standard electromagnetic processes was employed. Mainly the simulations with an electron beam input will be discussed here.

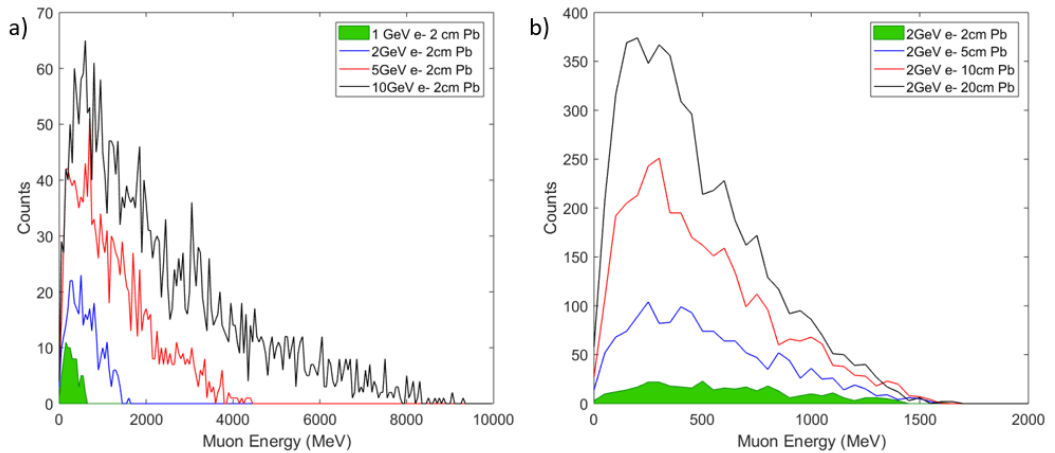


Figure 6.7: a) Muon energy spectrum for 2 cm thick lead converter target for several electron energies ranging 1-10 GeV and b) energy spectrum for constant energy of 2 GeV and different target thicknesses.

A comparison of muon energy spectra for varying incident electron beam energies and thicknesses is shown in figure 6.7. The area shaded in green represents the expected

tation with current laser parameters. Such a low muon signal is unlikely to be detected without specialised detection techniques, due to the vast numbers of other secondary radiation and particles, in particular x-rays and electrons. Although the achievable peak electron beam energies exceed 1 GeV, it is the charge above this energy which is crucial. The bremsstrahlung photon threshold energy for muon production is 211 MeV, thus it is essential that the electron beam energy exceeds this energy, and the bunch charge is reasonably high, in order to produce a high flux high energy bremsstrahlung which will go on to create muon pairs. It can be deduced from figure 6.7 a) that an increase in incident electron beam energy causes a marked increase in muon counts for constant lead converter thickness of 2 cm. The energy spectra have a similar Maxwellian-like shape for all incident beam energies, where most muons counts occur at low energies (10% of incident energy). Keeping the incident energy constant and increasing the converter thickness has a boosting effect too. In figure 6.7 b) the energy of the incident beam is 2 GeV and the thickness of the converter ranges from 2 cm to 20 cm. The area highlighted in green indicates the achievable results with current parameters. It is evident that increasing the thickness increases the number of muons considerably. Though the number of muons generated increases for thicker converters, it makes it less likely for any initially lower energy muons to escape, as they traverse it losing energy. Another problem that arises is that with increasing target thickness, the number of secondary particles and radiation would also increase. Thus, as discussed earlier, specially designed diagnostics are required.

Total muon counts for different input particle energies and thicknesses are plotted in figure 6.8. The black squares and red circles represent the gamma and electron incident beam respectively. The gamma beam causes greater muon yields as the interaction is ‘single-step’ where the gammas interact with target nuclei and produce muon pairs. The simulation using an electron beam yields less muons due to a two step process in which the electrons interact with the electric fields of the target atoms causing them to slow down and emit bremsstrahlung, which then goes on to produce muon pairs. In both scenarios the relationship between the muon yield and incident particle energy is close to linear. The muon yield more than doubles increasing the target thickness from

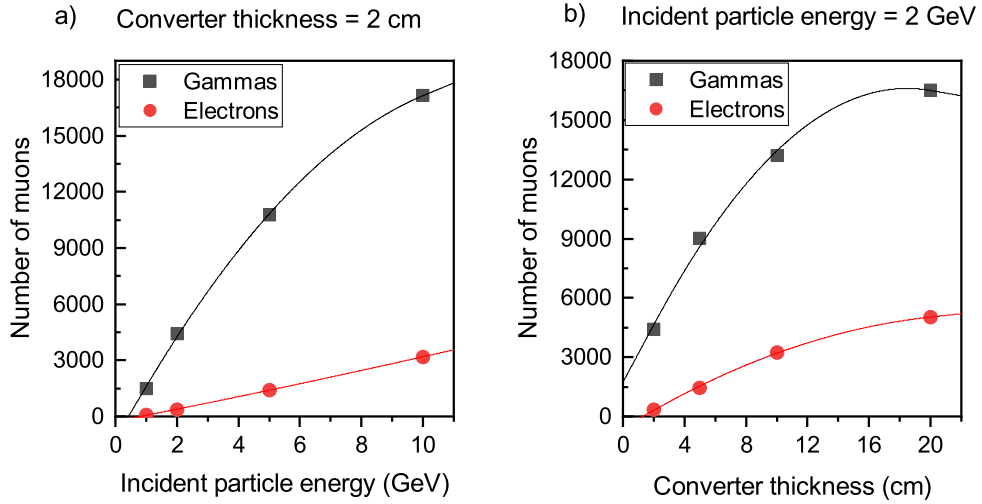


Figure 6.8: Number of muons as a) a function of incident particle energy and b) converter target thickness. Simulations performed using GEANT4 with 10^5 incident particles. The cross section of the muon production was raised by $\times 10000$ to increase the probability of the reactions occurring.

2 to 5 cm, but the rate of increase slows down between 10 and 20 cm. The electron beam loses a significant amount of energy in the lead target, reducing the energy of the produced bremsstrahlung. Bremsstrahlung photon energies may be below the threshold of 211 MeV, or even if this condition is met, the resulting muon energy may be so low that it is not able to escape the converter target.

It was also important to investigate the spatial profile of the muon beam with current laser parameters, and the improvement which could be achieved with the latest advances in laser engineering capabilities. The simulations revealed that the incident electron beam energy has an immense effect on the spatial profile of the muon beam as demonstrated in figure 6.9. A monoenergetic 1 GeV incident electron beam fired at a 2 cm thick lead target does not produce a good quality muon beam. The muons detected in the $1 \text{ m} \times 1 \text{ m}$ detector plane are scattered significantly and the flux density is extremely low (a)). For the 1 GeV electron beam 5 cm lead target case, the result is similar; the detected muons are scattered, but the overall number of detected muons

is much greater, thus it appears more beam-like (b)). Fivefold increase in the electron energy for a 5 cm converter shows a tremendous improvement in muon beam spatial profile, the beam is highly collimated compared to the 1 GeV cases. The muon beam becomes even narrower for 10 GeV electrons. The higher the electron beam energy, the less divergence it experiences, in turn causing a more directed muon beam. In addition, bremsstrahlung with higher energies is generated, increasing the energy of the muons created within the target, which also helps the directionality.

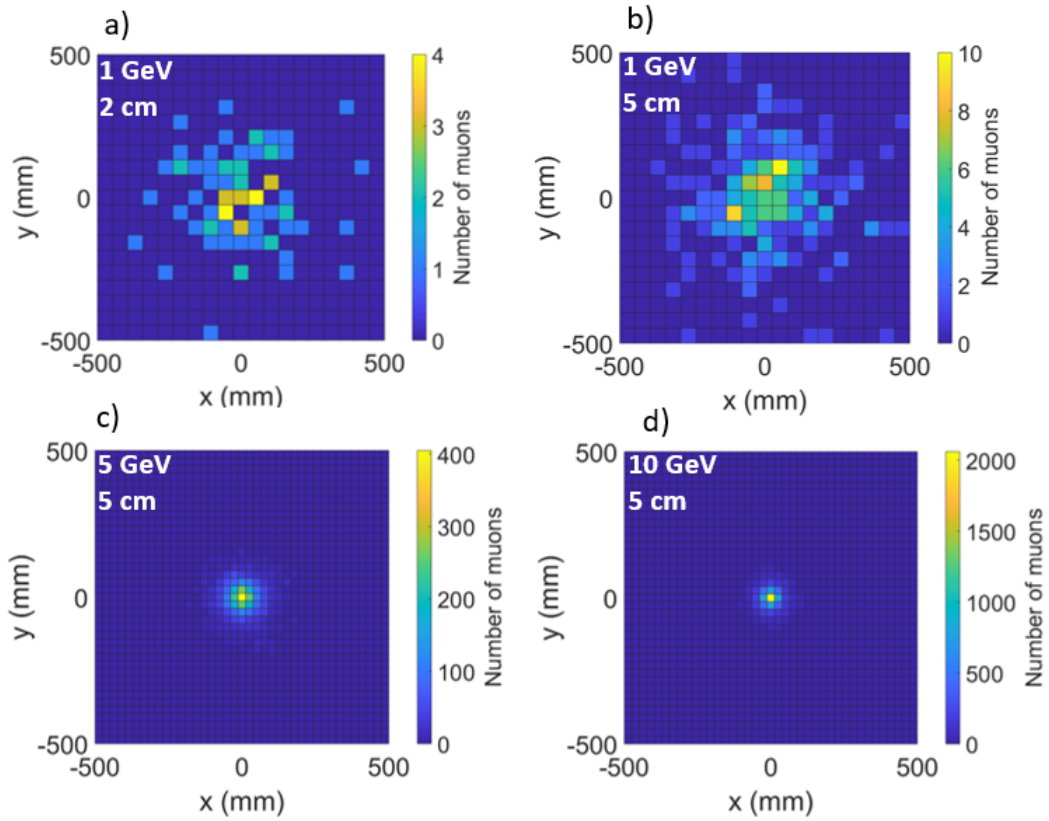


Figure 6.9: Simulations carried out using GEANT4. The directionality of the muon beam for different electron beam energies.

From the previous section summarising the analytical results of Titov *et al.*, and the GEANT4 numerical simulations, it can be seen that generation of muons using particle beams with equivalent parameters to those generated using lasers is possible. That being said, the numbers of muons with current laser (such as Gemini) parameters are

extremely low. Novel advanced techniques are required for detection of muons where a vast number of secondaries is expected to be present. The development of such a technique is presented in the following sections.

6.6 A Cherenkov radiation based muon detector

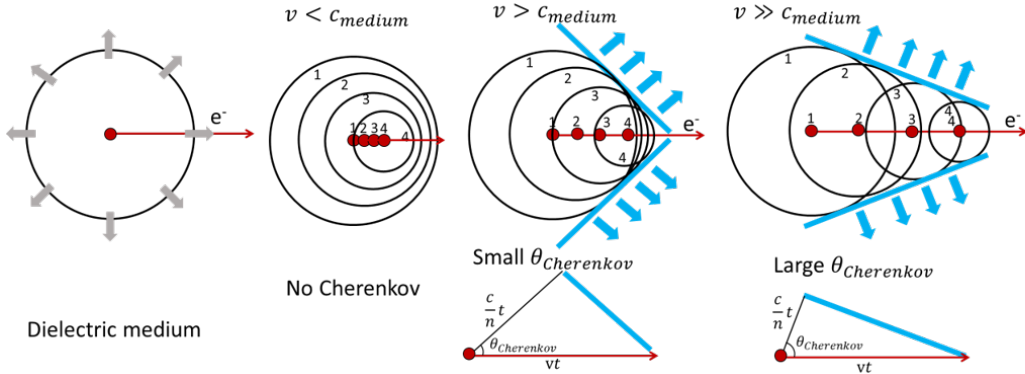


Figure 6.10: Illustration of Cherenkov radiation emission in a dielectric medium – blue arrows. Particles with velocity less than c_{medium} radiate dipoles but there is no constructive interference of the wavefronts therefore no Cherenkov emission. Particles whose velocity is greater than c_{medium} radiate dipoles that overlap and constructively interfere emitting light at small angle $\theta_{Cherenkov}$. When the velocity is much greater than c_{medium} , $\theta_{Cherenkov}$ is large.

Cherenkov radiation can be described as the deformation of the electromagnetic field of a charged, moving particle in a polarizable medium, and was predicted by O. Heaviside in 1888, by Kelvin in 1901, in 1904 by Somerfield. The phenomenon was first experimentally observed by Marie and Pierre Curie when studying radioactivity emission in the early 1900s. These studies were forgotten until 1934 when Cherenkov performed experiments to investigate the phenomenon, earning him the Nobel Prize in 1958 [160].

A charged particle travelling faster than the speed of light in that medium will produce Cherenkov radiation – a type of electromagnetic radiation in the UV and visible range, which will be emitted in a cone. The emission is caused by an asymmetric polarisation of the medium in front and at the rear of the charged particle, giving rise to a varying electric dipole moment. Some of the particle's energy is converted into

photons. A coherent wave front is generated, moving at velocity v at an angle θ_1 , known as the Cherenkov angle. Along the transition of a charged particle such as an electron or a muon, it interacts with molecules of the dielectric medium. Every interaction leads to polarisation and subsequent depolarisation of these molecules. The electric field of the electron creates induced dipoles which radiate outwards. This process leads to the emission of light in the form of spherical wavefronts. The velocity of the electron is v , and the velocity of the spreading of the wavefront is c_{medium}/n , where c_{medium} is the velocity of light in that medium and n is the refractive index. The electron is travelling much faster than the wavefronts and thus, they are lagging behind, and as they do so they lead to a constructive interference along a particular direction. This leads to a Cherenkov radiation beam.

6.6.1 Cherenkov threshold energy

For Cherenkov radiation emission it is required that $\beta > 1/n$, i.e. the phenomenon occurs in media with $n > 1$ (n is the refractive index). It is required that the energy of the charged particle must be higher than the threshold energy in order for Cherenkov radiation to be emitted. Threshold energy is found using the following equation:

$$\gamma = \frac{E}{m_0 c^2} = \frac{1}{\sqrt{1 - \beta_{min}^2}} = \frac{1}{\sqrt{1 - \frac{1}{n^2}}} \quad (6.1)$$

$$E_{th} = (\gamma - 1) m_0 c^2 \quad (6.2)$$

where γ is the Lorentz factor, E is the sum of rest and kinetic energies, m_0 is the rest mass of the particle, β_{min} is the minimum particle velocity for Cherenkov emission and is given by $\beta_{min} = 1/n$. Calculating γ will enable to determine E , since m_0 and c are known. Threshold energies for muon Cherenkov emission will vary for different materials depending on their index of refraction. The greater the refractive index the lower the threshold energy for Cherenkov emission.

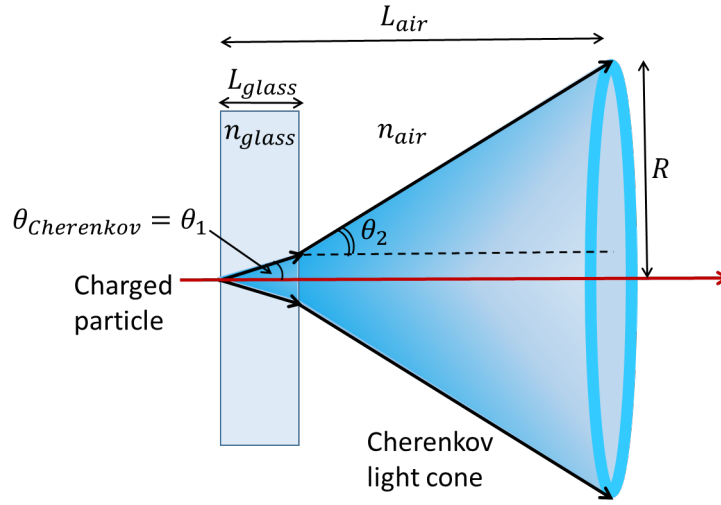


Figure 6.11: Cherenkov radiation is emitted in a cone. It makes a half-angle θ_1 with the charged particle, and refracts at θ_2 forming a ring on a detector screen.

6.6.2 Cherenkov emission angle

Cherenkov emission angle θ_1 is a function of the refractive index of the material which varies with wavelength $n(\lambda)$ (figure 6.15), and the velocity of the particle in terms of the speed of light $\beta = v/c$ and can be calculated using Equation 6.3 below [161, 162].

$$\cos\theta_1 = \frac{1}{n(\lambda)\beta} \quad (6.3)$$

The maximum Cherenkov angles occur as $\beta \rightarrow 1$, and it follows that the maximum Cherenkov angle $\cos\theta_{max} = 1/n$. The higher the energy of the particle, and in turn β , and the higher the refractive index, the larger the Cherenkov emission angle. The radius of the light cone ring size (figure 6.11) can be calculated using the following:

$$R = L_{glass}\tan(\theta_1) + L_{air}\tan(\theta_2) \quad (6.4)$$

where R is the radius of the ring, L_{glass} is the thickness of the Cherenkov medium, L_{air} from the radiator to the detector, θ_1 is the Cherenkov emission angle and θ_2 is the angle of refraction. As the distance to the detector is increased, the Cherenkov ring will increase, decreasing its intensity per unit area. In order to capture as many photons

as possible, the detector would have to be placed very close to the Cherenkov medium. This is not always feasible in experiments due to limited space in target areas. Another problem arises in the size of the active area of the fast photon detector. In the case of extremely fast MCP-PMT detectors with less than 0.5 ns FWHM response, the active area is up to 2×2 cm. CMOS and CCD cameras also usually have a limited size of ≈ 1 or 2 cm. This issue can be solved by using a focusing optic to collect and focus the light.

6.6.3 Cherenkov light yield

Cherenkov radiation has highest intensity at shorter wavelengths, i.e. in the UV range of the spectrum, and tails off into the visible part of the electromagnetic spectrum. The number of Cherenkov photons emitted will be referred to as Cherenkov light yield. The light yield is dependent on the charge and velocity of the particle (muons and electrons/antimuons and positrons). Cherenkov light yield dN/dx is given by the Frank-Tamm formula [163]:

$$\begin{aligned} \frac{dN}{dx} &= 2\pi\alpha z^2 \int_{\lambda_1}^{\lambda_2} \left(1 - \frac{1}{n^2(\lambda)\beta^2}\right) \frac{d\lambda}{\lambda^2} \\ &\approx 2\pi\alpha z^2 \sin^2\theta_1 \frac{\lambda_2 - \lambda_1}{\lambda_1\lambda_2} \end{aligned} \quad (6.5)$$

where α is the fine structure constant, z is the particle's charge, n is the refractive index of the medium, θ_1 is the Cherenkov emission angle measured in degrees and λ_1 and λ_2 are the wavelengths. The values of λ_1 and λ_2 inserted in the equation depend on the wavelengths that the detector is sensitive to. The equation for light yield can be simplified to the following forms $dN/dx = 390 \sin^2\theta$ [cm^{-1}] for 350-500 nm, $dN/dx = 490 \sin^2\theta$ [cm^{-1}] for 400-700 nm, $dN/dx = 1150 \sin^2\theta$ [cm^{-1}] for 200-700nm (includes UV) and similarly for other wavelength values.

The number of Cherenkov photons emitted is proportional to the inverse square of the wavelength $dN/dx \propto 1/\lambda^2$. The photon yield is highest for small wavelengths, where the intensity is highest. The wavelengths represent the range which the detector

is sensitive to, thus the larger the range of wavelengths that the detector can detect, the more signal will be measurable. The actual amount of light emitted is unaffected.

6.6.4 Total internal reflection of Cherenkov radiation in a medium

The higher the refractive index of the medium the light is traversing, the smaller the critical angle; $\theta_{crit} = \sin^{-1}(n_2/n_1)$, where θ_{crit} is the angle of incidence beyond which Cherenkov light photons passing through a denser medium are no longer refracted/transmitted, but instead are totally internally reflected. The angle of reflection is equal to the angle of incidence (larger than critical angle for that material), n_1 is the refractive index of the material light is travelling through (i.e. the Cherenkov medium), n_2 is the refractive index of the medium the light is entering (air). The larger the refractive index of the Cherenkov medium, the smaller the critical angle becomes, which means the amount of photons that are refracted lessens as they will start reflecting at smaller angles of incidence than in lower refractive index materials. The size of the Cherenkov photon emission angle is related to the energy (or the velocity) of the charged particle causing the emission (muon/electron); higher velocity particles yield larger emission angles according to Equation 6.3. Despite the fact that small critical angle means that not as many photons can be transmitted, it can also be advantageous when trying to eliminate noise arising from electron Cherenkov photon signal. Electron Cherenkov emission yields larger angles of photon emission due to their lighter mass and greater velocity in the relevant energy range. This means that the electron Cherenkov photons are reflected in the medium. If the muon Cherenkov angle is smaller (muon mass is much greater which causes them to travel at slower velocity) than the critical angle in that material, then the photons escape and refract. Tilting of the exit surface can be introduced to some degrees in order to optimise the escaping muon photon number, while confining the electron induced Cherenkov photons by total internal reflection. This will be investigated in a later section.

6.7 Muon Cherenkov detector design

Cherenkov detectors are primarily used in particle physics experiments for particle identification. There are several types of Cherenkov detectors that are commonly used in high energy physics environment: Threshold Cherenkov detector which consists only of a radiator and a light detector such as a photomultiplier. Differential Cherenkov detector that enables to determine θ -interval. Ring-Imaging-Cherenkov-Detector which measure the angle. They make use of a spherical mirror to focus light onto a photon detector, in which the centre of the ring is the direction in which the particle is travelling in. In high energy particle physics, the energy scales of detected particles is much greater than what can currently be achieved using laser driven sources.

Laser wakefield driven muons can reach only several hundreds of MeV and only very small fluxes with current parameters. Currently used Cherenkov techniques are not suitable for this scenario and need modifications to discriminate against other particles falling on the same detector. Therefore, a detailed study of a muon Cherenkov detector development for employment in laser-plasma experiments is undertaken.

The basic idea is to produce laser wakefield induced muons in a converter target, which will be incident onto a Cherenkov medium with a reasonably high refractive index. Any sufficiently fast muons will create Cherenkov photons in that medium which will be emitted in a cone with a characteristic Cherenkov half angle. The cone will be highly divergent, therefore a collimation method is required in order to be able to capture the light and focus it onto a photon detector. This section will introduce concepts for detector discrimination against secondary particles, discuss the potential Cherenkov materials for optimised Cherenkov production and collection and provide a concept for collimating the Cherenkov photon beam, all of which will lead to an optimised muon Cherenkov detector design for detection of 100 MeV muons in laser-plasma experiments.

6.7.1 Secondary particle discrimination

In order to reduce the number of secondary particles incident onto the detectors, a magnet can be placed after the iron convertor target causing the charged particle paths to deflect and neutral particles and high energy x-rays to continue in the forward direction.

However, there still remains a large flux of co-propagating electrons with significantly higher numbers relative to muons. The electrons are lighter and will be deflected more substantially than the muons. However, in a certain range of energies the signals will overlap causing difficulty in identifying the muons. For example, 20-100 MeV muons will follow the same path as 70-180 MeV electrons (see figure 6.12). The deflection angles of an electron, θ_e , and a muon, θ_μ , are given in equations 6.6 and 6.7. By equating these two equations, we can obtain a relationship for the energy of a co-propagating electron, E_{ke} , for a known energy muon, $E_{k\mu}$, which is given in equation 6.8.

$$\theta_e = \tan^{-1} \frac{eBl_B}{\sqrt{\left(\frac{E_{ke}}{m_e+1}\right)^2 - 1}m_e} \quad (6.6)$$

$$\theta_\mu = \tan^{-1} \frac{eBl_B}{\sqrt{\left(\frac{E_{k\mu}}{m_\mu+1}\right)^2 - 1}m_\mu} \quad (6.7)$$

$$E_{ke} = m_e \sqrt{207^2 \left[\left(\frac{E_{k\mu}}{m_\mu} + 1 \right)^2 - 1 \right] + 1 - m_e} \quad (6.8)$$

where E_{ke} and $E_{k\mu}$ are in MeV, m_μ and m_e are the rest masses of muon and electron respectively in MeV/ c^2 , e is the electronic charge, B is the magnetic field strength in Tesla and l_B is the length of the magnetic field in metres.

The solution proposed for this was to utilise a novel muon Cherenkov technique coupled to a light detector. Due to different travel times of muons and electrons, the electron signal can be filtered out using time-gating. Lower energy muons will be easier to detect with this method as their travel time is longer making time gating easier.

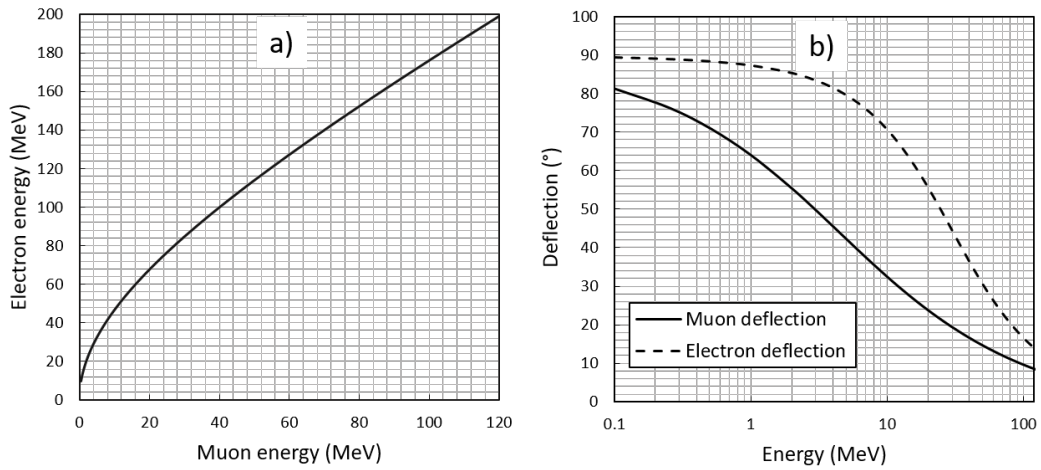


Figure 6.12: a) Energy relationship of co-propagating muons and electrons; 100 MeV muons follow the same path as 180 MeV electrons. b) Deflection of muons and electrons as a function of particle energy for a 1 Tesla 10 cm long magnet.

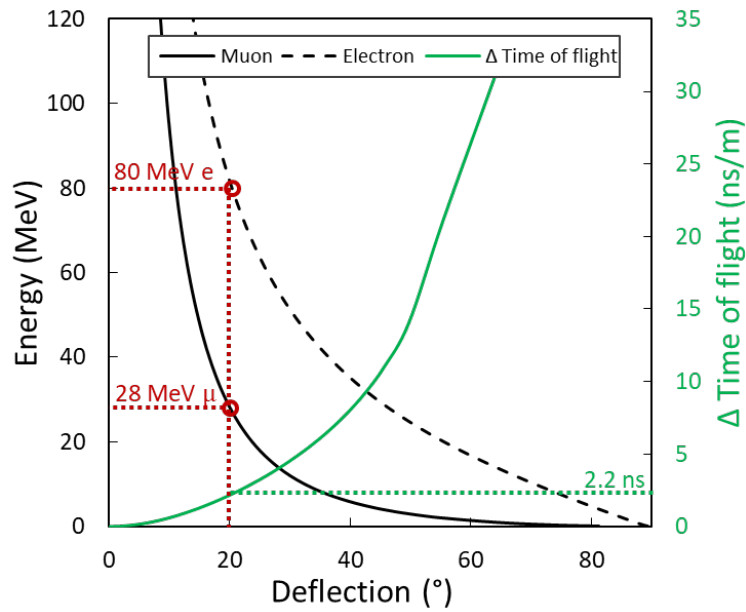


Figure 6.13: The difference in time-of-flight between muons and electrons for a 1 metre path. This time difference could be advantageous for time-gating. A 28 MeV muon and an 80 MeV electron deflection is 20°, a 1 m path time of flight difference is 2.2 ns.

There is a negligible difference in the time-of-flight for electrons with energy 70-180 MeV and co-moving muons.

Detection of a muon signal above an electron signal can be enhanced exploiting

characteristic emission angles of Cherenkov light, and tilted surfaces to confine electron induced emission by total internal reflection.

6.7.2 Investigation of materials and their properties and optimisation

Material	Refractive index (at 400 nm)	Critical angle	Particle	Energy min (MeV)	Energy max (flat geometry) (MeV)
Fused silica	1.47	42.9	muon	38	170
			co-propagating electron	97	254
Plastic (PMMA)	1.5	41.8	muon	36	130
			co-propagating electron	94	210
Sapphire	1.79	34	muon	22	37
			co-propagating electron	71	95
BGO	2.22	26.8	muon	13	17
			co-propagating electron	54	62

Figure 6.14: Summary of threshold energies for muon Cherenkov emission (Energy min) and the co-propagating electron energies, as well as muon energies (Energy max) whose photons escape in a flat geometry, for several materials.

Four different types of materials including a non-crystalline silica glass - fused silica (SiO_2), sapphire glass (Al_2O_3), plastic (PMMA) and an inorganic scintillator BGO (Bismuth Germanate ($\text{Bi}_4\text{Ge}_3\text{O}_{12}$)) were evaluated. They each have different refractive indices, which is a significant parameter in the production and properties of resulting Cherenkov radiation. As mentioned previously, the ideal medium has to meet transmission and Cherenkov threshold requirements. All four materials are transparent to visible light. Fused silica, sapphire and BGO are highly transmissive down to UV wavelengths, however plastic does not transmit light below 400 nm (UV upper wavelength).

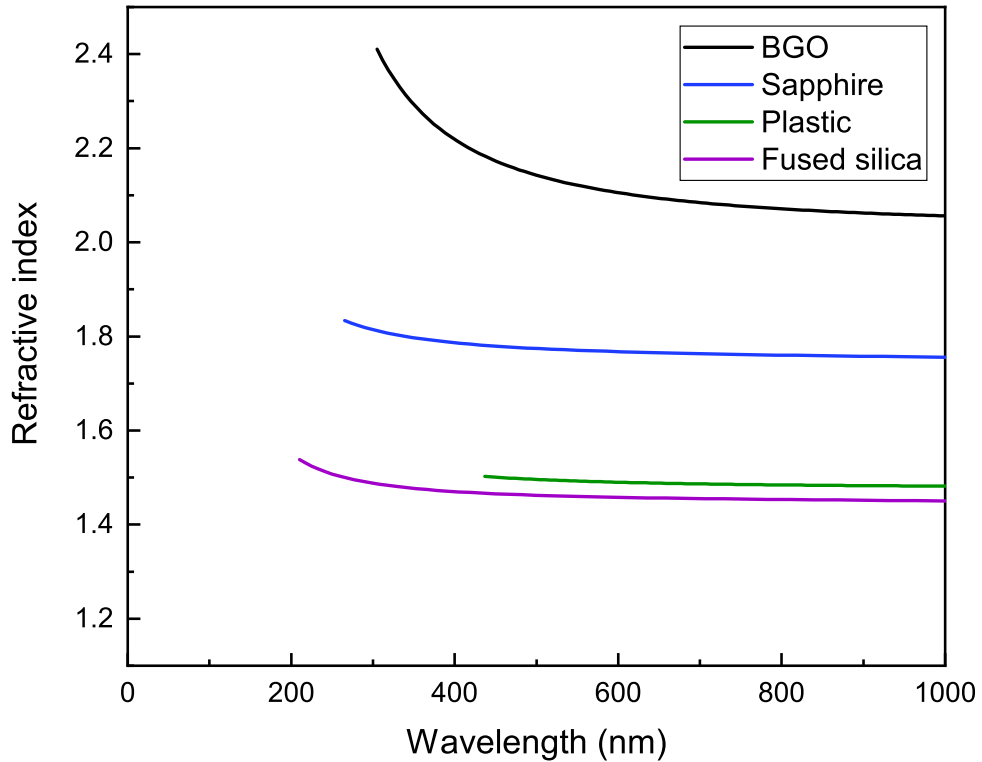


Figure 6.15: The refractive index of various materials dependence on the wavelength of light (obtained from a refractive index database: <https://refractiveindex.info>). It is highest at short wavelength.

These materials were chosen due to their wide commercial off-the shelf availability and affordable cost. Fused silica and sapphire are not known to be strong scintillators, but some types of plastics as well as BGO are. In the case of using a well-studied scintillator BGO, it is possible to gate out the scintillation signal as it is a much slower process than Cherenkov, or subtract the BGO scintillation spectrum from the total detected light spectrum.

Using a 1.5 GeV electron beam, most muon counts are predicted to occur at 20-40 MeV energy range, however, the counts vary by at the most a factor of two, below 100 MeV muon energy. Therefore a flat spectrum is suitable for this preliminary study and the below approximation is suitable to use;

$$N(\mu) = N_0 \quad (6.9)$$

$$N_\mu(E_\mu) = N_0 \quad (6.10)$$

$$N_\mu(E_\mu) = N_0 \text{ for } 0 < E_\mu < 100 \text{ MeV} \quad (6.11)$$

where N_0 represents the number of muons which is a constant, $N_\mu(E_\mu)$ is the number of muons as a function of muon energy E_μ .

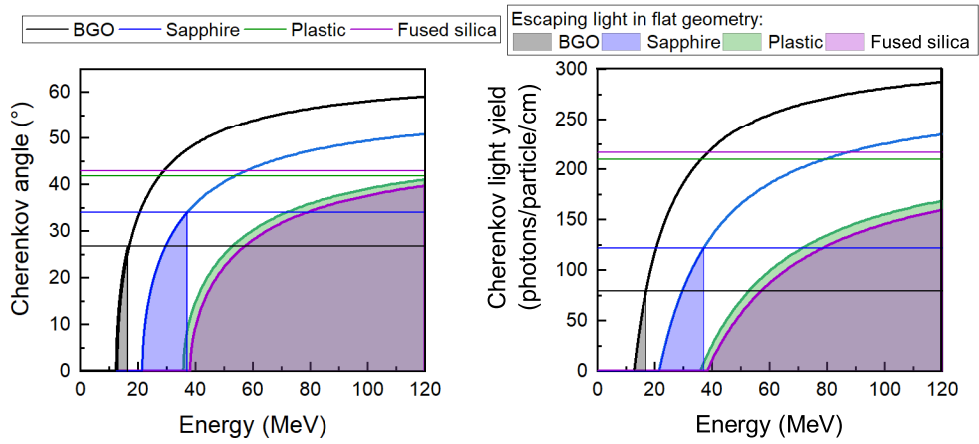


Figure 6.16: Muon Cherenkov light yield dN/dx for BGO, sapphire, plastic and fused silica for wavelengths 350-500 nm. The coloured horizontal lines indicate the critical angle for total internal reflection, and the shaded areas represent the muon energy region in which the generated Cherenkov photons escape in a flat geometry.

In order to maximise the number of muon Cherenkov photons emitted it was imperative to choose a material that meets certain requirements for light transmission and Cherenkov threshold. The light yield calculations show that the higher the refractive index of the material, the higher the number of photons emitted per unit length and the lower the threshold energy at which the emission starts (figure 6.16). For example, for fused silica ($n=1.45$) Cherenkov emission starts at a relatively high muon energy of ≈ 36 MeV, and for BGO ($n=2.1$) only ≈ 14 MeV, as shown. For comparison the light yield from electrons and muons in a flat fused silica window, figure 6.19, was plotted.

Electrons of the same energy as the muons will have greater emission angles and yield due to their lighter mass and hence greater velocity.

6.7.3 Maximising escaping muon Cherenkov photons

During the preliminary work carried out at the detector design, two types of geometry were examined initially: a flat fused silica window and a tilted sapphire window (to increase the number of escaping photons) (figure 6.18). Fused silica was chosen due to its high transmission, low cost and off-the-shelf availability. Sapphire was also chosen for the tilted design investigation due its relatively high refractive index and thus low emission threshold and high light yield.

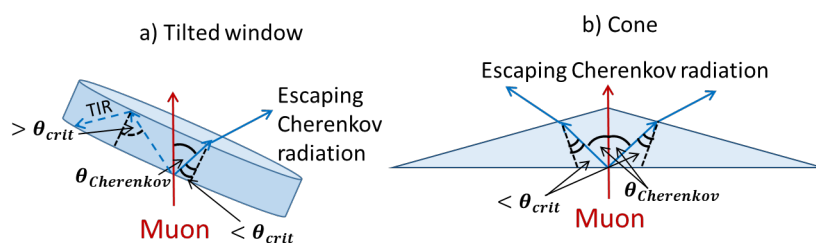


Figure 6.17: Tilt plots. For higher refractive index materials, tilting could be used to maximise escaping light (a)). To further maximise escaping photons, use symmetrical-cone design as shown in b).

A flat tilted window, or a cone could be used (figure 6.17). Using a flat window, approximately half of the emitted photons would be lost due to the angle inside becoming larger than critical (left hand side). In the fused silica case in figure 6.18 a) photons from up to 130 MeV muons are able to escape. In b) a sapphire cone design is depicted, where photons from muons up to 100 MeV can escape. This is good news, but the light cone emerging from the sapphire will be highly divergent, which would cause difficulty in detecting the light. The figure also shows the electron Cherenkov (red lines). The majority of it will be trapped inside in the fused silica, except for the very low energy electrons 0.175 MeV. This is not an issue in this case, as the energy region of interest is high energy muons ≈ 100 MeV, for which co-propagating electrons are of much higher energy. In the conical sapphire case, some Cherenkov due to very low energy electrons escapes, but is not relevant to the energy range of interest in this

study.

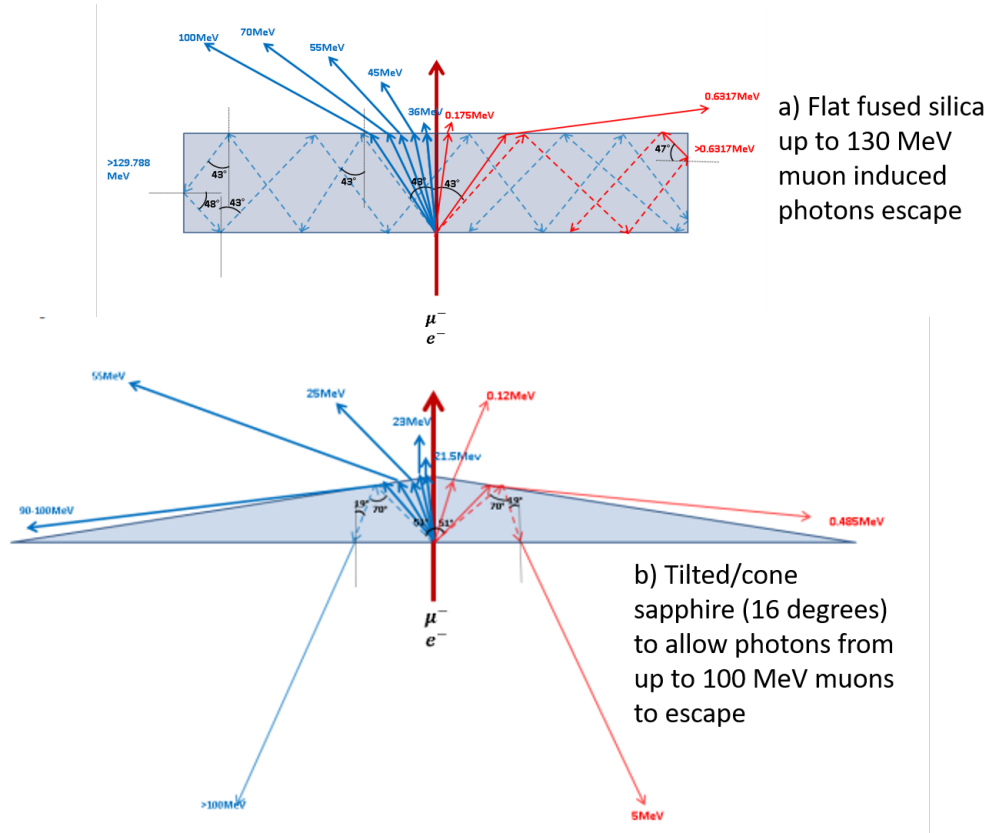


Figure 6.18: For higher refractive index materials, tilting could be used to maximise escaping light (a)). To further maximise escaping photons, use symmetrical-cone design as shown in b).

It can be seen in figure 6.19 that >0.1 MeV electrons in fused silica will start to generate Cherenkov photons, and >0.1 MeV will emit photons that will be totally internally reflected in the flat sapphire window. Only photons due to muons that are below ≈ 35 MeV will escape. With a tilted window photons from muon energies up to 100 MeV will be observed. However we only see less than half of the total yield due to the total internal reflection occurring on one half of the window. The angle of Cherenkov emission on the escape side is allowed to be larger due to tilting and this is why more photons are able to escape. However, the opposite happens on the other side – the angle of emission is such that the light is incident upon the glass-air interface at an angle larger than critical and is totally internally reflected. For this reason a conical

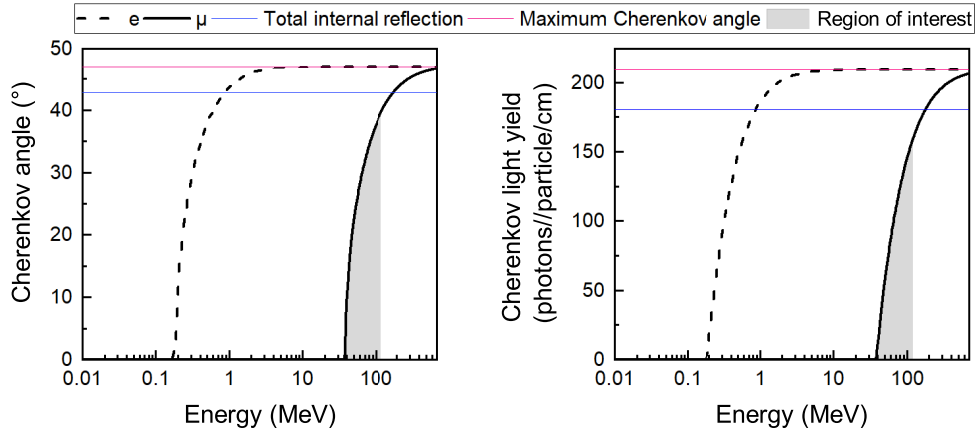


Figure 6.19: Cherenkov emission angle (left) in flat geometry and light yield dN/dx (right) due to electrons (e) and muons (μ) in fused silica for wavelengths 350-500 nm. Blue line marks the critical angle at which total internal reflection will occur, and the pink line shows the maximum Cherenkov emission angle. Grey area is the region of interest (20-120 MeV). Total internal reflection occurs at angle $\approx 43^\circ$ equivalent to 0.87 MeV electrons and 175 MeV muons.

surface geometry was proposed, which will allow photons on both sides to leave if the muons strike it approximately in the centre. The difficulty with this arrangement is the capture of light. The light cone refracting at the medium-air interface will spread even more, requiring a very large collection/focusing optic. This design introduces difficulty because due to the conical shape, high energy muons would cause the Cherenkov rays to refract at such large angles that the Cherenkov outgoing beam is not forward directed anymore, making it more complicated to detect.

The region of interest is highlighted in grey in figure 6.19. The muons generated using current Gemini laser parameters will be within this energy range. It shows that the majority of electron photons will be internally reflected. The sapphire window plane can be tilted in such a way that the electron Cherenkov photons remain in total internal reflection, whilst the number of escaping muon Cherenkov photons is increased. Co-propagating electron Cherenkov emission angle will be 34° and larger, meaning that the angle of incidence at the sapphire exit boundary will be 34° (larger than critical

angle – total internal reflection occurs).

θ_{tilt} is the maximum tilt angle before electron Cherenkov light starts to escape, once the angle that it strikes the Cherenkov medium at is large enough (all angles are measured from the normal), $\theta_{cherenkovmax}$ is the maximum Cherenkov emission angle and θ_{crit} is the critical angle in the material (when the refraction angle is 90°). The optimum tilting angle may be smaller than this angle, depending of the range of muon energies that are relevant.

The maximum tilt angle for sapphire is $\theta_{tilt} = 21^\circ$, and can be calculated for other materials using the following:

$$\theta_{tilt} = \theta_{cherenkovmax} - \theta_{crit} \quad (6.12)$$

The maximum angle at which the surface of the Cherenkov medium should be tilted to internally reflect the electron Cherenkov photons is given by Equation 6.12. The reason for tilting the surface is to allow escape of photons which were created by the higher energy muons. A flat geometry does not allow a very large range of energies since a significant amount of muon photons are reflected. Though we know the maximum allowed tilt, due to the limited predicted muon energy (up to 100 MeV), this angle can be less.

6.7.4 Muon Cherenkov light collection and detection

The thickness of the Cherenkov radiator window has to be sufficiently large to obtain an adequate number of Cherenkov photons produced by the charged particles, which in this case, are the muons. The charged particle passing through a dielectric medium will continuously emit Cherenkov photons and therefore the number of Cherenkov photons produced is proportional to the thickness of the radiator. Due to the limited size of the active area of the detector, the size of the Cherenkov ring formed must be considered. The size of the ring can be calculated using the Cherenkov emission angle and the distance to where the ring is being imaged.

Unfortunately, as a consequence of a limited electron beam energy and thus lim-

ited yield of muons, we will have a less than desirable number of Cherenkov photons produced. This means that the detector has to be placed as close as possible to the Cherenkov medium window to ensure that as many photons as possible are collected.

The detector should be located in a position along the angle of maximum emission. For example, if the distribution of muons produced in the experiment peak at say 25 MeV, then the Cherenkov photons will be emitted at 37° , and the detector should be positioned accordingly to collect them.

Alternatively, mirrors can be used to collect the light and focus it to a smaller area. This would maximise the number of muon Cherenkov photons incident onto the detector. Collecting as many photons as possible is critical due to the scarcity of muons (and hence muon Cherenkov signal). There will likely be bremsstrahlung x-rays produced in the Cherenkov medium. The majority of detectors are not immune to all particles and radiation meaning extra noise is introduced, making it nearly impossible to discriminate against and be confident that the detected signal comes from a muon and not a different particle/radiation. This drove the development of the muon Cherenkov detector. Using a mirror would be advantageous as it will allow us to collect the muon Cherenkov light emitted in the medium window and deflect it to the detector which would be put in a desirable position. The mirror will reflect visible photons, and depending on the type of coating used, UV photons. However it will not reflect x-ray photons (from bremsstrahlung) as they would travel through the mirror. This also applies to UV radiation for most mirrors, however, applying different coatings can enhance their ability to reflect. For example, a UV enhanced Aluminium mirror is able to reflect 250-600 nm wavelengths with 90% average reflectance. This method is also advantageous as it would allow to shield the detector from background noise to guarantee that the detector only records the Cherenkov photons emitted by the muons.

6.7.5 Muon energy loss in fused silica

To avoid complex geometries at the initial stages of the experimental campaign on muon generation, it was decided to employ a flat fused silica window and the design of the diagnostic was based on this material. The aim was to detect high energy muons (100

MeV), and for this energy fused silica is a suitable radiator due to its threshold energy and large critical angle, while also being widely commercially available for a low price. The Stopping and Range of Ions in Matter (SRIM) simulations [164] were performed to determine muon energy loss in a given thickness of fused silica. Muons behave as light protons therefore this programme is suitable to use. Muon energy loss is mainly by ionisation up to very high energies (GeV). The energy loss causes the emission angle at the entrance boundary to be different (larger) than the exit boundary, meaning that there will be an angular spread as the rays exiting the Cherenkov radiator.

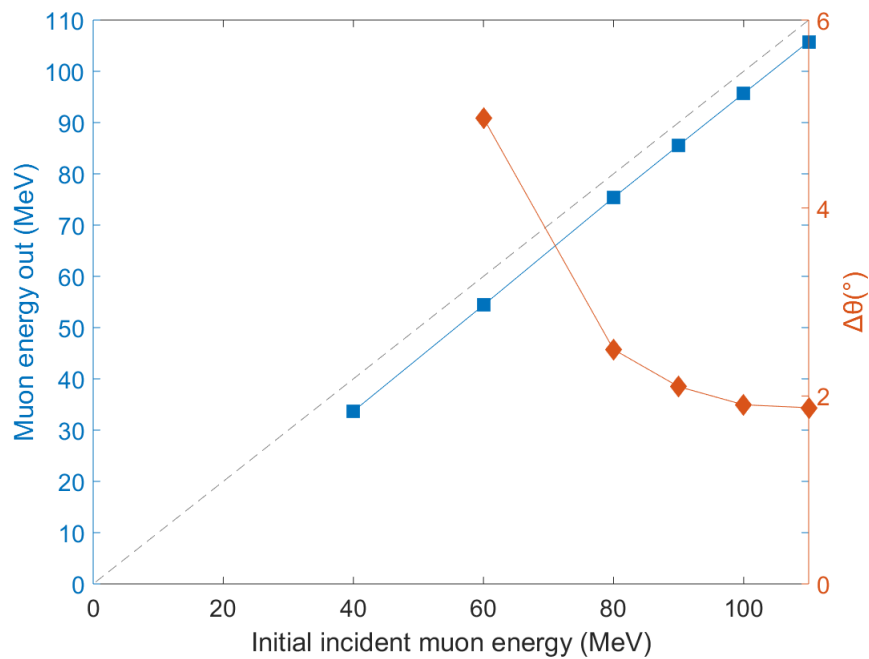


Figure 6.20: Graph showing muon energy after 1 cm travel through fused silica in blue and the difference in exit angle due to energy loss in red vs. initial muon energy.

The energy of a muon after travelling through 1 cm of fused silica as a function of its initial energy is shown in figure 6.20. It can be observed that the muon energy loss is relatively small and decreases as the incident energy increases. Even though the energy loss is small, it will have imperative effects in the light collection stage. The Cherenkov exit angle spread between the initial and final energies, $\Delta\theta$, is plotted on the secondary y-axis (orange). The difference in the angle is large for low muon energies and decreases

as the energy increases. A 100 MeV muon will lose approximately 4 MeV; $\Delta\theta$ is 2° . The energy loss and consequently the angular spread can be reduced by reducing the thickness of the Cherenkov radiator, however that would be unfavourable due to the reduced light yield.

6.7.6 Angular dispersion correction

A Cherenkov emission spectrum has a broad wavelength range, with a peak in the UV region and tails off into the visible part of the electromagnetic spectrum. The refractive index of a material changes with respect to wavelength which causes Cherenkov emission at different angles for a given energy muon. The Cherenkov exit angles (note that the exit angle is the angle of refraction at material-air boundary) are plotted against wavelength for 60, 80 and 100 MeV muons, in figure 6.21.

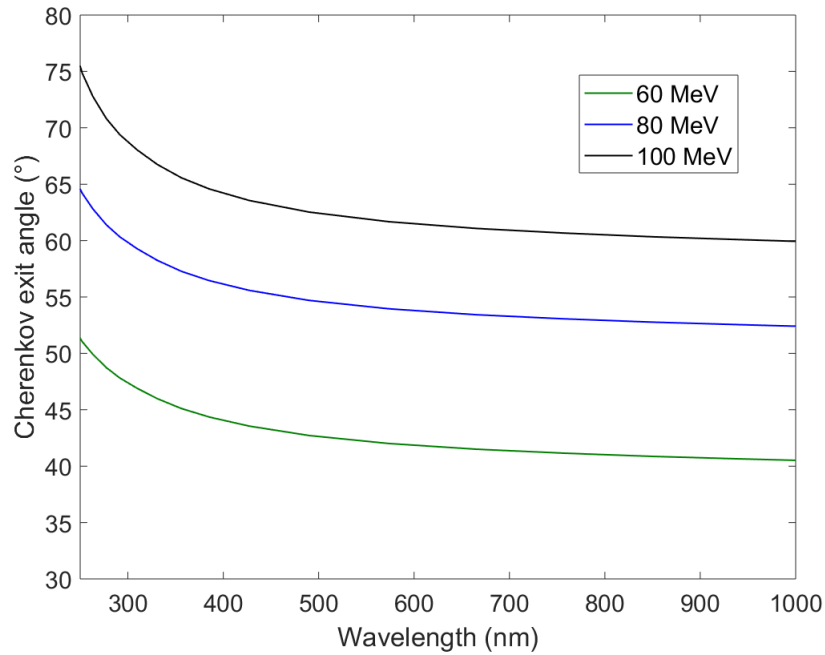


Figure 6.21: Plot showing the dependence of the Cherenkov light exit angle upon the wavelength of light. The dispersion is greater for shorter wavelengths. The region of interest is 380-700 nm. 380 nm is the lower wavelength cut-off for transmission in PMMA (prism), and beyond 700 nm Cherenkov emission is minimal.

In order to make light collection and focusing more effective, it was important to

minimise the spread of angles due to the chromatic effects. The use of a dish reflector was considered in order to direct the light emitted at an angle. However as a result of a relatively large spread, it would not be possible to produce a small detectable focal spot. In consequence, it was proposed to design a circular prism for chromatic angular dispersion correction. The aim was to model the prism such that the angular spread due to Cherenkov emission at different wavelengths is minimised. It is required that the rays leave the prism at an angle close to the vertical and travel onto an off-axis 90° parabolic mirror which will focus them to a small focal spot. It was found that a 77° angle of a prism made from plastic is optimum to fulfil those requirements. The off-axis parabola is aluminium coated and is able to reflect the entire wavelength spectrum that is expected to be generated.

The light will be focused by the parabola and imaged by an EMCCD (electron multiplying charge coupled device) detector for extremely low level light detection. A schematic of the detector is presented in figure 6.22. All the parallel travelling rays will be focused to a diffraction limited spot. The rays reaching the parabola at a different angle will not focus in the same position causing the ring shaped spot to be larger. A small focal spot is required due to low photon flux as well as high cost and limited size of available EMCCD detectors.

6.7.7 Final optimised detector design

The final design comprises a fused silica Cherenkov radiator, circular prism, off-axis parabolic mirror and an Andor Neo EMCCD detector (see figures 6.22 and 6.23). As a muon(s) traverses the fused silica, it will induce Cherenkov radiation which is emitted in a cone. The light rays will then refract leaving the glass and enter the prism. The prism will collimate the light rays, and as they leave they will be travelling approximately vertically. They will then be incident onto the off-axis parabola and focused to a spot on the EMCCD. The whole assembly is placed in a blackened steel box with only a hole for the Cherenkov radiator. Lead shielding is used to protect the camera chip from direct radiation.

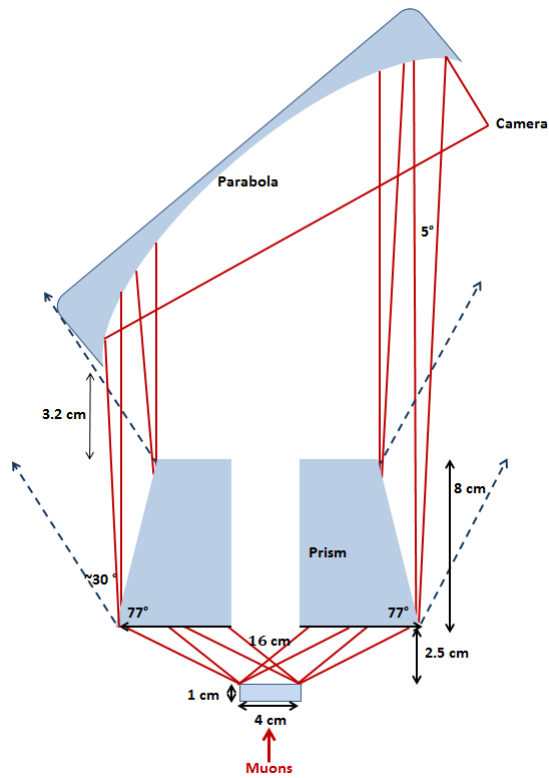


Figure 6.22: A schematic of the detector. It includes the 1 cm thick and 5 cm wide fused silica window as Cherenkov radiator, a 77° circular prism for correcting chromatic dispersion and an $f/0.6$ 90° off-axis aluminium coated parabolic mirror for focusing the light onto the Andor iXon EMCCD camera chip. Note that the prism has a 5 cm wide hole (filled with black nylon) in the middle to prevent more radiation being created inside it. The blue dashed lines represent Cherenkov radiation due to co-propagating electrons, which is emitted such that it misses the mirror.

6.8 Muon Cherenkov detector testing in ISIS facility

6.8.1 Experiment description

An experiment was carried out at the ISIS muon source [20] to test the muon Cherenkov detector described in section 6.7. ISIS is a pulsed neutron and muon source based on spallation reactions, located at the Rutherford Appleton Laboratory. Firstly, proton bunches are accelerated in a synchrotron to 800 MeV, with bunch frequency of 50 pulses per second. They are diverted to a target station, where the proton beam collides with a thin carbon target. The protons strike the carbon nuclei atoms, resulting in the

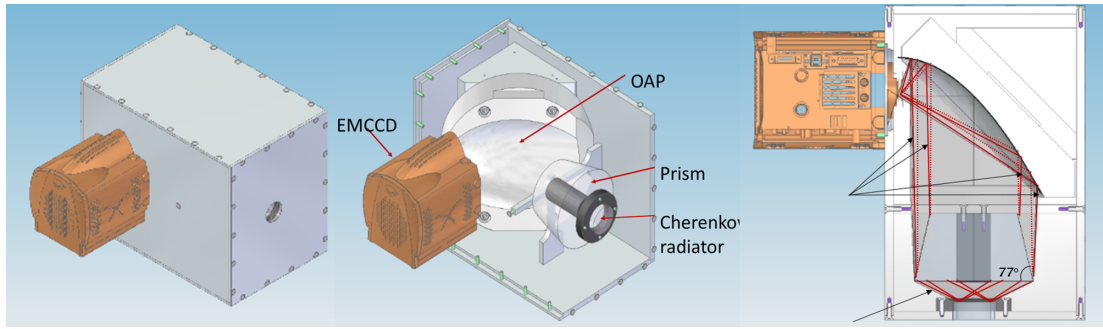


Figure 6.23: Drawing of the detector set-up. A fused silica cylinder at the front entrance for Cherenkov radiation, the prism for angular dispersion correction, the parabola for focussing and camera for light recording. The system is enclosed in a light tight black metal box.

emission of a neutrino and a pion. This is known as a spallation reaction. Pions are exotic particles which are unstable, and decay into muons (equation 6.13) after a short time, with a mean lifetime of 26 ns. The resultant muons are directed into the many muon experiment areas of ISIS.



The original muon Cherenkov detector design uses a fused silica window, however during this run it was replaced by sapphire due its lower Cherenkov threshold energy (21 MeV). The muon Cherenkov detector was placed in front of a 2 cm wide muon beam pipe. The muon bunches arrive in 70 ns long pulses, with a flux of approximately $1 \times 10^{6-7}$ muons per minute. The muons were incident onto the sapphire window acting as a Cherenkov medium, covered with black cinefoil to prevent light leaking into the system. The camera exposure time was set to 60 s. The muon energy range at ISIS is from 3.4 to 33 MeV. An energy scan was performed where the normally incident muon energies were varied between the minimum of 3.4 MeV and the maximum 33 MeV. This was done to investigate the cut-on of the Cherenkov emission and changes of light yield and beam profile with energy. In addition, data for 33 MeV muons with flux reduced to 50% was taken, to study the yield. The diagnostic was also tilted by 26° in order to

examine the angular dependency.

6.8.2 Results

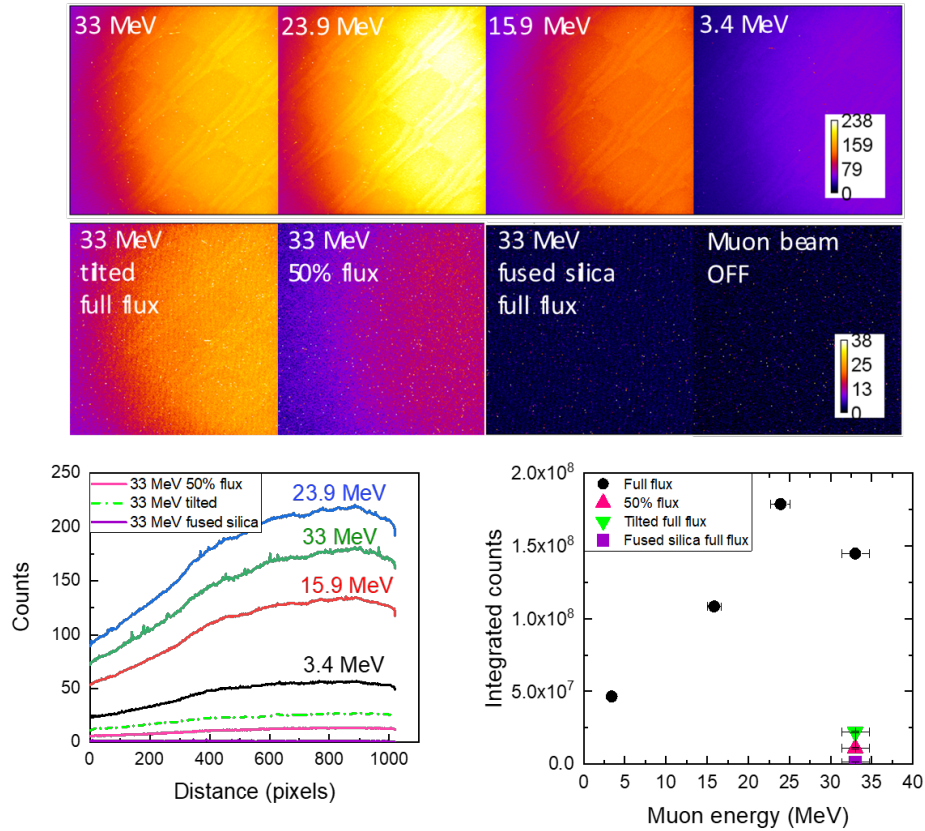


Figure 6.24: Data images obtained on the iXon EMCCD detector for different muon energies ranging from 3.4 MeV to 33 MeV. Data was taken with the muon flux reduced by 50% and with the muon beam off for reference. Horizontal lineouts of the beam profiles are plotted.

The integrated density for the full flux muon beam increases up to muon energy of 23.9 MeV, and then drops for 33 MeV, as shown in the image montage at the top and plot of integrated counts at the bottom right of figure 6.24. Let's recall that Cherenkov light yield is proportional to charged particle energy (and number of particles), but not necessarily to the deposited energy within the material. Scintillation on the other hand, is proportional to the amount of energy deposited by the particles.

SRIM simulations were conducted to investigate the energy deposited in 8 mm of

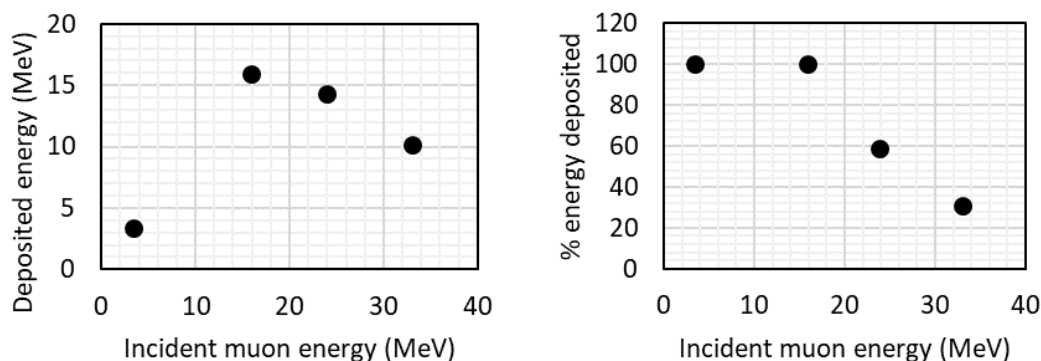


Figure 6.25: SRIM simulations of 3.4 MeV, 15.9 MeV, 23.9 MeV and 33 MeV muons in 8 mm sapphire.

sapphire for the energies: 3.4 MeV, 15.9 MeV, 23.9 MeV and 33 MeV. 3.4 MeV and 15.9 MeV muons deposit all of their energy in the sapphire (shown in figure 6.25). A portion of the 23.9 MeV muons are energetic enough to go all the way through the material; 60% of the initial energy is deposited. The 33 MeV muons deposit even less energy – only 30%, due to less interactions with the sapphire molecules. Going back to the experimental data to compare, we see that the trends are alike for the two low energies. However, 23.9 MeV shows an increase, which may indicate that a combination of light emitting processes are taking place, one of which could be Cherenkov radiation. Note that the threshold energy for Cherenkov emission in sapphire is 21 MeV, so this is a reasonable explanation. The drop in the integrated counts for 33 MeV muons may be due to the fact that as the energy of the muon beam is increased, the flux is reduced. Thus, if the number of the muons is less when the energy is 33 MeV, then the number of Cherenkov photons produced is also less.

The detected counts for the diagnostic assembly tilted to 26° (figure 6.24) (tilted sapphire window) are much less than the number of counts for normal incidence of the muon beam onto the sapphire. This is good evidence that the light emission in this experiment is not entirely due to scintillation which is omnidirectional. The amount of light detected should be the same. Tilting will alter the sapphire-air exit boundary orientation, which in turn will cause some of the emitted Cherenkov light to be totally internally reflected and will not reach the detector (approximately 0.5 of the normal

incidence case). When the flux of muons was reduced to 50% for the same energy, a very low amount of light was detected, which is unexpected. Due to the many setting changes to deliver the experiment, it is possible that a mistake in the setup was made leading to this anomalous result. The time access for the experiment enabled for measurements to be made for one afternoon, and due to this it was not possible to repeat the measurement and ensure reliability. If the emitted light was entirely scintillation, one would expect the integrated counts to be half of the normal incidence full flux case. Similarly, you would expect to half the Cherenkov signal.

It was expected that if this is indeed Cherenkov light, the beam-profile radius would be reduced for lower muon energies due to smaller Cherenkov emission angles. For example, beam radius of the light would be smaller for 23.9 MeV than 33 MeV. In addition, the emission would be cut off for muon energies lower than threshold for Cherenkov production. Nevertheless, there is no change either in beam-profile width, nor the disappearance of light below the Cherenkov cut-off energy (21 MeV). Due to short facility access time it was not possible to implement techniques to distinguish the two types of radiation.

The sapphire window was swapped with a fused silica window to investigate whether it possesses scintillating properties. The threshold energy for Cherenkov production in fused silica is 36 MeV which is greater than the maximum achievable muon energy in ISIS. Maximum muon energy (33 MeV) (purple curve in figure 6.24) and the minimum (3.4 MeV) were used. No light was observed in either instance. This result shows that fused silica does not scintillate for this range of muon energies. This makes it desirable due to close to none or little pollution in the detected signal due to scintillation. Limited muon energies did not allow to test for the switch on of Cherenkov radiation and potential scintillation properties caused by higher energies of muons.

To ensure that the light definitely came from the sapphire or fused silica windows, and was not produced by the positrons (which may be present in the arriving muon beam) in the PMMA prism, the maximum muon energy test was also run while having the window covered with black aluminium Cinefoil to stop the light from reaching the camera. No radiation was detected confirming that the light originates from the

Cherenkov radiator windows.

The sapphire used during the experiment on ISIS was later exposed to a Na-22 radioactive source which emits 511 keV x-rays with activity of 1.21×10^5 Bq (100 000 photons per second), to check for scintillation. Light was detected on the camera, which is indicative of sapphire having scintillating properties when irradiated with high energy photons. This means that the ISIS experimental results may have a significant scintillation component, and the light detected is a combination of both scintillation and Cherenkov radiation.

In order to distinguish between the two (or possibly more) types of radiation, a wavelength and temporal spectra should be measured using x-rays, as well as muons (or relevant energy electrons), and compared. In the x-ray scenario, no Cherenkov will be present and thus these spectra can be subtracted from the combined signal using charged particles. The timescales of the experiment did not enable us to implement this. Also the current imaging spectrometers require a very bright source for wavelength spectral measurements, likely brighter than was achieved in this campaign.

Further work to improve knowledge and understanding is required. Firstly, the sapphire scintillation spectra as well as temporal properties by exposing it either to charged particles which are below the Cherenkov threshold energy, or to x-rays. Secondly, a similar experiment could be performed again employing a spectrometer to measure the wavelength spectra of the detected light. These could then be compared; subtract scintillation spectrum from the total signal, which would leave the portion of the signal that is Cherenkov.

6.9 Summary of the muon Cherenkov detector

Muon detection utilising Cherenkov radiation was identified as a detection technique. Several materials were studied, namely fused silica, BC422Q, sapphire and BGO, in order to determine which material is the most suitable to use as a Cherenkov medium, in order to detect the photons produced by the muons with energies <100 MeV in a laser plasma experiment. Cherenkov yield increases with refractive index, however the

critical angle also increases, preventing the photons from exiting the medium. Tilting of the Cherenkov medium was considered in order to increase the number of escaping photons. Fused silica is readily available, has a reasonably high refractive index and does not require tilting. 100 MeV muons produce photons that will escape, and fused silica was therefore chosen as the Cherenkov radiator for the initial detector design.

High energy secondary particles and radiation will be present in a laser-plasma interaction. A magnet will be employed to deflect the charged particles, while the neutral particles and high energy x-rays will continue in the forward direction. However, a significantly large number of co-propagating electrons will remain. The co-propagating electron energies were calculated to be ≈ 180 MeV for 100 MeV muons. These are capable of producing electron Cherenkov radiation in the medium within the muon Cherenkov diagnostic. The resultant Cherenkov emission angle will be greater than critical, and thus the photons will be totally internally reflected within the radiator and not escape.

The problems inherent to the Cherenkov mechanism include the angular spread of outcoming light caused by muon energy loss traversing the medium, and the dispersion due to broad wavelength spectrum of Cherenkov light. The thickness of the Cherenkov radiator was optimised taking into consideration the muon energy loss and the light yield. A circular prism was designed to compensate for the chromatic dispersion and minimise the angular spread of the light in order to focus it to a small ring on to a sensitive EMCCD detector.

The diagnostic was deployed in an experiment using the Gemini laser, where the electron beam reached energies of 1.5 GeV. While this is sufficient to produce muons in a converter target, the muon numbers would be low in comparison to other secondary particles, making it complicated to detect. Higher beam energy and charge would increase the muon flux, their energy and directionality, and would increase the chance of detection.

The muon Cherenkov diagnostic was tested using the muon beam at the ISIS neutron and muon source. The maximum available energy is 33 MeV. Fused silica has a Cherenkov threshold energy of 35 MeV, and thus it was replaced by sapphire, which

has a higher refractive index and therefore lower threshold energy. A muon energy scan was carried out to investigate the light yield. The energies ranged from 3 MeV (well below the threshold) to 33 MeV. It was discovered that scintillation is also present in sapphire, as the light emission was detected for energies below the Cherenkov threshold. This rules out sapphire as a potential Cherenkov radiator. It is likely that the signal was a combination of both Cherenkov radiation and scintillation however without having been able to measure the spectra of emission or apply fast gating, it is difficult to draw a clear conclusion.

Due to the encountered issues and challenges, it was decided to simplify the design and study the Cherenkov mechanism using an electron beam.

6.10 Electron Cherenkov radiation generation and measurement in Gemini laser facility

6.10.1 Experimental method

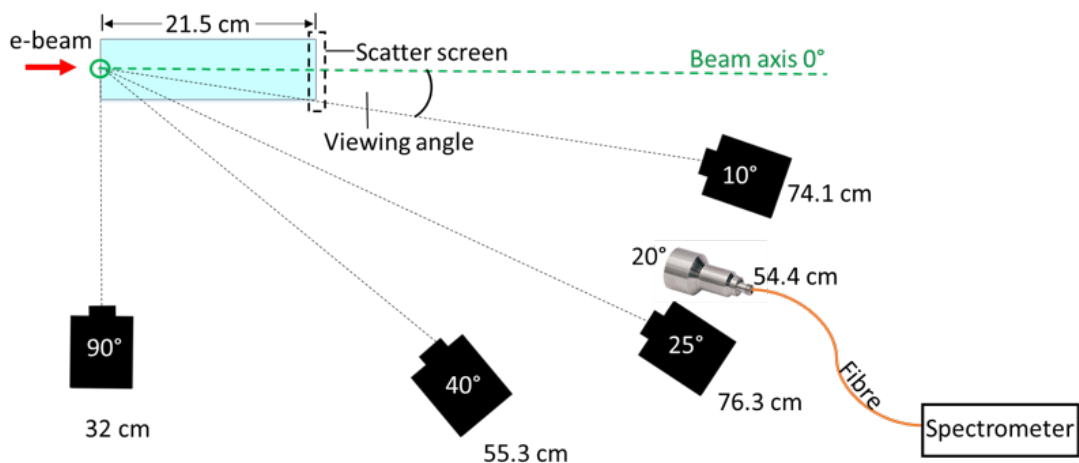


Figure 6.26: Top view diagram of the experimental layout. The four cameras used are Andor Neo, and were located at angles and distances shown next to them, measured from the beam axis (0°), and the reference point is the start of the fused silica cylinder (marked with green circle). A fibre optic with a collimating lens was also used coupled to an Andor Shamrock imaging spectrometer, to measure the spectrum of the light unsuccessfully.

Given the insights and the challenges that were realised in the first experiment to detect muons during the ISIS experiment, it is clear that further work was needed to understand the detection of Cherenkov radiation in a high background environment. To this end, an experiment was conducted using the Astra-Gemini laser Target Area 3 (TA3). A gas cell target was irradiated by an f/40, ≈ 40 fs high intensity 800 nm laser pulse. The focal spot size was of the order of a few tens of μm in diameter (FWHM) and the gas pressure was 320 mbar. The energy after the compressor onto gas target ranged between approximately 8 J and 12 J. Four energy settings were used which had average energy values of 12.3 ± 0.4 J, 11.2 ± 0.3 J, 10.1 ± 0.2 J and 8.4 ± 0.3 J. The radiator used for Cherenkov light generation was fused silica cylindrical block with one smooth base and the second base and the side walls were ground glass scatter screens.

The light emitted in the fused silica was measured on both, the exit scatter screen and the smooth side base. However, it was assumed that most of the radiation would travel in the forward direction, and therefore the results discussion is focused on the scatter screen measurements. Four Andor Neo CMOS cameras were used, utilising their high dynamic range and low noise. Those were located in four different positions (or viewing angles) with respect to the electron beam axis. A top plan view of this set-up is demonstrated in figure 6.26 and indicates the electron beam axis, the distances of each camera from the origin reference point (marked with green circle), as well as the viewing angles. The distances of the cameras were: 74.1 cm, 76.3 cm, 55.3 cm and 32 cm, and the respective viewing angles – 10° , 25° , 40° and 90° . An optical fibre was placed at 20° and fed through to an Andor Shamrock imaging spectrometer in an attempt to record the wavelength spectrum of the light. However, the losses induced by the collimator and the fibre potentially proved too great for the spectrometer to pick up enough signal. An x-ray scintillator detector was also placed in the target area to monitor background x-rays. It was positioned off-axis ≈ 2 m from the chamber kapton window. A correction factor was applied to the Neo data for normalisation, given the different distances and camera lens settings. Light shielding consisted of black cinefoil and was placed around the system and in front of reflective surfaces to reduce light leakage.

The electron beam exits the vacuum chamber through a thin kapton window and is incident onto the fused silica cylinder. The relativistic electrons travelling faster than the speed of light in the fused silica emit Cherenkov radiation (section 6.6) in a cone with a half angle given by Equation 6.3. A brightness correction test was performed in order to compare the apparent brightness of the cameras. This is taken into account and correction factors are applied for data captured on each detector. The prime goals were to record the angular distribution of the light and to gain insight into this technique in order to improve and deploy in future campaigns.

6.10.2 Experimental results

The experiment was aimed at detecting Cherenkov light emitted in a block of fused silica and to study the angular profile and gain deeper insight into the mechanism, as this technique would be almost immune to EMP which can be a significant issue when trying to evaluate beam charge. The goals were to investigate the effect of varying laser energy onto gas cell target and hence changing the electron beam energy, on the number of detected photons and the angular distribution. The amount of light at different viewing angles was recorded, and the angular profile on the end scatter screen was measured. Additional x-ray measurements were performed to show a correlation between the detected Cherenkov light and detected x-ray signal. On average the maximum electron energy reached was ≈ 600 MeV. We can see in figure 6.27 plotted using ESTAR NIST database, that 600 MeV electrons have a range of ≈ 30 cm. Of course, the electron spectra are not completely monoenergetic and there will be electrons of lower energies present with shorter range. The high energy portion of the beam will survive the whole length of the fused silica block, while lower energy parts will only travel some distance before stopping. This means that more light is being emitted the closer towards the front of the fused silica block. A montage of data for different viewing angles and laser energies is shown in figure 6.28, where the dimming of the light beam is apparent.

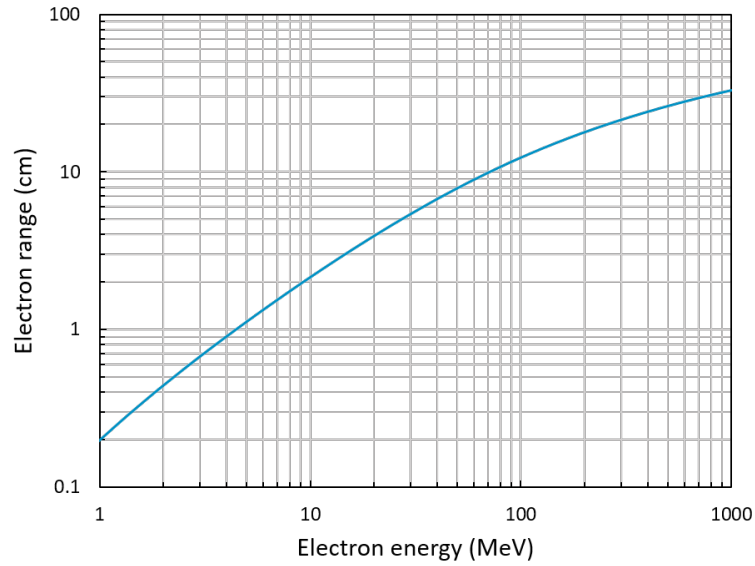


Figure 6.27: Electron range in SiO_2 as a function of incident electron energy. Range calculated from ESTAR NIST database.

Cherenkov radiation as a function of laser energy at different viewing angles

To investigate the relationship between laser energy and Cherenkov intensity, a laser energy scan was performed. The laser energy was varied from ≈ 12.3 to ≈ 8.4 J. A montage of typical shots for different energies and viewing angles was shown in figure 6.28. A graphical representation of the data measured on the the exit scatter screen is displayed in figure 6.30. The integrated counts were averaged for each different laser energy, which determines the electron beam energy and charge, and plotted against it. Evidently the integrated counts are greater for higher laser energies, and the signal seems to be diminished for laser energies of approximately 8.5 J. The integrated count error bars are the standard deviation of the averaged data. Laser energy error bars are also the standard deviation of the averaged laser energies. This outcome is as expected – greater laser energy induces a greater wakefield electron beam charge and energy, which consequently increases the number of Cherenkov photons.

To help this and future studies, an absolute calibration of the scatter screen was carried out by Patel *et al.* [165] using the same fused silica block and a Neo CMOS camera. A laser of 1 mW power and 532 nm central wavelength was shone through

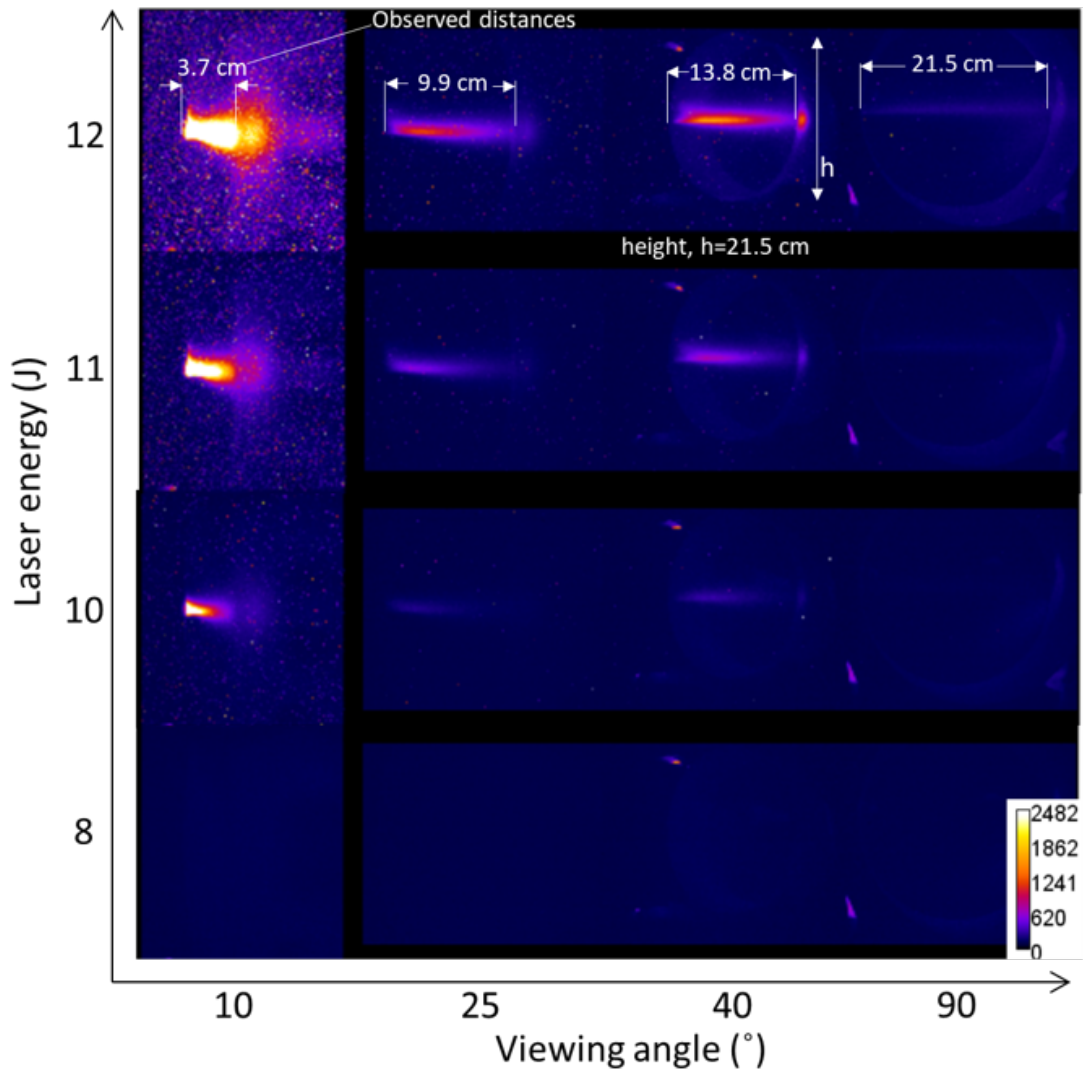


Figure 6.28: A montage of each camera images on shot. The images show data for the four viewing angles for 4 different shots where the laser energy was varied. The electron beam is incident from the left. Indicated in white are the observed distances of the cylinder from each viewing angle. The height, h remains constant.

the fused silica and the scattered light on the exit screen was measured. The number of photons, N_γ , incident on the scatter screen was calculated taking into account any neutral density filters used, and the plastic window transmission which was coupled to fused silica using a silica optical gel. In a similar setup as the TA3 experiment, images of the scattered flux of the laser spot were taken at various angles to normal (laser axis in the Gemini experiment), an angular distribution was produced, and number

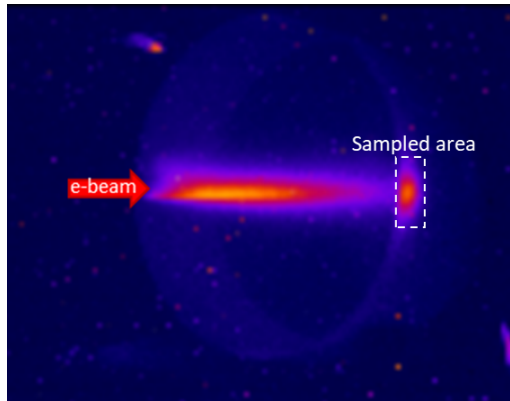


Figure 6.29: Dashed box indicates the sampled area which was used for the analysis. Background integrated counts were subtracted from the integrated counts of the sampled area.

of calibration photons, N_{counts} , calculated. The ratio of the number of incident laser photons to the number of counts determined from calibration, is applied to integrated counts of the experimental TA3 data, to yield an approximate number of Cherenkov photons, $N_{Cherenkov} = N_{\gamma}/N_{counts}$.

Patel *et al.* presents data plots showing the number of Cherenkov photons as a function of laser energy at three viewing angles [165]. The viewing angles used in these results are 14° , 34° and 50° , corresponding to TA3 angles 10° , 25° and 40° respectively. Here the correction ratio obtained from calibration measurements is applied to the TA3 experimental data. The calculated number of photons at the three angular positions agree well with each other. This outcome is expected, because the number of photons inside fused silica which generate the angular distribution pattern on the scatter screen remains the same, regardless of where the photon detector is placed. The results for the different angles were averaged, to produce a mean number of Cherenkov photons vs laser energy which is of the order of 10^{12} photons.

We can calculate the expected number of Cherenkov photons making some assumptions. There is currently no possibility to easily measure beam charge on shot, but typically the beam charge is of the order of several 100s pC. Although Cherenkov radiation has a broad bandwidth, not all of that light would have been detected due to the quantum efficiency curve of the Neo camera. It responds best to 500 nm to 700 nm

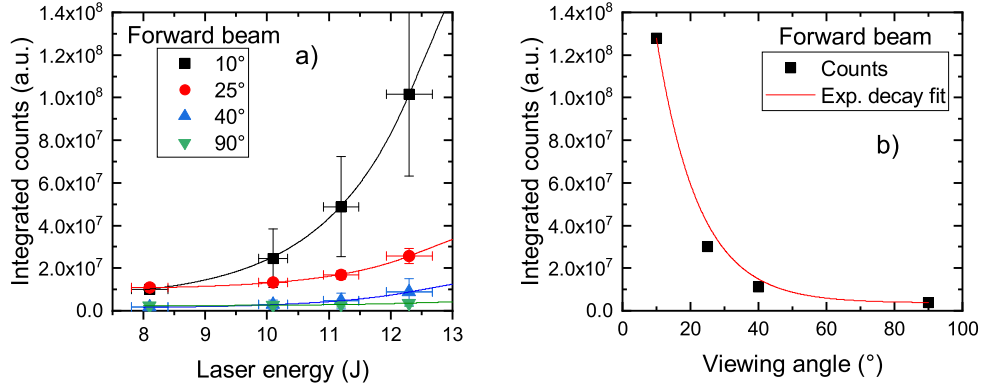


Figure 6.30: a) The integrated counts grow with increasing laser energy for all viewing angles with most pronounced signal measured by the camera situated at the smallest viewing angle, and lower signals for less narrow angles. b) Relationship between the forward beam integrated density and the viewing angle. The integrated counts are averaged over multiple shots with similar laser energies.

photons (Q.E. \approx 0.6), therefore the expected Cherenkov light yield was calculated using that range (Equation 6.5). The yield is of the order of 10^{12} and agrees well with the calibration results reported by Patel *et al.*. There is uncertainty in the yield calculation and scatter screen calibration results, as a wavelength calibration had not been carried out. However, there appears to not be unaccounted signal, which is a strong indication that this indeed is Cherenkov light.

It is more difficult to explain the results recorded on the smooth side of the fused silica block. The trend of integrated counts vs laser energy is similar to the scatter screen. According to initial calculations, simply using Snell's law, it was not expected for Cherenkov light from the primary high energy electrons to escape the side wall of the fused silica block. Cherenkov emission angle becomes maximum for electron energies as low as 10 MeV, i.e. $\theta_{cherenkovmax} = 46^\circ$ at $n_{fusedsilica}=1.45$ (at 500 nm). This means that the the angle of incidence on the side wall will be 44° which is equal to critical angle. However, Cherenkov radiation has an angular distribution width rather than a discrete emission angle, thus it is possible that a portion of light was able to escape. The light could also escape due to scattering effects of light within the the glass as well

as the surface if it is not well polished. However, no evidence of significant bulk material scattering was detected during the off line calibration tests, therefore eliminating this possibility.

GEANT simulations have confirmed that the primary electron beam ionises the material and some of the electrons in the glass block gain energy through collisions, producing secondary electrons. Those secondary electrons mainly travel in the forward direction due to conservation of energy and momentum. However, such electrons can emit Cherenkov light that would be forward biased but could readily escape through the side of the glass block. This is fully consistent with the camera signals and would also explain why the camera at 90 degrees to the glass block sees negligible emission compared to those in the forward direction.

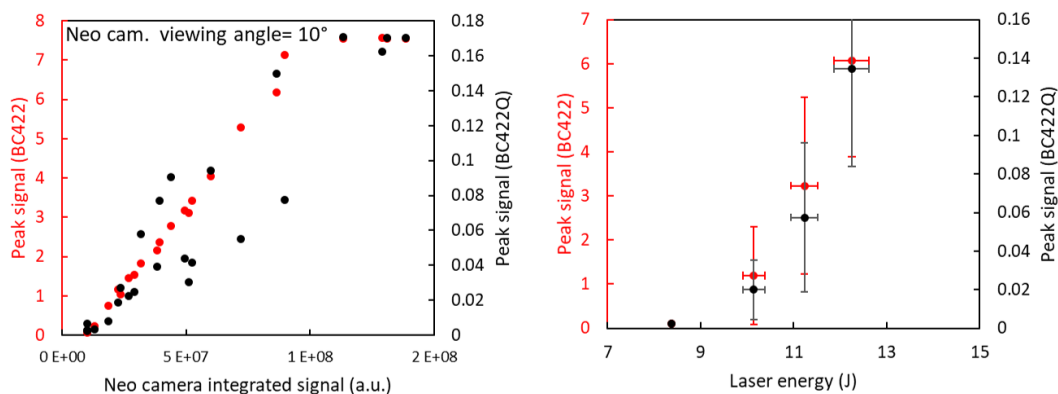


Figure 6.31: Doped (black) and undoped (red) scintillator peak signals plotted against integrated counts on Neo cameras (shown on the left). There is a linear like correlation between the two. Peak scintillator signals as a function of laser energy. Both undoped and doped scintillator peak signals grow with energy, analogous to the integrated counts on the Andor Neo detectors in figure 6.30.

Scintillation detectors for background/bremsstrahlung x-ray measurements were also run in parallel, namely undoped BC422 and doped BC422Q (0.5% benzophenone). They were placed approximately 2 m from the chamber window off-axis; the number of x-rays is expected to be correlated to the number of electrons generated. The scintillators were coupled to MCP-PMTs whose outputs were fed through to an oscilloscope where voltage traces were displayed and recorded. The peak voltages were

measured and are shown in figure 6.31. It can be seen that the scintillator peak signal is approximately proportional to the integrated counts on the Neo camera detecting Cherenkov. Doping (or quenching) increases the response time of the scintillator, yet the light output is significantly reduced. Hence the data for BC422Q is more scattered.

The similarity in the Cherenkov and scintillation intensity trends indicates that the number of generated wakefield electrons is proportional to the Cherenkov intensity at any viewing angle. Although current (or charge) monitor detectors currently exist and are being used in high current particle colliders, they are highly prone to EMP, making Cherenkov detectors advantageous due to being immune to EMP, which is present in laser-plasma environments. Although at high particle energies it is not yet possible to determine the energy spectrum, it can act as a relative charge monitor. The chamber window itself may act as a Cherenkov radiator and a camera can be used to measure the intensity of the signal in a similar manner that is presented here. This is useful due to the fact that the main electron beam diagnostic – the electron spectrometer, cannot be run during the shots on which data of secondary particles and radiation is taken.

Angular profile measurements

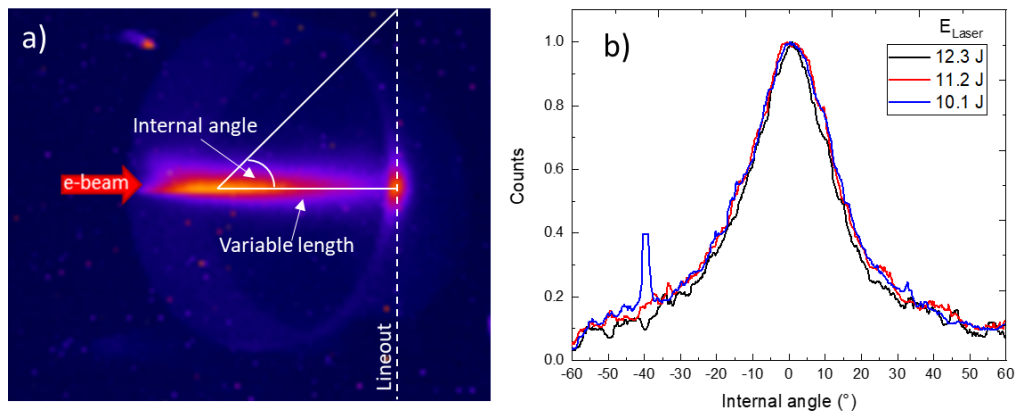


Figure 6.32: a) Vertical dashed line marks where the lineout was taken. The internal angles were measured from approximately the middle of the block (ie. 10 cm). b) Normalised counts as a function of internal angle are shown for different laser energies (viewed from 10°). No change in width is observed.

Vertical lineouts through the middle of the forward beam (on the scatter screen as shown in figure 6.32 a)) were taken to produce an angular profile of the light on the exit scatter screen surface. The internal angles were calculated using trigonometry measuring approximately from the middle of the fused silica block. This was done to give a more realistic representation as light is being created not just at the beginning of the fused silica but is being generated as the electrons pass through it. Due to the data on the camera being noisy, a median filter was applied to the data to smooth it. Figure 6.32 b) shows the profiles from 10° viewing angle for different laser energies. The laser energy does not appear to have an effect on the shape or the width of the beam profile. It is not too surprising, and could be explained by the fact that even though the laser energy is reduced, the numbers of generated wakefield electrons of sufficient energy is still large enough to produce light. For viewing angles 10° , 25° and 40° , the profiles are plotted in figure 6.33.

The beam profiles are centrally peaked and exhibit similar behaviour for all viewing angles. This is initially counter-intuitive as one may expect a ring like shape (3D) or a dip in the centre (2D), due to conical Cherenkov emission. Illustrated in figure 6.34 a) is the concept of a Ring Imaging Cherenkov Detector (RICH), common in high energy physics research. In this scheme, Cherenkov light is emitted in the radiator, the cone refracts as it exits into air and spreads, eventually being incident onto a photon detector array such as photomultiplier tubes (PMTs) or silicon photomultipliers (SiPMs). In the case of this experiment, where the detector plane is the scatter screen itself and is a part of the radiator, this may not be the case. The Cherenkov light would be emitted along the whole path of the beam but near the end of the block as the beam energy decreases, the emitted light would become more forward directed and hence lead to a centrally peaked emission. Unfortunately, as no simultaneous spectral measurements were possible, a detailed modelling in this case is not possible. Electron bunches created in laser-plasma experiments are multienergetic, which would also have an effect on the intensity profile.

Furthermore, the radiator in this case is very thick. This introduces effects of electron energy loss and stopping, which will affect significantly the number of photons

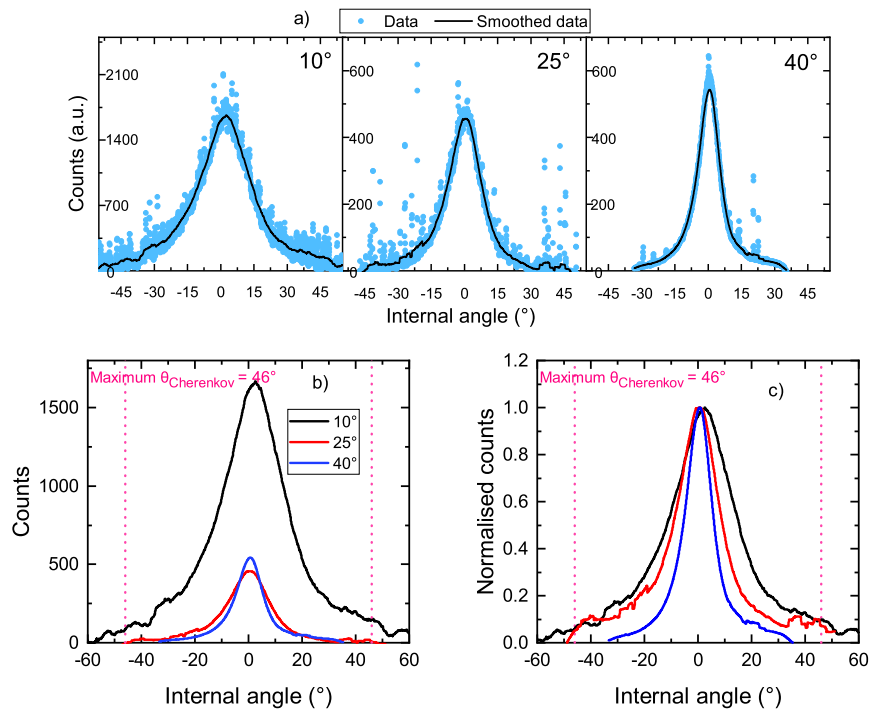


Figure 6.33: a) The angular profile of the forward beam as viewed from viewing angles of 10° , 25° and 40° . The beam is centrally peaked for all viewing angles. b) The smoothed data is presented on the same plot for comparison of brightness. The highest brightness was recorded on the 10° viewing angle camera. c) The smoothed data is normalised to 1 and peaks centered.

emitted and the emission angles at different points. The portions of the light cone which are incident in the direction of the curved surfaces will be scattered due to the ground glass surface and some may be internally reflected diffusely. The fact that the shape of the fused silica block is not symmetrical, makes it very difficult to model what the angular profile would be.

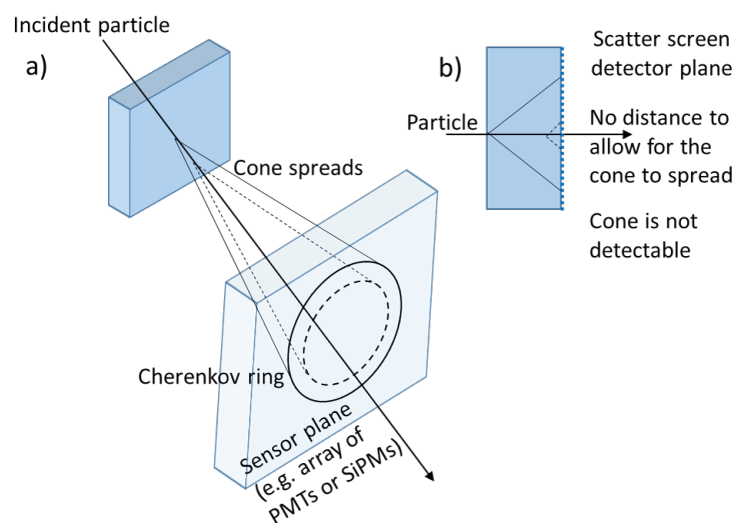


Figure 6.34: a) The concept of Ring Imaging Cherenkov Detector. Using this set up where the detector plane is some distance away from the Cherenkov radiator, a ring image with highest intensity at the edges is obtained. b) In the case of this experiment where the detector plane is the scatter screen, which is part of the cherenkov radiator, the ring (or diameter of the cone) is not able to spread, and thus the profile of this beam would not necessarily be a doughnut-like shape. Depending on the geometry and the size of the radiator many variants are possible. The radiator used in this experiment has a complicated shape which makes predicting the beam profile and confirming the mechanism/ source of the light extremely complicated.

Other potential sources of light

Scintillation was considered as a potential cause of the light emission, however it was ruled out because it would be isotropic. It does not appear to be omnidirectional in this data, rather it is beam like. Transition radiation is also not likely as the probability for x-ray creation for a single boundary thick glass block is very low. There is a lot of material to propagate through rather than to transition. It is emitted as a narrow cone whose half angle decreases for greater particle energies, and is hollow in the middle. However, this dip cannot be extracted from the experimental data in this chapter. It is either not present, or is masked by the other effects (e.g. Cherenkov from secondary scattered electrons). The transition radiation photon produced by electrons have wavelengths in the x-ray range, with energies typically in the range of 5 to 15 keV. The number of produced photons per interface crossing is very small. For particles

with $\gamma=2000$ about 0.8 x-ray photons are detected. 600 MeV electrons have a gamma factor of ≈ 1100 . Even if the probability for transition radiation photons remains the same, and all of the electrons in the bunch were 600 MeV, the number of photons produced would be of the order of 10^9 , which would not account for the number of recorded photons (after calibration). It is important to remember that the conditions are also not favourable for transition radiation to be produced due to a lack of multiple boundary materials with different dielectric constants. It is also likely that the high energy electrons traversing the fused silica would produce a forward going beam of x-rays, and these may produce some excitation, but again this would be expected to be isotropic.

Another potential source is photoluminescence (fluorescence or phosphorescence), where an electron absorbs a photon, enters an excited state becoming unstable, and re-emits a photon of longer wavelength (or lower energy). Although fused silica is very pure, defects still can be induced due to manufacturing process. Photoluminescence is a sensitive method for detection of defects. A number of studies have shown the detection of luminescence caused by defects [166–168]. A study by Fournier *et al.* showed emission at around 450 nm when irradiated by a 325 nm continuous He/Cd laser. Potentially the Cherenkov photons emitted are being absorbed by the electrons in the fused silica and re-emitted at lower wavelengths, making the detected light a combination of Cherenkov and photoluminescence. It would be useful to test the fused silica block with a second (400 nm) or third (200 nm) harmonic of the Gemini laser to check if any luminescence is recorded. This may give us an idea whether Cherenkov photons can induce additional light through luminescence.

Future work and implications for a novel muon detector

The experiment could be repeated with the radiator in a different orientation. For example, the electron beam incident on the smooth base of the fused silica cylinder. The signal would be recorded in a similar way on the exit base (scatter screen). This would make the analysis less complex and more accurate. In hindsight, it may be easier to use a very thin radiator, where particle stopping is less pronounced. This would

reduce the number of photons generated, but a shorter radiator would mean there would be no reflections and less losses inside and all of the signal would be incident onto the exit screen. If the electron beam is monoenergetic and of very high energy so that the energy losses do not significantly affect the Cherenkov emission angles, then a DIRC (Detection of Internally Reflected Cherenkov light) like method could be employed which utilises a long radiator, such as a bar with smooth surfaces, to totally internally reflect the Cherenkov light, which would exit at the end of the bar onto a photon detector. Alternatively, the end of the bar surface could be a scatter screen. This detection technique is more suited for charge monitoring applications rather than spectral measurements. It is simply not possible to effectively resolve the energy of the low energy particles because the Cherenkov emission angle changes very rapidly with energy and reach saturation at very low electron energies. Therefore the best use would be for measuring beam charge of monoenergetic electron bunches.

The most corroboratory and useful measurement which could be carried out in the future is detection of the emission wavelength spectrum. A sensitive spectrometer can be used for this. The previously employed spectrometer was an Andor Shamrock coupled to a fibre optic, however we believe that the losses in the fibre and the collimator were too great for the spectrometer to detect it. This could be redesigned to image by placing the Shamrock directly to where the light source is to increase the flux onto the spectrometer entrance slit. It is understandably not practical to have this running all the time, but a one off test to prove the concept would be useful. Cherenkov spectrum is broadband and most intense in the UV and blue and reduces as $1/\lambda^2$ into the red part of the electromagnetic spectrum. The spectrum obtained from the spectrometer could be compared to the known spectra as well as some recorded fused silica luminescence spectra to provide a more conclusive statement on the source of this light.

For more conclusive results, the spectral measurements with several materials should be carried out. In particular using materials with well known luminescence and scintillation properties. Tests could also be undertaken with different filters to block out unwanted wavelengths. Using materials with different refractive indices may reveal more angular information which may help confirm whether the radiation is Cherenkov.

6.11 Conclusions

Various particles are currently used for diagnostic and imaging purposes in medicine and industry. Some are better suited for particular applications than others. If available, a sufficiently strong muon flux can be used for security and defence purposes such as imaging large containers which may contain high Z prohibited nuclear materials at border control as well as inspecting nuclear drums containing spent nuclear fuel and interrogating power plant reactors for cracks and defects and as many others. Thanks to higher muon mass and penetrative capabilities, which is advantageous over using electron beams.

Laser driven wakefield electrons can be utilised to generate muons as theorised by Titov *et al.* and studied by Rao *et al.* [4, 169]. The properties of the muon beam can be tuned by changing the electron beam energy and converter target thickness. In thick targets a greater muon flux is created due to a higher number of electron-matter interactions as the electron beam traverses the material. However the thickness is limited by the stopping power of muons and eventually the flux will stop increasing. The electron beam energy has immense effects on the muon flux and directionality. For this method to become a viable application, electrons beams > 5 GeV and repetition rates of the order of a kHz would be ideal.

Cosmic ray muons are currently being employed in homeland security and imaging of large geological objects. However, data acquisition is very long due to low cosmic muon flux. Laser driven muons are becoming a reality with fast improving laser engineering technology and high energy electron beams. Laser wakefield produced muon energy is limited by the achievable electron beam energy. With future improvements, high energy muon beams may reach cosmic muon energies. Furthermore, this technique is of much smaller scale than spallation sources and potentially may become portable, thus the compact muon source could be taken to where it is needed instead of bringing the samples to laboratories across the world.

A large amount of secondary particles and radiation are produced in laser plasma interactions. Due to the lack of suitable diagnostics for this environment, a novel optical

detection technique based on Cherenkov radiation was studied and deployed. The diagnostic was developed for detection of high energy (100 MeV) muons in laser-plasma experiments. It was designed to be immune to x-rays, neutrons, protons and most importantly electrons. Electrons are discriminated against by utilising the total internal reflection of light in a medium as well as employing a high field magnet for deflection. This optical technique is also unsusceptible to EMP, which is of high abundance in laser plasma experiments and will become more problematic with increasing powers and repetition rates of new laser systems. It is not yet possible to produce a high enough flux good quality muon beams with current Astra-Gemini laser parameters, and so the diagnostic was deployed and tested in the ISIS neutron and muon facility at the Rutherford Appleton Laboratory and yielded interesting results. Analysis revealed that potentially the detected light is a combination of Cherenkov and scintillation. The Cherenkov radiator material used was sapphire, which prior to the experimental studies was not known to be scintillator, however light was detected below Cherenkov threshold. This confirmed that sapphire is not a good candidate for use as a radiator without being able to separate the scintillation and Cherenkov spectra. The same principle in a slightly different set up was used to detect Cherenkov light induced by high energy electrons in Gemini TA3. The prime aim was to test and gain a deeper understanding of this method as well as study the potential use as a charge monitor in laser wakefield experiments. The laser energy scan showed that the intensity of the detected light increased as laser energy increased. The results were also correlated with background x-ray signal and agreed well. A scatter screen was used to measure the angular profile of the emission revealing a Lorentzian like distribution. An absolute calibration of the number of photons was carried out post-experiment by Patel *et al.*. The number of photons from calibration were of the same order of magnitude as predicted by Frank-Tamm formula 10^{12} . This is a strong indication of Cherenkov emission.

Future diagnostic development work would include examining and defining high refractive index, non-scintillating materials ideal for Cherenkov emission. Laser engineering and technology must be improved to achieve detectable beams of laser wakefield induced muons. A new upcoming Extreme Photonics Applications Centre (EPAC) will

be able to produce higher energy electron beams with greater repetition rate making muon beams a possibility. This will enable better studies and tests to be carried out while also lessening the time required on the facility due to high repetition rates. Additional work to investigate Cherenkov light (and other mechanisms) in media other than fused silica, as well as simpler thinner geometries, may help us to decipher the mechanisms that cause this light emission. Measuring the wavelength spectra and comparing it to known Cherenkov and luminescence spectra would enable us to be more confident about the process which generates the light observed in the TA3 experiment. Electron charge monitors based on Cherenkov radiation could be used on shot as opposed to conventional magnetic spectrometers. The chamber window (often made from kapton) itself may be used as the Cherenkov medium. Relative charge can be recorded using this technique. An improvement can be made by calibrating it to obtain the absolute charge. The detected signal can be compared to the charge measured using a magnetic electron spectrometer in identical conditions and a calibration can be achieved. This would make it possible to take data and have an EMP-immune charge monitor running simultaneously.

Chapter 7

Summary and conclusions

This thesis presented experimental investigations into the scaling relationship of the sheath acceleration of protons and the electromagnetic pulse emission generated during high intensity (10^{19} W/cm²) laser-plasma interactions (chapter 4), and then investigated ways to control and mitigate these emissions (5). Finally, a development of an EMP resistant optical technique for charged particle detection was demonstrated 6. This chapter will summarise the main results and conclusions and suggest directions for future work to build on the findings of the thesis.

7.1 Scaling of EMP and proton acceleration in laser-solid interactions

The correlations between the EMP energy and the TNSA proton acceleration in high intensity (of the order of 10^{19} W/cm²) laser-solid interactions in the Vulcan laser facility were investigated. Both the EMP and proton acceleration are driven by the ejection of hot electrons from the target, which set up an electric sheath field on the target. The build up of a positive target charge induces a return current which propagates through the target mounting system generating EMP.

The laser intensity was varied either by changing the focal spot size (defocus scan), or by varying the laser energy on target (energy scan), while the remaining laser and target parameters were kept unchanged. We were able to show that the EMP en-

energy scales with intensity in both defocus and energy scans, and that the scaling is considerably slower in the defocus scan. By studying the escaping hot electrons and the accelerated protons in addition to the EMP, we observed similar scalings in the escaping electron and proton measurements, with more scatter present in the defocus scan. The escaping hot electron temperature and the maximum proton energy exhibit a linear relationship in agreement with the Mora model [55]. The maximum proton energies were higher than predicted for large focal spot sizes in the defocus scan. This could be a result of self-focusing in the preplasma, which would enhance the intensity, and generate more energetic electrons and in turn higher energy protons. Our defocus results are in line with a previous study in Gray *et al.* [127], where they report a much higher laser absorption for large focal spots compared to tight focus at equivalent intensity, and confirm via PIC simulations that it is a consequence of additional heating of the relativistic electrons which recirculate within the target between the sheath fields formed on the surfaces [128]. The recirculation of those electrons enhances the overall electron density and temperature at the target rear, subsequently increasing the TNSA proton energy. Despite the scatter observed in the measurements of the maximum proton energy as a function of intensity, any randomness disappears when plotted against EMP, providing a simple indirect measurement of both hot electron temperature and the maximum proton energy.

The work has demonstrated the need for greater numbers of and hotter electrons to produce higher energy sheath accelerated protons. The result is an increase in EMP. This can become problematic in high repetition rate and high power facilities, where many diagnostics will be online and thus highly susceptible to EMP disruption. We provided experimental evidence for the relationship of the expected EMP energy for a given maximum proton energy. Due to this, additional measures will be required, such as additional shielding to prevent interference in diagnostics, and changes to the target mounting system to mitigate EMP emissions, without influencing the ion acceleration.

7.2 Study of EMP Mitigation in Laser-Solid Interaction

An investigation was carried out to study the factors that affect the EMP emission in <1 ps laser-solid interactions at intensities of the order of 10^{20} W/cm². In particular, we studied the impact of varying the target diameter and the stalk length, which do not appear to have a significant impact on the escaping electron (>1 MeV) or ion populations. We observed a considerable reduction in EMP energy when using insulating components, instead of metallic, within the target mounting system. This was as expected as insulating materials exhibit a greater resistance to (return) current flow.

We measured an increase in EMP with increasing target diameters which is in line with the theory outlined in Consoli *et al.* [18]. This is a result of larger targets being able to reach greater capacitance and escaping charge, leading to an increased return current. We found the magnetic B-dot probe data to agree with ChoCoLaT2 simulation results, which indicate that the EMP emission increases for targets up to 10 mm in diameter, after which point it no longer grows. The D-dot probe measurements exhibit a similar trend, however the EMP continues to grow past 10 mm target size. We also showed that increasing the path for a return current to flow (the stalk length) from the nominal 25 mm to 35 mm, produced a factor of 2 reduction in EMP.

Improved high power and high repetition rate laser facilities will produce more EMP than current systems, therefore these results are important to help inform on the optimised target mounting system design for improved diagnostic operation. The techniques examined in this chapter are cheap, non-destructive, do not interfere with experimental measurements, and can be easily implemented.

Further work opportunities include studying a larger number of different target mounting component materials for optimisation. It would be beneficial to study in more detail how EMP varies with target size, in particular above 10 mm. This is important given the inconsistency in the measurements of the B-dot and D-dot in figure 5.4. It may also be advantageous to consider different target stalk thickness, as thinner stalks will have higher resistance.

7.3 Particle detection via Cherenkov radiation

The advent of laser wakefield electron acceleration has enabled scientists to investigate secondary sources of radiation for potential applications in medical and industrial imaging. High energy (> 1 GeV) electron beams can be employed to drive muon sources in high Z converter targets [4]. Laser wakefield driven muons are a promising candidate for imaging of large and dense objects, ranging from shipment containers to power plant reactors, owing to their low stopping power in materials. The advantage over cosmic muons is that given the right electron beam conditions, the muon flux can be substantially higher than that from cosmic rays. Using the GEANT4 simulation code, we confirmed that the muon flux increases for thicker targets. Modest numbers of muons were shown to be generated using routinely achievable 1-2 GeV electrons in Gemini. Directed high flux muon beams can be produced with >5 GeV electrons. In order to develop these sources into viable applications, high laser repetition rates (kHz) would be needed.

To detect muons in laser-plasma experiments, novel diagnostic techniques are necessary. We developed an optical based diagnostic for muon detection in laser-plasma experiments, capable of discrimination against co-propagating electrons. The diagnostic consists of fused silica medium where relativistic muons will induce Cherenkov radiation, a collimation prism, an off-axis parabola and an ultra-sensitive photon detector. The detector, with a slight modification to the Cherenkov radiator material, was deployed for testing on the ISIS muon beamline, however the results showed light emission below the threshold energy for Cherenkov, indicating additional light emission processes. As a result further work was required to better understand the Cherenkov mechanism.

An experiment was conducted in the Gemini facility to further investigate the production of Cherenkov radiation under conditions relevant for muon production. An electron beam of energy 1 GeV was incident onto a large fused silica block, and several cameras were placed at different angles some distance from the glass for imaging the signal (figure 6.26). We observed an increase in the signal for higher laser energies,

indicating a higher electron bunch charge. These measurements were compared to the background x-rays which were monitored throughout the experiment, and were in good agreement. The exit end of the fused silica was a scatter screen, and was used to measure the angular profile of the emitted light. This was not quite what is expected for Cherenkov radiation induced by high energy relativistic particles. On the other hand a calibration test data and the estimated number of Cherenkov photons [163] are both of the same order of magnitude. Other potential sources of light that contribute to the signal were discussed.

Future diagnostic development work could include measuring the spectra of the light emitted in the medium when irradiated with relativistic electrons. It would be useful to conduct an experiment where the same materials are exposed to x-rays, which are uncharged, and therefore do not produce radiation. A comparison of the spectra obtained from the electron and x-ray irradiation tests, would help us identify the light emission mechanisms in each case. For example it may be that the material exhibits scintillation, but if we know the magnitude and the spectra, it may be possible to subtract this component, resulting in one less mechanisms present in the total signal. Ideally, a high refractive index material that does not exhibit scintillation should be defined, enabling to measure Cherenkov signals only. Additionally, a simpler Cherenkov radiator geometries could be used. For example a thinner fused silica window would make the data analysis less complex, because the effect of particle stopping would essentially be eliminated. Although this diagnostic is in early developmental stages, it has shown to be a promising candidate for use as an on-shot beam charge monitor in wakefield experiments, as it is unaffected by EMP. In this case the window through which the electron beam exits the chamber, typically made from Kapton material, could itself be used as a Cherenkov radiator. This means that data can be taken and the beam charge can be monitored simultaneously, without affecting the electron beam.

Bibliography

- [1] J. L. Dubois, F. Lubrano-Lavaderci, D. Raffestin, J. Ribolzi, J. Gazave, A. Compant La Fontaine, E. D’Humières, S. Hulin, Ph Nicolaï, A. Poyé, and V. T. Tikhonchuk. Target charging in short-pulse-laser-plasma experiments. *Phys. Rev. E - Stat. Nonlinear, Soft Matter Phys.*, 89(1):1–15, 2014.
- [2] A. Poyé, J. L. Dubois, F. Lubrano-Lavaderci, E. D’Humières, M. Bardon, S. Hulin, M. Bailly-Grandvaux, J. Ribolzi, D. Raffestin, J. J. Santos, Ph Nicolaï, and V. Tikhonchuk. Dynamic model of target charging by short laser pulse interactions. *Phys. Rev. E - Stat. Nonlinear, Soft Matter Phys.*, 92(4):1–17, 2015.
- [3] P Bradford, N C Woolsey, G G Scott, G Liao, H Liu, Y Zhang, B Zhu, C Armstrong, C Brenner, P Brummitt, F Consoli, I East, R Gray, D Haddock, P Huggard, E Montgomery, I Musgrave, P Oliveira, D R Rusby, C Spindloe, B Summers, E Zemaityte, Y Li, P Mckenna, and D Neely. EMP control and characterisation on high-power laser systems. 6:1–8, 2018.
- [4] A. I. Titov, B. Kämpfer, and H. Takabe. Dimuon production by laser-wakefield accelerated electrons. *Phys. Rev. Spec. Top. - Accel. Beams*, 12(11):111301, 2009.
- [5] T Maiman. Stimulated Optical Radiation in Ruby. *Nature*, 187:493–494, 1960.
- [6] WI Linlor. Plasmas produced by laser bursts. *Bull. Am. Phys. Soc.*, 7, 1962.
- [7] WI Linlor. Some properties of plasma produced by laser giant pulse. *Phys. Rev. Lett.*, 12:383, 1964.
- [8] William I. Linlor. Ion energies produced by laser giant pulse. *Appl. Phys. Lett.*, 3(11):210–211, 1963.
- [9] NC Fenner. Ion energies in the plasma produced by a high power laser. *Phys. Lett.*, 22(4):421–422, 1966.
- [10] T. Tajima and J. M. Dawson. Laser Electron Accelerator. 4(4):267–270, 1979.

- [11] D Strickland and G Mourou. Compression of Amplified Chirped Optical Pulses. *Opt. Commun.*, 56(3):219–221, 1985.
- [12] D Umstadter. Relativistic laser-plasma interactions. *J. Phys. D. Appl. Phys.*, 36(8), 2003.
- [13] Chan Joshi and Victor Malka. Focus on laser- and beam-driven plasma accelerators. *New J. Phys.*, 12, 2010.
- [14] K. W.D. Ledingham and W. Galster. Laser-driven particle and photon beams and some applications. *New J. Phys.*, 12, 2010.
- [15] Colin N. Danson, Constantin Haefner, Jake Bromage, Thomas Butcher, Jean Christophe F. Chanteloup, Enam A. Chowdhury, Almantas Galvanauskas, Leonida A. Gizzi, Joachim Hein, David I. Hillier, Nicholas W. Hopps, Yoshiaki Kato, Efim A. Khazanov, Ryosuke Kodama, Georg Korn, Ruxin Li, Yutong Li, Jens Limpert, Jingui Ma, Chang Hee Nam, David Neely, Dimitrios Papadopoulos, Rory R. Penman, Liejia Qian, Jorge J. Rocca, Andrey A. Shaykin, Craig W. Siders, Christopher Spindloe, Sándor Szatmári, Raoul M.G.M. Trines, Jianqiang Zhu, Ping Zhu, and Jonathan D. Zuegel. Petawatt and exawatt class lasers worldwide. *High Power Laser Sci. Eng.*, 7(June), 2019.
- [16] A. Poyé, S. Hulin, M. Bailly-Grandvaux, J. L. Dubois, J. Ribolzi, D. Raffestin, M. Bardon, F. Lubrano-Lavaderci, E. D’Humières, J. J. Santos, Ph Nicolaï, and V. Tikhonchuk. Physics of giant electromagnetic pulse generation in short-pulse laser experiments. *Phys. Rev. E - Stat. Nonlinear, Soft Matter Phys.*, 91(4):1–6, 2015.
- [17] A. Poyé, S. Hulin, J. Ribolzi, M. Bailly-Grandvaux, F. Lubrano-Lavaderci, M. Bardon, D. Raffestin, J. J. Santos, and V. Tikhonchuk. Thin target charging in short laser pulse interactions. *Phys. Rev. E*, 98(3):1–12, 2018.
- [18] Fabrizio Consoli, Vladimir Tikhonchuk, Matthieu Bardon, Philip Bradford, David Carroll, Jakub Cikhardt, Mattia Cipriani, Robert Clarke, Tom Cowan,

- Colin Danson, Riccardo De Angelis, Massimo De Marco, Jean-Luc Dubois, Bertrand Etchessahar, Alejandro Laso Garcia, David Hillier, Ales Honsa, Weiman Jiang, Viliam Kmetik, Josef Krása, Yutong LI, Frédéric Lubrano, Paul McKenna, Josefine Metzkes-Ng, Alexandre Poyé, Irene Prencipe, Piotr Rączka, Roland Smith, Roman Vrana, Nigel Woolsey, Egle Zemaityte, Yihang Zhang, Zhe Zhang, Bernhard Zielbauer, and David Neely. Laser produced electromagnetic pulses: generation, detection and mitigation. *High Power Laser Sci. Eng.*, 8(February), 2020.
- [19] SR Bobbili, Jong Ho Jeon, Hyung Taek Kim, and Chang Hee Nam. Bright muon source driven by GeV electron beams from a compact laser wakefield accelerator. *Plasma Phys. Control. Fusion*, 60(9), 2018.
- [20] G.C. Stirling G.H. Eaton, A. Carne, S.F.J. Cox, J.D. Davies, R. DE Renzi, O. Hartmann, A. Kratzer, C. Ristori, C.A. Scott and T. Sundqvist. Commissioning of the Rutherford Appleton Laboratory Pulsed Muon Facility. *Nucl. Instruments Methods Phys. Res.*, 269:483–491, 1988.
- [21] Large Hadron Collider Study Group. The Large Hadron Collider. Technical report, 1995.
- [22] J. Cikhardt, J. Krása, M. De Marco, M. Pfeifer, A. Velyhan, E. Krouský, B. Cikhardtová, D. Klír, K. ezáč, J. Ullschmied, J. Skála, P. Kubeš, and J. Kravárik. Measurement of the target current by inductive probe during laser interaction on terawatt laser system PALS. *Rev. Sci. Instrum.*, 85(10), 2014.
- [23] J. L. Dubois, P. Rączka, S. Hulin, M. Rosiński, L. Ryć, P. Parys, A. Zaraś-Szydłowska, D. Makaruk, P. Tchórz, J. Badziak, J. Wołowski, J. Ribolzi, and V. Tikhonchuk. Experimental demonstration of an electromagnetic pulse mitigation concept for a laser driven proton source. *Rev. Sci. Instrum.*, 89(10):103301, 2018.
- [24] H. Barry Bebb and Albert Gold. Multiphoton ionization of hydrogen and rare-gas atoms. *Phys. Rev.*, 143(1):1–24, 1966.

- [25] Y. Gontier and M. Trahin. Energetic electron generation by multiphoton absorption. *J. Phys. B At. Mol. Phys.*, 13(22):4383–4390, 1980.
- [26] P. Agostini, F. Fabre, G. Mainfray, G. Petite, and N. K. Rahman. Free-free transitions following six-photon ionization of xenon atoms. *Phys. Rev. Lett.*, 42(17):1127–1130, 1979.
- [27] LV Keldysh. Ionization in the Field of a Strong Electromagnetic Wave. *J. Exp. Theor. Phys.*, 20(5), 1965.
- [28] Paul Gibbon. Short pulse laser interactions with matter: An introduction. *Short Pulse Laser Interact. with Matter An Introd.*, pages 1–312, 2005.
- [29] Scott C. Wilks and William L. Kruer. Absorption of ultrashort, ultra-intense laser light by solids and overdense plasmas. *IEEE J. Quantum Electron.*, 33(11):1954–1968, 1997.
- [30] FF Chen. *Erratum to: Introduction to Plasma Physics and Controlled Fusion*. Third edition, 2018.
- [31] D C Barnes. Laser Self-Trapping for the Plasma. (2):154–160, 1987.
- [32] P Gibbon and E Frster. Short-pulse laserplasma interactions. *Plasma Phys. Control. Fusion*, 38:769–793, 1996.
- [33] GJ Pert. Inverse bremsstrahlung in strong radiation fields at low temperatures. *Phys. Rev. E*, 51(5):4778–4789, 1995.
- [34] J R Davies. Laser absorption by overdense plasmas in the relativistic regime. *Plasma Phys. Control. Fusion*, 51(1):014006, 2009.
- [35] NG Denisov. On a singularity of the field of an electromagnetic wave propagated in an inhomogeneous plasma. *Sov. Phys. JETP-USSR*, 4(4):544–553, 1957.
- [36] F. Brunel. Not-so-resonant, Resonant Absorption. *Phys. Rev. Lett.*, 59(July 1987):52–55, 1987.

- [37] Paul Gibbon and A. R. Bell. Collisionless absorption in sharp-edged plasmas. *Phys. Rev. Lett.*, 68(10):1535–1538, 1992.
- [38] W. L. Kruer and Kent Estabrook. JXB heating by very intense laser light. *Phys. Fluids*, 28(1):430–432, 1985.
- [39] A. R. Bell, A. P.L. Robinson, M. Sherlock, R. J. Kingham, and W. Rozmus. Fast electron transport in laser-produced plasmas and the KALOS code for solution of the Vlasov-Fokker-Planck equation. *Plasma Phys. Control. Fusion*, 48(3), 2006.
- [40] J. J. Santos, F. Amiranoff, S. D. Baton, L. Gremillet, M. Koenig, E. Martinolli, M. Rabec Le Gloahec, C. Rousseaux, D. Batani, A. Bernardinello, G. Greison, and T. Hall. Fast Electron Transport in Ultraintense Laser Pulse Interaction with Solid Targets by Rear-Side Self-Radiation Diagnostics. *Phys. Rev. Lett.*, 89(2):8–11, 2002.
- [41] Alfvén Hannes. On the Motion of Cosmic Rays in Interstellar Space. *Phys. Rev.*, (5), 1939.
- [42] JR DAVIES. The Alfvén limit revisited and its relevance to laser-plasma interactions. *Laser Part. Beams*, 24(2):299–310, 2006.
- [43] A R Bell, J R Davies, S Guerin, and H Ruhl. Plasma Physics and Controlled Fusion Fast-electron transport in high-intensity short-pulse laser - solid experiments. *Plasma Phys. Control. Fusion*, 39:1–8, 1997.
- [44] B. Bezzerides, S. J. Gitomer, and D. W. Forslund. Randomness, maxwellian distributions, and resonance absorption. *Phys. Rev. Lett.*, 44(10):651–654, 1980.
- [45] J. Myatt, W. Theobald, J. A. Delettrez, C. Stoeckl, M. Storm, T. C. Sangster, A. V. Maximov, and R. W. Short. High-intensity laser interactions with mass-limited solid targets and implications for fast-ignition experiments on OMEGA EP. *Phys. Plasmas*, 14(5), 2007.
- [46] M. J.V. Streeter, P. S. Foster, F. H. Cameron, M. Borghesi, C. Brenner, D. C. Carroll, E. Divall, N. P. Dover, B. Dromey, P. Gallegos, J. S. Green, S. Hawkes,

- C. J. Hooker, S. Kar, P. McKenna, S. R. Nage, Z. Najmudin, C. A.J. Palmer, R. Prasad, K. E. Quinn, P. P. Rajeev, A. P.L. Robinson, L. Romagnani, J. Schreiber, C. Spindloe, S. Ter-Avetisyan, O. Tresca, M. Zepf, and D. Neely. Relativistic plasma surfaces as an efficient second harmonic generator. *New J. Phys.*, 13, 2011.
- [47] P. M. Nilson, W. Theobald, J. F. Myatt, C. Stoeckl, M. Storm, J. D. Zuegel, R. Betti, D. D. Meyerhofer, and T. C. Sangster. Bulk heating of solid-density plasmas during high-intensity-laser plasma interactions. *Phys. Rev. E - Stat. Nonlinear, Soft Matter Phys.*, 79(1):1–5, 2009.
- [48] F. N. Beg, A. R. Bell, A. E. Dangor, C. N. Danson, A. P. Fews, M. E. Glinsky, B. A. Hammel, P. Lee, P. A. Norreys, and M. Tatarakis. A study of picosecond laser-solid interactions up to 1019W cm⁻². *Phys. Plasmas*, 4(2):447–457, 1997.
- [49] Sc Wilks, Wl Kruer, M. Tabak, and Ab Langdon. Absorption of ultra-intense laser pulses. *Phys. Rev. Lett.*, 69(9):1383–1386, 1992.
- [50] Malcolm Haines. Scaling of the hot electron temperature and laser absorption in fast ignition.
- [51] Erik Lefebvre, Laurent Gremillet, Anna Lévy, Rachel Nuter, Patrizio Antici, Michael Carrié, Tiberio Ceccotti, Mathieu Drouin, Julien Fuchs, Victor Malka, and David Neely. Proton acceleration by moderately relativistic laser pulses interacting with solid density targets. *New J. Phys.*, 12, 2010.
- [52] C. M. Brenner, A. P.L. Robinson, K. Markey, R. H.H. Scott, R. J. Gray, M. Rosinski, O. Deppert, J. Badziak, D. Batani, J. R. Davies, S. M. Hassan, K. L. Lancaster, K. Li, I. O. Musgrave, P. A. Norreys, J. Pasley, M. Roth, H. P. Schlenvoigt, C. Spindloe, M. Tatarakis, T. Winstone, J. Wolowski, D. Wyatt, P. McKenna, and D. Neely. High energy conversion efficiency in laser-proton acceleration by controlling laser-energy deposition onto thin foil targets. *Appl. Phys. Lett.*, 104(8), 2014.

- [53] S. C. Wilks, A. B. Langdon, T. E. Cowan, M. Roth, M. Singh, S. Hatchett, M. H. Key, D. Pennington, A. MacKinnon, and R. A. Snavely. Energetic proton generation in ultra-intense laser-solid interactions. *Phys. Plasmas*, 8(2):542–549, 2001.
- [54] J. Badziak. Laser-driven generation of fast particles. *Opto-electronics Rev.*, 15(1):1–12, 2007.
- [55] P. Mora. Plasma Expansion into a Vacuum. *Phys. Rev. Lett.*, 90(18):4, 2003.
- [56] J. Schreiber, F. Bell, F. Grüner, U. Schramm, M. Geissler, M. Schnürer, S. Ter-Avetisyan, B. M. Hegelich, J. Cobble, E. Brambrink, J. Fuchs, P. Audebert, and D. Habs. Analytical model for ion acceleration by high-intensity laser pulses. *Phys. Rev. Lett.*, 97(4):1–4, 2006.
- [57] Alessandro Zani, Andrea Sgattoni, and Matteo Passoni. Parametric investigations of target normal sheath acceleration experiments. *Nucl. Instruments Methods Phys. Res. Sect. A Accel. Spectrometers, Detect. Assoc. Equip.*, 653(1):94–97, 2011.
- [58] L. Robson, P. T. Simpson, R. J. Clarke, K. W.D. Ledingham, F. Lindau, O. Lundh, T. McCanny, P. Mora, D. Neely, C. G. Wahlström, M. Zepf, and P. McKenna. Scaling of proton acceleration driven by petawatt-laser-plasma interactions. *Nat. Phys.*, 3(1):58–62, 2007.
- [59] M. Coury, D. C. Carroll, A. P. L. Robinson, X. H. Yuan, C. M. Brenner, M. Burza, R. J. Gray, M. N. Quinn, K. L. Lancaster, Y. T. Li, X. X. Lin, O. Tresca, C.-G. Wahlström, D. Neely, and P. McKenna. Influence of laser irradiated spot size on energetic electron injection and proton acceleration in foil targets. *Appl. Phys. Lett.*, 100(7):074105, 2012.
- [60] C.G. Brown, T.J. Clancy, D.C. Eder, W. Ferguson, and A.L. Throop. Analysis of electromagnetic pulse (EMP) measurements in the National Ignition Facility’s target bay and chamber. *EPJ Web Conf.*, 59:08012, 2013.

- [61] D C Eder, a Throop, C G Brown, J Kimbrough, D a White, P Song, N Back, a Macphee, H Chen, W Dehope, Y Ping, B Maddox, J Lister, G Pratt, T Ma, M Perkins, D O Brien, and P Patel. Mitigation of Electromagnetic Pulse (EMP) Effects from Short-Pulse Lasers and Fusion Neutrons. *Rep. LLNL-TR-411183, Lawrence Livermore Natl. Lab.*, 2009.
- [62] M. J. Mead, D. Neely, J. Gauoin, R. Heathcote, and P. Patel. Electromagnetic pulse generation within a petawatt laser target chamber. *Rev. Sci. Instrum.*, 75(10 II):4225–4227, 2004.
- [63] J E Bateman, M J Mead, and Harwell Oxford. Electromagnetic pulse generation in petawatt laser shots. *Rutherford Applet. Lab. Tech. Reports*, (RAL-TR-2012-005), 2012.
- [64] C. G. Brown, E. Bond, T. Clancy, S. Dangi, D. C. Eder, W. Ferguson, J. Kimbrough, and A. Throop. Assessment and mitigation of electromagnetic pulse (EMP) impacts at short-pulse laser facilities. *J. Phys. Conf. Ser.*, 244(PART 3), 2010.
- [65] C. G. Brown, A. Throop, D. Eder, and J. Kimbrough. Electromagnetic pulses at short-pulse laser facilities. *J. Phys. Conf. Ser.*, 112(Part 3), 2008.
- [66] N. L. Kugland, B. Aurand, C. G. Brown, C. G. Constantin, E. T. Everson, S. H. Glenzer, D. B. Schaeffer, A. Tauschwitz, and C. Niemann. Demonstration of a low electromagnetic pulse laser-driven argon gas jet x-ray source. *Appl. Phys. Lett.*, 101(2), 2012.
- [67] Zi Yu Chen, Jian Feng Li, Yong Yu, Jia Xiang Wang, Xiao Ya Li, Qi Xian Peng, and Wen Jun Zhu. Influence of lateral target size on hot electron production and electromagnetic pulse emission from laser-irradiated metallic targets. *Phys. Plasmas*, 19(11), 2012.
- [68] Fabrizio Consoli, Riccardo De Angelis, Pierluigi Andreoli, Giuseppe Cristofari, and Giorgio Di Giorgio. Measurement of the radiofrequency-microwave pulse

- produced in experiments of laser-plasma interaction in the ABC laser facility. *Phys. Procedia*, 62:11–17, 2015.
- [69] John L. Remo, Richard G. Adams, and Michael C. Jones. Atmospheric electromagnetic pulse propagation effects from thick targets in a terawatt laser target chamber. *Appl. Opt.*, 46(24):6166, 2007.
- [70] P. Raczka, J. L. Dubois, S. Hulin, V. Tikhonchuk, M. Rosiński, A. Zaraś-Szydłowska, and J. Badziak. Strong electromagnetic pulses generated in high-intensity short-pulse laser interactions with thin foil targets. *Laser Part. Beams*, 35(4):677–686, 2017.
- [71] T. S. Robinson, F. Consoli, S. Giltrap, S. J. Eardley, G. S. Hicks, E. J. Ditter, O. Ettliger, N. H. Stuart, M. Notley, R. De Angelis, Z. Najmudin, and R. A. Smith. Low-noise time-resolved optical sensing of electromagnetic pulses from petawatt laser-matter interactions. *Sci. Rep.*, 7(1):1–12, 2017.
- [72] F. Consoli, R. De Angelis, L. Duvillaret, P. L. Andreoli, M. Cipriani, G. Cristofari, G. Di Giorgio, F. Ingenito, and C. Verona. Time-resolved absolute measurements by electro-optic effect of giant electromagnetic pulses due to laser-plasma interaction in nanosecond regime. *Sci. Rep.*, 6(June):1–8, 2016.
- [73] D. R. Rusby, C. D. Armstrong, G. G. Scott, M. King, P. McKenna, and D. Neely. Effect of rear surface fields on hot, refluxing and escaping electron populations via numerical simulations. *High Power Laser Sci. Eng.*, 7:1–11, 2019.
- [74] John David Jackson. *Classical Electrodynamics*. John Wiley & Sons, 2 edition, 1975.
- [75] M. Borghesi, L. Romagnani, A. Schiavi, D. H. Campbell, M. G. Haines, O. Willi, A. J. Mackinnon, M. Galimberti, L. Gizzi, R. J. Clarke, and S. Hawkes. Measurement of highly transient electrical charging following high-intensity laser-solid interaction. *Appl. Phys. Lett.*, 82(10):1529–1531, 2003.

- [76] A Gopal, T May, S Herzer, A Reinhard, S Minardi, M Schubert, U Dillner, B Pradarutti, J Polz, T Gaumnitz, M C Kaluza, O Jckel, S Riehemann, W Ziegler, H-P Gemuend, H-G Meyer, and G G Paulus. Observation of energetic terahertz pulses from relativistic solid density plasmas. *New Journal of Physics*, 14(8):083012, aug 2012.
- [77] S Herzer, A Woldegeorgis, J Polz, A Reinhard, M Almassarani, B Beleites, F Ronneberger, R Grosse, G G Paulus, U Hbner, T May, and A Gopal. An investigation on THz yield from laser-produced solid density plasmas at relativistic laser intensities. *New Journal of Physics*, 20(6):063019, jun 2018.
- [78] A. Gopal, S. Herzer, A. Schmidt, P. Singh, A. Reinhard, W. Ziegler, D. Brömmel, A. Karmakar, P. Gibbon, U. Dillner, T. May, H-G. Meyer, and G. G. Paulus. Observation of gigawatt-class thz pulses from a compact laser-driven particle accelerator. *Phys. Rev. Lett.*, 111:074802, Aug 2013.
- [79] X.H. Yuan, Y. Fang, D.C. Carroll, D.A. MacLellan, F. Du, N. Booth, M. Burza, M. Chen, R.J. Gray, Y.F. Jin, and et al. Effects of target pre-heating and expansion on terahertz radiation production from intense laser-solid interactions. *High Power Laser Science and Engineering*, 2:e5, 2014.
- [80] Guoqian Liao, Yutong Li, Hao Liu, Graeme G Scott, David Neely, Yihang Zhang, and Baojun Zhu. Multimillijoule coherent terahertz bursts from picosecond laser-irradiated metal foils. *PNAS*, 116(10):3994–3999, 2019.
- [81] K. Quinn, P. A. Wilson, C. A. Cecchetti, B. Ramakrishna, L. Romagnani, G. Sarri, L. Lancia, J. Fuchs, A. Pipahl, T. Toncian, O. Willi, R. J. Clarke, D. Neely, M. Notley, P. Gallegos, D. C. Carroll, M. N. Quinn, X. H. Yuan, P. McKenna, T. V. Liseykina, A. MacChi, and M. Borghesi. Laser-Driven ultrafast field propagation on solid surfaces. *Phys. Rev. Lett.*, 102(19):3–6, 2009.
- [82] Satyabrata Kar, Hamad Ahmed, Rajendra Prasad, Mirela Cerchez, Stephanie Brauckmann, Bastian Aurand, Giada Cantono, Prokopis Hadjisolomou, Ciaran L.S. Lewis, Andrea Macchi, Gagik Nersisyan, Alexander P.L. Robinson,

- Anna M. Schroer, Marco Swantusch, Matt Zepf, Oswald Willi, and Marco Borghesi. Guided post-acceleration of laser-driven ions by a miniature modular structure. *Nat. Commun.*, 7:1–7, 2016.
- [83] Shigeki Tokita, Shuji Sakabe, Takeshi Nagashima, Masaki Hashida, and Shunsuke Inoue. Strong sub-terahertz surface waves generated on a metal wire by high-intensity laser pulses. *Sci. Rep.*, 5:1–6, 2015.
- [84] Glenn S. Smith. Teaching antenna radiation from a time-domain perspective. *Am. J. Phys.*, 69(3):288–300, 2001.
- [85] HERCULES 300 TW laser.
- [86] F. Wagner, C. P. João, J. Fils, T. Gottschall, J. Hein, J. Körner, J. Limpert, M. Roth, T. Stöhlker, and V. Bagnoud. Temporal contrast control at the PHELIX petawatt laser facility by means of tunable sub-picosecond optical parametric amplification. *Appl. Phys. B Lasers Opt.*, 116(2):429–435, 2014.
- [87] Chris Hooker, Yunxin Tang, Oleg Chekhlov, John Collier, Edwin Divall, Klaus Ertel, Steve Hawkes, Bryn Parry, and P. P. Rajeev. Improving coherent contrast of petawatt laser pulses. *Opt. Express*, 19(3):2193, 2011.
- [88] C. N. Danson. Vulcan petawatt : Design , operation and interactions at 5×10^{20} Wcm⁻². pages 87–93, 2005.
- [89] C Hernandez-Gomez, S P Blake, C Burton, R J Clarke, J L Collier, B Costello, V Dubrosky, A J Frackiewicz, M Galimberti, S Hancock, S J Hawkes, R Heathcote, A K Kidd, I O Musgrave, D Neely, M M Notley, B T Parry, D A Pepler, W Shaikh, T B Winstone, and B E Wyborn. An overview of the Target Area West short pulse upgrade. *CLF Annu. Rep.*, pages 260–261, 2007.
- [90] C. J. Hooker, S. Blake, O. Chekhlov, R. J. Clarke, J. L. Collier, E. J. Divall, K. Ertel, P. S. Foster, S. J. Hawkes, P. Holligan, B. Landowski, W. J. Lester, D. Neely, B. Parry, R. Pattathil, M. Streeter, and B. E. Wyborn. Commission-

- ing the Astra Gemini petawatt Ti:sapphire laser system. *2008 Conf. Quantum Electron. Laser Sci. Conf. Lasers Electro-Optics, CLEO/QELS*, pages 2–3, 2008.
- [91] H. Liu, G.-Q. Liao, Y.-H. Zhang, B.-J. Zhu, Z. Zhang, Y.-T. Li, G. G. Scott, D. R. Rusby, C. Armstrong, E. Zemaityte, D. C. Carroll, S. Astbury, P. Bradford, N. C. Woolsey, P. McKenna, and D. Neely. Cherenkov radiation-based optical fibre diagnostics of fast electrons generated in intense laser-plasma interactions. *Rev. Sci. Instrum.*, 89(8):083302, 2018.
- [92] Dean Richard Rusby. *Study of Escaping Electron Dynamics and Applications from High-Power Laser-Plasma Interactions*. PhD thesis, University of Strathclyde, 2017.
- [93] D. C. Carroll, P. Brummitt, D. Neely, F. Lindau, O. Lundh, C. G. Wahlström, and P. McKenna. A modified Thomson parabola spectrometer for high resolution multi-MeV ion measurements-Application to laser-driven ion acceleration. *Nucl. Instruments Methods Phys. Res. Sect. A Accel. Spectrometers, Detect. Assoc. Equip.*, 620(1):23–27, 2010.
- [94] D. Gwynne, S. Kar, D. Doria, H. Ahmed, M. Cerchez, J. Fernandez, R. J. Gray, J. S. Green, F. Hanton, D. A. Maclellan, P. McKenna, Z. Najmudin, D. Neely, J. A. Ruiz, A. Schiavi, M. Streeter, M. Swantusch, O. Willi, M. Zepf, and M. Borghesi. Modified Thomson spectrometer design for high energy, multi-species ion sources. *Rev. Sci. Instrum.*, 85(3), 2014.
- [95] JD Kraus, RJ Marhefka, and AS Khan. *Antennas and wave propagation*. 2006.
- [96] CA Balanis. *Antenna theory: analysis and design*. John Wiley & Sons.
- [97] Prodyn Technologies. D-Dot FD-5, 2013.
- [98] Prodyn Tech. B-Dot B-24, 2013.
- [99] P. Rączka, L. Nowosielski, M. Rosiński, D. Makaruk, J. Makowski, A. Zaraś-Szydłowska, P. Tchórz, and J. Badziak. Measurement of the electric field strength

generated in the experimental chamber by 10 TW femtosecond laser pulse interaction with a solid target. *J. Instrum.*, 14(04):P04008–P04008, 2019.

- [100] Kazuo A. Tanaka, Toshinori Yabuuchi, Takashi Sato, Ryosuke Kodama, Yoneyoshi Kitagawa, Teruyoshi Takahashi, Toshiji Ikeda, Yoshihide Honda, and Shuuichi Okuda. Calibration of imaging plate for high energy electron spectrometer. *Rev. Sci. Instrum.*, 76(1):013507, 2005.
- [101] Hui Chen, Anthony J. Link, Roger Van Maren, Pravesh K. Patel, Ronnie Shepherd, Scott C. Wilks, and Peter Beiersdorfer. High performance compact magnetic spectrometers for energetic ion and electron measurement in ultraintense short pulse laser solid interactions. *Rev. Sci. Instrum.*, 79(10):1–4, 2008.
- [102] C. D. Chen, J. A. King, M. H. Key, K. U. Akli, F. N. Beg, H. Chen, R. R. Freeman, A. Link, A. J. MacKinnon, A. G. MacPhee, P. K. Patel, M. Porkolab, R. B. Stephens, and L. D. Van Woerkom. A Bremsstrahlung spectrometer using k-edge and differential filters with image plate dosimeters. *Rev. Sci. Instrum.*, 79(10):4–7, 2008.
- [103] R. H.H. Scott, F. Pérez, M. J.V. Streeter, E. L. Clark, J. R. Davies, H. P. Schlenvoigt, J. J. Santos, S. Hulin, K. L. Lancaster, F. Dorchies, C. Fourment, B. Vauzour, A. A. Soloviev, S. D. Baton, S. J. Rose, and P. A. Norreys. Fast electron beam measurements from relativistically intense, frequency-doubled laser-solid interactions. *New J. Phys.*, 15, 2013.
- [104] Sadaoki Kojima, Takahito Ikenouchi, Yasunobu Arikawa, Shohei Sakata, Zhe Zhang, Yuki Abe, Mitsuo Nakai, Hiroaki Nishimura, Hiroyuki Shiraga, Tetsuo Ozaki, Shuji Miyamoto, Masashi Yamaguchi, Akinori Takemoto, Shinsuke Fujioka, and Hiroshi Azechi. Development of Compton X-ray spectrometer for high energy resolution single-shot high-flux hard X-ray spectroscopy. *Rev. Sci. Instrum.*, 87(4), 2016.

- [105] D. R. Rusby, C. D. Armstrong, C. M. Brenner, R. J. Clarke, P. McKenna, and D. Neely. Novel scintillator-based x-ray spectrometer for use on high repetition laser plasma interaction experiments. *Rev. Sci. Instrum.*, 89(7), 2018.
- [106] G. G. Scott, J. S. Green, D. Neely, F. Fiorini, D. Kirby, S. Green, M. R. Mitchell, P. McKenna, and J. Rickman. Characterisation of plastic scintillators for detection of laser-accelerated protons. *CLF Annu. Rep. 2010-2011*, 2011.
- [107] S. Agostinelli, J. Allison, K. Amako, J. Apostolakis, H. Araujo, P. Arce, M. Asai, D. Axen, S. Banerjee, G. Barrand, F. Behner, L. Bellagamba, J. Boudreau, L. Broglio, A. Brunengo, H. Burkhardt, S. Chauvie, J. Chuma, R. Chytracsek, G. Cooperman, G. Cosmo, P. Degtyarenko, A. Dell'Acqua, G. Depaola, D. Dietrich, R. Enami, A. Feliciello, C. Ferguson, H. Fesefeldt, G. Folger, F. Foppiano, A. Forti, S. Garelli, S. Giani, R. Giannitrapani, D. Gibin, J. J. Gomez Cadenas, I. Gonzalez, G. Gracia Abril, G. Greeniaus, W. Greiner, V. Grichine, A. Grossheim, S. Guatelli, P. Gumplinger, R. Hamatsu, K. Hashimoto, H. Hasui, A. Heikkinen, A. Howard, V. Ivanchenko, A. Johnson, F. W. Jones, J. Kallenbach, N. Kanaya, M. Kawabata, Y. Kawabata, M. Kawaguti, S. Kellner, P. Kent, A. Kimura, T. Kodama, R. Kokoulin, M. Kossov, H. Kurashige, E. Lamanna, T. Lampen, V. Lara, V. Lefebure, F. Lei, M. Liendl, W. Lockman, F. Longo, S. Magni, M. Maire, E. Medernach, K. Minamimoto, P. Mora de Freitas, Y. Morita, K. Murakami, M. Nagamatu, R. Nartallo, P. Nieminen, T. Nishimura, K. Ohtsubo, M. Okamura, S. O'Neale, Y. Oohata, K. Paech, J. Perl, A. Pfeiffer, M. G. Pia, F. Ranjard, A. Rybin, S. Sadilov, E. di Salvo, G. Santin, T. Sasaki, N. Savvas, Y. Sawada, S. Scherer, S. Sei, V. Sirotenko, D. Smith, N. Starkov, H. Stoecker, J. Sulkimo, M. Takahata, S. Tanaka, E. Tcherniaev, E. Safai Tehrani, M. Tropeano, P. Truscott, H. Uno, L. Urban, P. Urban, M. Verderi, A. Walkden, W. Wander, H. Weber, J. P. Wellisch, T. Wenaus, D. C. Williams, D. Wright, T. Yamada, H. Yoshida, and D. Zschesche. GEANT4 - A simulation toolkit. *Nucl. Instruments Methods Phys. Res. Sect. A Accel. Spectrometers, Detect. Assoc. Equip.*, 506(3):250–303, 2003.

- [108] Katsuya Amako, Susanna Guatelli, Vladimir N. Ivanchenko, Michel Maire, Barbara Mascialino, Koichi Murakami, Petteri Nieminen, Luciano Pandola, Sandra Parlati, Maria Grazia Pia, Michela Piergentili, Takashi Sasaki, and Laszlo Urban. Comparison of Geant4 electromagnetic physics models against the NIST reference data. *IEEE Trans. Nucl. Sci.*, 52(4):910–918, 2005.
- [109] H. Araujo, A. Howard, S. Chauvie, S. Guatelli, A. Mantero, B. Mascialino, M. G. Pia, M. Piergentili, S. Saliceti, V. Ivanchenko, F. Longo, P. Nieminen, L. Pandola, S. Parlati, L. Peralta, P. Rodrigues, and A. Trinidad. Geant4 low energy electromagnetic physics. *Monte Carlo 2005 Top. Meet.*, 00(C):1119–1127, 2005.
- [110] G. A.P. Cirrone, G. Cuttone, F. Di Rosa, L. Pandola, F. Romano, and Q. Zhang. Validation of the Geant4 electromagnetic photon cross-sections for elements and compounds. *Nucl. Instruments Methods Phys. Res. Sect. A Accel. Spectrometers, Detect. Assoc. Equip.*, 618(1-3):315–322, 2010.
- [111] T. D. Arber, K. Bennett, C. S. Brady, A. Lawrence-Douglas, M. G. Ramsay, N. J. Sircombe, P. Gillies, R. G. Evans, H. Schmitz, A. R. Bell, and C. P. Ridgers. Contemporary particle-in-cell approach to laser-plasma modelling. *Plasma Phys. Control. Fusion*, 57(11), 2015.
- [112] J. S. Pearlman and G. H. Dahlbacka. Charge separation and target voltages in laser-produced plasmas. *Appl. Phys. Lett.*, 31(7):414–417, 1977.
- [113] C. Courtois, A. Compant La Fontaine, O. Landoas, G. Lidove, V. ot, P. Morel, R. Nuter, E. Lefebvre, A. Boscheron, J. Grenier, M. M. Aonard, M. Gerbaux, F. Gobet, F. Hannachi, G. Malka, J. N. Scheurer, and M. Tarisien. Effect of plasma density scale length on the properties of bremsstrahlung x-ray sources created by picosecond laser pulses. *Phys. Plasmas*, 16(1), 2009.
- [114] Colin Danson, David Hillier, Nicholas Hopps, David Neely, Colin Danson, David Hillier, Nicholas Hopps, and David Neely. Petawatt class lasers worldwide. (January 2015), 2016.

- [115] Andrei G. Pakhomov, Damijan Miklavcic, and Marko S. Markov. Advanced Electroporation Techniques in Biology and Medicine, 2010.
- [116] Satoshi Yoshida, Naoki Hasegawa, and Shigeo Kawasaki. Experimental Demonstration of Microwave Power Transmission and Wireless Communication Within a Prototype Reusable Spacecraft. *IEEE Microw. Wirel. Components Lett.*, 25(8):556–558, 2015.
- [117] K H Schoenbach, R Nuccitelli, and S J Beebe. No Title No Title. *J. Chem. Inf. Model.*, 53(9):1689–1699, 2017.
- [118] Henry W. Ott. Electromagnetic Compatibility Engineering, 2009.
- [119] Paul Mason, Martin Divoký, Klaus Ertel, Jan Pila, Thomas Butcher, Martin Hanuš, Saumyabrata Banerjee, Jonathan Phillips, Jodie Smith, Mariastefania De Vido, Antonio Lucianetti, Cristina Hernandez-Gomez, Chris Edwards, Tomas Mocek, and John Collier. Kilowatt average power 100 J-level diode pumped solid state laser. *Optica*, 4(4):438, 2017.
- [120] Hiroyuki Daido, Mamiko Nishiuchi, and Alexander S Pirozhkov. Review of laser-driven ion sources and their applications. *Reports Prog. Phys.*, 75(5):056401, 2012.
- [121] K. Zeil, S. D. Kraft, S. Bock, M. Bussmann, T. E. Cowan, T. Kluge, J. Metzkes, T. Richter, R. Sauerbrey, and U. Schramm. The scaling of proton energies in ultrashort pulse laser plasma acceleration. *New J. Phys.*, 12, 2010.
- [122] J. Fuchs, P. Antici, E. D’Humières, E. Lefebvre, M. Borghesi, E. Brambrink, C. A. Cecchetti, M. Kaluza, V. Malka, M. Manclossi, S. Meyroneinc, P. Mora, J. Schreiber, T. Toncian, H. Pépin, and P. Audebert. Laser-driven proton scaling laws and new paths towards energy increase. *Nat. Phys.*, 2(1):48–54, 2006.
- [123] C. M. Brenner, P. McKenna, and D. Neely. Modelling the effect of laser focal spot size on sheath- accelerated protons in intense laser-foil interactions. *Plasma Phys. Control. Fusion*, 56(8), 2014.

- [124] N. P. Dover, M. Nishiuchi, H. Sakaki, Ko Kondo, M. A. Alkhimova, A. Ya Faenov, M. Hata, N. Iwata, H. Kiriya, J. K. Koga, T. Miyahara, T. A. Pikuz, A. S. Pirozhkov, A. Sagisaka, Y. Sentoku, Y. Watanabe, M. Kando, and K. Kondo. Effect of Small Focus on Electron Heating and Proton Acceleration in Ultrarelativistic Laser-Solid Interactions. *Phys. Rev. Lett.*, 124(8):84802, 2020.
- [125] A. J. Mackinnon, Y Sentoku, P. K. Patel, D. W. Price, S Hatchett, M. H. Key, R Andersen, R Snavely, and R. R. Freeman. Enhancement of Proton Acceleration by Hot-Electron Recirculation in Thin Foil Irradiated by Ultraintense Laser Pulses. *Phys. Rev. Lett.*, 88(21), 2002.
- [126] J. Buffechoux, S. and Psikal, J. and Nakatsutsumi, M. and Romagnani, L. and Andreev, A. and Zeil, K. and Amin, M. and Antici, P. and Burris-Mog, T. and Compant-La-Fontaine, A. and d'Humières, E. and Fourmaux, S. and Gaillard, S. and Gobet, F. and Hannachi,. Hot Electrons Transverse Refluxing in Ultraintense Laser-Solid Interactions. *Phys. Rev. Lett.*, 105(1), 2010.
- [127] R. J. Gray, R. Wilson, M. King, S. D.R. Williamson, R. J. Dance, C. Armstrong, C. Brabetz, F. Wagner, B. Zielbauer, V. Bagnoud, D. Neely, and P. McKenna. Enhanced laser-energy coupling to dense plasmas driven by recirculating electron currents. *New J. Phys.*, 20(3), 2018.
- [128] Y. Sentoku, T. E. Cowan, A. Kemp, and H. Ruhl. High energy proton acceleration in interaction of short laser pulse with dense plasma target. *Phys. Plasmas*, 10(5 II):2009–2015, 2003.
- [129] M. N. Quinn, X. H. Yuan, X. X. Lin, D. C. Carroll, O. Tresca, R. J. Gray, M. Coury, C. Li, Y. T. Li, C. M. Brenner, A. P.L. Robinson, D. Neely, B. Zielbauer, B. Aurand, J. Fils, T. Kuehl, and P. McKenna. Refluxing of fast electrons in solid targets irradiated by intense, picosecond laser pulses. *Plasma Phys. Control. Fusion*, 53(2), 2011.
- [130] Dean Rusby, Ross Gray, Nick Butler, Rachel Dance, Graeme Scott, Vincent Bagnoud, Bernhard Zielbauer, Paul McKenna, and David Neely. Escaping Electrons

from Intense Laser-Solid Interactions as a Function of Laser Spot Size. *EPJ Web Conf.*, 167:1–5, 2018.

- [131] B. Rus, P. Bakule, D. Kramer, J. Naylon, J. Thoma, M. Fibrich, J. T. Green, J. C. Lagron, R. Antipenkov, J. Bartoníček, F. Batysta, R. Baše, R. Boge, S. Buck, J. Cupal, M. A. Drouin, M. urák, B. Himmel, T. Havlíček, P. Homer, A. Honsa, M. Horáček, P. Hříbek, J. Hubáček, Z. Hubka, G. Kalinchenko, K. Kasl, L. Indra, P. Korous, M. Košelja, L. Koubíková, M. Laub, T. Mazanec, A. Meadows, J. Novák, D. Peceli, J. Polan, D. Snopek, V. Šobr, P. Trojek, B. Tykalewicz, P. Velpula, E. Verhagen, Š. Vyhlídka, J. Weiss, C. Haefner, A. Bayramian, S. Betts, A. Erlandson, J. Jarboe, G. Johnson, J. Horner, D. Kim, E. Koh, C. Marshall, D. Mason, E. Sistrunk, D. Smith, T. Spinka, J. Stanley, C. Stolz, T. Suratwala, S. Telford, T. Ditmire, E. Gaul, M. Donovan, C. Frederickson, G. Friedman, D. Hammond, D. Hidinger, G. Chériaux, A. Jochmann, M. Kepler, C. Malato, M. Martinez, T. Metzger, M. Schultze, P. Mason, K. Ertel, A. Lintern, C. Edwards, C. Hernandez-Gomez, and J. Collier. ELI-beamlines: progress in development of next generation short-pulse laser systems. In *Res. Using Extrem. Light Enter. New Front. with Petawatt-Class Lasers III*, volume 10241, page 102410J, 2017.
- [132] Sergei Kühn, Mathieu Dumergue, Subhendu Kahaly, Sudipta Mondal, Miklós Füle, Tamás Csizmadia, Balázs Farkas, Balázs Major, Zoltán Várallyay, Francesca Calegari, Michele Devetta, Fabio Frassetto, Erik Månsson, Luca Polletto, Salvatore Stagira, Caterina Vozzi, Mauro Nisoli, Piotr Rudawski, Sylvain Maclot, Filippo Campi, Hampus Wikmark, Cord L. Arnold, Christoph M. Heyl, Per Johnsson, Anne L’Huillier, Rodrigo Lopez-Martens, Stefan Haessler, Maïmona Bocoum, Frederik Boehle, Aline Vernier, Gregory Iaquaniello, Emmanuel Skantzakis, Nikos Papadakis, Constantinos Kalpouzos, Paraskevas Tzallas, Franck Lépine, Dimitris Charalambidis, Katalin Varjú, Károly Osvay, and Giuseppe Sansone. The ELI-ALPS facility: The next generation of attosecond sources. *J. Phys. B At. Mol. Opt. Phys.*, 50(13), 2017.

- [133] S. Gales, K. A. Tanaka, D. L. Balabanski, F. Negoita, D. Stutman, O. Tesileanu, C. A. Ur, D. Ursescu, I. Andrei, S. Ataman, M. O. Cernaianu, L. D'Alessi, I. Dancus, B. Diaconescu, N. Djourellov, D. Filipescu, P. Ghenuche, D. G. Ghita, C. Matei, K. Seto, M. Zeng, and N. V. Zamfir. The extreme light infrastructure - Nuclear physics (ELI-NP) facility: New horizons in physics with 10 PW ultra-intense lasers and 20 MeV brilliant gamma beams. *Reports Prog. Phys.*, 81(9), 2018.
- [134] Stratasy. Vero datasheet.
- [135] Polymer Properties Database.
- [136] F. Consoli, R. De Angelis, M. De Marco, J. Krasa, J. Cikhardt, M. Pfeifer, D. Margarone, D. Klir, and R. Dudzak. EMP characterization at PALS on solid-target experiments. *Plasma Phys. Control. Fusion*, 60(10), 2018.
- [137] J. Psikal, V. T. Tikhonchuk, J. Limpouch, and O. Klimo. Lateral hot electron transport and ion acceleration in femtosecond laser pulse interaction with thin foils. *Phys. Plasmas*, 17(1), 2010.
- [138] O. Tresca, D. C. Carroll, X. H. Yuan, B. Aurand, V. Bagnoud, C. M. Brenner, M. Coury, J. Fils, R. J. Gray, T. Kühl, C. Li, Y. T. Li, X. X. Lin, M. N. Quinn, R. G. Evans, B. Zielbauer, M. Roth, D. Neely, and P. McKenna. Controlling the properties of ultraintense laser-proton sources using transverse refluxing of hot electrons in shaped mass-limited targets. *Plasma Phys. Control. Fusion*, 53(10), 2011.
- [139] A. P.L. Robinson, A. V. Arefiev, and D. Neely. Generating "superponderomotive" electrons due to a non-wake-field interaction between a laser pulse and a longitudinal electric field. *Phys. Rev. Lett.*, 111(6):1–5, 2013.
- [140] SR Nagel. *Studies of Electron Acceleration Mechanisms in Relativistic Laser-Plasma Interactions*. PhD thesis, 2009.

- [141] S P D Mangles, C D Murphy, Z Najmudin, A G R Thomas, J L Collier, A E Dangor, E J Divall, P S Foster, J G Gallacher, C J Hooker, D A Jaroszynski, A J Langley, W B Mori, P A Norreys, F S Tsung, R Viskup, B R Walton, and K Krushelnick. Monoenergetic beams of relativistic electrons from intense laser plasma interactions. *Nature*, 431:535–538, 2004.
- [142] K W D Ledingham Galster and W. Laser-driven particle and photon beams and some applications. *New J. Phys.*, 2010.
- [143] G Sarri, W Schumaker, A Di Piazza, K Poder, J M Cole, and M Vargas. Laser-driven generation of collimated ultra-relativistic positron beams. 2013.
- [144] G Sarri, K Poder, J M Cole, W Schumaker, A Di Piazza, B Reville, T Dzelzainis, D Doria, L A Gizzi, G Grittani, S Kar, C H Keitel, K Krushelnick, S Kuschel, S P D Mangles, Z Najmudin, N Shukla, L O Silva, D Symes, A G R Thomas, M Vargas, J Vieira, and M Zepf. Generation of neutral and high-density electron-positron pair plasmas in the laboratory. *Nat. Commun.*, 6:1–8, 2015.
- [145] R M Deas, L A Wilson, D Rusby, A Alejo, R Allott, P P Black, S E Black, Laser Facility, and Stfc Rutherford. A laser driven pulsed X-ray backscatter technique for enhanced penetrative imaging. *J. Xray. Sci. Technol.*, 23:791–797Deas, R. M., Wilson, L. A., Rusby, D., Alej, 2015.
- [146] J M Cole, J C Wood, N C Lopes, K Poder, R L Abel, S Alatabi, and J S J Bryant. Laser-wakefield accelerators as hard x-ray sources for 3D medical imaging of human bone. *Sci. Rep.*, pages 1–7, 2015.
- [147] W P Leemans, A J Gonsalves, H Mao, K Nakamura, C Benedetti, C B Schroeder, Cs Tóth, J Daniels, D E Mittelberger, S S Bulanov, J Vay, C G R Geddes, E Esarey, and Lawrence Berkeley. Multi-GeV Electron Beams from Capillary-Discharge-Guided Subpetawatt Laser Pulses in the Self-Trapping Regime. 245002(December):1–5, 2014.
- [148] H K M Tanaka, T Nakano, S Takahashi, J Yoshida, and K Niwa. Development of an emulsion imaging system for cosmic-ray muon radiography to explore the

- internal structure of a volcano , Mt . Asama. *Nucl. Instruments Methods Phys. Res. A*, 575:489–497, 2007.
- [149] C L Morris, C C Alexander, J D Bacon, K N Borozdin, D J Clark, R Chartrand, C J Espinoza, A M Fraser, M C Galassi, J A Green, J S Gonzales, J J Gomez, N W Hengartner, G E Hogan, A V Klimenko, M F Makela, P Mcgaughey, J J Medina, F E Pazuchanics, W C Priedhorsky, J C Ramsey, A Saunders, R C Schirato, L J Schultz, M J Sossong, and G S Blanpied. Tomographic Imaging with Cosmic Ray Muons. *Taylor Fr.*, pages 37–53, 2008.
- [150] O Catalano, M Del Santo, T Mineo, G Cusumano, M C Maccarone, and G Pareschi. Volcanoes muon imaging using Cherenkov telescopes. *Nucl. Instruments Methods Phys. Res. A*, 807:5–12, 2016.
- [151] Hiroyuki K M Tanaka, Hideaki Taira, Tomihisa Uchida, Manobu Tanaka, Minoru Takeo, Takao Ohminato, Yosuke Aoki, Ryuichi Nishitama, and Daigo Shoji. Three dimensional computational axial tomography scan of a volcano with cosmic ray muon radiography. *J. Geophys. Res.*, 115, 2010.
- [152] C. Steera J. Burns, S. Quillin, M. Stapleton and S. Snow. A drift chamber tracking system for muon scattering tomography applications. *J. Instrum.*, 2015.
- [153] G. Bonomi, D. Cambiaghi, L. Dassa, A. Donzella, M. Subieta, V. Villa, A. Zenoni, M. Furlan, A. Rigoni, S. Vanini, G. Viesti, G. Zumerle, M. Benettoni, P. Checchia, F. Gonella, M. Pegoraro, P. Zanuttigh, G. Calvagno, P. Calvini, and S. Squarcia. Muon Tomography As a Tool To Detect Radioactive Source Shielding in Scrap Metal Containers. *Int. J. Mod. Phys. Conf. Ser.*, 27:1460157, 2014.
- [154] The CMS Collaboration. The performance of the CMS muon detector in proton proton collisions at $s = 7$ TeV at the LHC. *J. Instrum.*, 2014.
- [155] S. Weingarten O. Pooth, T. Radermacher and L. Weinstock. Scintillator tiles read out with silicon photomultipliers. Technical report, 2015.

- [156] Kondo Gnanvo, Leonard V Grasso, Marcus Hohlmann, Judson B Locke, Amilkar Quintero, and Debasis Mitra. Imaging of high- Z material for nuclear contraband detection with a minimal prototype of a muon tomography station based on GEM detectors. *Nucl. Instruments Methods Phys. Res. A*, 652:16–20, 2011.
- [157] Science & Technology Facilities Council. ISIS Neutron and Muon Source Annual Review 2018. Technical report, 2018.
- [158] Science & Technology Facilities Council. ISIS Neutron and Muon Source Annual Review 2019. Technical report, 2019.
- [159] Donald E. Groom, Nikolai V. Mokhov, and Sergei I. Striganov. Muon Stopping Power and Range Tables 10 MeV – 100 TeV. *At. Data Nucl. Data Tables*, 78(2):183–356, 2001.
- [160] P. A. Cherenkov. Visible luminescence of pure liquids under the influence of γ -radiation. *Dokl. Akad. Nauk SSSR*, 2(8):451–454, 1934.
- [161] T. Watanabe, M. Babzien, K. Kusche, and V. Yakimenko. Beam angle measurement using cherenkov radiation. In *Proceedings of the 2005 Particle Accelerator Conference*, pages 3742–3744, 2005.
- [162] Alan A. Watson. The discovery of cherenkov radiation and its use in the detection of extensive air showers. *Nuclear Physics B - Proceedings Supplements*, 212-213:13 – 19, 2011. Proceedings of the Cosmic Ray International Seminars (CRIS 2010).
- [163] I.M. Frank and I.E. Tamm. Coherent visible radiation of fast electrons passing through matter. *Compt.\ Rend.\ Acad.\ Sci.\ URSS*, 14(3):109—114, 1937.
- [164] James F Ziegler, M D Ziegler, and J P Biersack. Nuclear Instruments and Methods in Physics Research B SRIM The stopping and range of ions in matter (2010). *Nucl. Inst. Methods Phys. Res. B*, 268:1818–1823, 2010.
- [165] JK Patel, D Symes, E Zemaityte, R Gray, R Deas, D Neely, and CD Armstrong. Obtaining absolute number of Cherenkov photons by angular calibration of a

fused silica scatter screen. Technical report, Rutherford Appleton Laboratory, 2020.

- [166] Jiangning Zhou and Bincheng Li. Origins of a damage-induced green photoluminescence band in fused silica revealed by time-resolved photoluminescence spectroscopy. *Opt. Mater. Express*, 7(8):2888, 2017.
- [167] J. Fournier, J. Néauport, P. Grua, E. Fargin, V. Jubera, D. Talaga, and S. Jouanigot. Evidence of a green luminescence band related to surface flaws in high purity silica glass. *Opt. Express*, 18(21):21557, 2010.
- [168] Kadir Aslan and Chris D Geddes. Directional Surface Plasmon Couples Luminescence for Analytical Sensing Application: Which Metal, What Wavelength, What Observation Angle? *Anal. Chem.*, 81:6913–6922, 2009.
- [169] Bobbili Sanyasi Rao, Jong Ho Jeon, Hyung Taek Kim, and Chang Hee Nam. Bright muon source driven by GeV electron beams from a compact laser wakefield accelerator. *Plasma Phys. Control. Fusion*, 60(9), 2018.